Vitaly Yu. Topolov

Heterogeneous Ferroelectric Solid Solutions

Phases and Domain States

Second Edition



Springer Series in Materials Science

Volume 151

Series editors

Robert Hull, Troy, USA
Chennupati Jagadish, Canberra, Australia
Yoshiyuki Kawazoe, Sendai, Japan
Richard M. Osgood, New York, USA
Jürgen Parisi, Oldenburg, Germany
Udo W. Pohl, Berlin, Germany
Tae-Yeon Seong, Seoul, Republic of Korea (South Korea)
Shin-ichi Uchida, Tokyo, Japan
Zhiming M. Wang, Chengdu, China

The Springer Series in Materials Science covers the complete spectrum of materials physics, including fundamental principles, physical properties, materials theory and design. Recognizing the increasing importance of materials science in future device technologies, the book titles in this series reflect the state-of-the-art in understanding and controlling the structure and properties of all important classes of materials.

More information about this series at http://www.springer.com/series/856

Vitaly Yu. Topolov

Heterogeneous Ferroelectric Solid Solutions

Phases and Domain States

Second Edition

With 47 Figures



Vitaly Yu. Topolov Department of Physics Southern Federal University Rostov-on-Don Russia

ISSN 0933-033X ISSN 2196-2812 (electronic) Springer Series in Materials Science ISBN 978-3-319-75519-9 ISBN 978-3-319-75520-5 (eBook) https://doi.org/10.1007/978-3-319-75520-5

Library of Congress Control Number: 2018932171

1st edition: © Springer-Verlag Berlin Heidelberg 2012

2nd edition: © Springer International Publishing AG, part of Springer Nature 2018

This work is subject to copyright. All rights are reserved by the Publisher, whether the whole or part of the material is concerned, specifically the rights of translation, reprinting, reuse of illustrations, recitation, broadcasting, reproduction on microfilms or in any other physical way, and transmission or information storage and retrieval, electronic adaptation, computer software, or by similar or dissimilar methodology now known or hereafter developed.

The use of general descriptive names, registered names, trademarks, service marks, etc. in this publication does not imply, even in the absence of a specific statement, that such names are exempt from the relevant protective laws and regulations and therefore free for general use.

The publisher, the authors and the editors are safe to assume that the advice and information in this book are believed to be true and accurate at the date of publication. Neither the publisher nor the authors or the editors give a warranty, express or implied, with respect to the material contained herein or for any errors or omissions that may have been made. The publisher remains neutral with regard to jurisdictional claims in published maps and institutional affiliations.

Printed on acid-free paper

This Springer imprint is published by the registered company Springer International Publishing AG part of Springer Nature

The registered company address is: Gewerbestrasse 11, 6330 Cham, Switzerland

Preface

A solid-solution series is the continuous sequence of substances with compositions intermediate between two distinct mineral phases, called end members. In a solid-solution series, the components may be thought to substitute for one another on a molecular level in the crystal structure; the intermediate members have properties that vary continuously with composition from those of one end member to those of another. Solid-solution series are said to be complete if examples of complete variation exist in nature or have been synthesized in the laboratory...

... only the appearance of the computer provided a qualitative jump and made it possible to perform effective study of really complex systems in various areas of knowledge. Actually, the concern is with coarse qualitative criteria, differentiating simple systems from complex; if the structure and behaviour of a system can be studied by a single man in a reasonable time, the system is called simple. If the efforts of many persons and the use of special technical equipment (computers) are required to draw the whole picture, the system is called complex.

Encyclopædia Britannica Ultimate Reference Suite

In the last decades, crystallographic and compositional engineering has become an important tool in the development of functional materials and in enhancing their physical properties and related parameters. Ferroelectrics represent a vast class of modern functional materials that find applications from medical equipment to aeronautics. Intricate domain, twin and heterophase structures, sequences of structural phase transitions (mainly the first-order phase transitions), complex systems of solid solutions with different structural and polar orderings and outstanding electromechanical properties in the poled state make ferroelectric materials attractive for basic research within the framework of the well-known dependency triangle of 'composition-structure-properties'. As is known from numerous experimental studies, the first-order phase transitions in ferroelectrics are characterized by jumps of the spontaneous polarization, unit-cell parameters, by heterophase states concerned with an internal mechanical field, etc. The present book is intended to discuss recent experimental and theoretical results on heterophase states and to provide crystallographic interpretations of heterophase structures in the ferroelectric solid solutions, especially in the presence of heavily twinned phases.

vi Preface

The most studied group of ferroelectric solid solutions is characterized by the perovskite-type structure (from the mineral perovskite, CaTiO₃). Components of these solid solutions are perovskite oxides with a composition ABO₃, where A and B are cation elements or mixtures of two or more such elements, or vacancies. The importance of ferroelectric perovskite-type materials is concerned with the almost unlimited isomorphism of their crystal structure. As a consequence, a continuous change in the composition, structural characteristics and physical properties is achieved by substitution of different elements at equivalent positions (A and/or B). The isomorphism favours the formation of the ferroelectric solid solutions with properties that can be varied within a wide range. It should be added that many of the ferroelectric perovskite-type solid solutions exhibit excellent piezoelectric and pyroelectric properties, and such a performance makes these materials the important group of modern active dielectrics. Experimental data on various perovskite-type solid solutions show that the heterophase states in these materials are observed in certain ranges of temperature, composition and electric field strength, where volume densities of free energy of the coexisting phases are approximately equal. Recent studies on the representative perovskite-type solid solutions (for instance, ferroelectric Pb(Zr_{1-x}Ti_x)O₃, KNbO₃-based and BaTiO₃-based, and relaxor-ferroelectric $(1 - x)Pb(L_{1/3}Nb_{2/3})O_3 - xPbTiO_3$ with L = Mg or Zn) show that the heterophase states therein are of particular interest because of the presence of intermediate phases and their considerable influence on the physical properties, phase coexistence and stress relief near the morphotropic phase boundary. In comparison to the first edition [1], the second edition contains the new chapter devoted to heterophase lead-free ferroelectric solid solutions and features of domain states and phase contents in these materials (see Chap. 6). Lead-free ferroelectric and piezoelectric materials are under intensive studies and become attractive due to their physical properties [2, 3] that are comparable to many lead-containing materials [4]. It is believed that such a 'competition of properties' will influence the research subjects in the field of ferroelectrics and related materials. The inclusion of new results on the domain states and phase contents in Chap. 6 makes the second edition of the book many-sided in the research sense and enables the readers to consider the well-known dependency triangle of 'composition-structure-properties' from a new viewpoint.

The present book has been written on the basis of the author's research results obtained mainly at the Rostov State University (Russia, until December 2006), Southern Federal University (Russia, since December 2006) and Karlsruhe Research Centre (Germany, 2003–04). The academic style of presentation of the results and the discussion about them indicate that the book would be useful to researchers, engineers, postgraduate students and lecturers working in the field of ferroelectrics, ferroelastics, multiferroics and other modern functional materials. The present book fills a gap in materials science, crystallography of ferroelectrics and related materials and in physics of heterogeneous ferroelectrics and, therefore, will be of benefit to all specialists looking to understand behaviour and physical

Preface vii

properties of modern heterogeneous materials suitable for various applications. Some chapters and sections of the book could serve as a basis for a university course devoted to ferroelectric solid solutions.

Rostov-on-Don, Russia November 2017 Prof. Dr. Vitaly Yu. Topolov

References

- Topolov VYu (2012) Heterogeneous ferroelectric solid solutions. Phases and domain states. Springer, Berlin, Heidelberg
- 2. Priya S, Nahm S (eds) (2012) Lead-free piezoelectrics. Springer, New York Dordrecht Heidelberg London
- 3. Hong C-H, Kim H-P, Choi B-Y, Han H-S, Son J S, Chang W A, Jo W (2016) Lead-free piezoceramics where to move on? J Materiomics 2:1–24
- 4. Xu Y (1991) Ferroelectric materials and their applications. North-Holland, Amsterdam London New York Toronto

Acknowledgements

The author is grateful to Prof. Dr. A. V. Turik, Prof. Dr. V. G. Gavrilyachenko, Prof. Dr. A. E. Panich, Prof. Dr. V. P. Sakhnenko, Prof. Dr. O. E. Fesenko, Prof. Dr. A. A. Nesterov, Dr. V. V. Eremkin, Dr. A. F. Semenchev, Dr. V. G. Smotrakov, and Dr. V. A. Shuvaeva (Southern Federal University, Russia), Prof. Dr. O. Kraft and Prof. Dr. M. Kamlah (Karlsruhe Institute of Technology, Germany), Prof. Dr. B. Noheda (University of Groningen, The Netherlands), Prof. Dr. A. M. Glazer (University of Oxford, UK), Prof. Dr. C. R. Bowen (University of Bath, UK), Prof. Dr. E. K. H. Salje (University of Cambridge, UK), Prof. Dr. D. Pandey (Banaras Hindu University, India), Prof. Dr. R. Ranjan (Indian Institute of Science, Bangalore, India), Prof. Dr. D. Viehland and Dr. H. Cao (Virginia Tech, VA, USA), Prof. Dr. A. S. Sidorkin and Prof. Dr. B. M. Darinsky (Voronezh State University, Russia), and Prof. Dr. L. N. Korotkov and Prof. Dr. S. A. Gridnev (Voronezh State Technical University, Russia) for their interest in the research problems and for their important papers that have been cited in the present book.

The author expresses his sincere gratitude to Prof. Dr. C. Ascheron and Mrs. E. Sauer (Springer, Germany) for their effective and timely cooperation in the field of editing and producing the second edition of the book. The author is also grateful to Prof. Dr. C. R. Bowen and Dr. R. W. C. Lewis (University of Bath, UK) for their careful reading of the manuscript. Copyright permissions obtained from American Institute of Physics (www.aip.org), American Physical Society (www.aps.org), Elsevier (www.elsevier.com), IOP Publishing (www.iop.org), Pleiades Publishing (www.maik.ru), Taylor & Francis (www.tandfonline.com) and Wiley-VCH (www.wiley-vch.de) are acknowledged with due gratitude and formulations.

Financial support that promoted the fruitful research collaboration and writing this book is gratefully acknowledged. Hereupon gratefully and proudly the author would like to mention the timely and effective support from the Karlsruhe Research Centre (now Karlsruhe Institute of Technology, Germany), Helmholtz Society (Germany) and Rostov State University (now Southern Federal University, Russia). In the present book, the results on the research project No. 11.1627.2017/4.6 PCh

x Acknowledgements

have been represented within the framework of the state task in the scientific activity area at the Southern Federal University. This research has been performed by using the equipment of the Centre of Collective Use 'High Technologies' at the Southern Federal University.

Contents

1	Cry	stallogi	aphic Aspects of Interfaces in Ferroelectrics				
	and	Relate	d Materials	1			
	1.1	Domain Structures and Interfaces Between Polydomain					
		Regions					
		1.1.1	Formation of Domain Structures in Ferroelectric				
			Single Crystals	2			
		1.1.2	Elastic-Matching Concept and Its Application				
			to Domain Boundaries	4			
		1.1.3	Classification of Domain Boundaries in Ferroelectric				
			Single Crystals	8			
		1.1.4	Crystallographic Interpretation of Interfaces Between				
			Complicated Domain Structures	9			
	1.2	Phase	Coexistence at First-Order Phase Transitions	13			
		1.2.1	Elastic Matching of Phases and Zero-Net-Strain				
			Planes	13			
		1.2.2	Stress Relief and Conical Interphase Boundaries	17			
		1.2.3	Three-Phase States	19			
	1.3	Polyde	omain/Heterophase Ferroelectrics	20			
	Refe	erences		21			
2	Two	Dhaca	States	25			
_	2.1		e Matching of Morphotropic Phases in $Pb(Zr_{1-x}Ti_x)O_3$	27			
	2.1	2.1.1		21			
		2.1.1	Crystallographic Interpretation	27			
		2.1.2		21			
		2.1.2	of the Intermediate Monoclinic Phase	30			
	2.2	Dhace	Coexistence in $(1 - x)$ Pb $(Mg_{1/3}Nb_{2/3})$ O_3 – x PbTi O_3	50			
	2.2		the Morphotropic Phase Boundary	34			
		2.2.1	Phase Coexistence Without the Monoclinic Phase	34			
		2.2.2	Phase Coexistence in the Presence of the Intermediate	54			
		۷.۷.۷		39			
			Monoclinic Phases	39			

xii Contents

		2.2.3 Effect of Non-180° Domains on Phase Coexistence	41
	2.2	2.2.4 Different Scenarios of Stress Relief	47
	2.3	Model of Interpenetrating Phases: Application	
		to $(1 - x)$ Pb $(Mg_{1/3}Nb_{2/3})O_3$ - x PbTi O_3 Near the	
		Morphotropic Phase Boundary	51
	2.4	Domain and Heterophase States in $(1 - x)Pb(Zn_{1/3}Nb_{2/3})O_3$	
		xPbTiO ₃ Near the Morphotropic Phase Boundary	55
		2.4.1 Phase Transitions and Intermediate Phases	55
		2.4.2 Crystallographic Study of Elastic Matching of	
		Morphotropic Phases	57
		2.4.3 Interpenetrating Phases in 0.90Pb(Zn _{1/3} Nb _{2/3})O ₃ –	
		0.10PbTiO ₃ Single Crystals	60
	2.5	Two-Phase States and Stress Relief in Ferroelectric	
		Solid Solutions	62
	Refe	rences	63
3	Pha	se Coexistence Under Electric Field	69
	3.1	Heterophase Pb(Mg _{1/3} Nb _{2/3})O ₃ at the Induced Phase	0)
	5.1	Transition	69
	3.2	Domain State–Interface Relationships at Electric	0)
	3.2	Field <i>E</i> [001]	72
		3.2.1 Heterophase $(1 - x)Pb(Mg_{1/3}Nb_{2/3})O_3 - xPbTiO_3$	72
		3.2.2 Heterophase $(1 - x)Pb(Zn_{1/3}Nb_{2/3})O_3 - xPbTiO_3$	81
	3.3	Domain State–Interface Relationships at Electric	01
	5.5	Field <i>E</i> [110]	87
	3.4	Domain State–Interface Relationships at Electric	07
	J. T	Field <i>E</i> [111]	89
	3.5	Role of Intermediate Phases in Heterophase States	95
		prences	96
4	Thre	ee-Phase States	99
	4.1	Model of Three-Phase Single Crystal	100
	4.2	Application of Model Concepts to PbZrO ₃ and Pb($Zr_{1-x}Ti_x$)O ₃	
		$(x \approx 0.22) \ldots \ldots \ldots \ldots$	102
		4.2.1 Phase Coexistence in PbZrO ₃ Single Crystals	102
		4.2.2 Phase Coexistence in $Pb(Zr_{1-x}Ti_x)O_3$ Single Crystals	
		$(x \approx 0.22) \dots $	104
	4.3	Application of Model Concepts to $(1 - x)Pb(Mg_{1/3}Nb_{2/3})O_3$	
		<i>x</i> PbTiO ₃	104
	4.4	Three-Phase Coexistence and Complete Stress Relief	
		in $(1 - x)$ Pb $(Zn_{1/3}Nb_{2/3})O_3 - x$ PbTi O_3	106
	4.5	Thermodynamic Description of Three-Phase States	
		in Ferroelectric Solid Solutions	110

Contents xiii

	4.6		ographic and Thermodynamic Studies	117
	Dafa		Phase States	117 118
5	Ove		Structures and Transition Regions	121
	5.1		ping Structures in Pb(Zn _{1/3} Nb _{2/3})O ₃	121
	5.2		rface Relationships in $Pb(Zn_{1/3}Nb_{2/3})O_3 \dots$	123
	5.3		on Regions in $(1 - x)Pb(Zn_{1/3}Nb_{2/3})O_3 - xPbTiO_3 \dots$	127
	5.4		elief at Variable Unit-Cell Parameters	131
	Refe	rences		132
6	Rela	tions Bet	tween Domain States and Heterophase Structures	
			Ferroelectric Solid Solutions	135
	6.1		oexistence in $(1 - x)(Na_{1/2}Bi_{1/2})TiO_3 - xBaTiO_3 \dots$	136
		6.1.1 D	Domain States and Elastic Matching of Phases	136
		6.1.2 P	Phase Contents Near the Morphotropic Phase	
		В	Boundary	137
			Anisotropy of Unit-Cell Distortions and Heterophase	
		S	Structures	141
	6.2	Phase Co	oexistence in $Ba(Ti_{1-x}Ce_x)TiO_3$	141
		6.2.1 R	Relations Between Domain and Heterophase States	
			Near the Morphotropic Phase Boundary	142
		6.2.2 A	Anisotropic Spontaneous Strains and Stress-Relief	
			Conditions	145
	6.3		of Heterophase States in $Ba(Ti_{1-x}Zr_x)O_3$ and Related	
			olutions	145
	6.4		States and Phase Contents in $Ba(Ti_{1-x}Sn_x)O_3$	
			$\Gamma_{1-x}Hf_x$)O ₃ Near the Morphotropic Phase Boundary	153
	6.5	Behavior	ur of Unit-Cell Parameters and Heterophase Structures	158
	Refe	rences		159
7	Fron	n a Unit	Cell to Morphotropic Polydomain/Heterophase	
				163
	7.1		Domain and Heterophase Structures	163
	Refe	•	*	166
A ==	nond	s A. Mo	ethods for Description of Heterophase	
Αþ	pena		d Polydomain Single Crystals	167
		and	1 Torydolliani Single Crystais	107
Ap	pend	_	timal Volume Fractions in Terms of	
			gles Between Spontaneous Polarization Vectors	
		Nea	ar the Morphotropic Phase Boundary	183
Ab	out t	he Autho	or	189
Inc	dex .			191

Abbreviations

BT BaTiO₃

DS Domain structure FE Ferroelectric

 $\begin{array}{ll} M_A & Monoclinic \ phase \ of \ the \ A-type \\ M_B & Monoclinic \ phase \ of \ the \ B-type \\ M_C & Monoclinic \ phase \ of \ the \ C-type \\ MPB & Morphotropic \ phase \ boundary \end{array}$

NBT $(Na_{1/2}Bi_{1/2})TiO_3$

NBT-xBT System of ferroelectric solid solutions of

 $(1 - x)(Na_{1/2}Bi_{1/2})TiO_3 - xBaTiO_3$

PCR Piezoelectric ceramic from Rostov-on-Don (Russia)

PMN $Pb(Mg_{1/3}Nb_{2/3})O_3$

PMN-xPT System of relaxor-ferroelectric solid solutions of

 $(1 - x)Pb(Mg_{1/3}Nb_{2/3})O_3 - xPbTiO_3$

PZN $Pb(Zn_{1/3}Nb_{2/3})O_3$

PZN-xPT System of relaxor-ferroelectric solid solutions of

 $(1 - x)Pb(Zn_{1/3}Nb_{2/3})O_3 - xPbTiO_3$

PZT System of ferroelectric solid solutions of $Pb(Zr_{1-x}Ti_x)O_3$

SC Single crystal

ZNSP Zero-net-strain plane

ZTS Piezoelectric ceramic of the Pb(Zr, Ti)O₃ type (Russia)

Chapter 1 Crystallographic Aspects of Interfaces in Ferroelectrics and Related Materials



Abstract Analysis of results on the study and classification of various interfaces in polydomain and heterophase ferroelectric single crystals and related materials is carried out. Classification of domain boundaries in ferroelectric single crystals is highlighted. An emphasis is placed on crystallographic methods that can be applied to study complicated domain (twin) structures and their rearrangement, heterophase states, features of the formation of the new phase, etc., in ferroelectric solid solutions. Examples of complete stress relief and zero-net-strain planes at the interphase boundaries in two-phase single crystals are discussed for many cases of first-order phase transitions.

Experimental studies of single crystals (SCs) of polar dielectrics show that, in an external electric field E, these materials can exhibit either linear or nonlinear behaviour [1, 2]. A nonlinear dependence of the polarization P on E in a certain range of E is observed, for instance, in ferroelectric (FE) and antiferroelectric SCs [1, 3, 4], poled ceramics, and SCs of FE solid solutions [3, 4] and composites based on FE ceramics [5]. The presence of FE and ferroelastic domains (or mechanical twins), heterophase regions and fluctuations of composition make the P(E) dependence complicated and is caused by many physical and crystallographic factors that are studied in the last decades [1, 3, 4]. Moreover, the dependence of physical properties on domain structure (DS) in FE SCs and ceramic grains represents an independent problem that is solved by means of experimental and theoretical methods [6–8]. An interest in the aforementioned subjects stems from a necessity to study an important link between the domain configurations and physical properties of FEs, to consider the role of the domain-orientation processes in forming the physical properties, to describe their anomalies in heterophase states on mesoscopic and macroscopic levels, and to predict ways for the formation and rearrangement of DS at the structural phase transitions. To solve these and related problems, it is important to understand the physical phenomena that are concerned with the presence of both DS and heterophase states in FEs. One of the main links in the interpretation of the physical phenomena in polydomain and/or heterophase FE SCs is the interfaces [9] that represent systems of boundaries between the domains (or domain regions) and boundaries between the phases (they can be split into domains). It should be added that the polydomain SC as a model object plays the leading role in the hierarchy of the physical properties 'single-domain FE SC—polydomain FE SC—FE polycrystal—poled FE ceramic—composite based on FE ceramic', and an important example of this hierarchy was first analysed for FEs of the PbTiO₃ type [7, 8, 10].

This chapter is devoted to the analysis of some important results in the study and classification of various interfaces that are observed in polydomain and heterophase FE SCs and related materials. An emphasis is placed on crystallographic methods [9] that are applied to study complicated DSs and their rearrangement, heterophase states, features of the formation of the new phase, etc., in FE solid solutions.

1.1 Domain Structures and Interfaces Between Polydomain Regions

1.1.1 Formation of Domain Structures in Ferroelectric Single Crystals

Below the temperature of the FE phase transition many SCs are split into domains, or regions with different orientations of the spontaneous polarization vector P_s [1–3]. The FE domains are also regarded as macroscopic regions wherein the unit cells have parallel orientations of the spontaneous dipole moments at E=0. An aggregate of the domains divided by the interfaces (domain walls, boundaries between the domain regions, etc.) constitutes DS observed and described in experimental works (see, e.g. monographs [1–4, 11–13]). Analogous regions corresponding to certain orientations of the spontaneous polarization vectors of the sublattices $\pm P_a$ are observed in antiferroelectric SCs [2, 3, 13]. The regions with different tensors of spontaneous strains in an initial co-ordinate system form ferroelastic SCs that are often regarded as mechanical analogues of FEs [12].

The first principal propositions on a correlation between the orientation of the FE domains, domain walls and macrosymmetry of the physical properties of the SC sample were formulated by Zheludev and Shuvalov [14–19]. In the absence of external influences, such as electric or mechanical fields, the appearance of the FE domains is equally probable along each of the crystallographically equivalent directions that are regarded as polar axes. FE SCs are traditionally divided into two groups in accordance with the number of polar axes [2, 3, 11, 13]. The first group contains electrically uniaxial SCs that are divided only into the 180° domains with antiparallel spontaneous polarization directions, $+P_s$ and $-P_s$. The second group represents electrically multiaxial SCs with non-180° domains oriented along the crystallographically equivalent directions in the FE phase. In the second group, the 180° domains are present side by side with the non-180° domains. The number of permissible orientations of the spontaneous polarization vectors is $n = N_1/N_2$, where N_1 and N_2 are orders of the point symmetry group of the prototype phase and the

domain (twin component), respectively. If all the possible domain types are present in the SC sample in equal volume fractions, then this sample is characterized by the same point symmetry group as in the prototype phase [2, 13, 18, 19]. However, not all the domain types can be observed in real SCs [11, 13] because of an influence of crystal-growth conditions, phase-transition kinetics, external fields, etc.

Changes in the energy of the system at the structural phase transition are main reasons for the domain formation in FE SCs. According to results [1–3, 11], the reason for 180° -domain formation is jump of the depolarizing field at the first-order phase transition, and the reason for non- 180° domain formation is the jump of the spontaneous strains of the SC unit cell. Both the jumps are caused by a change in the spontaneous polarization P_s at the phase transition. In a case of the paraelectric-FE first-order phase transition, the jump of P_s (from 0 to a certain value) takes place at Curie temperature T_C . Various 180° domain patterns are formed under the influence of an internal electric field and by a screening of the spontaneous polarization by free charge carriers in the SC sample [11]. The domain-formation processes lead to a minimization of an electric contribution to the free energy of the SC sample [20]. The electric contribution comprises the volume energy of the depolarizing field of the sample as a whole and the surface energy of domain walls or domain boundaries therein.

Theoretical concepts on domain walls and the formation of DSs [21] at the first-order phase transition are based on the determination of the effective free energy as a function of the polarization field. This approach is useful, for example at the description of the effect of the elastic strain on the non-180° DS that takes place, for example, in the tetragonal phase of perovskite-type FEs (BaTiO₃, PbTiO₃, KNbO3, etc.) and related solid solutions. The free energy of FE SC depends on inhomogeneous regions, such as domain walls and modulated structures. Based on the thermodynamic study of the free energy of FE, Cao [22] analysed inhomogeneous microstructures in the FE phase of solid solutions of $(Pb_{1-3x/2}La_x)TiO_3$. In a certain x range, these inhomogeneous microstructures represent spatial amplitude modulations inside domains of this system, and the development of the modulated structure is caused by La dopants. A time evolution of the 90° DS in FE was predicted in work [23]. As follows from results [23], the elastic long-range interactions between the polarization fields lead to a lamellar 90° DS (mechanical twins) and frozen domain patterns which are observed in a series of FE SCs. The model proposed in paper [24] enables one to describe the lamellar or spiked morphology of the 180° domains in FE SCs by taking into account the electrostatic interaction. The model concept [24] is applied for a prediction of trends in the formation (or subsequent rearrangement) of the DS in the presence of the external electric field.

Experimental results on the formation of 180° and 90° DSs in the tetragonal phase of multiaxial FE SCs of the perovskite type at the first-order phase transition were generalized by Fesenko et al. [11]. According to experimental data, the FE phase in BaTiO₃ SCs is split into both the 180° and 90° domains near the Curie temperature $T_{\rm C} = 393$ K. The corresponding DS being formed in the BaTiO₃ SC sample, wherein a planar interphase boundary moves at the paraelectric–FE phase transition, remains almost unchanged on cooling down to room temperature. Rules

in the formation of the DS are formulated [11] with due regard for jumps of the depolarizing field, spontaneous strains and entropy at the first-order phase transition. These jumps are caused by the jump of the spontaneous polarization $P_s(T_C)$. Based on numerous experimental results, Fesenko et al. proposed a classification of domain patterns [11] affected by the jumps of the physical parameters in multiaxial FE SCs. In this classification, some interconnections between the jumps are taken into account. In addition to the electric and elastic fields, that are directly concerned with complex DSs in multiaxial FE SCs, the latent heat also influences [11] phase-transition kinetics, the motion of the interphase boundary [25] over the SC sample and the formation of the DS.

Taking into consideration numerous experimental results on polydomain (twinned) FE SCs [1–4, 11, 25], one can mention the following factors that actively influence the formation of the DS: electrostatic energy of the depolarizing field of SC, electric conductivity of SC at the phase transition, elastic energy concerned with the phase coexistence and defects, surface energy of domain wall (boundaries), anisotropy of the physical properties, the simultaneous formation of a number of nuclei of the new phase, external electric and/or elastic fields, temperature gradient over the SC sample and cooling rate of this sample undergoing the FE phase transition. Examples of the quantitative description of the influence of the separate factors on the formation of the 180° and non-180° DSs are present in monographs [1–3, 11].

1.1.2 Elastic-Matching Concept and Its Application to Domain Boundaries

The elastic interaction between the phases in SCs [26] and between the domains in the FE phase plays the important role in the formation of DS [11, 25] with various planar, wedge-shaped, zigzag or diffused interfaces. The domains that are observed near these interfaces are mainly non-180° and promote minimization of an elastic contribution into the free energy of the SC sample. In contrast to the traditional 180° (FE) domains, these domains are often termed 'elastic domains' [26] or 'twins' [11]. Moreover, aggregates of the plane-parallel twins form a polysynthetic twin (polytwin), and the polysynthetic twin can be a part of a more complicated hierarchical structure (polysandwich structure) in SC samples. As noted by Roytburd [26], the polysandwich structure is characteristic of many phase-transition types in solids, for instance martensitic, ferroelastic, ordering, diffusion and decomposition types. The polysandwich structure can be detected in SCs that undergo both the first-order and second-order phase transitions. Decreasing the elastic energy at the formation of the new phase in solids can be concerned with the integration of DSs, or in other words, with the formation of hierarchical DSs. Hereby the polytwins serve as individual domains and form DSs of the second order, third order, etc. [26].

The study of the formation of DS in FE SCs is often carried out in terms of crystallographic [9, 27] and thermodynamic [26, 28, 29] theories. Lowering the energy of the internal mechanical stress field associated with the phase coexistence leads to the certain (preferable) orientation of the nucleus of the new phase or the interphase boundary and to the formation of equilibrium DSs. Theoretical studies [28] show that the plate-like shape of the nucleus of the new phase provides the maximum localization of the elastic field at the structural phase transition. The equilibrium DS is one of the milestones in the interpretation of experimental data on phase transitions of the martensitic type [11, 25], i.e. the first-order phase transitions going through a coherent heterophase state [29] at the jump in unit-cell strains. According to the idea developed in work [30-32], the new polydomain phase retains its contact with the parent phase, and consequently, the interphase boundary must be undistorted (or unstrained) on average. This boundary, being one of the interfaces studied in solids, is termed 'zero-net-strain plane' (ZNSP) [9, 27], 'invariant plane' [26], 'plane of the zero averaged distortion' [30, 31], or 'stress-free plane'. The zero-averaged distortion means that averaging the elements of distortion matrices is carried out over a macroscopic volume that involves a large number of domains within a specific phase.

The authors of papers [29–31] considered important examples of the martensitic phase transitions in metals and alloys. A reconstruction of the crystal structure at these phase transitions is associated with a strain field that give rise to changes in the shape of the sample, and atomic displacements therein are less than the unit-cell parameters. While this transformation does not need a diffusion of atoms at a large distance, the martensitic phase transition is often regarded as diffusionless. The twins appearing at the martensitic phase transition are regarded rather as elastic domains [26] than as a result of deformation twinning of the martensitic phase. In the last decades, the phase transitions of the martensitic type were studied not only in metals and alloys, but also in molecular SCs, ferroelastics, FEs and antiferroelectrics [11]. Examples of the application of the concepts of the martensitic phase transition to the FE phase transition in perovskite-type SCs are given in monograph [11]. The martensitic phase transitions that lead to polydomain structures with the non-zero elastic energy (i.e. without the formation of ZNSPs) were studied in terms of thermodynamics [29].

The presence of the interphase boundary, that obey conditions for ZNSPs at the first-order phase transition means, that the excessive elastic energy concerned with the jumps of the unit-cell parameters of SC vanishes in the heterophase state. It is also assumed that the interphase boundary remains coherent at the phase transformation [32, 33]. As noted by Larché [33], the concept of coherency is crystallographic in nature. Lowering the elastic energy and, as a consequence, the minimization of the free energy of the heterophase system undergoing the structural phase transition may be concerned with the loss of coherency and twinning. In case of loss of coherency, systems of dislocations and cracks [33] can arise in solids to give rise to considerable stress relief at the phase transition.

The crystallographic description of the interphase boundary at the first-order phase transition was proposed in a series of papers (see, e.g. [30, 31]). According to results [30, 31], the ZNSP with an optimal orientation arises from conditions for complete stress relief in the two-phase SC sample. Vanishing the elastic energy means that the new phase (with lower symmetry) is split into domains of two types, and these domains are mechanical twin components. Optimal volume fractions of the domain types are determined in terms of the unit-cell parameters of the coexisting phases [30, 31] or in terms of spontaneous strains [11, 27] of the low-symmetry phase. The further mathematical modification of the crystallographic method by means of transformation distortion matrices was made by many authors, for example Bilby and Christian [32] and Boulesteix et al. [34]. The infinitesimal deformation approach and simple analytical solutions for interphase boundaries [35] make the crystallographic method more attractive for analysis of relationships between the parent and product phases in solids.

The problem of the existence of a planar unstrained interphase boundary between a prototype paraelastic phase and a ferroelastic phase was solved in work [34]. Based on this solution, Boulesteix et al. determined all possible orientations of the interphase boundaries in the analytical form. The general solution is realized [34] for phase transitions without a change in the unit-cell volume. Among 30 variants of the symmetry changes at the ferroelastic phase transitions in SCs, one can choose 8 variants that correspond to exact solutions suitable for determination of the interphase-boundary orientations. In other cases, the planar interphase boundary would appear at certain restrictions on the spontaneous strain tensor components. Results of the theoretical study are experimentally corroborated for a sequence of phase transitions in ferroelastic SCs [34, 36]. We note that the approach developed in papers [34, 36] can be effectively applied for the crystallographic interpretation of the interfaces in FE SCs.

The crystallographic method for the description of the two-phase SCs and formation of domains was developed in a series of papers (see, e.g. [37–42]). The allowable domain walls are determined to be walls that do not create long-range electric and elastic fields in FE SCs [37]. The absence of elastic fields is also required for domain walls that arise in the antiferroelectric and ferroelastic SCs [40]. This general requirement will be one of the principal conditions at the consideration of different interfaces in our monograph.

Permissible domain-wall orientations and possible types of corresponding walls related to all FE species were first determined by Fousek and Janovec [37–39]. It is assumed that in the FE species, the polarization is the order parameter of the phase transition. In an infinite and perfect FE SC, the condition for elastic matching between two domains with spontaneous polarization vectors $P_{s'}$ and $P_{s''}$ along the domain wall requires that the length of an elementary vector $ds(ds_1, ds_2, ds_3)$ remains unchanged when crossing the domain wall. It means that the components of the vector ds obey condition [37].

$$hds_1 + kds_2 + lds_3 = 0,$$
 (1.1)

where (hkl) are Miller indices of the unstrained domain wall. Equation (1.1) can be written in terms the physical properties of the adjacent domains with P_s and P_s as follows:

$$\sum_{k,l=1}^{3} \Delta_{kl} ds_k ds_l = 0, \tag{1.2}$$

where the coefficients Δ_{kl} from (1.2) are given by

$$\Delta_{kl} = \sum_{i=1}^{3} g_{ikl}(P'_i - P''_i) + \sum_{i,j=1}^{3} Q_{ijkl}(P''_i P''_j - P'_i P'_j). \tag{1.3}$$

In (1.3), the piezoelectric coefficients g_{ikl} link the mechanical strain and electric displacement [2, 3] in the single-domain state and Q_{ijkl} are electrostrictive coefficients that link the mechanical strain and squared polarization [2] of the single-domain SC. Fousek and Janovec [37] described the FE domain walls of W_{∞} - and W_f -types with arbitrary (∞) and fixed (f) orientations, and a few kinds of the S-type walls that can be observed in polydomain FE SCs. The S-type domain walls have orientations [37] depending on directions of P_s ' and P_s ", values of g_{ikl} and/or Q_{ijkl} from (1.3). Tables of allowed orientations for the domain walls in all crystallographic species of SCs are given in paper [37].

The determination of the permissible domain walls and their orientations in ferroelastic SCs is carried out using (1.1), (1.2) and condition [40]

$$\det \|\Delta k l'\| = 0, \tag{1.4}$$

where $\Delta_{kl}' = S_{kl}' - S_{kl}''$ is the difference between the tensor components of the spontaneous strains S_{kl}' and S_{kl}'' in the unit cells that belong to the adjacent domains (twin components). The tensor components S_{kl}' and S_{kl}'' correspond to the co-ordinate axes of the prototype phase of the SC sample. Taking into account (1.4) and symmetry features of the domains, Sapriel determined the following types of the permissible planar domain walls [40]: W-walls with invariable orientations and W'-walls with orientations depending on the relative values of S_{kl}' and S_{kl}'' . It should be added that the methods [37–40, 43] for determination of the domain-wall orientations were successfully used to characterize the forbidden domain boundaries in ferroelastic SCs [42] due to the significant influence of the elastic field therein.

Besides the domain-wall types described above, we mention the walls that are sometimes termed 'antiphase boundaries' or '360° domain walls'. They arise as a result of elastic matching of two domain pairs with the 180° orientation of the spontaneous polarization vectors and with different tensors of spontaneous strains in separate domains. Some examples of these domain walls were observed in SCs exhibiting the FE and ferroelastic properties (see, e.g. papers [44–46]).

The description of the domain walls and complex DS containing intersections of the domain (twin) walls, triple junctions and irregular interfaces was carried out by Salje [47] in terms of dislocation densities. According to this concept, a possible break of the lattice planes in the domain (twin) walls is described as a continuous contribution of dislocations in ferroelastic and co-elastic SCs. The intersecting domain walls obey the condition for a minimum of the wall energy. Differences in the domain-pattern formations were interpreted [48-52] at the study of elastic interactions in SCs at the structural phase transitions. The atomically coherent domain boundary obeys compatibility relations [40] (i.e. principles formulated by Sapriel) for components of the spontaneous strain tensor or the distortion tensor. However, the real domain conjunction in SCs spreads the anisotropic lattice distortion over some region around the domain boundary [49] with a fine 'tweed texture' [40, 50] (or tweed microstructure [51]) of lamellar domains, even in the case of the unstrained domain boundary. The presence of the tweed texture is consistent with the concept [26] of higher order DSs in solids. The results of experimental and theoretical studies of tweed microstructures in ferroelastic and co-elastic SCs are discussed in papers [50, 51]. Systems of crosshatched tweed-like domains in FE phases were studied by Viehland et al. [53] in SCs of solid solutions of (1 - x)Pb $(Mg_{1/3}Nb_{2/3})O_3 - x$ PbTi O_3 (PMN - xPT) with compositions near the morphotropic phase boundary (MPB). The PMN - xPT SCs are of great research interest due to the remarkable electromechanical and FE properties and complicated DS in heterophase states [53–57]. As follows from the experimental study [53], the domain self-organization is driven by the elastic compatibility, and the change between the miniature crosshatched domains and the fine well-aligned striation domains also satisfies conditions for the elastic compatibility in the heterophase system.

1.1.3 Classification of Domain Boundaries in Ferroelectric Single Crystals

Besides the domain boundaries considered in Sect. 1.1.2, one can find other interesting examples of the domain boundaries described in experimental studies. The domain boundaries observed in FE SCs are classified [9] using a series of criteria (Fig. 1.1).

In the present review, we did not consider in detail some exotic situations concerned, for instance with the formation of the non-coherent domain boundaries or even single-domain states [58] at the FE phase transition. As follows from results [58], the heterophase system comprising the single-domain FE phase also promotes a decrease of the elastic contribution into the free energy of the system, but conditions for complete stress relief [30, 31] at the interphase boundary cannot be satisfied due to peculiarities of jumps of the unit-cell parameters at the phase transition. This behaviour is observed in FE-ferroelastic $Gd_2(MoO_4)_3$ SCs where the single-domain phase appears [59] at the FE phase transition. An analysis of the elastic-energy contribution caused by the phase coexistence enabled one to find the

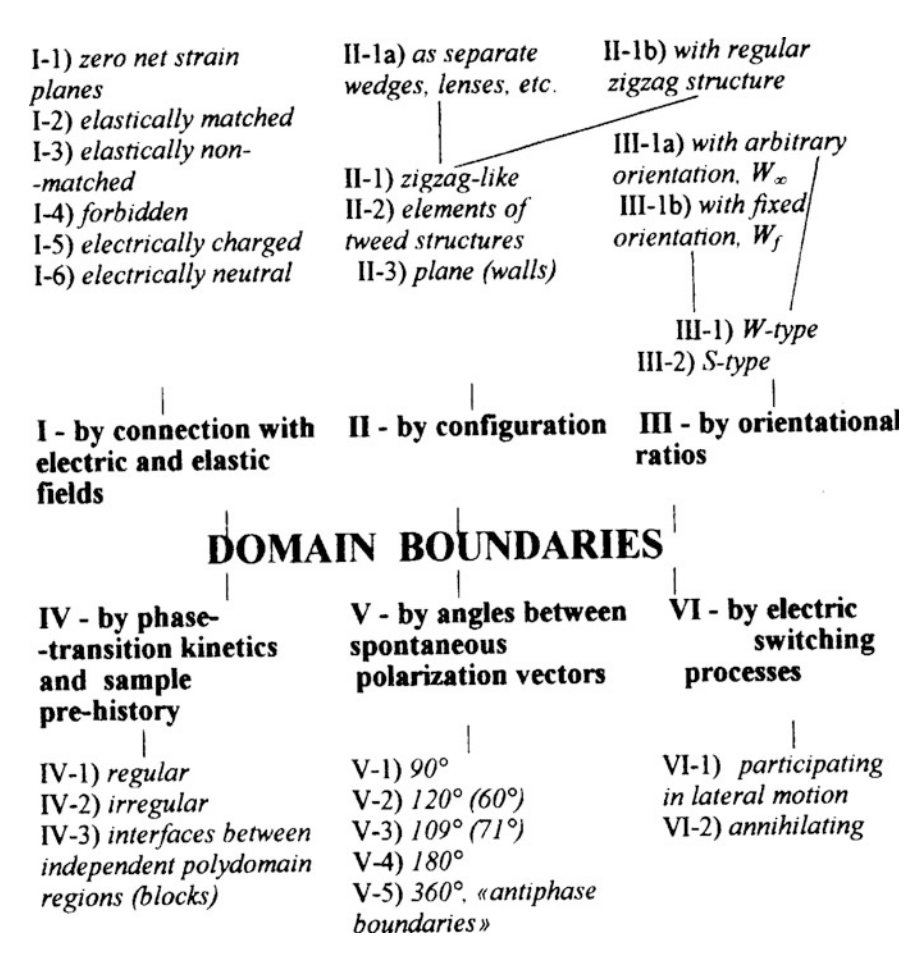


Fig. 1.1 Classification of domain boundaries observed in FE SCs (reprinted from paper by Topolov [9], with permission from Taylor and Francis)

preferable orientation [58] of the crystallographic axes in the single-domain phase of Gd₂(MoO₄)₃. Finally, the effect of clamping the domain boundary in SCs leads to the appearance of irregularly shaped domains whose sizes are generally larger than those in the tweed microstructures [48].

1.1.4 Crystallographic Interpretation of Interfaces Between Complicated Domain Structures

Metrat [60] developed the crystallographic theory [30–32] to describe the complex DS and its transformation at the first-order phase transition in FE SCs. The solution

[60] allows the determination of the mutual orientation of the interface and the DS within one of the phases in case of elastic matching of two polydomain phases or domain regions. It should be mentioned that 'interface' in this context means either the interphase boundary separating the coexisting phases or the domain boundary separating the domain regions of some polydomain (twinned) phase. A mathematical description of elastic matching of the coexisting phases (or domain regions) along the interface in FE or related SCs is based on the crystallographic concept [60].

According to Metrat [60], the coexisting polydomain phases (or domain regions) are characterized by the distortion matrices $||M_{ij}||$ and $||N_{ij}||$ that are expressed in terms of distortions of several domain types, their volume fractions and angles of mutual rotation [30, 31] of the crystallographic axes of the adjacent domains. In contrast to the assumptions used in (1.2)–(1.4), conditions for complete stress relief and the formation of the ZNSP along the interface are written in the more strict form:

$$\det ||D_{ij}|| = 0 \tag{1.5}$$

and

$$(D'_{ii})^2 \ge 0,$$
 (1.6)

where elements of the $||D_{ij}||$ matrix (3 × 3) from (1.5) are given by

$$D_{ij} = \sum_{k=1}^{3} (N_{ik}N_{jk} - M_{ik}M_{jk}), \tag{1.7}$$

 N_{ik} and M_{ik} are taken from the aforementioned distortion matrices, and $(D_{ij}')^2 = D_{ij}^2 - D_{ii}D_{jj}$ (ij = 12 and 13). Metrat [60] takes into account the second powers of the distortions of the adjacent phases or domain regions, see (1.7). This leads to complicated nonlinear relationships between the volume fractions of the domains in the coexisting phases. The necessary conditions for the existence of the ZNSP [30, 31] are generalized and given by (1.6). Based on the matrix elements D_{ij} from (1.7), one can determine the Miller indices (hkl) of the planar unstrained interfaces [60] as follows:

$$h_{1,2} = D_{11}/D_{1,2}, k_{1,2} = (D_{12} \pm D'_{12})/D_{1,2}$$
 and
 $l_{1,2} = (D_{13} \pm D'_{13})/D_{1,2},$ (1.8)

where $D_{1,2} = [D_{11}^2 + (D_{12} \pm D_{12}')^2 + (D_{13} \pm D_{12}')^2]^{1/2}$ is written in terms of D_{ij} and D_{ij}' from (1.7) to (1.6), respectively. The possibility of application of conditions (1.5)–(1.8) for description of the polydomain (twinned) and heterophase SCs demonstrates obvious advantages of the Metrat's algorithm [60] in comparison to methods [30–32, 35, 37–40] proposed earlier. A comparative analysis of the

crystallographic methods and some examples of calculations of characteristics of heterophase SCs are considered in Appendix A.

The Metrat's algorithm [60] and the matrix approach concerned with this algorithm were applied to FEs and antiferroelectrics of different structural types for interpretation of experimental data on heavily twinned SCs, structural phase transitions, formation and rearrangement of DS, and features of phase coexistence at changes in temperature, molar concentration or external stress (see, e.g. papers [27, 58, 61–64]). The matrix approach is also helpful in studying a connection between the elastic interaction of the phases and the behaviour of their unit-cell parameters in wide temperature or molar-concentration ranges [61, 64]. Based on experimental data and the Metrat's algorithm, Balyunis et al. [65] first characterized four types of the S-type boundaries in heavily twinned PbZrO₃ SCs and generalized the concepts by Fousek and Janovec [37] for a case of four twin components in the FE phase. Analytical conditions determining the thermal stability of the orientation of the S-type boundary studied in work [65] may be applied to various FE (antiferroelectric) perovskite-type SCs with complex DS or systems of twin components. Furthermore, it is possible to determine the unit-cell parameters more exactly using data from optical studies and crystal-geometry of domain (twinned) regions with the S-type domain boundary whose orientation remains stable in a certain temperature range. This possibility was first demonstrated at the determination of the temperature dependence of the shear angle ω of the perovskite unit cell in the antiferroelectric *Pbam* phase of PbZrO₃ SC [66].

The crystallographic study of the S-type boundaries [65, 66] in perovskite-type FE and antiferroelectric SCs revealed a difference between the orientation relations from the Metrat's algorithm [see (1.8)] and the formulae derived from work by Fousek and Janovec [37]. In a case of elastic matching of the 60° domains (Fig. 1.2) in the orthorhombic phase of such SCs as KNbO₃, the distortion matrices of domains 1 and 2 are

$$||M_{ij}|| = \begin{pmatrix} \eta_a & 0 & \eta \\ 0 & \eta_b & 0 \\ \eta & 0 & \eta_a \end{pmatrix} \text{ and }$$

$$||N_{ij}|| = \begin{pmatrix} \eta_b & 0 & 0 \\ 0 & \eta_a & \eta \\ 0 & \eta & \eta_a \end{pmatrix},$$
(1.9)

respectively, where η_a , η_b and η are distortions of the perovskite unit cell along the a-, b-directions and in the (ac)-plane, respectively. The distortions from (1.9) can be written in terms of the spontaneous strains ξ_a^s , ξ_b^s and ξ^s of the perovskite unit cell as follows: $\eta_a = 1 + \xi_a^s$, $\eta_b = 1 + \xi_b^s$ and $\eta = 1 + \xi^s$. Based on (1.5)–(1.9), we conclude that the following orientations of normal vectors to the unstrained domain wall are possible: $n_1(1\ \overline{1}\ 0)$ and $n_2(hhl)$. The normal vector n_2 characterizes the orientation of the S wall [27, 67]. In accordance with (1.8), components of the n_2 vector are linked by the ratio

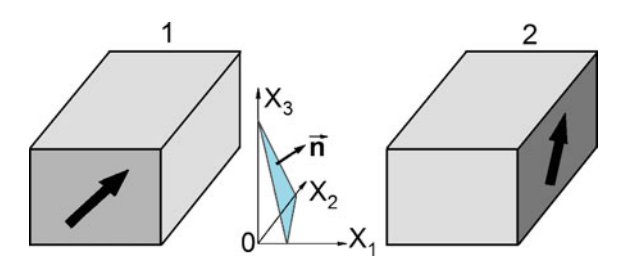


Fig. 1.2 Schematic arrangement of domains in the orthorhombic phase of perovskite-type FE SCs. Spontaneous polarization vectors of domains 1 and 2 are shown by arrows. $(X_1X_2X_3)$ is the rectangular co-ordinate system with axes parallel to the perovskite unit-cell axes in the cubic phase, n is the normal vector to the domain wall

$$(l/h)_{M} = 4\eta \eta_{a}/(\eta_{a}^{2} - \eta_{b}^{2} + \eta^{2}). \tag{1.10}$$

The similar ratio of the Miller indices determined in terms of work [37] is expressed as follows:

$$(l/h)_{FI} = 2\eta/(\eta_a - \eta_b).$$
 (1.11)

Comparing the l/h ratios from (1.10) to (1.11), one can state that $\kappa = (l/h)_{FJ}/(l/h)_M \neq 1$ in the general case. As follows from evaluations [67] based on experimental values of the unit-cell parameters, κ equals 0.996 (BaTiO₃ SC at temperature T=277 K), 0.995 (PbHfO₃ SC at T=298 K) or 0.998 (KNbO₃ SC at T=298 K) [67]. The difference $1-\kappa$ increases with increasing the difference $\eta_a-\eta_b$ (i.e. as the difference of the unit-cell parameters a-b increases) under the condition that $\eta^2 \ll \eta_a - \eta_b$. Data on the thermal stability of the orientation of the S wall in PbZrO₃ SC (see Appendix A) suggest that the inequality $0.99 < \kappa < 1$ is valid in the wide temperature range. The reason for $\kappa \neq 1$ lies in the choice of basic conditions [38, 60] for elastic matching of the adjacent domains [see (1.3) and (1.7)]. It is pertinent to add that (1.10) was applied for the more precise determination of the temperature dependence of the shear angle $\omega(T)$ of the perovskite unit cell in PbZrO₃ SC [66].

The approach developed in papers [65, 66] was applied to the S-type domain boundaries with various temperature dependences of the normal vector $n_2(hhl)$ in orthorhombic $Pb(Zr_{1-x}Sn_x)O_3$ SCs. In papers [65, 66] the S-type boundaries play the role of interfaces separating the regions with 90° DS, and four non-180° domain types are involved in the crystallographic description of elastic matching of the domain regions. This crystallographic approach was also useful to interpret the non-monotonic temperature dependence of the S-type boundary orientation in two orthorhombic phases of $Pb(Yb_{0.5}Nb_{0.5})O_3$ SCs [68] and to show a link between the $n_2(hhl)$ orientation and the unit-cell behaviour in a wide temperature range.

1.2 Phase Coexistence at First-Order Phase Transitions

1.2.1 Elastic Matching of Phases and Zero-Net-Strain Planes

The overwhelming majority of structural phase transitions in FE materials belong to the first-order transitions [1–4, 11]. They are accompanied by jumps of the unit-cell parameters, formation and growth of new-phase nuclei, motions of interphase boundaries, appearance or rearrangement of DS, and other physical phenomena. In every case, the transition of the system into a new stable state proceeds through a metastable state, and the system represents a heterogeneous (heterophase) medium wherein two [11, 61, 62, 69] or even three [63, 70] phases can coexist. These phases can be split into domains (mechanical twins) according to conditions [9, 27, 60] for effective stress relief in the heterophase medium.

Below the Curie temperature, many FEs and related materials undergo structural phase transitions or a series of phase transitions between phases with different symmetry and DS [1–4]. Some results of determination of characteristics of the interphase boundaries and DS [71] within the framework of the Metrat's algorithm [60] are shown in Table 1.1. It is assumed that elastic matching of the coexisting phases and the full screening of electric fields of bond charges at surfaces of nuclei of the new

Table 1.1	Interphase	boundaries	and DSs	which	obey	conditions	(1.5)	and ((1.6)	for Z	NSPs in
perovskite-	type SCs										

Point symmetry groups of coexisting phases	Domain types and volume fractions	Optimal orientations $(hkl)^a$ (or φ_{opt}) of interphase boundaries and optimal volume fractions of domains [71]					
m3m and 4mm	Figure 1.3	BaTiO ₃ : (506) ($\varphi_{\text{opt}} = 40.15^{\circ}$) and $m_{\text{opt}} = 0.706$ KNbO ₃ : (405) ($\varphi_{\text{opt}} = 37.95^{\circ}$) and $m_{\text{opt}} = 0.725$ PbTiO ₃ : (203) ($\varphi_{\text{opt}} = 33.76^{\circ}$) and $m_{\text{opt}} = 0.764$					
m3m and 222	Figure 1.4	PbHfO ₃ : (025) ($\varphi_{\text{opt}} = 68.03^{\circ}$) and $m_{\text{opt}} = 0.877$					
4mm and mm2	Figure 1.5a	BaTiO ₃ : (010) and $q_{\text{opt}} = 0.548$, $x_{\text{opt}} = 0.500$, and $y_{\text{opt}} = 0.259$					
4mm and 3m	Figure 1.5b	Pb($Zr_{1-x}Ti_x$)O ₃ near the MPB: the optimal orientation ^b is close to (010) at $t_{\text{opt}} = 0.294 - 0.554$					
4mm and 4mm	Figure 1.5c	PbTiO ₃ : the orientation changes from (708) at $m \rightarrow 0$ to (627) at $m \rightarrow 1$, the optimal volume fraction is $q_{\text{opt}} = A_{2,3} + B_{2,3}m$, where $A_2 = 0.0315$ and $B_2 = 0.953$, or $A_3 = 0.0143$ and $B_2 = 0.995$					

^aMiller indices (hkl) are determined with respect to the perovskite unit-cell axes in the cubic phase ^bThe spontaneous polarization vector in the single-domain 3m phase (Fig. 1.5b) can be oriented along a body diagonal of the perovskite unit cell, i.e. directions [111], [111], [111], etc., are equivalent, and conditions for ZNSPs hold at the phase coexistence. The orientation of the spontaneous polarization vector in the 3m phase slightly influences the optimal volume fraction t_{opt} only

phase takes place. This screening promotes a lowering of the energy of the depolarizing field in the SC sample [11]. The domains (twin components) shown in Figs. 1.3, 1.4 and 1.5 are separated by unstrained domain (twin) walls in accordance with the concept [37, 38]. Table 1.1 comprises data on the interphase boundaries at the following first-order phase transitions: paraelectric—FE, paraelectric—antiferroelectric and FE—FE. In Figs. 1.3, 1.4 and 1.5 each polydomain (twinned) phase contains the minimum number of the FE domain types (or twin components in the antiferroelectric state) at which complete stress relief can be achieved.

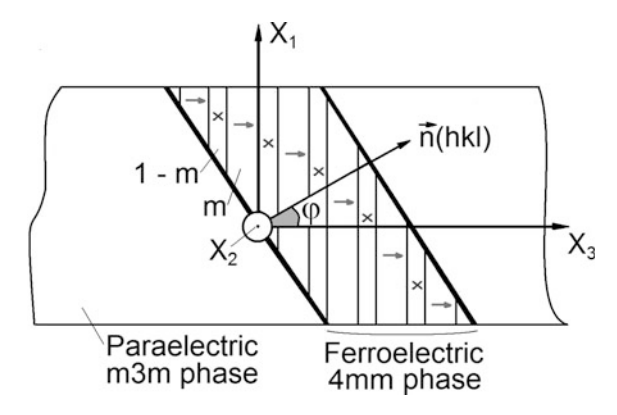


Fig. 1.3 Schematic arrangement of the lamellar nucleus (polydomain FE phase) in the paraelectric matrix. Directions of the spontaneous polarization vectors of 90° domains in the 4mm phase are shown by arrows (volume fraction m) and crosses (volume fraction 1-m). n is the normal vector to the interphase boundary, $\varphi = (n, ^{\wedge} OX_3)$ is the angle of the orientation of the interphase boundary. Co-ordinate axes OX_j are parallel to the perovskite unit-cell axes in the cubic phase

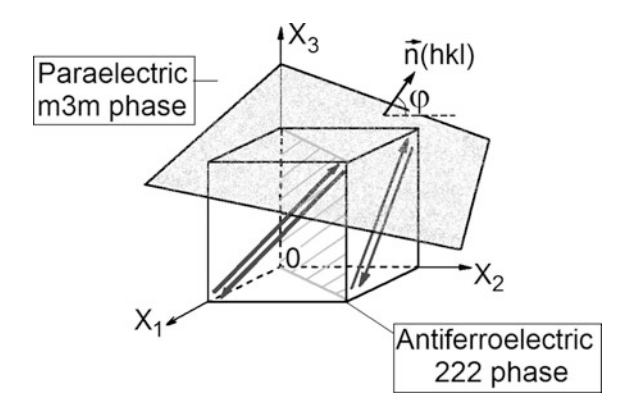
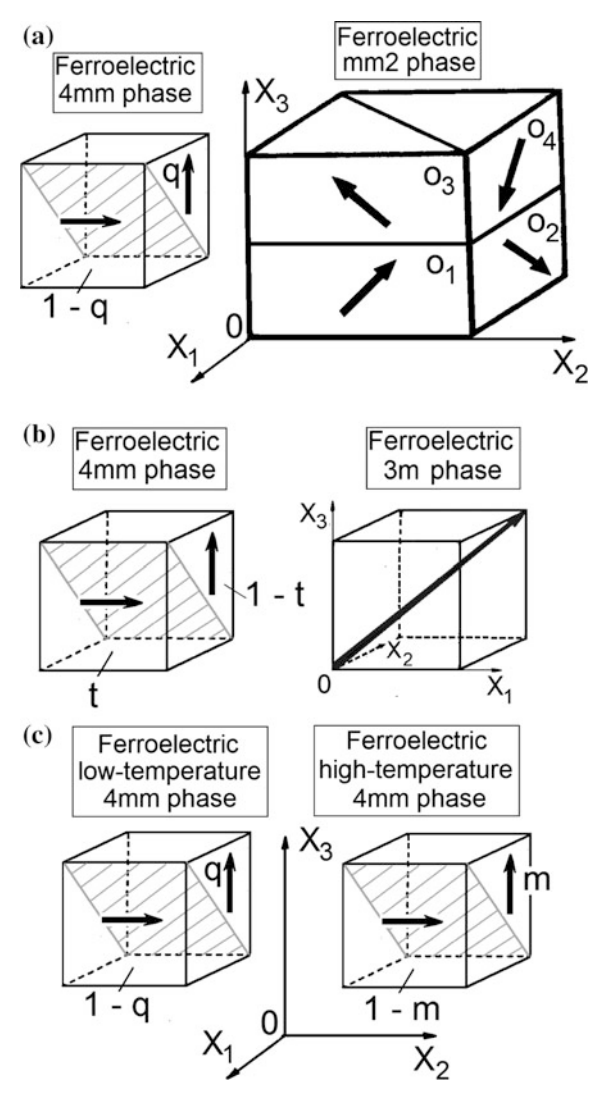


Fig. 1.4 Schematic arrangement of 60° twin components in the antiferroelectric 222 phase at the m3m—222 phase transition. Directions of the spontaneous antipolarization vectors are shown by arrows, m and 1—m are volume fractions of the domains. n is the normal vector to the interphase boundary, $\varphi = (n, ^{\circ} OX_2)$ is the angle of the orientation of the interphase boundary. Co-ordinate axes OX_i are parallel to the perovskite unit-cell axes in the cubic phase



The majority of quantitative results from Table 1.1 are in good agreement with experimental data (see, e.g., [11, 69]). Metrat's algorithm [60] and the matrix approach for description of complex DSs promoted studying a connection between the elastic interaction in heterophase (polydomain) states and the behaviour of the unit-cell parameters in FE, antiferroelectric and ferroelastic SCs. This behaviour is concerned with the necessary conditions [72] for the existence of the ZNSP at elastic matching of two polydomain phases. The necessary conditions introduced for the interphase boundaries at the cubic-tetragonal and cubic-orthorhombic phase transitions [30, 31] were generalized for the phase transitions between two polydomain phases of either tetragonal or orthorhombic symmetry. Based on the generalized necessary conditions, Topolov [72] formulated a series of selection rules to analyse experimental relations between the unit-cell distortions of the coexisting polydomain phases in perovskite-type FEs. These relations show that possibilities for the formation of the interphase boundary obeying conditions for ZNSP are more favourable at the FE-FE, FE-antiferroelectric and antiferroelectric-antiferroelectric phase transitions than at the transitions between the FE (or antiferroelectric) and paraelectric phases. The polydomain phase with anisotropic spontaneous strains that strongly depend on the volume fraction and orientation of the non-180° domains provides additional 'degrees of freedom' for stress relief in the heterophase structure wherein a few domain types (mechanical twin components) are present. We write 'degrees of freedom' in a figurative sense to avoid an analogy with a moving mechanical system.

A similar conclusion can be formulated on the basis of results [73] on the crystallographic description of the DS rearrangement and ZNSPs at the sequence of the first-order phase transitions m3m-4mm-mm2-3m in BaTiO₃ SC. It should be added that paper [73] is the first publication where the Metrat's algorithm [60] was applied to the whole sequence of the phase transitions in polydomain FE SCs.

An unexpected issue is brought up in the study of the FE phase transition m3m— 4mm in K(Ta_{0.65}Nb_{0.35})O₃ SC. Following the algorithm [60], one can obtain $\varphi_{\rm opt} = 40.42^{\circ}$ and $m_{\rm opt} = 0.704$ at the phase coexistence (Fig. 1.3), so that the interphase boundary is oriented close to (506) in the perovskite axes. At the same time, the experimental study of the phase transition in K(Ta_{0.65}Nb_{0.35})O₃ SC [11] shows that the FE 4mm phase remains single domain, but its plate-like nucleus is parallel to (506). To the best of our knowledge, such behaviour has no analogues among FE SCs undergoing the first-order phase transition. The reason for the single-domain FE phase [71] lies in a small elastic energy of the single-domain nucleus in comparison with the energy that might be accumulated in the 90° domain walls after splitting this nucleus into the domains with the optimal volume fraction $m = m_{\rm opt}$ (Fig. 1.3). Such a peculiarity takes place in the solid solution as the molar concentration of KTaO₃ approaches the value at which the first-order phase transition becomes the second-order one. According to data [11], the jump of the spontaneous polarization in this SC at the first-order phase transition is $P_s(T_C) = 0.05 \text{ C/m}^2$, and this value is approximately four times smaller than that in BaTiO₃ SC at the FE m3m—4mm phase transition and 8.4 times smaller than $P_s(T_C)$ in PbTiO₃ SC at the FE m3m—4mm phase transition. Moreover,

spontaneous strains of the perovskite unit cell of K(Ta_{0.65}Nb_{0.35})O₃ SC are one–two orders-of-magnitude lower than in BaTiO₃ SC and two orders-of-magnitude lower than in PbTiO₃ SC.

Peculiarities of the elastic interaction between the polydomain phases of the FE nature have been studied in the last decades (see, for instance, papers [60, 67–72]). As follows from this study, the crystallographic description of elastic matching of the phases (or domain regions) in terms of the Metrat's algorithm [60] is not exhaustive and should be supplemented by the thermodynamic theory of FEs [3, 11, 71, 74] and by the elasticity theory of anisotropic media [75, 76].

1.2.2 Stress Relief and Conical Interphase Boundaries

In Sect. 1.2.1, we did not mention possibilities of stress relief at the cubic–rhombohedral phase transition. The first-order phase transition between the paraelectric cubic and FE rhombohedral phases is observed, for example in SCs of PbZrO₃ [77], Pb(Mg_{1/3}Nb_{2/3})O₃ (PMN) under the external electric field [62], PMN – xPT [78], etc. The first attempt to provide a crystallographic interpretation of the interphase boundaries at the cubic–rhombohedral phase transition was made in work on PbZrO₃ SC [77]. Its rhombohedral (R3m) phase remains stable in the narrow temperature range (about 10 K) only. As is known from experimental data [77], the interphase boundaries in PbZrO₃ SCs have a complicated conical shape with a variable curvature radius, and the more complicated configuration of the boundary is observed near small domains of the rhombohedral phase. Moreover, virtually straight parts of the interphase boundary are observed when moving away from the domain wall. At the same time, changes in the non-180° DS of the rhombohedral phase are insignificant and would not considerably influence the orientation and shape of the moving interphase boundary.

In the crystallographic study [77] of the cubic–rhombohedral phase transition in PbZrO₃ SC, the shape of the interphase boundary is approximated by a second-degree surface. This surface is described in the rectangular co-ordinate system $(X_1X_2X_3)$ as follows:

$$\sum_{i,j=1}^{3} D_{ij} x_i x_j = 0, \tag{1.12}$$

where the elements D_{ij} are expressed in terms of distortions of the coexisting phases, see (1.7). The rhombohedral phase is assumed to be split into 71° (109°) domains with the fixed orientations and variable volume fractions [77]. The surfaces are classified taking into account signs of the following invariants of (1.12):

$$I = D_{11} + D_{22} + D_{33}, D = \det |D_{ij}| \quad \text{and}$$

$$J = \begin{vmatrix} D_{11} & D_{12} \\ D_{21} & D_{22} \end{vmatrix} + \begin{vmatrix} D_{22} & D_{23} \\ D_{32} & D_{33} \end{vmatrix} + \begin{vmatrix} D_{33} & D_{31} \\ D_{13} & D_{11} \end{vmatrix}.$$
(1.13)

Conical surfaces obey one of the following pairs of inequalities:

$$DI < 0 \text{ and } J < 0, \tag{1.14}$$

$$DI < 0 \text{ and } J > 0,$$
 (1.15)

or

$$DI > 0 \text{ and } J < 0.$$
 (1.16)

Inequalities

$$DI > 0 \text{ and } J > 0 \tag{1.17}$$

characterize an imaginary cone apex. Finally, conditions

$$DI = 0 \text{ and } J < 0 \tag{1.18}$$

are related to a planar interphase boundary oriented parallel to the ZNSP. Conditions (1.14)–(1.18) are written in terms of invariants I, D and J from (1.13). The conical interphase boundaries, that obey conditions (1.14), (1.15) or (1.16), can provide partial (incomplete) stress relief because of $D \neq 0$ while the planar boundaries parallel to the ZNSPs provide complete stress relief in the heterophase state. We note that conditions (1.18) are written in the more strict form as compared to conditions (1.5) and (1.6) from the Metrat's algorithm. In case of fulfilment of conditions (1.17), some rearrangement of the DS in the FE phase can take place to promote further stress relief in the SC sample.

It should be mentioned that conditions (1.14)–(1.18) were first applied [77] for a description of various interphase boundaries observed in PbZrO₃ at the FE phase transition. A possible way of the evolution of the heterophase structure in PbZrO₃ SCs can be concerned with the formation of a large number of nuclei in the form of wedges or prisms and with the further interaction of these nuclei [77]. An interaction between the nuclei of the new phase, especially in a relatively narrow temperature range (as observed in PbZrO₃ SC below the Curie temperature $T_{\rm C}$), represents an independent problem in the kinetics of structural phase transitions. This interaction leads to the formation of the heavily twinned phases, and their physical properties can be affected by this interaction.

Results of the crystallographic description of the interphase boundaries in PbZrO₃ SCs [77] are represented in the diagram that links volume fractions of the 71° (109°) domain types in the FE rhombohedral phase. The diagram contains a curve that corresponds to ZNSPs in a restricted volume-fraction range, however these ZNSPs were not predicted on the basis of the necessary conditions formulated in papers [30, 31]. Generally speaking, the presence of the ZNSP at the cubic–rhombohedral phase transition is caused by the commensurability [77] of the diagonal and off-diagonal components of the spontaneous strains in the polydomain phase of PbZrO₃. This circumstance is to be taken into account when formulating

the necessary conditions [30, 31] for the existence of ZNSPs in heterophase and heavily twinned SCs. Hereby it is assumed that these SCs undergo the structural phase transitions between low-symmetry phases wherein the unit-cell shear strain may play the important role in the balance of the strains that influence elastic matching of the phases or domain regions.

The crystallographic concept [77] was applied for description of a system of the interphase boundaries at the electric-field-induced cubic-rhombohedral phase transition in plate-like PMN SCs [62]. The role of the mechanical stress field at the monoclinic-orthorhombic phase transition in Pb₂CoWO₆ SCs [61] was also studied on the basis of the concept from work [77]. A correlation between the value of invariant *D* from (1.13) and the volume density of elastic energy was first revealed at the description of the heterophase Pb₂CoWO₆ SCs [61]. It should be added that jumps in the unit-cell parameters at the monoclinic-orthorhombic phase transition in Pb₂CoWO₆ SC [79] do not promote complete stress relief in the heterophase system. As a consequence, the conical interphase boundaries in this SC would appear in the presence of the internal stress. An additional possibility for stress relief may be concerned with the formation of transition regions that are characterized by variations of the unit-cell parameters of Pb₂CoWO₆ [61]. A detailed crystallographic description of the transition region in FE solid solutions is proposed in Sect. 5.3.

1.2.3 Three-Phase States

An important feature of FE solid solutions consists in a coexistence of three phases at temperatures T near the Curie point T_C and at compositions located close to the MPB at phase diagrams [54, 56, 74, 80, 81]. The three-phase states appear at almost equal volume densities of free energy of the coexisting phases, and this coexistence is often affected by an internal stress field that influences the elastic energy in a heterophase structure and, therefore, the total energy of the system. The three-phase states can be also observed in SCs where relatively narrow temperature ranges of stability of some phases are detected. Examples of such states are observed, for instance in PbZrO₃ SCs [70]. In multiferroic (1-x)BiFeO₃ - xPbTiO₃ with compositions close to the MPB, two different structural phase transition scenarios on cooling from the cubic paraelectric phase are observed, and three FE phases coexist at variations of T and x [82]. Such a phase coexistence is related to the (1 - x)BiFeO₃ – xPbTiO₃ compositions that exhibit giant tetragonality that may be an additional stimulus to find proper ways for stress relief. An important example of the three-phase state is observed in (Ba_{0.85}Ca_{0.15})(Ti_{0.90}Zr_{0.10})O₃ ceramic samples [83], and this ceramic in the poled state is characterized by largest piezoelectric coefficient d_{33} among the lead-free (Ba, Ca)(Ti, Zr)O₃ compositions. We note that at room temperature, the d_{33} value of the poled $(Ba_{0.85}Ca_{0.15})(Ti_{0.90}Zr_{0.10})O_3$ ceramic is approximately 3.1 times larger [83] than d_{33} of the poled BaTiO₃ ceramic [80]).

Thermodynamic and crystallographic studies on the three-phase states in perovskite-type solid solutions [74, 84–86] show that the internal mechanical stress associated with spontaneous strains at the first-order phase transition influences the temperature and molar-concentration ranges, where two and three phases can coexist. It is obvious that conditions (1.18) for the ZNSPs are to be examined for different kinds of interphase boundaries in three-phase samples and by taking into account volume fractions and orientations of specific domain types (or twins) in the adjacent FE (antiferroelectric) phases. The problem of stress relief at the three-phase coexistence [70, 71, 86] has no universal solutions, and at the moment one can consider examples where complete stress relief at elastic matching of phases is achieved and three phases coexist. We discuss some examples of the three-phase states and related heterophase structures in Chap. 4.

1.3 Polydomain/Heterophase Ferroelectrics

In this chapter, we considered various examples of interfaces in SCs of FEs and related materials. The interfaces, such as domain walls, domain boundaries, interphase boundaries, etc., are one of the factors that actively influence physical properties of heterogeneous FE and related materials. An influence of heterophase structures on the piezoelectric effect and electromechanical coupling factors of FE solid solutions with compositions close to the MPB is of interest in the context of various piezotechnical applications [4, 10, 80, 83]. Knowledge of the interfaces, their hierarchy and characteristics promote the successful study of the physical properties, structural phase transitions, heterophase states and interrelations in the fundamental triangle 'composition–structure–properties'.

Among the problems concerning the interfaces in heterogeneous FEs (including FE solid solutions), of particular interest are

- (i) determination of the orientation of the domain and interphase boundaries in heavily twinned FE SCs,
- (ii) study of correlations between the DS and interphase boundary by taking into account the unit-cell behaviour at the structural phase transition (polymorphic, morphotropic or field-induced),
- (iii) analysis of conditions for complete (or partial) stress relief at elastic matching of morphotropic phases in polydomain/heterophase FE SCs,
- (iv) analysis of relations between the unit-cell parameters and phase contents in polydomain/heterophase FE SCs (two- and three-phase states).
- (v) application of crystallographic methods for interpretation of experimental results on the rearrangement of the DS at the phase transitions,
- (vi) role of heterophase states and alternative stress-relief ways in FE solid solutions near the MPB, and

(vii) specifics of heterophase states in lead-free FE solid solutions near the MPB.

The aforementioned and related problems are considered in Chaps. 2–6 of the present book.

References

- Lines M, Glass A (1977) Principles and application of ferroelectrics and related materials. Clarendon Press, Oxford
- Zheludev IS (1971) Physics of crystalline dielectrics, vol 2: Electrical properties. Plenum, New York
- 3. Smolensky GA, Bokov VA, Isupov VA, Krainik NN, Pasynkov RE, Sokolov AI, Yushin NK (1985) Physics of ferroelectric phenomena. Nauka, Leningrad (in Russian)
- 4. Xu Y (1991) Ferroelectric materials and their applications. North-Holland, Amsterdam London New York Toronto
- Fang D-N, Soh AK, Li C-Q, Jiang B (2001) Nonlinear behavior of 0–3 type ferroelectric composites with polymer matrices. J Mater Sci 36:5281–5288
- Malbec A, Liu T, Lynch CS (2004) Characterization and modeling of domain engineered relaxor ferroelectric single crystals. J de Physique IV (France) 115:59–66
- Turik AV (1970) Elastic, piezoelectric, and dielectric properties of single crystals of BaTiO₃ with a laminar domain structure. Sov Phys Solid State 12:688–693
- Topolov VYu, Bondarenko EI, Turik AV, Chernobabov AI (1993) The effect of domain structure on electromechanical properties of PbTiO₃-based ferroelectrics. Ferroelectrics 140:175–181
- Topolov VYu (1999) Interfaces in ferroelectrics and related materials with complex domain structures. Ferroelectrics 222:41–52
- Topolov VYu, Bowen CR (2009) Electromechanical properties in composites based on ferroelectrics. Springer, London
- 11. Fesenko EG, Gavrilyachenko VG, Semenchev AF (1990) Domain structure of multiaxial ferroelectric crystals. Rostov University Press, Rostov-on-Don (in Russian)
- 12. Rudyak VM (1986) Switching processes in nonlinear crystals. Nauka, Moscow (in Russian)
- Shuvalov LA, Urusovskaya AA, Zheludev IS, Zalessky AV, Semiletov SA, Grechishnikov BN, Chistyakov IG, Pikin SA (1981) Modern crystallography, vol. 4. Nauka, Moscow (in Russian)
- Zheludev IS, Shuvalov LA (1956) Ferroelectric phase transitions and symmetry of crystals.
 Kristallografiya 1:681–688 (in Russian)
- Zheludev IS, Shuvalov LA (1957) Orientation of domains and macrosymmetry of properties of ferroelectric single crystals. Izvestiya Akademii Nauk SSSR. Seriya Fizicheskaya 21: 264–274 (in Russian)
- Shuvalov LA (1963) Crystallographic classification of ferroelectrics. Ferroelectric phase transitions and features of the domain structure and some physical properties of ferroelectrics of different classification species. Kristallografiya 8:617–624 (in Russian)
- 17. Shuvalov LA (1964) Crystallophysical classification of ferroelectrics and its applications. Izvestiya Akademii Nauk SSSR. Seriya Fizicheskaya 28:660–665 (in Russian)
- 18. Shuvalov LA (1970) Symmetry aspects of ferroelectricity. J Phys Soc Jpn 28 (Suppl.):38-51
- Zheludev IS (1971) Ferroelectricity and symmetry. Solid state physics: advances in research and applications, vol 26. Academic Press, New York London, pp 429–464
- Mitsui T, Furuichi J (1953) Domain structure of Rochelle salt and KH₂PO₄. Phys Rev 90:193–202

- 21. Cao W, Cross LE (1991) Theory of tetragonal twin structures in ferroelectric perovskites with a first-order phase transition. Phys Rev B44:5–12
- Cao W (1995) Defect stabilized periodic amplitude modulations in ferroelectrics. Phase Transitions 55:69–78
- Nambu S, Sagala DA (1994) Domain formation and elastic long-range interaction in ferroelectric perovskites. Phys Rev B 50:5838–5847
- 24. Rosakis P, Jiang Q (1995) On the morphology of ferroelectric domains. Int J Eng Sci 33:1-12
- 25. Dec J (1990) Orientacija i kinetyka granic fazowych w monokryształach PbTiO₃, NaNbO₃ i PbZrO₃, Universytet Śląski, Katowice (in Polish)
- Roytburd AL (1993) Elastic domains and polydomain phases in solids. Phase Transitions 45:1–33
- Topolov VYu, Turik AV (1995) Crystallographic aspects of interfaces in ferroelectrics.
 Defect Diffus Forum Pt A 123–124:31–50
- 28. Roitburd AL (1974) The theory of the formation of a heterophase structure in phase transformations in solids. Sov Phys Uspehi 17:326–344
- Roitburd AL (1990) On the thermodynamics of martensite nucleation. Mater Sci Eng A 127:229–238
- 30. Wechsler MS, Lieberman DS, Read TA (1953) On the theory of the formation of martensite. Trans AIME J Metals 197:1503–1515
- 31. Lieberman DS, Wechsler MS, Read TA (1955) Cubic to orthorhombic diffusionless phase change—experimental and theoretical studies of AuCd. J Appl Phys 26:473–484
- 32. Bilby BA, Christian JW (1956) Martensistic transformations. The mechanism of phase transformations in metals. The Institute of Metals, London, pp 121–172
- 33. Larché FC (1990) Coherent phase transformations. Annu Rev Mater Sci 20:83-99
- 34. Boulesteix C, Yangui B, Ben Salem M, Manolikas C, Amelinckx S (1986) The orientation of interfaces between a prototype phase and its ferroelastic derivatives: theoretical and experimental study. J de Physique (France) 47:461–471
- Kato M, Shibata-Yanagisawa M (1990) Infinitesimal deformation approach of the phenomenological crystallographic theory of martensitic transformations. J Mater Sci 25: 194–202
- Dudnik EF, Shuvalov LA (1989) Domain structure and phase boundaries in ferroelastics.
 Ferroelectrics 98:207–214
- Fousek J, Janovec V (1969) The orientation of domain walls in twinned ferroelectric crystals.
 J Appl Phys 40:135–142
- Fousek J (1971) Permissible domain walls in ferroelectric species. Czech J Phys B 21:955– 968
- 39. Janovec V (1976) A symmetry approach to domain structures. Ferroelectrics 12:43-53
- 40. Sapriel J (1975) Domain-wall orientations in ferroelastics. Phys Rev B 12:5128-5140
- 41. Vagin SV, Dudnik EF (1983) Method of interpreting the domain structure of ferroelastics. Bull Acad Sci U.S.S.R. Phys Ser 47(3):78–81
- 42. Shuvalov LA, Dudnik EF, Pozdeyev VG (1987) Forbidden domain boundaries in ferroelastics. Izvestiya Akademii Nauk SSSR. Seriya Fizicheskaya 51:2119–2123 (in Russian)
- 43. Boulesteix C (1984) A survey of domains and domain walls generated by crystallographic phase transitions causing a change of lattice. Physica Status Solidi (a) 86:11–42
- 44. Barkley JR, Jeitschko W (1973) Antiphase boundaries and their interactions with domain walls in ferroelastic-ferroelectric Gd₂(MoO₄)₃. J Appl Phys 44:938–944
- Capelle B, Malgrande C (1984) Antiphase domain walls in ferroelectric-ferroelastic GDMO crystals. In: Applications of X-ray topographic methods to materials science: proceedings of France–U.S.A. Seminar, Village, Colo., 7–10 August 1983. New York London, pp 511–522
- Rychetsky I, Schranz W (1993) Antiphase boundaries in Hg₂Br₂ and KSCN. J Phys Condens Matter 5:1455–1472
- 47. Salje EKH (1990) Phase transitions in ferroelastic and co-elastic crystals. Cambridge University Press, Cambridge New York Oakleigh

References 23

48. Heine V, Bratkovsky AM, Salje EKH (1994) The effect of clamped and free boundaries on long range strain coupling in structural phase transitions. Phase Transitions 52:85–93

- Wruck B, Salje EKH, Zhang M, Abraham T, Bismayer U (1994) On the thickness of feroelastic twin walls in lead phosphate Pb₃(PO₄)₂: an X-ray diffraction study. Phase Transitions 48:135–148
- 50. Bratkovsky AM, Salje EKH, Heine V (1994) Overwiew of the origin of tweed texture. Phase Transitions 52:77–83
- Putnis A, Salje E (1994) Tweed microstructures: experimental observations and some theoretical models. Phase Transitions 48:85–105
- 52. Bratkovsky AM, Marais SC, Heine V, Salje EKH (1994) The theory of fluctuations and texture embryos in structural phase transitions mediated by strain. J Phys Condens Matter 6:3679–3696
- 53. Viehland D, Li JF, Colla EV (2004) Domain structure changes in $(1 x)Pb(Mg_{1/3}Nb_{2/3})$ $O_3 xPbTiO_3$ with composition, dc bias, and ac field. J Appl Phys 96:3379–3381
- Noheda B (2002) Structure and high-piezoelectricity in lead oxide solid solutions. Curr Opin Solid State Mater Sci 6:27–34
- 55. Bokov AA, Ye Z-G (2004) Domain structure in the monoclinic *Pm* phase of Pb(Mg_{1/3}Nb_{2/3}) O₃–PbTiO₃ single crystals. J Appl Phys 95:6347–6359
- 56. Shuvaeva VA, Glazer AM, Zekria D (2005) The macroscopic symmetry of $Pb(Mg_{1/3}Nb_{2/3})_{1-x}Ti_xO_3$ in the morphotropic phase boundary region (x=0.25-0.5). J Phys: Condens Matter 17:5709–5723
- Bokov AA, Ye Z-G (2006) Recent progress in relaxor ferroelectrics with perovskite structure.
 J Mater Sci 41:31–52
- 58. Topolov VYu, Turik AV (1990) Elastic interaction of phases of Gd₂(MoO₄)₃ crystals. Izvestiya Vysshikh Uchebnykh Zavedeniy, Fizika 33(3):68–72 (in Russian)
- 59. Nakamura T, Kondo T, Kumada A (1971) Observation of phase boundaries between ferroand paraelectric phases in Gd₂(MoO₄)₃ crystals. Solid State Commun 9:2265–2268
- Metrat G (1980) Theoretical determination of domain structure at transition from twinned phase: application to the tetragonal-orthorhombic transition of KNbO₃. Ferroelectrics 26: 801–804
- Topolov VYu, Rabe H, Schmid H (1993) Mechanical stresses and transition regions in polydomain Pb₂CoWO₆ crystals. Ferroelectrics 146:113–121
- 62. Topolov VYu, Ye Z-G, Schmid H (1995) A crystallographic analysis of macrodomain structure in Pb(Mg_{1/3}Nb_{2/3})O₃. J Phys Condens Matter 7:3041–3049
- 63. Topolov VYu, Ye Z-G (1996) Formation of the stress-induced *mm*2 phase at the ferroelastic —antiferroelectric $\overline{4}3m$ — $\overline{4}2m$ phase transition in Cr–Cl boracite. J Phys Condens Matter 8:6087–6094
- 64. Topolov VYu (2007) Peculiarities of coexistence of heavily twinned phases in the (1-x)Pb (Mg_{1/3}Nb_{2/3})TiO₃ xPbTiO₃ solid solutions at 0.23 $\le x \le 0.30$. Crystallogr Rep 52: 297–301
- Balyunis LE, Topolov VYu, Bah IS, Turik AV (1993) The S-type domain and twin boundaries in plate-like PbZrO₃ crystals having complicated twinned structures. J Phys Condens Matter 5:1419–1426
- 66. Topolov VYu, Balyunis LE, Turik AV, Eremkin VV, Sori BI (1992) S-type twinning (domain) boundaries in PbZrO₃ crystals. Sov Phys Crystallogr 37:223–226
- 67. Topolov VYu (1990) On variety of conditions for realization of S-type domain boundaries in ferroelectric crystals. In: Proceedings of the all-union conference "real structure and properties of acentric crystals", September 17–22, 1990, Aleksandrov, VNIISIMS. Pt 2. Blagoveshchensk, pp 20–29 (in Russian)
- 68. Topolov VYu, Gagarina ES, Demidova VV (1995) Domain structure and related phenomena in PbYb_{0.5}Nb_{0.5}O₃ crystals. Ferroelectrics 172:373–376
- Balyunis LE, Topolov VYu, Turik AV, Fesenko OE (1990) Optical and crystallographic studies of twin and phase boundaries in antiferroelectric PbHfO₃. Ferroelectrics 111:291–298

- 70. Topolov VYu, Turik AV, Fesenko OE, Eremkin VV (1995) Mechanical stresses and three-phase states in perovskite-type ferroelectrics. Ferroelectr Lett Sect 20:19–26
- 71. Topolov VYu (1987) Electromechanical interactions in heterogeneous systems at ferroelectric phase transitions. Author's Abstract to the Thesis, Cand. Sci. (Phys. & Math.). Rostov State University, Rostov-on-Don (in Russian)
- Topolov VYu (1989) Analysis of conditions necessary for the existence of a flat non-deformed boundary separating polydomain ferroelastic phases. Bull Acad Sci USSR Phys Ser 53 (7), 51–54
- Kuhn W (1991) Domain structures induced by phase transitions in BaTiO₃ single crystals. Ferroelectr Lett Sect 13:101–108
- Topolov VYu (1998) Some features of three-phase states in PbZr_{1 x}Ti_xO₃ crystals. Crystallogr Rep 43:68–73
- 75. Lekhnitsky SG (1977) Elasticity theory of the anisotropic solid. Nauka, Moscow (in Russian)
- 76. Mura T (1987) Micromechanics of defects in solids. Martins Nijhoff Publications, Dordrecht
- Topolov VYu, Balyunis LE, Turik AV, Bah IS, Fesenko OE (1992) Interphase boundaries at cubic-rhombohedral phase transition in PbZrO₃ crystals. Bull Russ Acad Sci Phys 56: 1588–1593
- Ye Z-G, Topolov VYu (2001) Complex domain and heterophase structures in Pb(Mg_{1/3}Nb_{2/3})
 O₃-PbTiO₃ single crystals. Ferroelectrics 253:79–86
- 79. Sciau PH, Calvarin G, Sun BN, Schmid H (1992) X-ray study of phase transitions of the elpasolite-like ordered perovskite Pb₂CoWO₆. Physica Status Solidi (a) 129:309–321
- 80. Jaffe B, Cook WR, Jaffe H (1971) Piezoelectric ceramics. Academic Press, London
- 81. Noheda B, Cox DE, Shirane G (2002) Phase diagram of the ferroelectric relaxor (1 x)Pb $(Mg_{1/3}Nb_{2/3})O_3 x$ PbTiO₃. Phys Rev B 66:054104–10 p
- Kothai V, Senyshyn A, Ranjan R (2013) Competing structural phase transition scenarios in the giant tetragonality ferroelectric BiFeO₃-PbTiO₃: isostructural vs multiphase transition. J Appl Phys 113:084102–8 p
- 83. Brajesh K, Tanwar K, Abebe M, Ranjan R (2015) Relaxor ferroelectricity and electric-field-driven structural transformation in the giant lead-free piezoelectric (Ba, Ca) (Ti, Zr)O₃. Phys Rev B 92:224112–8 p
- 84. Topolov VYU, Ye Z-G (2004) Coexistence of morphotropic phases in (1 x)Pb(Mg_{1/3}Nb_{2/3}) O₃–xPbTiO₃ solid solutions. Phys Rev B 70:094113–8 p
- 85. Topolov VYu (2004) Unique three-phase states in (1 x)Pb(Zn_{1/3}Nb_{2/3})O₃-xPbTiO₃ single crystals. J Phys Condens Matter 16:2455–2461
- 86. Topolov VYu, Brajesh K, Ranjan R, Panich AE (2017) Plausible domain configurations and phase contents in two- and three-phase BaTiO₃-based lead-free ferroelectrics. J Phys D Appl Phys 50:065307–11 p

Chapter 2 Two-Phase States



Abstract Two-phase states and related heterophase structures are considered in ferroelectric solid solutions and some ferroelectric single crystals to highlight the validity of conditions for complete stress relief at elastic matching of the adjacent phases. The role of some non-90° domain types in achieving complete stress relief for compositions chosen near the morphotropic phase boundary is discussed in terms of unit-cell parameters, unit-cell spontaneous strains or unit-cell distortions. The effect of intermediate monoclinic (or orthorhombic) phases on the phase coexistence close to the morphotropic phase boundary is described in terms of the crystallographic method. Diagrams put forward suggest that there are a few possible scenarios of stress relief in the studied heterophase ferroelectric solid solutions.

Since the 1950s, the perovskite-type FE solid solutions are regarded as important objects for the study of interconnections in the fundamental triangle 'composition—structure—properties'. The FE solid solutions, especially those based on such well-known components as PbTiO₃, BaTiO₃ or KNbO₃, have been of great interest due to various electromechanical, FE and other properties [1–3]. In this chapter, we focus attention on the following perovskite-type solid solutions: Pb(Zr_{1-x}Ti_x)O₃ (PZT), PMN–xPT and (1-x)Pb(Zn_{1/3}Nb_{2/3})O₃–xPbTiO₃ (PZN–xPT). The compositions are chosen near the MPB that represents a transition region [4] where the crystal structure changes abruptly and extreme values of the physical properties [5] are observed when changing the molar concentration *x*. The PZT, PMN–xPT, PZN–xPT (SCs and ceramics) and related systems of solid solutions have been intensively studied in the last decades [6–18], and it is caused by many reasons.

First, the phase diagrams (x - T diagrams) of the aforementioned solid solutions are refined [11, 12, 15–18] after the discovery of the intermediate monoclinic phases [6, 7] with a FE nature. Before the discovery of the intermediate monoclinic phases, the distinguishing feature of the x - T diagrams of PZT [5, 6], PMN–xPT [13] and PZN–xPT [14] near the MPB consisted in the neighbourhood of vast regions of thermodynamic stability of the paraelectric cubic (Pm3m) phase and the FE tetragonal (P4mm) and rhombohedral (R3m) phases (Fig. 2.1a). The phase diagrams refined for these systems in the 2000s comprise the relatively narrow

regions of stability of the intermediate phase(s) close to the MPB [7, 11, 12, 15, 16, 19], and symmetry of the intermediate phase is either monoclinic or orthorhombic. Based on numerous experimental and theoretical results on PZT, PMN–xPT and PZN–xPT near the MPB [7, 8, 11, 12, 15, 16], we schematically show the region of stability of the intermediate phase(s) as a shaded area (Fig. 2.1b).

Second, the intermediate phases observed near the MPB often coexist with the adjacent FE phase [8, 11, 15–22] and influence the physical properties of solid solutions. The intricate DS [17, 24, 25] and coexistence of the FE phases from different symmetry classes [17, 19, 23, 24] make the aforementioned solid solutions attractive for the study of conditions for stress relief in the wide *x* and *T* ranges and at the electric-field-induced phase transition. In this context, we mention the theory of the adaptive FE phase [26]. This theory was put forward to predict the microdomain-averaged crystal lattice parameters of the structurally inhomogeneous state in PMN–*x*PT and PZN–*x*PT SCs. According to Jin et al. [26], the adaptive phase is the particular (miniaturized) case of conventional martensite with stress-accommodating domains, which can only be expected in situations where the domain-wall energy is abnormally small.

Third, domain-engineered PMN–*x*PT and PZN–*x*PT SCs poled along the fixed crystallographic directions exhibit extremely high piezoelectric activity [3, 25, 27, 28] that is important for sensor, actuator, energy-harvesting and other piezotechnical applications [29]. The considerable dependence of the physical properties on the orientation of the main crystallographic axes and the effect of the relaxor component (PMN or PZN) on the physical properties of the solid-solution system [3, 25, 28] are of independent interest.

Fourth, the exact location of the MPB is not yet well defined in the aforementioned and other perovskite-type solid solutions. Problems of the heterophase states close to the MPB and important results on this subject [10, 18, 23, 30–36] are discussed in the last decades.

The above-formulated reasons give rise to questions on elastic matching of the morphotropic phases, their domain contents, stability of the two-phase states and

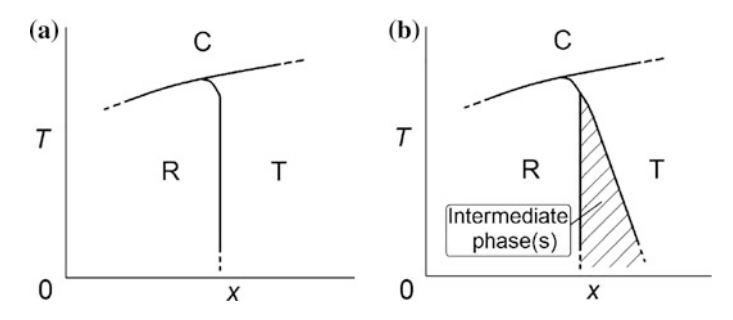


Fig. 2.1 Schematic drawing of the fragment of the x-T diagram of the solid solutions of PZT in the vicinity of the MPB before (a) and after discovery of the intermediate phases (b). C, cubic phase, R, rhombohedral phase and T, tetragonal phase. The MPB was regarded as a vertical line (a) between the regions of stability of the rhombohedral and tetragonal phases with the FE nature

stress-relief conditions in the two-phase systems. To answer these and other questions, in this chapter, we consider important examples of the two-phase states and discuss stress-relief ways in the presence of complex DSs in the adjacent FE phases.

2.1 Elastic Matching of Morphotropic Phases in Pb(Zr_{1-x}Ti_x)O₃

2.1.1 Tetragonal–Rhombohedral Phase Coexistence and Crystallographic Interpretation

In Sect. 2.1.1, we discuss features of the phase coexistence of the FE tetragonal (*P*4*mm*) and rhombohedral (*R*3*m*) phases near the MPB in PZT [1, 5]. It is assumed that the stability regions of these phases are separated by the near vertical MPB [5] (like that shown schematically in Fig. 2.1a), and no intermediate phase is observed. Results on the coexistence of the tetragonal and rhombohedral phases in PZT or related solid solutions are considered in numerous studies [4, 30–37] that were carried out long before the discovery of the intermediate monoclinic phases. An example of the detailed study of DSs in the rhombohedral phase of PZT SCs is given in work [39].

As follows from analysis of the perovskite unit-cell parameters of various PZT and related materials [30, 35, 36] near the MPB, these parameters at room temperature obey the condition

$$a_{\mathrm{T}} < a_{\mathrm{R}} < c_{\mathrm{T}},\tag{2.1}$$

where subscripts refer to the coexisting tetragonal (T) and rhombohedral (R) phases. Inequality (2.1) has the form similar to that for the unit-cell parameters of the tetragonal and cubic phases in FE SCs of BaTiO₃, PbTiO₃, etc. [1, 34]. The cubic–tetragonal interfaces can be ZNSPs if the tetragonal phase is split into the 90° domains of two types (see, for instance, Table 1.1). The validity of condition (2.1) enables us to consider elastic matching of the single-domain rhombohedral and polydomain tetragonal phases of PZT. In this case, the minimum number of domain types in a heterophase SC is three.

In the course of the crystallographic description of the phase coexistence, we assume that the rhombohedral phase is represented by one domain type (1, 2, 3 or 4 in Fig. 2.2a), and the tetragonal phase is characterized by the regular 90° DS with the domain orientations shown in Fig. 2.2b, c. The 90° domains are separated, according to Fousek and Janovec [38], by the unstrained domain walls that are parallel to the {110} planes (Fig. 2.2b, c) of the perovskite unit cell. A formation of the 180° DS in the coexisting phases does not influence their elastic matching, and therefore, we do not consider the 180° domains or alternative antiparallel domain orientations to those shown in Fig. 2.2.

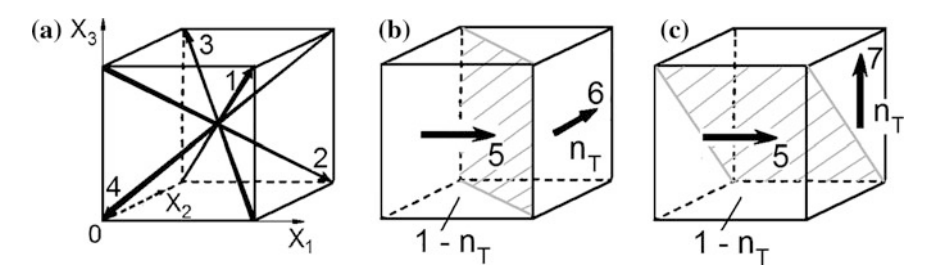


Fig. 2.2 Orientations of spontaneous polarization vectors in non-180° domains of the rhombohedral (**a**) and tetragonal (**b** and **c**) phases of PZT. The coordinate axes OX_j are parallel to the perovskite unit-cell axes in the cubic phase. n_T and $1 - n_T$ are volume fractions of the 90° domain types (twin components) in the tetragonal phase. The domains in the tetragonal phase are separated by the 90° walls (shaded areas, **b** and **c**)

Distortion matrices of the coexisting phases in PZT are written with respect to the rectangular coordinate axes (OX_j) shown in Fig. 2.2. The distortion matrices of the domains 1, 2, 3 and 4 in the rhombohedral phase (see the domain orientations in Fig. 2.2a) are

respectively. The distortion matrices of the polydomain tetragonal phase are written in the following form:

$$\|N_{ij}^{(5-6)}\| = n_T \begin{pmatrix} \varepsilon_{a} & 0 & 0 \\ 0 & \varepsilon_{a} & 0 \\ 0 & 0 & \varepsilon_{a} \end{pmatrix}$$

$$+ (1 - n_T) \begin{pmatrix} \cos \varphi_{T} & -\sin \varphi_{T} & 0 \\ \sin \varphi_{T} & \cos \varphi_{T} & 0 \\ 0 & 0 & 1 \end{pmatrix} \begin{pmatrix} \varepsilon_{a} & 0 & 0 \\ 0 & \varepsilon_{a} & 0 \\ 0 & 0 & \varepsilon_{a} \end{pmatrix}$$

$$(2.3)$$

(domain types 5 and 6, see Fig. 2.2b) and

$$\|N_{ij}^{(5-7)}\| = n_T \begin{pmatrix} \varepsilon_a & 0 & 0 \\ 0 & \varepsilon_a & 0 \\ 0 & 0 & \varepsilon_a \end{pmatrix}$$

$$+ (1 - n_T) \begin{pmatrix} \cos \varphi_T & 0 & -\sin \varphi_T \\ 0 & 1 & 0 \\ \sin \varphi_T & 0 & \cos \varphi_T \end{pmatrix} \begin{pmatrix} \varepsilon_a & 0 & 0 \\ 0 & \varepsilon_a & 0 \\ 0 & 0 & \varepsilon_a \end{pmatrix}$$

$$(2.4)$$

(domain types 5 and 7, see Fig. 2.2c). Equations (2.2)–(2.4) are written in terms of the perovskite unit-cell distortions $\mu_a = a_R \cos \omega_R/a_C$, $\mu = a_R \sin \omega_R/a_C$, $\varepsilon_a = a_T/a_C$ and $\varepsilon_c = c_T/a_C$. The angle $\varphi_T = \arccos{[2\varepsilon_a\varepsilon_c/(\varepsilon_a^2 + \varepsilon_c^2)]}$ in (2.3) and (2.4) describes a rotation of the crystallographic axes of the adjacent 90° domains [40] in the tetragonal phase. The unit-cell distortions depend on the unit-cell parameters of the rhombohedral (a_R and ω_R), tetragonal (a_T and c_T) and cubic (a_C) phases. The unit-cell parameter a_C of the unstrained paraelectric cubic phase is assumed to be extrapolated to room temperature at which the coexistence of the morphotropic phases in PZT is studied. The value of a_C does not influence the results on the ZNSPs that are described below.

To consider possibilities of complete stress relief in the heterophase system, we examine the validity of conditions (1.5) and (1.6) using the distortion matrices from (2.2) to (2.4) and the experimental unit-cell parameters of PZT + 2% Nd ceramics [35] near the MPB. Wersing et al. [35] presented data on these ceramics prepared by two methods, the mixed oxide method and the method of spray drying of salt solutions. As seen from Table 2.1, the optimal volume fractions $n_{\rm T}^{\rm opt}$ of the 90° domains in the tetragonal phase (see Fig. 2.2b, c) remain almost constant with the change in the molar concentration x. The similar constancy ($n_{\rm T}^{\rm opt} \approx 0.3$ or 0.7) takes place if we use the room-temperature unit-cell parameters [35] of PZT compositions prepared by spray drying of salt solutions. The interphase boundary separating the polydomain tetragonal and single-domain rhombohedral phases is oriented close to

Table 2.1 Optimal volume fractions^a n_T^{opt} that correspond to ZNSPs at elastic matching of the tetragonal (P4mm) and rhombohedral (R3m) phases of PZT + 2% Nd ceramics

x	$n_{\rm T}^{\rm opt}$ (domain 1 or 3 in the rhombohedral	$n_{\rm T}^{\rm opt}$ (domain 2 or 4 in the rhombohedral
	phase)	phase)
0.42	0.293 or 0.704	0.299 or 0.703
0.44	0.292 or 0.705	0.298 or 0.704
0.46	0.291 or 0.706	0.298 or 0.705
0.48	0.286 or 0.711	0.293 or 0.710

^aValues of $n_{\rm T}^{\rm opt}$ were calculated on assumption that the tetragonal phase is split into the 90° domains of types 5 and 6 (Fig. 2.2b). The $n_{\rm T}^{\rm opt}$ values listed in the second column are also attained at elastic matching of the tetragonal phase (domains 5 and 7, Fig. 2.2c) and the rhombohedral phase (domain 1 or 4, Fig. 2.2a). The $n_{\rm T}^{\rm opt}$ values listed in the third column are also attained at elastic matching of the tetragonal phase (domains 5 and 7, Fig. 2.2c) and the rhombohedral phase (domain 2 or 3, Fig. 2.2a)

the (010) plane of the perovskite unit cell. This orientation determined using (1.8) is accounted for by fulfilment of the necessary conditions [41] $N_{11} = M_{11}$ and $N_{33} = M_{33}$, where the matrix elements N_{ii} are taken from (2.3) or (2.4), and the matrix elements M_{ii} are taken from (2.2). These conditions are simultaneously valid with accuracy to 5% at the optimal volume fraction $n_{\rm T}^{\rm opt}$ in the tetragonal phase.

The results on the phase coexistence are in agreement with experimental data on PZT near the MPB. The widespread of the 90° domains in comparison to the 71° (109°) domains [7, 37] is concerned with the leading role of the 90° DS and the anisotropy of the unit-cell distortions ε_a and ε_c in stress relief in the heterophase system. A model of the MPB [37] is based on the experimental study of the DS in grains of ceramic PZT. According to the model put forward in work [37], the spontaneous polarization vectors of the domains in the morphotropic phases are oriented along the following unit-cell directions: $[001] \rightarrow [111] \rightarrow [010]$ $[111] \rightarrow [001] \rightarrow ...$ This sequence suggests that the 90° domains of the tetragonal phase coexist with the single-domain rhombohedral phase, and even an internal stress field caused by the interaction between the ceramic grains of PZT would not considerably affect elastic matching of the morphotropic phases. Moreover, the interphase boundaries in the model put forward by Lucuţa et al. [37] are parallel to the {100} planes of the perovskite unit cell, but reasons for these orientations were not discussed from the energetic viewpoint.

It should be added that influence of the internal stress field on the tetragonal–rhombohedral phase coexistence in the PZT grain was studied within the framework of the thermodynamic method [41]. As follows from estimations in work [41], the width of the molar-concentration x range, in which the morphotropic phases may coexist at room temperature, varies from 0 (at complete stress relief) to about 0.074 (no stress relief is achieved). The latter value is comparable to that known for PZT ceramics [7, 34] wherein the considerable internal stress field is present in compositions around the MPB.

2.1.2 Elastic Matching and Stress Relief in the Presence of the Intermediate Monoclinic Phase

Experimental results [7, 8] show that the intermediate FE monoclinic phase in PZT (M_A phase in terms of work [42]) exists near the MPB (see the shaded area in Fig. 2.1b). The symmetry group of the M_A phase Cm is a subgroup of both the tetragonal (P4mm) and rhombohedral (R3m) groups. High-resolution synchrotron X-ray powder diffraction measurements [7] on highly homogeneous PZT samples suggest that the M_A phase is stable over certain ranges of x and x and the phase coexistence is observed in various compositions (for example, at x = 0.45, 0.46 and 0.51) in the wide temperature range. The single-domain M_A phase is characterized by the spontaneous polarization vector $P_x(P_x; P_y; P_z)$ with $P_x = P_y < P_z$. This vector is confined to the mirror plane ($1\overline{10}$) of the perovskite unit cell, and the spontaneous

polarization vectors of the adjacent phases are assumed to be parallel to the unit-cell directions [001] (tetragonal phase) and [111] (rhombohedral phase) [42]. In Sect. 2.1.2, we analyse elastic matching of the phases in PZT to indicate the role of the intermediate monoclinic phase in the heterophase states and stress relief. Our analysis is based on experimental values of the unit-cell parameters [7] of the phases coexisting in PZT.

In the course of the crystallographic description of the heterophase states, we consider a two-phase SC (or a ceramic grain) that undergoes one of the following first-order phase transitions: tetragonal-rhombohedral (P4mm-R3m), tetragonal- M_A (P4mm-Cm) or rhombohedral- M_A (R3m-Cm). It is assumed that the tetragonal phase is split into the 90° domains of types 5 and 7 (Fig. 2.2c). The rhombohedral phase is single-domain (see type 4 in Fig. 2.2a). The non-180° domains in the M_A phase are characterized by the unit-cell vectors (a_M , b_M , c_M) with approximate orientations ([110], [110], [001]) and ([011], [011], [100]) and volume fractions n_M and $1-n_M$, respectively. The aforementioned orientations of the unit-cell vectors are given in the perovskite unit-cell axes.

The distortion matrices of the tetragonal and rhombohedral phases are $\left\|N_{ij}^{(5-7)}\right\|$ from (2.4) and $\left\|M_{ij}^{(4)}\right\|$ from (2.2), respectively. The distortion matrix of the M_A phase is written in terms of the unit-cell distortions η_a , η_b , ... by analogy with (2.4):

$$\|N_{ij}^{(MA)}\| = n_{M} \begin{pmatrix} \eta_{a} & \eta_{ab} & \eta_{ac} \\ \eta_{ab} & \eta_{b} & \eta_{bc} \\ \eta_{ac} & \eta_{bc} & \eta_{c} \end{pmatrix}$$

$$+ (1 - n_{M}) \begin{pmatrix} \cos \varphi_{M} & 0 & -\sin \varphi_{M} \\ 0 & 1 & 0 \\ \sin \varphi_{M} & 0 & \cos \varphi_{M} \end{pmatrix} \begin{pmatrix} \eta_{c} & -\eta_{bc} & -\eta_{ac} \\ \eta_{bc} & \eta_{b} & \eta_{ab} \\ \eta_{ac} & \eta_{ab} & \eta_{a} \end{pmatrix} .$$

$$(2.5)$$

In (2.5), $\varphi_{\rm M}=\arccos{[2\eta_{\rm a}\eta_{\rm c}/(\eta_{\rm a}^2+\eta_{\rm c}^2)]}$ is the angle of the rotation of the crystal-lographic axes of the adjacent domains. This angle is introduced by analogy with $\varphi_{\rm T}$ from (2.4). Taking $\left\|N_{ij}^{(5-7)}\right\|$ from (2.4), $\left\|M_{ij}^{(4)}\right\|$ from (2.2) and $\left\|N_{ij}^{({\rm MA})}\right\|$ from (2.5) in pairs, we examine the validity of conditions (1.5) and (1.6) for complete stress relief in the two-phase states of PZT.

Results shown in Table 2.2 and Fig. 2.3 suggest that the temperature and molar-concentration dependences of the unit-cell parameters of PZT [8] are favourable for the formation of the ZNSP (see points 1–5 and 7 in Fig. 2.3) or slightly strained interphase boundaries (see points 6 and 8 in Fig. 2.3). The strained interphase boundaries can be in the form of planar or conic [43] surfaces with a sufficiently small curvature. According to formulae from (1.8), the orientations of the ZNSPs are approximated [43] by the Miller indices $\{0kl\}$ in the perovskite unit-cell axes, where the k/l ratio depends on T, x and volume fractions of the non-180° domains in the coexisting phases.

Table 2.2 Features of elastic matching of ferroelectric phases in $Pb(Zr_{1-x}-Ti_x)O_3$ solid solution	s
(reprinted from paper by Tolpolov and Turik [43], with permission from IOP Publishing	

Coexisting phases	x	T, K	Optimal volume fractions corresponding to elastic matching along ZNSPs	Conditions for slightly strained interphase boundaries (if no	Points in Fig. 2.3
				ZNSPs are determined)	
P4mm and	0.45	550	$n_{\rm T,opt} = 0.691 \text{ or}$	_	1
R3m			$n'_{\text{T,opt}} = 0.309$		
		500	$n_{\rm T,opt} = 0.698 \text{ or}$	_	2
			$n'_{\text{T,opt}} = 0.302$		
R3m and	0.45-	300	$n_{\mathrm{M,opt}} = 0.700 \text{ or}$	_	3
Cm	0.46		$n'_{\rm M,opt} = 0.300$		
		20	$n_{\mathrm{M,opt}} = 0.724 \text{ or}$	_	4
			$n'_{\rm M,opt} = 0.276$		
P4mm and	0.46	400	$n_{\text{T,opt}} = 1$ and $n_{\text{M,opt}} = 1$ or	_	5
Cm			$n'_{\text{T,opt}} = 0$ and $n'_{\text{M,opt}} = 0$		
	0.47-	300	_	$n_{\rm T} \rightarrow 1 \text{ and } n_{\rm M} \rightarrow 1 \text{ or}$	6
	0.48			$n_{\rm T}' \to 0 {\rm and} n_{\rm M}' \to 0$	
	0.51-	300	$n_{\text{T,opt}} = 1$ and $n_{\text{M,opt}} = 1$ or	_	7
	0.52		$n'_{\text{T,opt}} = 0$ and $n'_{\text{M,opt}} = 0$		
		20		$n_{\rm T} \rightarrow 1 \text{ and } n_{\rm M} \rightarrow 1 \text{ or}$	8
				$n_{\mathrm{T}}' \to 0 \text{ and } n_{\mathrm{M}}' \to 0$	

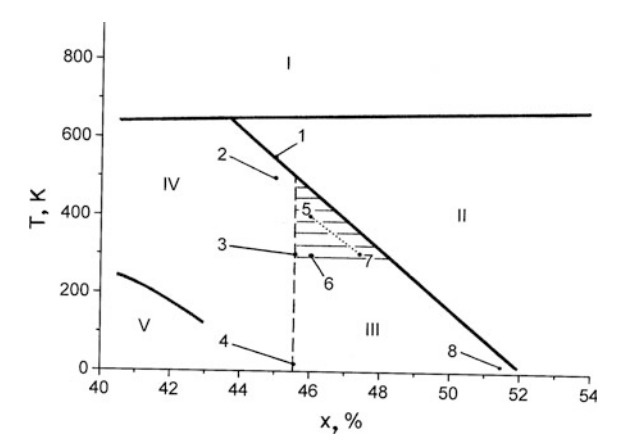


Fig. 2.3 Fragment of the x-T diagram of PZT around the MPB. I, II, III, IV and V denote the Pm3m, P4mm, Cm, R3m and R3c phases, respectively. The hatched area represents the region of the coexistence of the P4mm and Cm phases. Points 1–8 correspond to different variants of elastic matching of the adjacent single-domain or polydomain phases in accordance with results from Table 2.2 (reprinted from paper by Topolov and Turik [43], with permission from IOP Publishing)

The constancy of the optimal volume fractions $n_{T,\text{opt}}$ and $n_{M,\text{opt}}$ (or $n'_{T,\text{opt}}$ and $n'_{M,\text{opt}}$, respectively) and complete stress relief at the interphase boundaries, separating the single-domain rhombohedral phase and polydomain tetragonal or M_A phase, take place over a narrow molar-concentration range ($\Delta x \approx 0.01$) and a very wide temperature range ($\Delta T > 500$ K, see Table 2.2). Complete stress relief is attained due to the non-180° domains in the tetragonal and M_A phases. It should be noted that these polydomain phases are characterized by similar anisotropies of the spontaneous strains [43]. Splitting the rhombohedral phase into the 71° (109°) domains does not lead to considerable changes in Table 2.2: the optimal volume fractions $n_{T,\text{opt}}$, $n_{M,\text{opt}}$, $n'_{T,\text{opt}}$ and $n'_{M,\text{opt}}$ would deviate by less than 1%. The values of $n_{T,\text{opt}}$ and $n'_{T,\text{opt}}$ (Table 2.2), which correspond to the ZNSPs at rhombohedral–tetragonal interphase boundaries, are almost equal to the n_T^{opt} values from Table 2.1. We mention that the n_T^{opt} values listed in Table 2.1 were calculated using the unit-cell parameters [35] measured on the PZT ceramic samples long before the discovery of the intermediate monoclinic phases in these solid solutions.

As follows from work [44], the virtual constancy of the optimal volume fractions of the non-180° domains (Table 2.2) is concerned with a relation between the unit-cell parameters. For example, the angle of the monoclinic distortion β of the perovskite unit cell obeys the inequality $\beta - 90^{\circ} < 0.5^{\circ}$, and spontaneous strains of the perovskite unit cell in the tetragonal and M_A phases obey the condition $(\xi_{11}^s)_{MA} \approx (\xi_{22}^s)_{MA} \approx (\xi_{rr}^s)_T$, where r=1 and 2, and subscripts MA and T refer to the M_A and tetragonal phases, respectively. We see that the single-domain M_A and tetragonal phases in PZT can be elastically matched along the ZNSP or slightly strained interphase boundary (see points 5–8 in Fig. 2.3) in the case when the x and x values correspond to the new MPB [7] separating the stability regions of the tetragonal and x phases. The orientation of the interphase boundary (ZNSP) at the coexistence of the single-domain x and tetragonal phases is close to x of the perovskite unit cell [44].

The linear segment, that connects points 5 and 7 in Fig. 2.3 and corresponds to the ZNSPs, is parallel to the tetragonal– M_A MPB [44]. We note that such a correlation has no analogues among the FE solid solutions near the MPB. The mutual location of segment 5–7 (Fig. 2.3) and the tetragonal– M_A boundary in the x-T diagram of PZT [8] means that the interphase boundaries between the single-domain phases are slightly strained near this segment. In this case, the internal mechanical stress would be insufficient to give rise to splitting one of the phases into the non-180° domains. The results shown in Table 2.2 agree with assumptions [8] on the active role of the non-180° domains in stress relief in heterophase PZT. Elastic matching of the single-domain (untwined) phases along the ZNSPs rarely occurs in FE and related SCs (see, for instance, work [45, 46]) and, most likely, is not realized in PZT ceramics because of the internal mechanical stress field, composition fluctuations, etc.

It should be noted for comparison, that, according to the synchrotron X-ray diffraction data [22], $Pb(Zr_{0.525}Ti_{0.475})O_3$ ceramic is characterized by nearly pure monoclinic phase composition [47] with Cm symmetry at room temperature, and no

essential phase coexistence is detected. We mention that this composition is located just under point 7 in Fig. 2.3, and therefore, possibilities for the phase coexistence in this region may be very restricted. Singh et al. [47] studied important features of the electromechanical properties of PZT ceramics (x = 0.475, 0.480, 0.485, etc.) in a wide temperature range. At room temperature, these compositions are located under segment 6–7 in Fig. 2.3. The higher piezoelectric response of these ceramic compositions is accounted for by softening of elastic moduli on approaching the tetragonal–monoclinic phase transition [47]. The strong correlation between phase-transition structural changes and corresponding changes in the electromechanical properties is concerned with the elastic instability of the PZT ceramics [47]. In our opinion, this elastic instability can be concerned with the features of elastic matching of the tetragonal and M_A phases in the near single-domain state (see Table 2.2, points 6 and 7).

The results discussed in Sect. 2.1 illustrate different ways for stress relief at elastic matching of the FE phases in PZT near the MPB. The intermediate M_A phase plays the important role in stress relief and can be really regarded as a bridging phase (as termed in work [8]). The results presented in Table 2.2 were obtained on assumption [43, 44] that the phase coexistence takes place in bulk SCs or separate stress-free grains. It is clear that conditions for stress relief in the ceramic grains surrounded by an aggregate of the similar grains differ from the conditions considered above. Nevertheless, the features of the behaviour of the unit-cell parameters, the spontaneous strains and distortions in PZT are the most significant factor in effective stress relief in heterophase structures.

2.2 Phase Coexistence in (1 - x)Pb $(Mg_{1/3}Nb_{2/3})O_3$ -xPbTi O_3 Near the Morphotropic Phase Boundary

2.2.1 Phase Coexistence Without the Monoclinic Phase

SCs of the PMN–*x*PT solid solutions are expected to synergetically combine the properties of both relaxor PMN and regular FE PbTiO₃. In domain-engineered relaxor-FE PMN–*x*PT SCs with compositions close to the MPB, the extremely large piezoelectric coefficients (e.g. the longitudinal piezoelectric coefficient $d_{33} > 2000$ pC/N at x = 0.28, 0.30 [48] and 0.33 [49]) and the very high electromechanical coupling factor ($k_{33} \approx 90\%$ at x = 0.28 [48] and 0.33 [49]) are achieved at room temperature. In the general case, PMN–*x*PT and other relaxor-based FE SCs crystals are characterized by complex DS [25, 50], banded and crossing domain patterns [51, 52], etc. The 90° and 180° domains are observed in the tetragonal phase, the 71°, 109° and 180° domains are present in the rhombohedral phase of PMN–*x*PT, etc. The DS and heterophase states in PMN–*x*PT SCs near the MPB [53] considerably depend on the molar concentration *x*, temperature *T*, electric field *E* and other factors.

For example, the DS of PMN–0.20PT SCs is characterized by rhombohedral symmetry (R3m) of the perovskite unit cell and by weak birefringence at room temperature. PMN–0.50PT SCs are characterized by tetragonal symmetry (P4mm) of the perovskite unit cell and by strong birefringence. PMN–0.35PT SCs with the composition close to the MPB exhibit heterophase structures (R3m + P4mm) and complex domain patterns (see examples in Fig. 2.4). As follows from the experimental study, the DSs in PMN–0.35PT SCs are composed of regions of the rhombohedral and tetragonal phases intimately mixed with multiple orientation states [53]. The important feature of MPB behaviour of PMN–xPT SCs is the fact that the sequence and temperatures of the phase transitions considerably depend on the local DS and molar concentration x [24, 53].

The crystallographic interpretation of the various non-180° DSs and heterophase structures observed in PMN–xPT SCs is carried out by using experimental data [24, 54–56] on the unit-cell parameters in a wide range of T and x. To analyse the coexistence of the cubic paraelectric and tetragonal FE phases, we assume that the tetragonal phase is split into the 90° domains of two types (Fig. 2.2b, c), and the corresponding distortion matrices of the polydomain phase are given by (2.3) and (2.4). Distortions of the unstrained cubic phase are described by the identity 3×3 matrix. The validity of conditions (1.5) and (1.6) suggests that the cubic–tetragonal interphase boundaries are ZNSPs as the optimal volume fractions of the 90° domains $n_{\text{T,opt}}$ and $1 - n_{\text{T,opt}}$ are attained in the tetragonal phase [53]. The orientation of these interphase boundaries is approximated by the Miller indices {h0l} [53] in the perovskite unit-cell axes. The values of the h/l ratio are approximately equal to 7/8, 4/5 and 1/1 at molar concentrations x = 0.40, 0.35 and 0.30, respectively. The corresponding ratios of the optimal volume fractions of the 90° domains

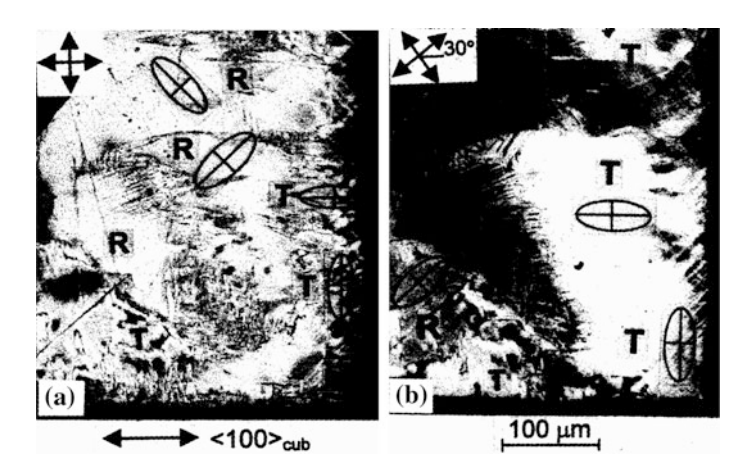


Fig. 2.4 Morphotropic DS and phase transition in a $(001)_{\text{cub}}$ PMN-0.35PT platelet (thickness 3.4×10^{-5} m). **a** Coexistence of the tetragonal (T) and rhombohedral (R) phases at T = 25 °C. **b** Rhombohedral-tetragonal phase transition at 70 °C. The tetragonal phase grows at the expense of the rhombohedral phase (reprinted from paper by Ye and Topolov [53], with permission from Taylor & Francis)

 $n_{\mathrm{T,opt}}/(1-n_{\mathrm{T,opt}})$ undergo changes within the relatively narrow range. According to data [53], $n_{\mathrm{T,opt}} = 0.667$ or 0.333 at x = 0.30 and $n_{\mathrm{T,opt}} = 0.639$ or 0.361 at x = 0.40, and $n_{\mathrm{T,opt}}/(1-n_{\mathrm{T,opt}}) \approx 2$ at $0.30 \leq x \leq 0.40$. We add for comparison that the interphase boundary in PbTiO₃ SCs (x = 1) at the cubic–tetragonal phase transition also obeys the conditions for ZNSP's (see Table 1.1).

The cubic–rhombohedral interphase boundary in PMN–xPT SCs can be described by means of the *domain state–interface diagrams* [53, 57]. It is assumed that the rhombohedral phase is split into the 71° (109°) domains with the orientations shown in Fig. 2.5. The volume fractions of these domains are expressed in terms of the parameters x_R and y_R as follows: $o_1 = (1 - x_R)(1 - y_R)$, $o_2 = (1 - x_R)y_R$, $o_3 = x_R(1 - y_R)$ and $o_4 = x_Ry_R$. The distortion matrix of the polydomain rhombohedral phase with the orientation of the non-180° domains shown in Fig. 2.5 is written as

$$||N_{ij}|| = \begin{pmatrix} \mu_{a} & \mu(2y_{R} - 1) & \mu(2x_{R} - 1)(2y_{R} - 1) \\ \mu(2y_{R} - 1) & \mu_{a} & \mu(2x_{R} - 1) \\ \mu(2x_{R} - 1)(2y_{R} - 1) & \mu(2x_{R} - 1) & \mu_{a} \end{pmatrix}, (2.6)$$

where $\mu_a = (a_R \cos \omega_R)/a_C$ and $\mu = (a_R \sin \omega_R)/a_C$ are the unit-cell distortions, a_R and ω_R are the linear unit-cell parameter and shear angle of the perovskite unit cell in the rhombohedral phase and a_C is the unit-cell parameter in the cubic phase. The domain state-interface diagrams shown in Fig. 2.6 were calculated by taking into account (1.14)–(1.18) and using experimental values of the unit-cell parameters of PMN-xPT [24]. All the curves on the diagrams shown in Fig. 2.6 are situated symmetrically with respect to lines $x_R = 0.5$ and $y_R = 0.5$. Such an arrangement is concerned with structure of the distortion matrix from (2.6). A remarkable feature of the diagrams consists in the fact that their major areas correspond to the stressed conical interphase boundaries (see, for instance, regions II and III in Fig. 2.6a, as

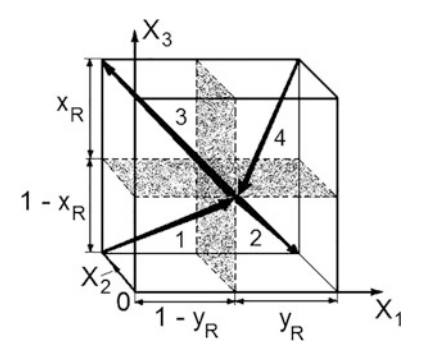


Fig. 2.5 Schematic arrangement of 71° (109°) domains (mechanical twins) in the polydomain rhombohedral phase of PMN–xPT SCs. Directions of the spontaneous polarization vectors in the domains 1–4 (see Fig. 2.2a) are shown by arrows. The domains are separated by the domain walls (see shaded areas). Parameters x_R and y_R characterize the volume fractions of domains (twins) 3–4 and 2–4, respectively. The coordinate axes OX_j are parallel to the perovskite unit-cell axes in the cubic phase

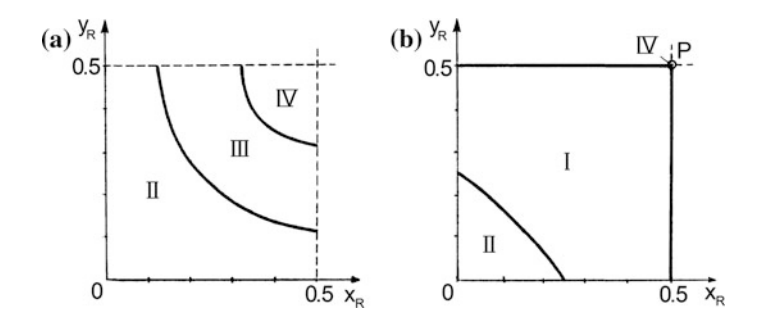


Fig. 2.6 Domain state—interface diagrams calculated for the cubic—rhombohedral (Pm3m - R3m) phase transition in PMN–xPT SCs at x = 0.20 (a) and x = 0.25 (b). The rhombohedral phase is assumed to be split into domains as shown in Fig. 2.5. Regions I, II and III correspond to real cones that obey conditions (1.16), (1.14) and (1.15), respectively. Region IV corresponds to the imaginary cone apex, see conditions (1.17). In diagram (b) region IV is represented by the point P (reprinted from paper by Ye and Topolov [53], with permission from Taylor & Francis)

well as regions I and II in Fig. 2.6b). Conditions for the ZNSP hold [53] for lines $x_R = 0.5$ and $y_R = 0.5$, except for the P point (i.e. at $x_R = y_R = 0.5$) in Fig. 2.6b.

It is important to compare the diagrams shown in Fig. 2.6 to the diagram calculated for PMN SCs at the electric-field-induced transition (Fig. 2.7a). The orientations of the domains in the rhombohedral phase are shown in Fig. 2.7b. An analogy between the diagrams calculated for x = 0 (Fig. 2.7a) and x = 0.20 (Fig. 2.6a) is concerned [53] with the similar ratios of the unit-cell distortions μ_a/μ for these compositions and with the considerable remoteness of the compositions with $x \le 0.20$ from the MPB. A composition located in the phase diagram closer to the MPB (for instance, x = 0.25) considerably influences the μ_a/μ ratio and hence the configuration and position of the curves on the diagram (see Fig. 2.6b). This behaviour can be interpreted in terms of the local structure and related properties of the PMN–xPT system [54, 55] that undergoes changes from a relaxor-FE regime with lower Ti⁴⁺-concentration ($x \to 0$) to a long-range-ordered normal FE state.

Our analysis of conditions for complete stress relief [53] in heterophase structures suggests that the interphase boundaries separating the rhombohedral and tetragonal phases in PMN–xPT SCs around the MPB are in general stressed and have either conical or more complicated shapes. For example, no ZNSPs are present at elastic matching of these phases with various non-180° DSs in PMN–xPT SCs of MPB composition (x = 0.35) at room temperature, Examples of the DSs in the coexisting phases are schematically shown in Figs. 2.2b, c and 2.5. One of the possible reasons [53] for this stressed state is associated with a difference in the ratios of unit-cell distortions

$$\Delta_{\mathrm{T-R}} = (\mu_{\mathrm{a}}/\varepsilon_{\mathrm{a}}) - (\mu_{\mathrm{a}}/\varepsilon_{\mathrm{c}}) = a_{\mathrm{R}}\cos\omega_{\mathrm{R}} \left(a_{\mathrm{T}}^{-1} - c_{\mathrm{T}}^{-1}\right),\tag{2.7}$$

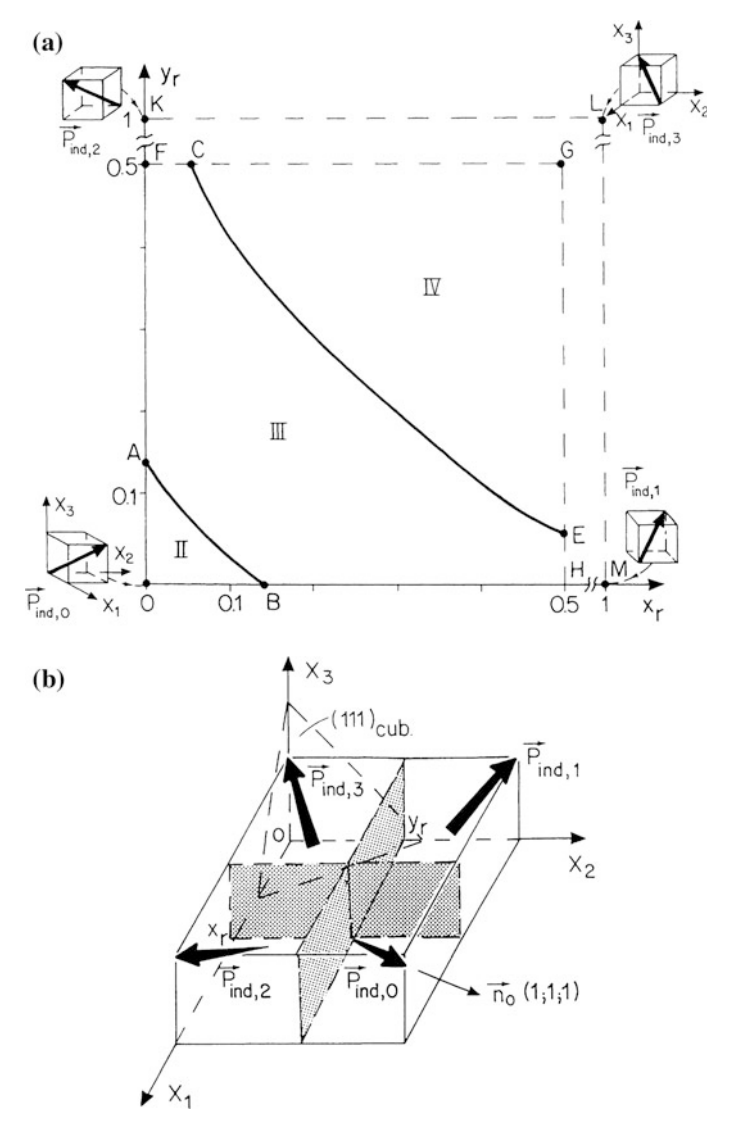


Fig. 2.7 Domain state–interface diagram (**a**) calculated for the cubic–rhombohedral (Pm3m-R3m) phase transition induced by the electric field $E \parallel [001]$ in PMN SCs. Orientations of vectors of the induced polarization $P_{\mathbf{ind},j}$ in domains of the rhombohedral phase are shown in schematic (**b**). The coordinate axes OX_j are parallel to the perovskite unit-cell axes in the cubic phase. Volume fractions o_j of the domains with $P_{\mathbf{ind},j}$ are expressed in terms of the parameters x_r and y_r as follows: $o_0 = (1 - x_r)(1 - y_r)$, $o_1 = x_r(1 - y_r)$, $o_2 = (1 - x_r)y_r$ and $o_3 = x_ry_r$. Regions II and III correspond to real cones that obey conditions (1.14) and (1.15), respectively. Region IV corresponds to the imaginary cone apex that obey conditions (1.17) (reprinted from paper by Topolov et al. [57], with permission from IOP Publishing)

where ε_a , ε_c and μ_a are the linear unit-cell distortions of the coexisting phases [see (2.3), (2.4) and (2.6)], a_T , c_T , a_R and ω_R are the unit-cell parameters of the phases. As follows from the unit-cell behaviour [54, 55] at x = 0.35, the parameter from (2.7) $\Delta_{T-R} < 1\%$, and the corresponding unit-cell distortions of PMN–xPT do not satisfy the necessary conditions [41] for the ZNSPs to exist.

Contrary to the compositions of PMN–xPT SCs, the unit-cell parameters of the tetragonal and rhombohedral phases in PZT solid solutions provide complete stress relief at room temperature within a wide range of x (see Sect. 2.1). Our calculations performed using the room-temperature unit-cell parameters of PZT compositions near the MPB [33, 35] show that the inequality $\Delta_{T-R} > 2\%$ is valid, where Δ_{T-R} is the parameter from (2.7). In our opinion, the discrepancy between the Δ_{T-R} values [53] calculated for the morphotropic compositions of PMN–xPT and PZT lies in the difference of values of the perovskite unit-cell shear angle ω_R that considerably influences the shear distortion of the rhombohedral phase [see (2.6)] and, therefore, elastic matching of the phases around the MPB.

2.2.2 Phase Coexistence in the Presence of the Intermediate Monoclinic Phases

Recent studies on the PMN–xPT system led to a series of important experimental results on the physical nature and crystallographic features of the intermediate phases near the MPB. The intermediate monoclinic phase in the MPB region at room temperature was first reported by Singh and Pandey [58]. Based on X-ray diffraction data for unpoled PMN–0.34PT ceramic samples, Singh and Pandey ascertained [58] that this intermediate phase is of the M_C type (in terms of the theoretical description by Vanderbilt and Cohen [42]) with space group *Pm*. Kiat et al. independently reported [59] the existence of the M_C-type phase in PMN–xPT at low temperatures on account of a phase transition from a room-temperature FE tetragonal phase.

The further confirmation of the experimental results [58, 59] was given in work [15] where synchrotron X-ray powder diffraction measurements were performed on the unpoled PMN–xPT ceramic samples with $0.30 \le x \le 0.39$. Noheda et al. [15] studied temperature and molar-concentration dependences of the unit-cell parameters in the MPB region as well as two-phase mixtures, e.g. rhombohedral + M_C or M_C + tetragonal phases. Based on the numerous structural data, Noheda et al. [15] proposed the new phase diagram for the PMN–xPT system and showed the following stability regions of the M_C phase around the MPB: $0.31 \le x \le 0.37$ at temperature T = 20 K and $0.31 \le x \le 0.35$ at T = 300 K. The coexistence of the M_C and tetragonal phases was then confirmed [60] by rigorous Rietveld analysis of the room-temperature X-ray diffraction data. Singh and Pandey [60] showed that some of the PMN–xPT compositions ($0.27 \le x \le 0.30$), believed to be rhombohedral in paper [15], are indeed characterized by monoclinic symmetry: the

corresponding morphotropic phase with space group Cm was designated as the M_B -type phase following notations from work [42]. It should be mentioned that the common feature of the intermediate M_B and M_C phases consists in the presence of the spontaneous polarization vector confined to the (010) plane of the perovskite unit cell.

The existence of the M_B phase in highly homogeneous and stoichiometric PMN–0.29PT samples was confirmed [61] in the powder neutron diffraction study. On the basis of the Rietveld analysis and dielectric measurements on the ceramic samples at room temperature, four composition ranges were determined [60] for the following dominant phases: rhombohedral (R3m) at $0 \le x \le 0.26$, M_B (Cm) at $0.27 \le x \le 0.30$, M_C (Pm) at $0.31 \le x \le 0.34$ and tetragonal (P4mm) at $0.35 \le x \le 1$. The presence of the two FE monoclinic phases in between the well-studied rhombohedral and tetragonal phases of PMN–xPT is consistent with the theoretical results from work [42]. The coexistence of the M_B and M_C phases in ceramic PMN–xPT ($0.26 \le x \le 0.30$) is observed in experimental work [62]. According to data [62], the M_B phase (which follows the wide stability range of the rhombohedral phase) is also observed in the molar-concentration range $0.23 \le x \le 0.25$ at room temperature.

Various heterophase structures [17, 23, 63] and DSs [64–69] are observed in PMN–xPT SCs within certain ranges of temperatures T, molar concentrations x and electric field E. The DSs and heterophase structures in PMN–xPT SCs depend on the orientation of the crystal faces. In the range $0.30 \le x \le 0.39$, the first-order phase transitions often bring about the formation of different heterophase states, for instance, the cubic–tetragonal [53, 70], cubic–rhombohedral [24, 53, 70], tetragonal–rhombohedral [24, 53, 70], M_B – M_C [60] and M_C –tetragonal phases [60]. The coexistence of the tetragonal and M_B phases was observed in unpoled PMN–xPT ceramic samples in a very wide temperature range ($\sim 10^2$ K) [20].

The physical properties of the monoclinic phases in PMN–xPT, PZN–xPT, PZT, etc., are concerned with the consequence of adaptive phases [26] formed by stress-and depolarization electric-field-accommodating microdomains in the tetragonal or rhombohedral phase. The example of the phase coexistence in PMN–0.37PT over the wide temperature range (0 < T < 200 K) suggests that the unit-cell parameters in the tetragonal and M_C phases are interrelated. Wang proposed three intrinsic relationships of the unit-cell parameters [71] between the M_C and tetragonal phases in PMN–xPT and PZN–xPT near the MPB. Good agreement between the theoretical and experimental results on the unit-cell parameters is attained in wide ranges of T, x and E. The largest difference between the parameters takes place around the tetragonal– M_C phase boundary [71], where the largest error in measurements of the unit-cell parameters might arise around this boundary.

The phase coexistence in PMN–xPT and related solid solutions, according to Jin et al. [26], may reflect the proximity of the composition to the MPB and the small fluctuations in PT content within the SC sample. Experimental studies of the PMN–xPT and PZN–xPT solid solutions and their unit-cell behaviour near the MPB enabled one to conclude [26] that the monoclinic phases are adaptive phases with a mixed nanoscale structure and the unit-cell parameters in the monoclinic phases can

be predicted within the framework of the theory of the adaptive phase [72]. Bhattacharyya et al. [73] carried out the direct observation of tetragonal 90° nanodomains (nanotwins) within the $M_{\rm C}$ phase of PMN–0.35PT SCs by means of the high-resolution transmission electron microscopy. Experimental results [73] confirm concepts [74] on the adaptive phase that is characterized as a structurally heterogeneous state with a high domain wall density. In this state, the stress accommodation is achieved by a conformal miniaturization of twinning to near atomic scales in PMN–xPT and PZN–xPT.

The *hierarchical* DS in monoclinic PMN–xPT SCs near the MPB was studied [75] by means of the polarized light microscopy, transmission electron microscopy and convergent-beam electron diffraction. The monophase (M_C) region (from the optical viewpoint) is represented by a number of lamellar 90° nanodomains (width of about 10 nm) with the projection traces of the walls directed approximately along [110] and [1 $\overline{10}$] of the perovskite unit cell. These nanodomains are assembled into a submicrodomain with a width of 50–200 nm. Microdomains observed in work [75] exhibit the monoclinic state (M_C type) due to the average effect.

Shvartsman and Kholkin [66] studied the complex polar structure in PMN–0.20PT SCs by means of high-resolution piezoresponse force microscopy. The composition with x = 0.20 is located in the phase diagram of the PMN–xPT system [15] aside from the MPB (by about 0.10–0.15 on the x axis), namely, in the region of thermodynamic stability of the rhombohedral phase. However, in this case, the hierarchy of the domains is also observed. According to experimental results [66], relatively large FE domains with embedded nanodomains are visualized in as-grown $(001)_{\text{cub}}$ -oriented PMN–0.20PT SC samples. The ribbon-shaped antiparallel micron-sized domains are not continuous, irregular and can form labyrinth structures. A large number of nanodomains of opposite orientation are present in the microdomains studied. The formation of this polar structure on the micro- and nanolevels is concerned with a certain distribution of random electric fields in relaxor-FE SCs and with the existence of polar nanoscale regions in a wide temperature range [66].

The phase coexistence in the presence of the monoclinic phase in the PMN–xPT system was discussed in a series of papers (see, for instance, [12, 15, 17, 23, 27, 63, 67]). In Sects. 2.2.3 and 2.2.4, we analyse the role of the intermediate FE phases in PMN–xPT by taking into account the complex non-180° DSs and possibilities of stress relief at elastic matching of the phases with different symmetry around the MPB.

2.2.3 Effect of Non-180° Domains on Phase Coexistence

Now, we consider examples of the phase coexistence in the PMN–xPT system with $0.23 \le x \le 0.30$ at room temperature. Following the concept [42, 76] on the polarization rotation path near the MPB, we assume that the spontaneous polarization vector in a single-domain state changes the orientation from [111]

(rhombohedral phase) to [001] (tetragonal phase), as shown for the perovskite unit cell (Fig. 2.8, left part, bottom). The relationship between the orientations of the spontaneous polarization vectors of the non-180° domains in the FE phases is shown in Fig. 2.8. This means that the rhombohedral– $M_{\rm B}$ and $M_{\rm B}$ – $M_{\rm C}$ phase transitions, that occur with an increase in the molar concentration x at room temperature, are associated with the rotation of the spontaneous polarization vectors of four domain types in each FE phase.

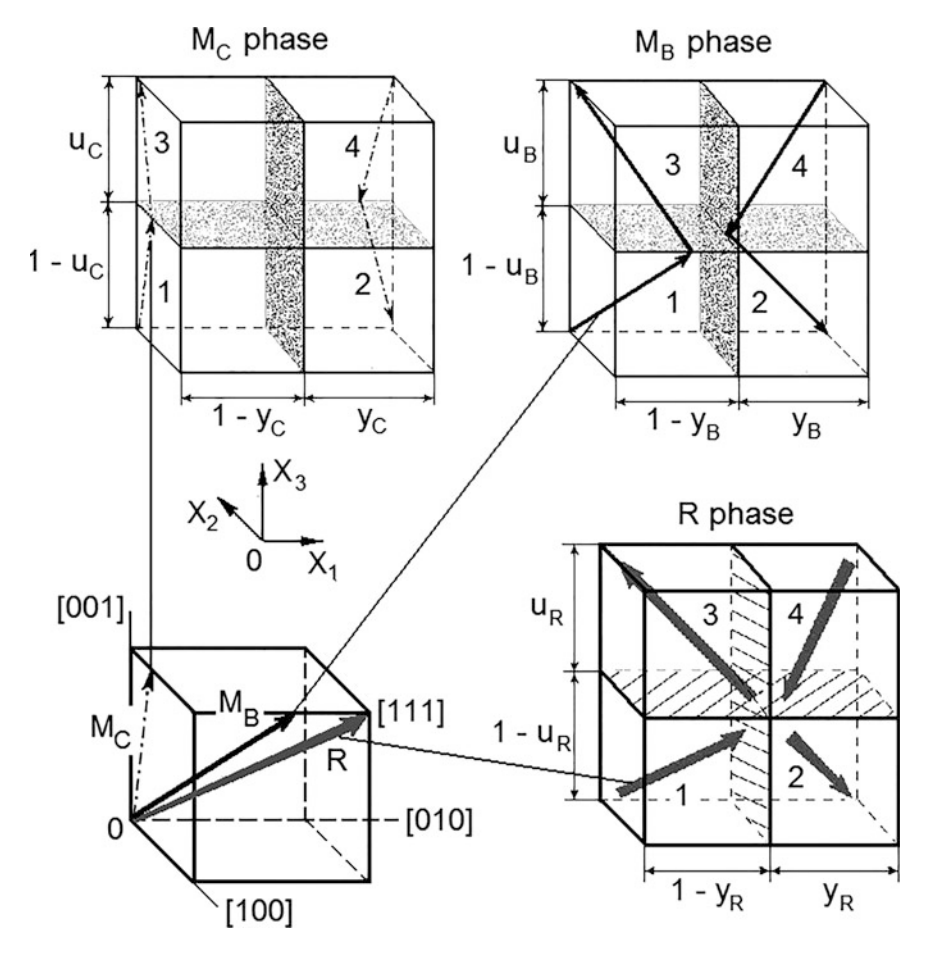


Fig. 2.8 Relationship between the polarization path [111] \rightarrow [001] in the perovskite unit cell (left part, bottom) and non-180° DSs in FE phases of the PMN–xPT system. 1, 2, 3 and 4 denote domain types in the rhombohedral (R), M_B and M_C phases and spontaneous polarization vectors of the adjacent domains in these phases are shown with arrows. Coordinate axes OX_j are parallel to the perovskite unit-cell axes in the cubic phase. Volume fractions of the non-180° domains are determined in terms of u_R and y_R (rhombohedral phase), u_B and y_B (M_B phase) and u_C and y_C (M_C phase)

We assume that the non-180° domains being components of mechanical twins (see Fig. 2.8) are located in a head-to-tail manner, form a regular structure and are separated, according to work [38], by planar stress-free domain walls. The crystal-geometric similarity of the laminar DSs (or twinned structures) in the rhombohedral, M_B and M_C phases near the MPB indicates the possibility of their description and the analysis of elastic matching in terms of analogous parameters (u_R and v_R , v_B and v_B are parameters characterize relative thicknesses of twin bands that consist of two types of the non-180° domains in the FE phases, as shown in Fig. 2.8.

The distortion matrices of the rhombohedral, M_B and M_C phases split into the non-180° domains of types 1–4 are represented in the coordinate axes OX_j (Fig. 2.8) as

$$\begin{split} \left\| N_{ij}^{(R)} \right\| &= \begin{pmatrix} \mu_{a} & \mu(2y_{R}-1) & \mu(2u_{R}-1)(2y_{R}-1) \\ \mu(2y_{R}-1) & \mu_{a} & \mu(2u_{R}-1) \\ \mu(2u_{R}-1)(2y_{R}-1) & \mu(2u_{R}-1) & \mu_{a} \end{pmatrix}, \\ \left\| N_{ij}^{(MB)} \right\| &= (1-y_{B}) \begin{pmatrix} \lambda_{c} & 0 & 0 \\ 0 & \lambda_{a} & \lambda(2u_{B}-1) \\ 0 & \lambda(2u_{B}-1) & \lambda_{a} \end{pmatrix} \\ &+ y_{B} \begin{pmatrix} \cos \varphi_{B} & -\sin \varphi_{B} & 0 \\ \sin \varphi_{B} & \cos \varphi_{B} & 0 \\ 0 & 0 & 1 \end{pmatrix} \begin{pmatrix} \lambda_{c} & 0 & \lambda(2u_{B}-1) \\ 0 & \lambda_{c} & 0 \\ \lambda(2u_{B}-1) & 0 & \lambda_{a} \end{pmatrix} \\ \text{and} \\ \left\| N_{ij}^{(MC)} \right\| &= (1-y_{C}) \begin{pmatrix} \eta_{b} & 0 & 0 \\ 0 & \eta_{a} & \eta(2u_{C}-1) \\ 0 & \eta(2u_{C}-1) & \eta_{c} \end{pmatrix} \\ &+ y_{C} \begin{pmatrix} \cos \varphi_{C} & -\sin \varphi_{C} & 0 \\ \sin \varphi_{C} & \cos \varphi_{C} & 0 \\ 0 & 0 & 1 \end{pmatrix} \begin{pmatrix} \eta_{a} & 0 & \eta(2u_{C}-1) \\ 0 & \eta_{b} & 0 \\ \eta(2u_{C}-1) & 0 & \eta_{c} \end{pmatrix}, \end{split}$$

respectively. In (2.8), μ_a and μ are unit-cell distortions in the rhombohedral phase, λ_a , λ_c and λ are unit-cell distortions in the M_B phase, φ_B = arccos $[2\lambda_a\lambda_c/(\lambda_a^2 + \lambda_c^2)]$ is the angle of rotation of the crystallographic axes of the adjacent domains in the M_B phase, η_a , η_b , η_c and η are unit-cell distortions in the M_C phase, and φ_C = arccos $[2\eta_a\eta_b/(\eta_a^2 + \eta_b^2)]$ is the angle of rotation of the crystallographic axes of the adjacent domains in the M_C phase. Comparing $\|N_{ij}^{(M_B)}\|$ and $\|N_{ij}^{(M_C)}\|$ from (2.8), one can establish the following transformation [77] for the perovskite-cell distortions at the M_B - M_C phase transition: $\lambda_a \to \eta_c$, $\lambda_b = \lambda_a \to \eta_a$ and $\lambda \to \eta_b$. This transformation is in agreement with the experimental molar-concentration dependences [60] of the linear parameters a, b and c of the perovskite unit cells in these phases, namely, with an increase in x, transitions from $a_B(x)$ to $c_C(x)$, $b_B(x)$ to $a_C(x)$ and $c_B(x)$ to $b_C(x)$ occur, where subscripts $a_B(x)$ and $a_B(x)$ to denote the $a_B(x)$ to $a_B(x)$ to $a_B(x)$ to $a_B(x)$ occur, where subscripts $a_B(x)$ denote the $a_B(x)$ and $a_B(x)$ to $a_B(x)$ to

The dependence of elements of $||D_{fg}||$ from (1.7) on four parameters [for example, at the coexistence of the rhombohedral and M_B phases, $D_{fg} = D_{fg}(u_R, y_R, u_B, y_B)$] hinders consideration of conditions (1.5) and (1.6) in a wide range of volume fractions of individual types of domains shown in Fig. 2.8. However, the crystal-geometric similarity of the DSs of the neighbouring phases (Fig. 2.8) suggests a constancy [77] of the relative thickness of twins in the coexisting phases. Corresponding conditions imposed on the parameters from Fig. 2.8 are written as follows:

$$u_{\rm B} = u_{\rm R} \text{ and } |y_{\rm B} - y_{\rm R}| \le 0.05$$
 (2.9)

(rhombohedral and M_B phases),

$$u_{\rm C} = u_{\rm R} \text{ and } |y_{\rm C} - y_{\rm R}| \le 0.05$$
 (2.10)

(rhombohedral and M_C phases), and

$$u_{\rm B} = u_{\rm C} \,\text{and} \, |y_{\rm B} - y_{\rm C}| \le 0.05$$
 (2.11)

(M_B and M_C phases). The presence of the factor 0.05 in expressions (2.9)–(2.11) means that the heterophase states in PMN–xPT allow weak (to 5%) changes in the relative thickness of twins along the OX_1 axis (Fig. 2.8) at a transition through the interphase phase boundary.

In the further examination of conditions (2.9)–(2.11), experimental molar-concentration (*x*) dependences of the unit-cell parameters of PMN–*x*PT at room temperature [62] are used. Possible versions of the interphase boundaries are considered in work [77]. These boundaries obey general conditions (1.5) and (1.6) for ZNSPs and conditions for the almost constant relative thickness of twins [i.e. conditions (2.9) and (2.10), or (2.9) and (2.11), or (2.10) and (2.11)].

Interconnections between the parameters from conditions (2.9)–(2.11) are shown in Figs. 2.9, 2.10 and 2.11. The presence of the ZNSPs at the rhombohedral– M_B phase transition suggests a variation in y_R in narrow ranges (Fig. 2.9). Both narrow ranges of allowable values of y_R and discontinuities of the ranges of allowable values (u_R , v_R) at v_R at v_R (Fig. 2.9a, b) hinder the formation of the ZNSP along the interphase boundary. It can be mentioned for comparison that the previous experiments [60] did not reveal the coexistence of the rhombohedral and v_R phases in the wide molar-concentration range.

Diagrams in Fig. 2.10 show that conditions (1.5), (1.6) and (2.10) are satisfied at variation in y_R in wider (in comparison with those shown in Fig. 2.9) ranges. This circumstance facilitates the formation of heterophase states at the rhombohedral— M_C phase transition (0.26 $\leq x \leq$ 0.27).

We note that conditions (1.5), (1.6) and (2.11), which are related to the ZNSPs at the coexistence of the M_B and M_C phases, are satisfied in wide ranges of y_B and at any u_B (Fig. 2.11b–d). The validity of conditions (1.5), (1.6) and (2.11) is a favourable factor for the coexistence of intermediate M_B and M_C phases at

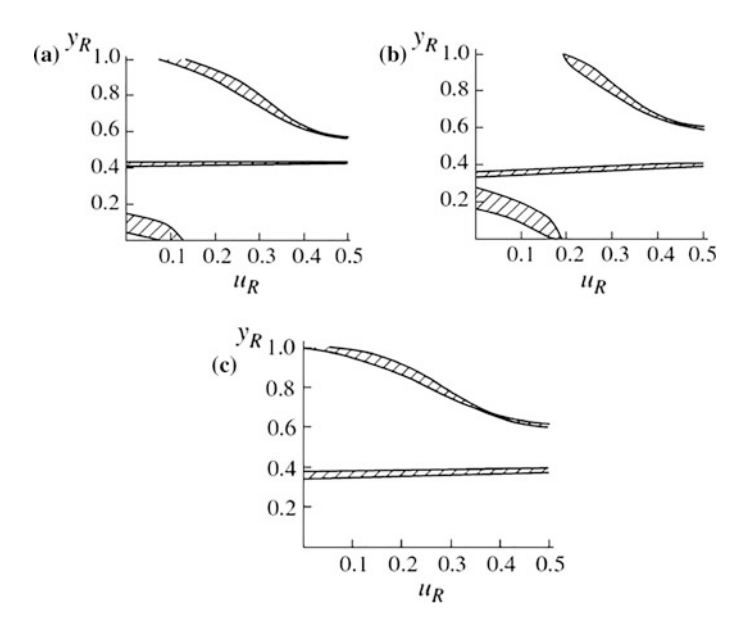


Fig. 2.9 Diagrams that link the parameters u_R and y_R of the polydomain rhombohedral phase at the formation of ZNSPs at the interphase boundaries in PMN–xPT SCs with x = 0.23 (a), 0.26 (b) and 0.27 (c). The interphase boundaries separate the rhombohedral (R3m) and M_B (Cm) phases and satisfy conditions (1.5), (1.6) and (2.9). The phases are split into the non-180° domains as shown in Fig. 2.8. The region $0.5 \le u_R \le 1$ is obtained by means of reflecting the region $0 \le u_R \le 0.5$ of the diagram in the plane of symmetry $u_R = 0.5$ (reprinted from paper by Topolov [77], with permission from Pleiades Publishing)

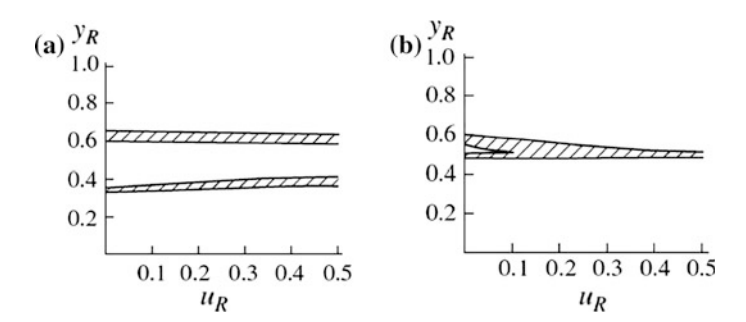


Fig. 2.10 Diagrams that link the parameters u_R and y_R of the polydomain rhombohedral phase at the formation of ZNSPs at the interphase boundaries in PMN-xPT SCs with x = 0.26 (a) and 0.27 (b). The interphase boundaries separate the rhombohedral (R3m) and M_C (Pm) phases and satisfy conditions (1.5), (1.6) and (2.10). The phases are split into the non-180° domains as shown in Fig. 2.8. The region $0.5 \le u_R \le 1$ is obtained by means of reflecting the region $0 \le u_R \le 0.5$ of the diagram in the plane of symmetry $u_R = 0.5$ (reprinted from paper by Topolov [77], with permission from Pleiades Publishing)

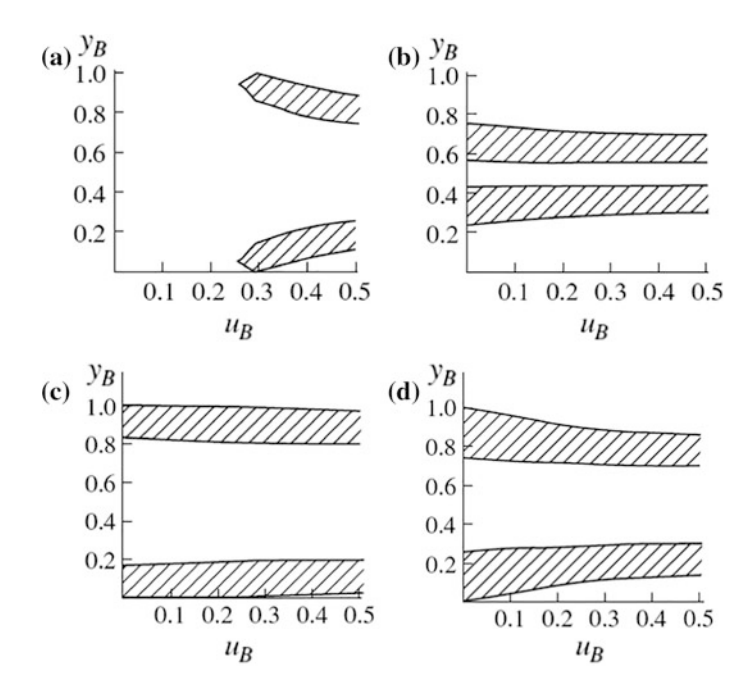


Fig. 2.11 Diagrams that link the parameters u_B and y_B of the polydomain M_B phase at the formation of ZNSPs at the interphase boundaries in PMN–xPT SCs with x = 0.26 (a), 0.27 (b), 0.29 (c) and 0.30 (d). The interphase boundaries separate the M_B (*Cm*) and M_C (*Pm*) phases and satisfy conditions (1.5), (1.6) and (2.11). The phases are split into the non-180° domains as shown in Fig. 2.8. The region $0.5 \le u_R \le 1$ is obtained by means of reflecting the region $0 \le u_R \le 0.5$ of the diagram in the plane of symmetry $u_R = 0.5$ (reprinted from paper by Topolov [77], with permission from Pleiades Publishing)

 $0.26 < x \le 0.30$. This coexistence was experimentally observed in the PMN–xPT system [60, 62] at room temperature.

The reason for such behaviour of the parameters in conditions (2.9)–(2.11) is related to the particular role of the rhombohedral phase in the formation of heterophase states. As follows from (2.8), independent of the splitting of the rhombohedral phase into the non-180° domains (see Fig. 2.8), all diagonal elements of the $||N_{ij}^{(R)}||$ matrix are equal to each other, similar to the diagonal distortions of the cubic unit cell. In contrast, the diagonal elements of the $||N_{ij}^{(MB)}||$ and $||N_{ij}^{(MC)}||$ matrices from (2.8) strongly depend on the parameters y_B and y_C , which characterize the DSs (Fig. 2.8). As a result, changes in y_B and y_C in wide ranges and the corresponding accommodation rearrangement of twin structures in the monoclinic phases lead to the validity of the inequality from conditions (2.11). Our analysis of conditions (2.9)–(2.11) enables us to conclude that it would be more difficult to satisfy the same inequality in the presence of the rhombohedral phase, i.e. at the rhombohedral– M_B or rhombohedral– M_C phase coexistence. The probability of the

formation of ZNSPs in the two-phase states [77] increases with an increase in the area of the hatched ranges of allowable values of the parameters in Figs. 2.9, 2.10 and 2.11. Orientations of the interphase boundaries in the two-phase states in the wide x range are determined on the basis of (1.8). According to data from work [77], the interphase boundaries studied in the PMN–xPT system are oriented close to {hk0} of the perovskite unit cell.

Comparison of the diagrams build for PMN–xPT at $0.26 \le x \le 0.27$ (Figs. 2.9b, c, 2.10 and 2.11a, b) shows that the possibilities of the formation of three-phase states with the simultaneous validity of conditions (2.9)–(2.11) are fairly limited. Indeed, the ranges of allowable values of (u_R , y_R) (Figs. 2.9c and 2.10b) and (u_B , y_B) (Fig. 2.11b), which are related to the two-phase samples, can be matched at the molar concentration x = 0.27 and only partially.

Thus, the studied two-phase states in the PMN–xPT system take place at the almost constant relative thicknesses of twins (see Fig. 2.8) of the coexisting phases near the MPB, i.e. without significant displacements of the twin walls at a transition through the interphase boundary. The corresponding conditions for complete stress relief at elastic matching of the heavily twinned M_B and M_C phases are most favourable at $0.26 \le x \le 0.30$.

2.2.4 Different Scenarios of Stress Relief

Examples of the phase coexistence in PMN–0.32PT ceramics on cooling were considered in recent experimental studies [18, 20]. According to experimental data [18], the tetragonal (P4mm) and M_C (Pm symmetry) phases coexist in a wide temperature range. At the same time, experimental studies [20] show that the tetragonal and M_B (Cm) phases coexist in unpoled PMN–0.32PT ceramic samples in the temperature range $\sim 10^2$ K. Such unusual behaviour is associated with the effect of a local stress field and with the clampdown and blocking effect [20]. These experimental results and the martensitic-like phase transitions [20] in the PMN–xPT system stimulate an analysis of the heterophase states that would appear on cooling or under different conditions for internal stress relief.

It is assumed that non-180° domains in the FE phases (tetragonal, M_B and M_C) of PMN–0.32PT are located in a head-to-tail manner and form regular laminar structures. Fragments of the polydomain M_B and M_C phases are schematically represented in Fig. 2.8. In the tetragonal phase, the following domain patterns are considered: the first domain pattern comprises the 90° domains with the spontaneous polarization vectors $P_T^{(3)} \parallel [001]$ (volume fraction t_3) and $P_T^{(1)} \parallel [100]$ (volume fraction $1-t_3$), and the second domain pattern comprises the 90° domains with $P_T^{(1)} \parallel [100]$ (volume fraction $1-t_1$). The aforementioned domains in the FE phases are separated, according to Fousek and Janovec [38], by the unstrained domain walls.

Distortion matrices of the M_B and M_C phases, $\left\|N_{ij}^{(MB)}\right\|$ and $\left\|N_{ij}^{(MC)}\right\|$, are given in (2.8). The polydomain tetragonal phase is characterized by the distortion matrices analogous to $\left\|N_{ij}^{(5-6)}\right\|$ from (2.3) and $\left\|N_{ij}^{(5-7)}\right\|$ from (2.4). To analyse elastic matching of these phases in the two-phase states, we use different temperature dependences of the unit-cell parameters of the PMN-0.32PT ceramic [18, 20].

According to experimental data [20], cooled ceramic samples of PMN–0.32PT undergo a first-order cubic–tetragonal phase transition at temperature $T_{\rm CT}$ = (423 \pm 5) K and exhibit the non-equilibrium coexistence of the tetragonal and M_B phases at 193 K $\leq T \leq$ 408 K. The unit-cell behaviour of PMN–0.32PT [20] obeys conditions (1.18) for ZNSPs at the cubic–tetragonal phase transition. The optimal volume fraction of the 90° domains in the tetragonal phase (either with $P_T^{(3)}$ and $P_T^{(1)}$ or $P_T^{(2)}$ and $P_T^{(1)}$) [78] is $t_j^{\rm opt} = 0.313$ or 0.687. It is assumed that a further cooling of the sample in the stability region of the tetragonal phase will not give rise to changes in the volume fraction of the 90° domains arising at the cubic–tetragonal phase transition.

The domain state-interface diagrams calculated for the coexistence of the tetragonal (at $t_i = t_i^{\text{opt}}$) and M_B phases in the wide temperature range are shown in Fig. 2.12. These diagrams illustrate interconnections between the parameters $u_{\rm B}$ and y_B which characterize the relative thickness of twins (Fig. 2.8) in the M_B phase. The diagrams shown in Fig. 2.12, a, f and g correspond to the highest temperature (T = 408 K) at which the unit-cell parameters of the coexisting T and M_B phases were measured in work [20]. These diagrams suggest that irrespective of the orientation of $P_T^{(j)}$ in the tetragonal phase, the almost single-domain M_B phase would appear to satisfy conditions (1.18) for ZNSPs. The M_B phase in the near single-domain state is characterized by one of the following pairs of the parameters: $y_{\rm B}=0$ and $u_{\rm B}\to 0$, $y_{\rm B}=0$ and $u_{\rm B}\to 1$, $y_{\rm B}\to 0$ and $u_{\rm B}=1$, or $y_{\rm B}=0$ and $u_{\rm B} \rightarrow 1$. Moreover, the diagram shown in Fig. 2.12, a enables us to suppose an interesting possibility of the formation of the polydomain M_B phase with the parameters $y_B \rightarrow t_3 = 0.313$ and $u_B = 1/2$. In this case, the interphase boundary that obeys conditions (1.18) would appear in a heterophase structure with the almost constant relative thickness of twins along the OX_1 axis [78].

Now we compare the diagrams (Fig. 2.12a–e) related to the fixed orientation of the non-180° domains in the tetragonal and M_B phases coexisting in the wide temperature range. It turns out that each single-domain state of the M_B phase at T=408 K can give rise to a stressed interphase boundary on cooling because of violation of conditions (1.18) for ZNSPs. For example, the interphase boundaries are conical (region I or II) at T=373 K (Fig. 2.12b), 323 K (Fig. 2.12c), 273 K (Fig. 2.12d), or 193 K (Fig. 2.12e). Such a scenario of stress relief [78] would need additional changes in the volume fractions of the 90° domains in the tetragonal phase being thermodynamically stable at higher temperatures.

The polydomain M_B phase with the parameters $y_B \rightarrow t_3 = 0.313$ and $u_B = 1/2$ would also promote the formation of the stressed conical interphase boundaries on

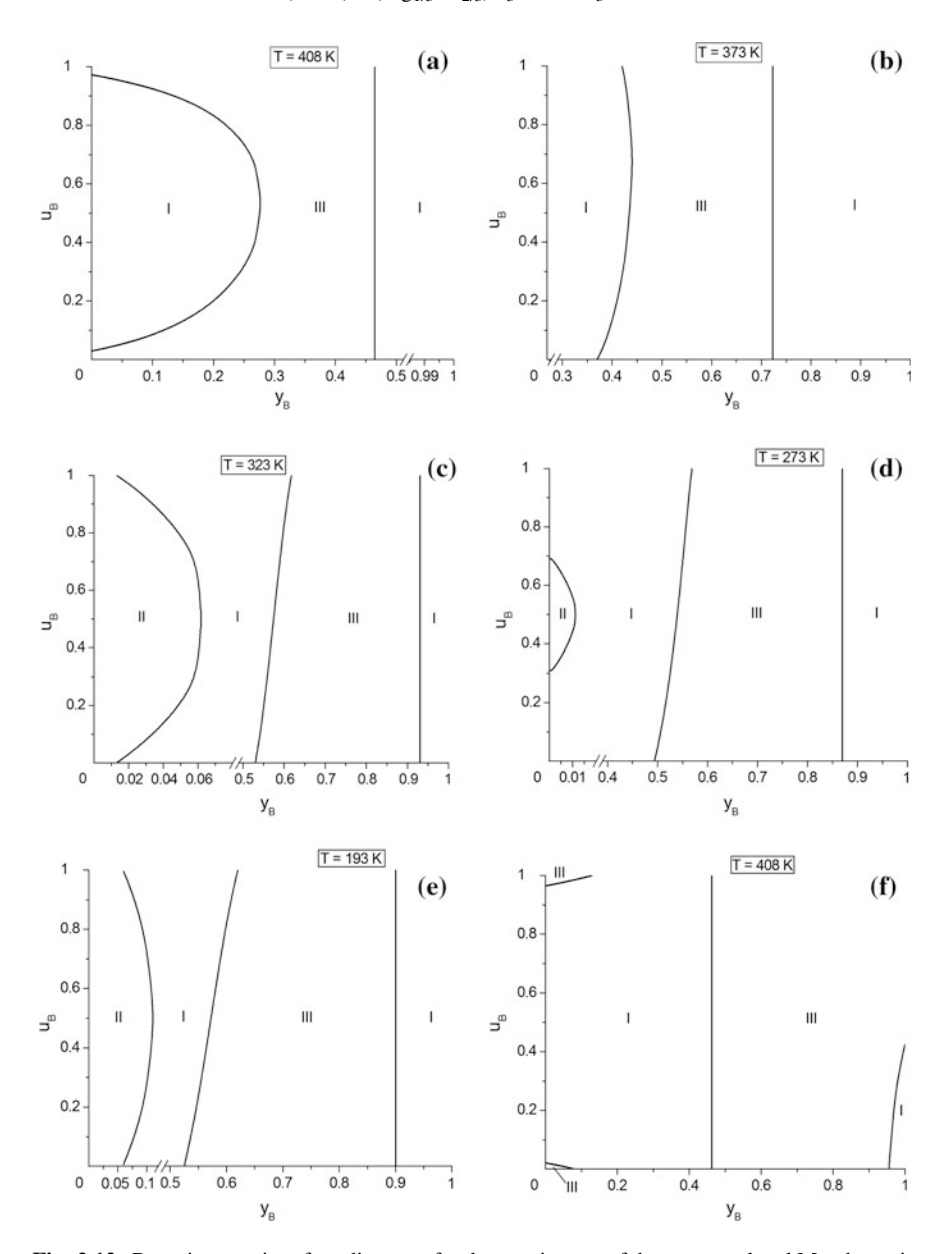


Fig. 2.12 Domain state—interface diagrams for the coexistence of the tetragonal and M_B phases in PMN-0.32PT. Graphs (a-e) correspond to the transition from the tetragonal phase (domains with $P_T^{(1)}$ and $P_T^{(3)}$) at the optimal volume fraction $t_3 = 0.313$, graph (f) corresponds to the transition from the tetragonal phase (domains with $P_T^{(1)}$ and $P_T^{(3)}$) at the optimal volume fraction $t_3 = 0.687$, and graph (g) corresponds to the transition from the tetragonal phase (domains with $P_T^{(1)}$ and $P_T^{(2)}$) at the optimal volume fraction $t_1 = 0.313$. Conditions (1.14), (1.15) and (1.16) are valid in regions I, II and III, respectively. Calculations were made using experimental data on unit-cell parameters [20] (reprinted from paper by Topolov [78], with permission from Taylor & Francis)

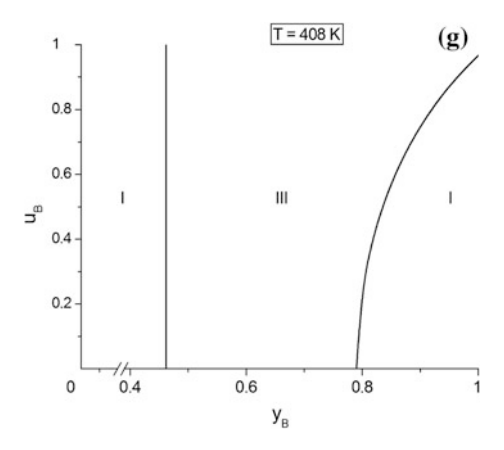


Fig. 2.12 (continued)

cooling. The curve that separates the regions I and III in the left part of the diagram in Fig. 2.12a shifts towards the larger $y_{\rm B}$ values (see Fig. 2.12b, c) and then demonstrates small displacements (Fig. 2.12d, e). This scenario of stress relief [78] means that an additional rearrangement of the DS in the M_B phase can be appreciable down to $T \approx 320$ K at the constant volume fraction $t_j = t_j^{\rm opt}$ in the tetragonal phase.

It seems to be probable that the ceramic PMN–0.32PT samples cooled below T = 408 K are heterophase in the wide temperature range and no effective stress relief takes place at the coexistence of the polydomain tetragonal and M_B phases. An additional reason for this phase coexistence in the wide temperature range [20] may lie in compositional fluctuations [32, 34] that appear close to the MPB.

In work [18], the temperature dependence of the unit-cell parameters of PMN–0.32PT was determined by means of the powder neutron diffraction. As follows from this unit-cell behaviour, the interphase boundaries at the cubic–tetragonal phase transitions obey conditions (1.18) for ZNSPs at the volume fraction $t_j^{\rm opt} = 0.405$ or 0.595. The M_C phase that appears on further cooling can coexist with the tetragonal phase split into the 90° domains. The domain state–interface diagrams (Fig. 2.13) calculated using the unit-cell parameters from work [18] suggest that conditions (1.18) are valid in the presence of the M_C phase being either e-domain or polydomain. For example, lines *AB* and *CD* (Fig. 2.13a) and *AD* (Fig. 2.13b) correspond to the ZNSPs. The single-domain M_C phase corresponds to the points *A* and *D* in Fig. 2.13. A curve that separates regions I and III in Fig. 2.13b corresponds to the ZNSPs in the presence of the M_C phase split into either two (at $y_C = 0$) or four (at $y_C > 0$) domain types. Undoubtedly, these variants of the T–M_C phase coexistence in PMN–0.32PT are related to similar scenarios of stress relief [78] in the presence of

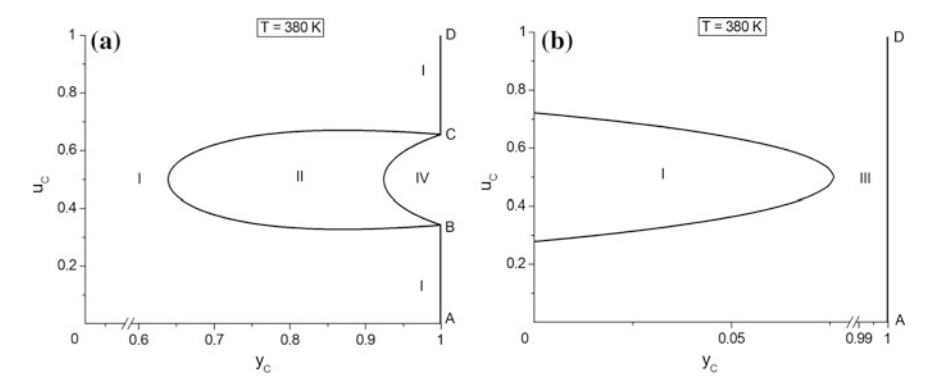


Fig. 2.13 Domain state–interface diagrams for the coexistence of the tetragonal and M_C phases in PMN–0.32PT. Graph (a) corresponds to the transition from the polydomain tetragonal phase (domains with $P_T^{(1)}$ and $P_T^{(3)}$) at the optimal volume fraction $t_3 = 0.595$, graph (b) corresponds to the transition from the polydomain tetragonal phase (domains with $P_T^{(1)}$ and $P_T^{(2)}$) at the optimal volume fraction $t_1 = 0.405$. Conditions (1.14), (1.15), (1.16) and (1.17) are valid in regions I, II, III and IV, respectively. Calculations were made using experimental data on unit-cell parameters [18] (reprinted from paper by Topolov [78], with permission from Taylor & Francis)

the tetragonal phase with the optimal volume fractions of the 90° domains with the known $P_T^{(j)}$ orientations. The heterophase states corresponding to complete stress relief in the above-considered versions of the phase coexistence in PMN–0.32PT (Figs. 2.12 and 2.13) suggest that there is a correlation between the unit-cell parameters of the adjacent phases (i.e. cubic, tetragonal, M_B and M_C) in some temperature ranges. This correlation causes, for example, possibilities for the formation of the single-domain monoclinic phase (either M_B or M_C) at the first-order phase transition from the tetragonal phase split into the 90° domains in accordance with conditions for ZNSPs at the high-temperature cubic–tetragonal phase transition. To the best of our knowledge, such behaviour of the PMN–xPT system near the MPB has no analogues among the studied FE solid solutions.

2.3 Model of Interpenetrating Phases: Application to $(1 - x)Pb(Mg_{1/3}Nb_{2/3})O_3$ -xPbTiO₃ Near the Morphotropic Phase Boundary

In Sect. 2.3, we consider the *model of interpenetrating phases* that are elastically matched along the ZNSP's in PMN–*x*PT near the MPB. The first example of elastic matching of two interpenetrating FE phases (tetragonal and orthorhombic) in PZN–0.10PT SCs was discussed in work [79]. Hereby, the volume-fraction behaviour of the coexisting FE phases was interpreted in terms of unit-cell parameters and orientations of different domain (twin) types [79].

According to the model of interpenetrating phases [79, 80], a SC sample consists of two types of heterophase regions (Fig. 2.14a) with volume fractions v and v' = 1 - v, respectively, and each region (hereafter the v- or v'-region) represents the two-phase state. This means that a phase inclusion in a given region becomes a phase matrix in the adjacent region, and vice versa. The equality of the volume fractions v = v' = 1/2 corresponds to a distribution of the v- and v'-regions without any preference of one type over another. In the case of the coexistence of the rhombohedral and monoclinic phases, we introduce volume fractions m and v to define a volume fraction of the inclusion-phase in the v- and v'-regions, respectively. At the monoclinic-tetragonal

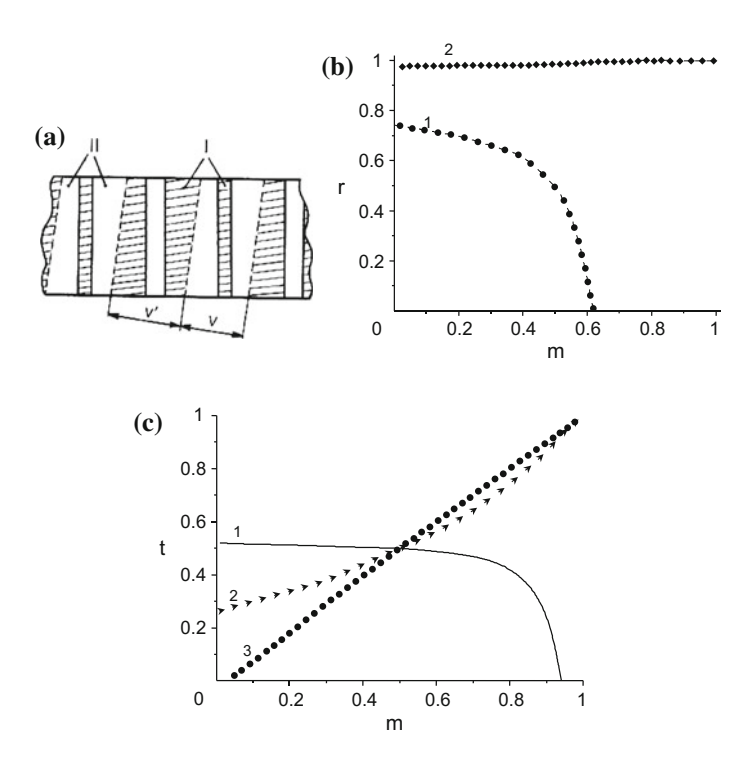


Fig. 2.14 Schematic arrangement of interpenetrating phases (**a**) and examples of the r(m) (**b**) and t(m) (**c**) dependences calculated for two-phase PMN–xPT solid solutions within the framework of the model of interpenetrating phases by using the unit-cell parameters from work [15]. Heterophase regions in schematic (**a**) are characterized by volume fractions v and v'. I, the inclusion-phase in the v-region and the matrix-phase in the v-region; II, the inclusion-phase in the v-region and the matrix-phase in the v-region. Curves 1, 2 and 3 in graphs (**b**) and (**c**) correspond to different volume-fraction dependences that satisfy conditions for ZNSPs. Calculations were made at the following constant parameters: $f_M = g_R = u_R = 1/2$ [M_C + rhombohedral phases, graph (**b**)] or $f_M = 1/2$ [M_C + tetragonal phases, graph (**c**)] (reprinted from paper by Topolov and Ye [80], with permission from the American Physical Society)

phase coexistence that arises from the rhombohedral-monoclinic phase coexistence with increasing the molar concentration x, the volume fractions t and m of the inclusion-phase are to be introduced in the v'- and v-regions, respectively.

The $||K_j||$ matrices related to the monoclinic–rhombohedral phase coexistence are determined by taking into account a mutual influence of the internal stress fields of the interpenetrating phases and can be derived from a series of equations [80]:

$$||K_1|| = m||K_2|| \cdot ||N_M|| + (1-m)||N_R|| \text{ and }$$

$$||K_2|| = r||K_1|| \cdot ||N_R|| + (1-r)||N_M||.$$
 (2.12)

In (2.12), the items $m\|K_2\|\cdot\|N_M\|$ and $r\|K_1\|\cdot\|N_R\|$ reflect an influence of the adjacent heterophase region on the phase inclusion. The distortion matrices $\|N_M\|$ and $\|N_R\|$ of the monoclinic and rhombohedral phases, respectively, are written with due regard for the domain orientations in the coexisting phases (Fig. 2.8). We assume that the tetragonal phase is split into 90° domains with the unit-cell vectors (a_{Tj}, b_{Tj}, c_{Tj}) lying along ([100], [010], [001]) (j = 1, volume fraction n_T) and ([010], [001], [100]) (j = 2, volume fraction $1 - n_T$). The M_C phase is represented by four domain types with the unit-cell vectors (a_{Mk}, b_{Mk}, c_{Mk}) , where c_{Mk} | [001] and k = 1, 2, 3, 4 [80]. The crystallographic directions are given with respect to the perovskite unit cell. The volume fractions of the domain types in the M_C phase are expressed in terms of two parameters, $0 \le f_M \le 1$ and $0 \le w_M \le 1$, as follows: $n_{M1} = f_M w_M$, $n_{M2} = (1 - f_M)w_M$, $n_{M3} = f_M(1 - w_M)$ and $n_{M4} = (1 - f_M)(1 - w_M)$. The rhombohedral phase is split into the 71° (109°) domains as shown in Fig. 2.5.

Elastic matching of the adjacent phases is studied in terms of matrix elements

$$D_{ij} = \sum_{t=1}^{3} (K_{2,it} K_{2,jt} - K_{1,it} K_{1,jt}). \tag{2.13}$$

The matrix elements D_{ij} from (2.13) are analogous to those from (1.7) and depend on elements of $||K_1||$ and $||K_2||$ which are to be found from (2.12). In (2.13), subscripts it and jt are used for listing the matrix elements, and i, j, t = 1, 2 and 3. The matrix elements D_{ij} from (2.13) are examined to satisfy conditions (1.18) for ZNSPs.

Diagrams in Fig. 2.14b, c illustrate various possibilities of the formation of ZNSPs in accordance with the model concepts put forward. However, only curve 1 (Fig. 2.14b, c) satisfies the physical meaning of the MPB, i.e. changing the molar concentration x should lead to an increase in one of the volume fractions in (2.12), for instance, the volume fraction m, and to a simultaneous decrease in another volume fraction, for instance, r. Curve 2 in Fig. 2.14b and curves 2 and 3 in Fig. 2.14c are related to the volume fractions that monotonously increase. Such behaviour implies a simultaneous increase in the volume fractions of the coexisting phases and, strictly speaking, does not refer to the two-phase states shown in Fig. 2.14a. The stress-free interphase boundaries corresponding to curve 1 in Fig. 2.14b, c are described by Miller indices $\{h0l\}$ in the perovskite axes [80].

As follows from Fig. 2.15a, b, conditions for ZNSPs within the framework of our model of interpenetrating phases are well fulfilled within a fairly wide range of molar concentrations x. Very slight changes (up to 3%) of the v_i values appear as the unit-cell parameters are taken from a narrower range, for example, at x = 0.31 (rhombohedral phase), x = 0.33 (M_C phase) and x = 0.35 (tetragonal phase).

The changes of v_i at 0.30 < x < 0.39 points out the stability of results [80] and the good correlation between the calculated data (Fig. 2.15a, b) and experimental data from [15, 80].

The model of interpenetrating phases was also applied [80] to interpret the coexistence of the intermediate phases (M_B and M_C) in the PMN–xPT system. Experimental results by Singh and Pandey [60] suggest that the following sequence of the FE phases is observed at $0.20 \le x \le 0.40$ on increasing x: rhombohedral $(R3m) \to M_B(Cm) \to M_C(Pm) \to \text{tetragonal}(P4mm)$. Changes in both symmetry and unit-cell parameters strongly influence elastic matching of the coexisting phases

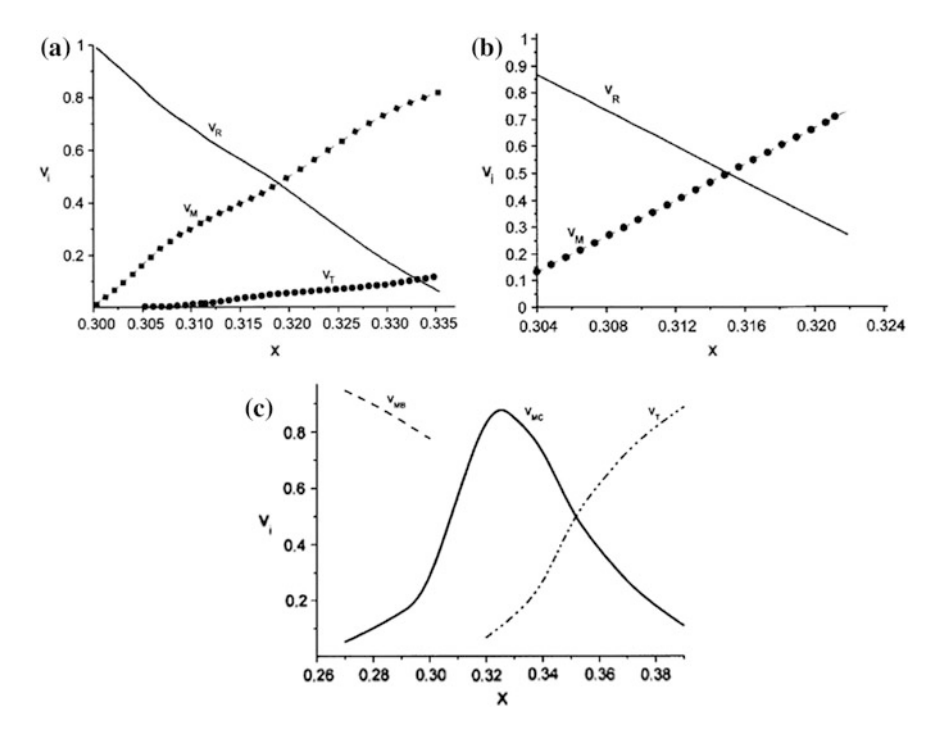


Fig. 2.15 $v_i(x)$ dependences calculated for two-phase PMN-xPT solid solutions within the framework of the model of interpenetrating phases by using the unit-cell parameters from [15] (a and b) and [60] (c). Diagram (a) was built for the rhombohedral–M_C phase coexistence (taking into account curve 1 in Fig. 2.14b), and diagram (b) was built for the M_C-tetragonal phase coexistence (taking into account curve 1 in Fig. 2.14c). Subscripts R, M and T in diagrams (a) and (b) denote the rhombohedral, M_C and tetragonal phases, respectively. Subscripts MB, MC and T denote the M_B, M_C and tetragonal phases, respectively (reprinted from paper by Topolov and Ye [80], with permission from the American Physical Society)

and conditions for stress relief in heterophase samples. Calculations in work [80] show that the unit-cell behaviour in PMN–xPT at $x \ge 0.27$ [60] favours the formation of ZNSPs in heterophase states described in terms of the model of interpenetrating phases. The corresponding volume fractions $v_i(x)$ are shown in Fig. 2.15c. Calculations were made using the room-temperature unit-cell parameters [60] related to the following molar concentrations:

- (i) x = 0.27 (M_B) and x = 0.31 (M_C) for the M_B-M_C phase coexistence at $0.27 \le x \le 0.30$,
- (ii) x = 0.31 (M_C) and x = 0.35 (tetragonal) for the M_C-tetragonal phase coexistence at $0.32 \le x \le 0.34$, and
- (iii) x = 0.34 (M_C) and x = 0.40 (tetragonal) for the M_C-tetragonal phase coexistence at $0.35 \le x \le 0.39$.

A transition from the first set of the unit-cell parameters to the second set is connected with changes in derivatives $d\nu_{M_C}/dx$ and $d\nu_T/dx$ at $x\approx 0.35$, where the largest jumps of the unit-cell parameters [60] $a_{M_C}\to a_T, c_{M_C}\to c_T\to$ and $\omega_{M_C}\to 0$ take place at the M_C -tetragonal phase transition.

The calculated $v_{\rm M_B}(x)$, $v_{\rm M_C}(x)$ and $v_{\rm T}(x)$ dependences (Fig. 2.15c) are in good agreement with experimental results [60] on the phase coexistence. This interesting example of elastic matching of the morphotropic phases in PMN–xPT represents an independent confirmation of the essential interconnection between changes in unit-cell parameters and stress-relief possibilities in FE solid solutions.

2.4 Domain and Heterophase States in (1 - x)Pb(Zn_{1/3}Nb_{2/3})O₃-xPbTiO₃ Near the Morphotropic Phase Boundary

2.4.1 Phase Transitions and Intermediate Phases

Relaxor-FE PZN–xPT is the third important example of the heterogeneous system wherein the intermediate phases of the FE nature were revealed [6, 16] in the 2000s. Domain-engineered PZN–xPT SCs [81] with MPB compositions exhibit anomalously high dielectric constant and excellent piezoelectric performance. For example, the large piezoelectric coefficient d_{33} (approximately 2000–2900 pC/N), the high electromechanical coupling factor k_{33} (91–94%) at molar concentrations x = 0.045-0.080 [82] as well as large absolute values of the piezoelectric coefficient d_{31} (-1700 pC/N) and electromechanical coupling factor k_{31} (80.8%) [83] promote electromechanical transducer, sensor, actuator and other piezotechnical applications of the domain-engineered SCs. The outstanding electromechanical properties are closely related to an enhanced polarizability (or electric softness) due to the coexistence of the FE phases near the MPB [28, 84, 85] and to engineered domain reorientations by appropriate poling processes [86, 87]. Optical studies carried out

on the heavily twinned PZN-xPT SC samples at the MPB ($x \approx 0.090$) before the discovery of the intermediate phases show that the first-order FE Pm3m - P4mm, Pm3m - R3m and P4mm - R3m phase transitions are observed [88, 89].

As an example, we consider PZN-0.09PT SCs that are characterized by various non-180° DSs and heterophase states [90]. The micrograph in Fig. 2.16, a shows the complex DS of the (001)_{cub} PZN-0.09PT SC platelet at room temperature, where subscript cub denotes that the Miller indexes are related to the perovskite unit cell. Two distinct orientation states can be identified, one with extinction directions along <110>_{cub} (Domains R), the other with extinction directions parallel to <100>_{cub} (Domains T). The former indicates the rhombohedral symmetry, while the latter corresponds to the tetragonal phase. It is seen that the rhombohedral (R3m) and tetragonal (P4mm) phases coexist in PZN-0.09PT. Upon heating, the rhombohedral phase transforms into the tetragonal phase, with an increase in the volume of the domains in the tetragonal phase at the expense of the rhombohedral phase (Fig. 2.16b), and this transformation is characterized as a first-order phase transition. Upon further heating, the tetragonal phase transforms into the cubic (Pm3m) phase with emergence and growth of the isotropic area (Fig. 2.16c). The presence of the intimately mixed phases in PZN-0.09PT SCs [25, 90] reflects the behaviour of this solid-solution system near the MPB. This behaviour is in agreement with the phase diagram by Kuwata et al. [14] (see also Fig. 2.1b, just on the left from the vertical MPB). We add that the rhombohedral-tetragonal phase coexistence in PZN-xPT SCs near the MPB was also observed in different studies, see, e.g. papers [88, 89, 91, 92].

The experimental study by Durbin et al. [93] shows that the coexistence of the rhombohedral and tetragonal domains in PZN–0.08PT SCs poled in the [001] perovskite-cell direction results in a monoclinic distortion of the rhombohedral phase. An interpretation of this phenomenon and the electric-field-induced phase transitions in PZN–xPT SCs was carried out [93] within the framework of the phenomenological Devonshire theory [94] developed by Abe et al. [95]. Durbin et al. [93] showed that the thermodynamically stable monoclinic phase would not exist in PZN–0.08PT SCs. Their monoclinic distortion revealed in the X-ray powder diffraction study can be accounted for by strains resulting from the domain walls in the neighbouring tetragonal phase [93].

In the subsequent experimental study, the intermediate orthorhombic (*Bmm*2) phase in PZN–0.08PT SCs was irreversibly induced by the electric field [96]. This phase is regarded as a limiting case of the M_C -type phase with space group Pm and equality of the unit-cell parameters a=c. The polarization rotation path [76, 96] shown in Fig. 2.8 (see the perovskite unit cell on the left bottom) provided for the orthorhombic phase with the spontaneous polarization along the [101] direction. Based on the experimental results, La-Orauttapong et al. [16] proposed the modified phase diagram of the PZN–xPT system at $0 \le x \le 0.20$. The x-T diagram from work [16] includes the orthorhombic phase in a region similar to the hatched area in Fig. 2.1b. Comparison of the x-T diagram [16] to the modified diagrams of PZT [15] and PMN–xPT [17, 18] enables us to underline that the region of stability of the orthorhombic phase in PZN–xPT takes the least area in the diagram.

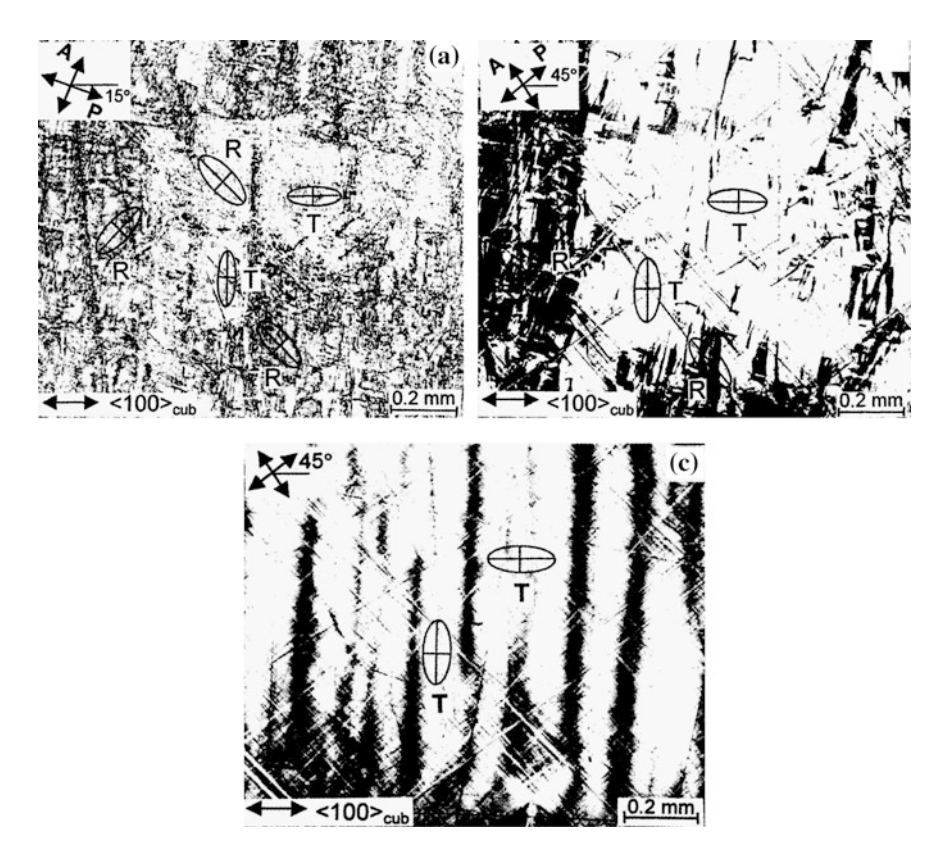


Fig. 2.16 DSs and phase sequences in a $(001)_{\text{cub}}$ PZN-0.09PT SC platelet $(4.8 \times 10^{-5} \text{ m thick})$: **a** coexistence of the polydomain rhombohedral (R) and tetragonal (T) phases at T = 25 °C, **b** phase transition from the rhombohedral (in extinction) to the tetragonal phase upon heating at T = 70 °C with growing tetragonal domains and **c** tetragonal-cubic phase transition upon heating at T = 175 °C (reprinted from paper by Topolov and Ye [90], with permission from Taylor & Francis)

2.4.2 Crystallographic Study of Elastic Matching of Morphotropic Phases

In this section, we consider conditions for ZNSPs and stressed interphase boundaries in PZN–xPT SCs near the MPB. It is assumed that the rhombohedral phase contains four types of the 71° (109°) domains shown in Fig. 2.5. The tetragonal phase is characterized by three 90°-domain types with the spontaneous polarization vectors $P_T^{(1)}(0; P; 0)$, $P_T^{(2)}(P; 0; 0)$ and $P_T^{(3)}(0; 0; P)$. The orientations of the $P_T^{(j)}(0; P)$ vectors are defined in the coordinate system $(X_1X_2X_3)$ shown in Fig. 2.5. The coordinate axes OX_j are parallel to the axes of the cubic perovskite unit cell as follows: $OX_1 \parallel [100]$, $OX_2 \parallel [010]$ and $OX_3 \parallel [001]$. Because of the possibility of elastic matching of the rhombohedral and tetragonal phases along the ZNSP in the

presence of two 90°-domain types (see Sect. 2.1.1), one can consider two versions of the tetragonal phase split into the 90° domains. We assume that in Version 1 the tetragonal phase is characterized by the 90° domains with $P_T^{(1)}$ (volume fraction m) and $P_T^{(2)}$ (volume fraction 1-m). In Version 2, there are domains with $P_T^{(2)}$ (volume fraction t) and t0 (volume fraction t1 – t1). Distortion matrices of the polydomain rhombohedral and tetragonal phases are written on analogy with (2.3), (2.4) and (2.6). Experimental values of the unit-cell parameters of PZN-t2 in the vicinity of the MPB [14] are used in our analysis [90].

At equal volume fractions of the 71° (109°) domains in the rhombohedral phase (i.e. at $x_R = y_R = 1/2$ in Fig. 2.5), there are no off-diagonal distortions in the matrix from (2.6) that characterizes the rhombohedral phase. The unit-cell parameters of PZN-0.09PT SC at room temperature does not satisfy the conditions for ZNSPs, and conical interphase boundaries separating these polydomain phases are expected within restricted volume-fraction ranges. According to data from work [90], these ranges are $0 \le m \le 0.615$ (Version 1) and $0 \le t \le 0.385$ (Version 2). The conical interfaces are also present at elastic matching of the single-domain rhombohedral phase (one of the domain types shown in Fig. 2.5 is given) and the polydomain tetragonal phase (Version 1 or 2).

At the coexistence of the single-domain rhombohedral and polydomain tetragonal phases, one can compare the results concerned with Versions 1 and 2 of the 90° domain orientations. It is assumed that the domain 1 (Fig. 2.5) is present in the rhombohedral phase only, i.e. $x_R = y_R = 0$. Results from work [90] show that Version 1 becomes more favourable for elastic matching of the morphotropic phases. The corresponding interphase boundaries are ZNSPs oriented along (001) or (010) of the perovskite unit cell with accuracy up to 5%, and the volume fractions of the 90° domains are listed in Table 2.3. A monotonic behaviour of the optimal volume fraction $m_{\rm opt}$ of the 90° domains with $P_T^{(1)}$ at molar concentrations

Table 2.3 Volume fractions of 90° domains in Version 1 at elastic matching of the single-domain rhombohedral ($x_R = y_R = 0$) and polydomain tetragonal phases in PZN–xPT SCs at room temperature (reprinted from paper by Topolov and Ye [90], with permission from Taylor & Francis)

x, rhombohedral phase	x, tetragonal phase	Optimal volume fraction m_{opt} obeying conditions for ZNSPs	Ranges of volume fractions <i>m</i> corresponding to conical interphase boundaries
0.080	0.090	_	$0 \le m \le 0.145 \text{ and} \\ 0.855 \le m \le 1$
0.090	0.090	0.620	$ \begin{array}{cccccccccccccccccccccccccccccccccccc$
0.090	0.095	0.707	$\begin{vmatrix} 0 \le m \le 0.793 \text{ and} \\ m \ne 0.707 \end{vmatrix}$
0.090	0.100	0.798	$0 \le m \le 0.950 \text{ and} $ $m \ne 0.798$
0.090	0.105	0.878	$0 \le m \le 1 \text{ and } m \ne 0.878$

 $x \ge 0.090$ in the coexisting phases, as well as the sufficiently wide m ranges related to the conical interphase boundaries enable us to expect an appearance of the analogous heterophase states with fluctuations of the molar concentration x or with inhomogeneous distributions of Ti^{4+} ions in PZN–xPT SC samples. We also mention that elastic matching of the single-domain rhombohedral phase ($x_R = y_R = 0$) and the polydomain tetragonal phase, as described in Version 2, leads to stressed conical interphase boundaries only. The corresponding volume fractions t are varied within a wide range. For example, at t = 0.090 in the coexisting phases, the conical interphase boundaries would appear at 0.359 t < 1 [90].

It should be noted for comparison that the spontaneous strain ξ_a^s of the perovskite unit cell at the tetragonal-rhombohedral phase transition in PZN-0.09PT SC has an order of magnitude of 10^{-3} and 10^{-5} ; see experimental data from papers [14] and [91], respectively. At the same time, the spontaneous strain ξ_a^s of the perovskite unit cell is almost equal to 3×10^{-3} in accordance with results [14, 91].

The discrepancy in the ξ_a^s values at ξ_a^s = const leads to different optimal volume fractions m_{opt} and orientations (h0l) of the interphase boundaries that obey conditions for ZNSPs. As a consequence, for the phase coexistence in Version 1, the values

$$m_{\rm opt} = 0.596 \,\text{and} \quad h/l \approx 3/2$$
 (2.14)

are obtained using the unit-cell parameters from work [14], whereas the values

$$m_{\rm opt} = 0.970 \,\text{and} \quad h/l \approx 11/2$$
 (2.15)

are obtained using the unit-cell parameters from work [91]. It is seen that the $m_{\rm opt}$ value from (2.14) is in good agreement with $m_{\rm opt}$ = 0.620 from Table 2.3. In this context, the 90° DS favours elastic matching of the tetragonal and rhombohedral phases without excessive internal stress. However the interphase boundary [88, 89], that separates the tetragonal and rhombohedral phases, has an orientation close to the (101) plane of the perovskite unit cell, and this orientation, undoubtedly, is close to the h/l ratio from (2.15).

The results of crystallographic analysis [90] are testified by the various heterophase structures and DSs which were observed in plate-like PZN–*x*PT SCs [89]. Some single-domain rhombohedral regions are occasionally surrounded by the polydomain tetragonal phase, but the interphase boundaries that separate these phases have the analogous orientations despite the possible inhomogeneous distribution of the Ti⁴⁺-concentration [89].

60 2 Two-Phase States

2.4.3 Interpenetrating Phases in $0.90Pb(Zn_{1/3}Nb_{2/3})O_3-0.10PbTiO_3$ Single Crystals

In Sect. 2.4.3, we consider elastic matching of the polydomain (twinned) phases in PZN-0.10PT SCs. This composition is characterized by following sequence of the phases on zero-field cooling in accordance with the x - T diagram [16]: cubic paraelectric-tetragonal FE-orthorhombic FE. Below the temperature of the tetragonal-orthorhombic phase transition $T_{T-O} = 320$ K, PZN-0.10PT SC remains heterophase. Conditions for elastic matching of the polydomain tetragonal and orthorhombic phases are studied [79] within the framework of the model of interpenetrating phases. The SC sample is represented as a set of two types of heterophase regions with phases I and II in each of them (see Fig. 2.14a). The tetragonal phase is assumed to be divided into the 90° domains (Fig. 2.2c) with volume fractions $n_{\rm T}$ and $1 - n_{\rm T}$. The orthorhombic phase is split into the domains of four types with the unit-cell vectors $c_0 \parallel [001]$ (Fig. 2.17). Volume fractions of $n_{\text{O2}} = (1 - x_{\text{O}})y_{\text{O}}, \quad n_{\text{O3}} = x_{\text{O}}(1 - y_{\text{O}})$ $n_{O1} = x_O y_O$ $n_{\rm O4} = (1 - x_{\rm O})(1 - y_{\rm O})$ are expressed in terms of the parameters $x_{\rm O} = |OA_1|/|OA_2|$ and $y_0 = |A_2B_1|/|A_2B_2|$ which characterize the volume fractions of mechanical twins 1–3 and 1–2 (Fig. 2.17). Volume fractions of 'inclusions' in the ν - and ν' -type regions shown in Fig. 2.14, a equal $r_{\rm T}$ (tetragonal phase) and $r_{\rm O}$ (orthorhombic phase). Assuming that the v- and v'-type regions in the model are uniformly distributed over the SC sample and that their volume fractions v = v' = 1/2 [79], one can write a relation between r_T and r_O as follows: $r_T + r_O = 1$.

Taking into account (2.12), (2.13) and (2.15), one can obtain dependences of the optimal volume fractions of the domains (twins) of various types in coexisting phases (e.g. $n_{\text{T,opt}}$, $x_{\text{O,opt}}$ and $y_{\text{O,opt}}$) on the volume fraction r_{T} of the tetragonal phase. These optimal volume fractions correspond to the interphase boundary that separates the v- and v'-type regions (Fig. 2.14a) and satisfies conditions (1.18) for ZNSPs.

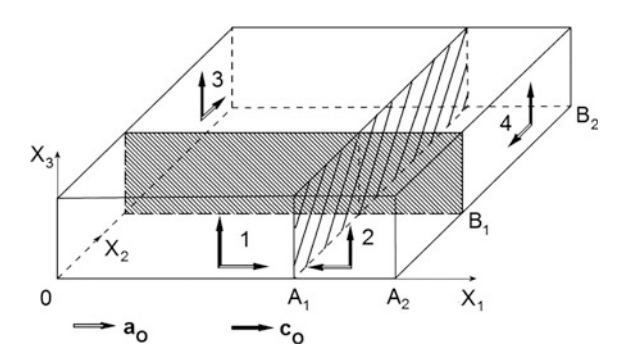
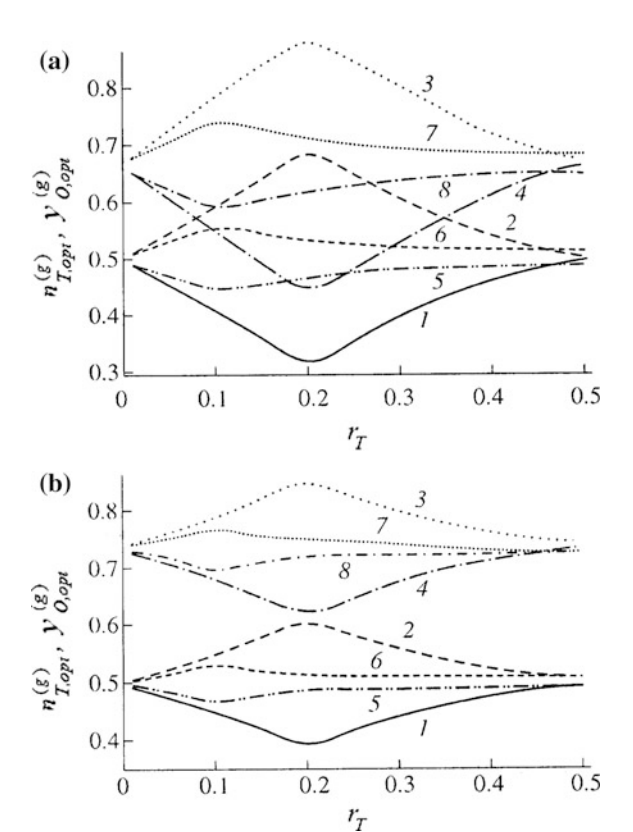


Fig. 2.17 Schematic arrangement of domains in the orthorhombic phase of PZN-0.10PT SC. Domain types 1-4 are characterized by different orientations of the unit-cell vector a_0 . Domain walls are shown as hatched areas. Coordinate axes OX_j are parallel to the perovskite unit-cell axes in the cubic phase. The unit-cell vectors a_0 and c_0 in domains are shown by arrows

The most interesting case of elastic matching of the tetragonal and orthorhombic phases along ZNSPs is actualized at fixed $x_{\rm O}$ values. The corresponding optimal fractions of the domains in the tetragonal phase $(n_{\rm T,opt})$ and twins in the orthorhombic phase $(y_{\rm O,opt})$ are non-monotonic functions of $r_{\rm T}$ (Fig. 2.18). Inequalities $n_{\rm T,opt}^{(1)}(r_{\rm T}) < n_{\rm T,opt}^{(2)}(r_{\rm T}) < n_{\rm T,opt}^{(2)}(r_{\rm T}) < y_{\rm O,opt}^{(1)}(r_{\rm T}) < y_{\rm O,opt}^{(1)}(r_{\rm T})$ are related to conic interphase boundaries that give rise to partial stress relief in heterophase SC samples.

Extremum points in the $n_{\mathrm{T,opt}}^{(g)}(r_{\mathrm{T}})$ and $y_{\mathrm{O,opt}}^{(g)}(r_{\mathrm{T}})$ curves are observed at $r_{\mathrm{T}} \approx 0.1$ –0.2 (Fig. 2.18), and their positions and values considerably vary with the parameter x_O that describes the volume fractions of the twins 1–3 and 2–4 (Fig. 2.17). Changes in temperature T at x_O = const lead to changes in the values of extremum points of $n_{\mathrm{T,opt}}^{(g)}(r_{\mathrm{T}})$ and $y_{\mathrm{O,opt}}^{(g)}(r_{\mathrm{T}})$ without changing their positions on the r_{T} axis. Orientations of the interphase boundaries that satisfy conditions (1.18) for ZNSPs are specified at x_O = 0.5 and $r_{\mathrm{T}} \approx 0.2$ by the $\{h0l\}$ planes of the perovskite unit cell [79], where the Miller indices h and l depend on temperature. It is seen that both max $[n_{\mathrm{T,opt}}^{(2)}(r_{\mathrm{T}}) - n_{\mathrm{T,opt}}^{(1)}(r_{\mathrm{T}})]$ and max $[y_{\mathrm{O,opt}}^{(1)}(r_{\mathrm{T}}) - y_{\mathrm{O,opt}}^{(2)}(r_{\mathrm{T}})]$ are located near

Fig. 2.18 Optimal volume fractions $n_{T,opt}^g(r_T)$ and $y_{\text{O.opt}}^g(r_{\text{T}})$ which characterize DSs of the coexisting tetragonal and orthorhombic phases in PZN-0.10PT SC at $T = 300 \text{ K } (\mathbf{a}) \text{ and } 20 \text{ K } (\mathbf{b})$: $n_{\text{T,opt}}^{(1)}(r_{\text{T}})$ (curves 1 and 5), $n_{\text{T,opt}}^{(2)}(r_{\text{T}})$ (curves 2 and 6), $y_{O,opt}^{(1)}(r_T)$ (curves 3 and 7) and $y_{0,opt}^{(2)}(r_T)$ (curves 4 and 8). Curves 1-4 were calculated at $x_{\rm O} = 0.5$, and curves 5–8 were calculated at $x_0 = 0.1$ (reprinted from paper by Topolov [79], with permission from Pleiades Publishing)



62 2 Two-Phase States

 $r_{\rm T}$ = 0.2 (see Fig. 2.18). It seems probable that this volume fraction of the tetragonal phase and the parameter $x_{\rm O}$ = 0.5 in the orthorhombic phase provide stress relief in PZN–0.10PT SCs to the greater degree. We note for comparison that, according to experimental data [16], the volume fraction of the tetragonal phase coexisting with the thermodynamically stable orthorhombic phase in PZN–0.10PT SCs at T = 20–300 K is about 20%. One of the reasons for the almost constant volume fraction $r_{\rm T}$ in the wide temperature range lies in the temperature dependences of the unit-cell parameters $a_{\rm O}(T)$ and $c_{\rm O}(T)$ in the orthorhombic phase and $a_{\rm T}(T)$ and $c_{\rm T}(T)$ in the tetragonal phase [16].

2.5 Two-Phase States and Stress Relief in Ferroelectric Solid Solutions

In this chapter, we have analysed examples of the two-phase states, elastic matching of the phases and stress relief in such solid solutions as PZT, PMN-xPT and PZNxPT. There systems are of interest because the MPB region between the FE phases with different permissible directions of spontaneous polarization vectors of domains is favourable to a high piezoelectric activity, strong electromechanical coupling, large dielectric permittivity [1-5], etc. Examples of the phase coexistence in the PbZrO₃ and PMN SCs have been considered additionally. The phase diagrams of PZT, PMN-xPT and PZN-xPT in the vicinity of the MPB [5-17] are characterized by the presence of vast regions of thermodynamic stability of the FE tetragonal and rhombohedral phases and by the presence of intermediate (almost monoclinic) phases. As a rule, the structural phase transitions in the studied systems are the first-order phase transitions, and therefore the role of spontaneous strains $\xi_{\rm pr}^{\rm s}$ of the unit cell and the influence of these strains on the heterophase state are to be taken into account. It has been shown that at changes in the molar concentration x and/or temperature T, complete stress relief can be achieved in heterophase structures either with the intermediate phase or without this phase. Hereby, the key role of specific non-90° domain types in forming the heterophase structures at complete stress relief in specific x and T ranges near the MPB has been emphasized. This role is inseparably linked with the anisotropic spontaneous strains $\xi^s_{\rm pr}$ at the phase transition, and the anisotropy of ξ_{pr}^s depends on the chemical composition, temperature and symmetry of the FE phase. Moreover, permissible orientations of the non-90° domains and their volume fractions in a monophasic region influence elastic matching of the coexisting phases and can promote complete stress relief in a heterophase sample.

The study on the domain states and heterophase structures is carried out within the framework of the crystallographic method (see Sect. 1.2), and examples of agreement between the experimental and calculated results are considered. The crystallographic description of the heterophase states enables us to build the domain state—interface diagrams that demonstrate important links between some domain

types and characteristics of the interphase boundaries in the two-phase state. The diagrams put forward in this chapter suggest that there are a few possible scenarios of stress relief in the studied heterophase systems. It seems to be probable that such scenarios may lead to different properties of heterophase solid solutions in the MPB region. We add that some examples of the two-phase coexistence and phase contents will be considered and compared in Chap. 6 on lead-free FE solid solutions.

The results discussed in this chapter are to be taken into account at the interpretation of various domain and two-phase states, heterophase structures and their evolution near the MPB, at changes of the molar concentration x and temperature T.

References

- 1. Xu Y (1991) Ferroelectric materials and their applications. North-Holland, Amsterdam London New York Toronto
- Helke G, Lubitz K (2008) Piezoelectric PZT ceramics. In: Heywang W, Wersing W, Lubitz K (eds) Piezoelectricity. Evolution and future of a technology. Springer, Berlin, pp 89–130
- 3. Cross LE (2008) Relaxor ferroelectrics. Ibid., pp 132-155
- Ahart M, Somayazulu M, Cohen RE, Ganesh P, Dera P, Mao H-K, Hemley RJ, Ren Y, Liermann P, Wu Z (2008) Origin of morphotropic phase boundaries in ferroelectrics. Nature 451:545–548
- 5. Jaffe B, Cook WR, Jaffe H (1971) Piezoelectric ceramics. Academic Press, London
- Eremkin VV, Smotrakov VG, Fesenko EG (1990) Structural phase transitions in PbZr_{1-x}Ti_xO₃ crystals. Ferroelectrics 110:137–144
- Noheda B, Cox DE, Shirane G, Guo R, Jones B, Cross LE (2001) Stability of the monoclinic phase in the ferroelectric perovskite PbZr_{1-x}Ti_xO₃. Phys Rev B 63:014103–6 p
- Noheda B, Cox DE (2006) Bridging phases at the morphotropic boundaries of lead oxide solid solutions. Phase Transitions 79:5–20
- Eitel R, Randall CA (2007) Octahedral tilt-suppression of ferroelectric domain wall dynamics and the associated piezoelectric activity in Pb(Zr,Ti)O₃. Phys Rev B 75:094106–8 p
- Reznitchenko LA, Shilkina LA, Razumovskaya ON, Yaroslavtseva EA, Dudkina SI, Demchenko OA, Yurasov YuI, Esis AA, Andryushina IN (2008) Phase x−T diagram of actual solid solutions of the (1 − x)PbZrO₃−xPbTiO₃ system (0.37 ≤ x ≤ 0.57). Phys Solid State 50:1527–1533
- Zhang N, Yokota H, Glazer AM, Ren Z, Keen DA, Keeble DS, Thomas PA, Ye Z-G (2014)
 The missing boundary in the phase diagram of PbZr_{1-x}Ti_xO₃. Nat Commun 5:5231–5239
- Cordero F (2015) Elastic properties and enhanced piezoelectric response at morphotropic phase boundaries. Materials 8:8195–8245
- 13. Choi SW, Shrout TR, Jang DJ, Bhalla AS (1989) Dielectric and pyroelectric properties in the Pb(Mg_{1/3}Nb_{2/3})O₃–PbTiO₃ system. Ferroelectrics 100:29–38
- Kuwata J, Uchino K, Nomura S (1981) Phase transitions in the Pb(Zn_{1/3}Nb_{2/3})O₃–PbTiO₃ system. Ferroelectrics 37:579–582
- 15. Noheda B, Cox DE, Shirane G, Gao J, Ye Z-G (2002) Phase diagram of the ferroelectric relaxor (1-x)Pb(Mg_{1/3}Nb_{2/3})O₃-xPbTiO₃. Phys Rev B 66:054104–10 p
- 16. La-Orauttapong D, Noheda B, Ye Z-G, Gehring PM, Toulouse J, Cox DE, Shirane G (2002) Phase diagram of the relaxor ferroelectric (1 − *x*)Pb(Zn_{1/3}Nb_{2/3})O₃−*x*PbTiO₃. Phys Rev B 65: 144101−7 p

64 2 Two-Phase States

17. Shuvaeva VA, Glazer AM, Zekria D (2005) The macroscopic symmetry of Pb($Mg_{1/3}Nb_{2/3}$)₁ $_{-x}Ti_xO_3$ in the morphotropic phase boundary region (x = 0.25-0.5). J Phys: Condens Matter 17:5709–5723

- 18. Singh AK, Pandey D, Zakharko O (2006) Powder neutron diffraction study of phase transitions in and a phase diagram of $(1-x)[Pb(Mg_{1/3}Nb_{2/3})O_3]$ – $xPbTiO_3$. Phys Rev B 74: 024101–18 p
- 19. Xu G, Luo H, Xu H, Yin Z (2001) Third ferroelectric phase in PMNT single crystals near the morphotropic phase boundary composition. Phys Rev B 64:020102–3 p
- Li J-B, Rao GH, Liu GY, Chena JR, Lua L, Jing X, Li S, Liang JK (2006) Structural transition in unpoled (1 – x)PMN–xPT ceramics near the morphotropic boundary. J Alloy Compd 425 (2006):373–378
- Singh AK, Pandey D (2005) On the discovery of two new monoclinic phases in the morphotropic phase boundary region of Pb[(Mg_{1/3}Nb_{2/3})O₃]–xPbTiO₃ ceramics. Ferroelectrics 326:91–99
- 22. Singh AK, Pandey D, Yoon S, Baik S, Shin N (2007) High-resolution synchrotron x-ray diffraction study of Zr-rich compositions of Pb(Zr_xTi_{1-x})O₃ (0.525 $\leq x \leq$ 0.60): evidence for the absence of the rhombohedral phase. Appl Phys Lett 91:192904–3 p
- 23. Zekria D, Glazer AM (2004) Automatic determination of the morphotropic phase boundary in lead magnesium niobate titanate Pb(Mg_{1/3}Nb_{2/3})_(1-x)Ti_xO₃ within a single crystal using birefringence imaging. J Appl Crystallogr 37:143–149
- 24. Ye Z-G, Dong M (2000) Morphotropic domain structures and phase transitions in relaxor-based piezo-/ferroelectric (1 x)Pb(Mg_{1/3}Nb_{2/3})O₃–xPbTiO₃ single crystals. J Appl Phys 87:2312–2319
- Ye Z-G (2002) Crystal chemistry and domain structure of relaxor piezocrystals. Curr Opin Solid State Mater Sci 6:35–44
- Jin YM, Wang YU, Khachaturyan AG, Li JF, Viehland D (2003) Adaptive ferroelectric states in systems with low domain wall energy: tetragonal microdomains. J Appl Phys 94:3629–3640
- 27. Davis M (2007) Picturing the elephant: giant piezoelectric activity and the monoclinic phases of relaxor-ferroelectric single crystals. J Electroceram 19:23–45
- 28. Ye Z-G (ed) (2008) Handbook of advanced dielectric, piezoelectric and ferroelectric materials: synthesis, properties and applications. Woodhead, Cambridge
- Topolov VY, Bowen CR (2009) Electromechanical properties in composites based on ferroelectrics. Springer, London
- Ari-Gur P, Benguigui L (1974) X-ray study of the PZT solid solutions near the morphotropic phase transition. Solid State Commun 15:1077–1079
- 31. Ari-Gur P, Benguigui L (1975) Direct determination of the coexistence region of solid solutions Pb(Zr_xTi_{1-x})O₃. J Phys D Appl Phys 8:1856–1862
- 32. Kakegawa K, Mohri J, Takahashi T, Yamamura H, Shirasaki S (1977) Compositional fluctuation and properties of Pb(Zr, Ti)O₃. Solid State Commun 24:769–772
- 33. Kala T (1983) Contibution to the study of tetragonal and rhombohedral phase coexistence in the PbZrO₃–PbTiO₃ system. Phys Status Solidi (a) 78:277–282
- Smolensky GA, Bokov VA, Isupov VA, Krainik NN, Pasynkov RE, Sokolov AI, Yushin NK (1985) Physics of ferroelectric phenomena. Nauka, Leningrad (in Russian)
- 35. Wersing W, Rossner W, Eckstein G, Tomandl G (1985) The morphotropic phase boundary in PZT ceramics prepared by spray drying of salt solutions and by the mixed oxide methods. Silic Indus 50:41–46
- 36. Kupriyanov MF, Konstantinov GM, Panich AE (1991) Ferroelectric morphotropic transitions. Rostov University Publishing, Rostov-on-Don (in Russian)
- 37. Lucuţa PG, Teodorescu V, Vasiliu F (1985) SEM, SAED, and TEM investigations of domain structure in PZT ceramics at morphotropic phase boundary. Appl Phys Solid Surf 37:237–245
- 38. Fousek J, Janovec V (1969) The orientation of domain walls in twinned ferroelectric crystals. J Appl Phys 40:135–142
- 39. Eknadiosiants EI, Borodin VZ, Smotrakov VG, Eremkin VV, Pinskaya AN (1990) Domain structure of rhombohedral PbTi_xZr_{1-x}O₃ crystals. Ferroelectrics 111:283–289

References 65

 Metrat G (1980) Theoretical determination of domain structure at transition from twinned phase: application to the tetragonal-orthorhombic transition of KNbO₃. Ferroelectrics 26: 801–804

- Topolov VYu, Turik AV (1990) Elastic effects at the morphotropic phase transition in solid solutions of the PbZr_{1-x}Ti_xO₃ system. Izvestiya SKNTs VSh. Yestestvennye Nauki N 1(69): 72–77 (in Russian)
- 42. Vanderbilt D, Cohen MH (2001) Monoclinic and triclinic phases in higher-order Devonshire theory. Physical Review B 63:094108–19 p
- 43. Topolov VYu, Turik AV (2001) A new monoclinic phase and features of stress relief in PbZr_{1-v}Ti_vO₃ solid solutions. J Phys: Condens Matter 13:L771–L775
- 44. Topolov VYu, Turik AV (2001) A new monoclinic phase and elastic effects in PbZr_{1-x}Ti_xO₃ solid solutions. Phys Solid State 43:1585–1588
- Topolov VYu, Balyunis LE, Turik AV, Fesenko OE (1990) Twinning of orthorhombic phases of PbHfO₃ crystals. Soviet Phys Crystallogr 35:441–444
- Topolov VYu, Turik AV (1990) Elastic interaction of phases of Gd₂(MoO₄)₃ crystals.
 Izvestiya Vysshikh Uchebnykh Zavedeniy. Fizika 33(3):68–72 (in Russian)
- 47. Singh AK, Mishra SK, Ragini, Pandey D, Yoon S, Baik S, Shin N (2008) Origin of high piezoelectric response of Pb(Zr_xTi_{1-x})O₃ at the morphotropic phase boundary: role of elastic instability. Appl Phys Lett 92:022910–3 p
- Zhou D, Wang F, Luo L, Chen J, Ge W, Zhao X, Luo H (2008) Characterization of complete electromechanical constants of rhombohedral 0.72Pb(Mg_{1/3}Nb_{2/3})-0.28PbTiO₃ single crystals. J Phys D Appl Phys 41:185402-4 p
- Zhang R, Jiang B, Cao W (2001) Elastic, piezoelectric, and dielectric properties of multidomain 0.67Pb(Mg_{1/3}Nb_{2/3})O₃-0.33PbTiO₃ single crystals. J Appl Phys 90:3471-3475
- Liu T, Lynch CS (2006) Domain engineered relaxor ferroelectric single crystals. Continuum Mech Thermodyn 18:119–135
- 51. Han J, Cao W (2003) Interweaving domain configurations in [001]-poled rhombohedral phase 0.68Pb(Mg_{1/3}Nb_{2/3})O₃–0.32PbTiO₃ single crystals. Appl Phys Lett 83:2040–2042
- Shin MC, Chung SJ, Lee SG, Feigelson RS (2004) Growth and observation of domain structure of lead magnesium niobate-lead titanate single crystals. J Cryst Growth 263:412– 420
- Ye Z-G, Topolov VYu (2001) Complex domain and heterophase structures in Pb(Mg_{1/3}Nb_{2/3})
 O₃-PbTiO₃ single crystals. Ferroelectrics 253:79–86
- Noblanc O, Gaucher P, Calvarin G (1996) Structural and dielectric studies of Pb(Mg_{1/3}Nb_{2/3})
 O₃-PbTiO₃ ferroelectric solid solutions around the morphotrophic phase boundary. J Appl Phys 79:4291–4297
- 55. Shrout T, Chang ZP, Kin M, Markgraf S (1990) Dielectric behavior of single crystals near the (1-x)Pb(Mg_{1/3}Nb_{2/3})O₃-xPbTiO₃ morphotropic phase boundary. Ferroelectr Lett Sect 12:63–69
- Bunina OA, Zakharchenko IN, Timonin PN, Sakhnenko VP (1995) Structural phase transformations in disordered Pb(Mg_{1/3}Nb_{2/3})_{0.8}Ti_{0.2}O₃ ferroelectric. Kristallografiya 40: 708–712 (in Russian)
- 57. Topolov VYu, Ye Z-G, Schmid H (1995) A crystallographic analysis of macrodomain structure in $Pb(Mg_{1/3}Nb_{2/3})O_3$. J Phys Condens Matter 7:3041–3049
- 58. Singh AK, Pandey D (2001) Structure and the location of the morphotropic phase boundary in $(1 x)[Pb(Mg_{1/3}Nb_{2/3})O_3]$ -xPbTiO₃. J Phys Condens Matter 13:L931–L936
- Kiat J-M, Uesu Y, Dkhil B, Matsuda M, Malibert C, Calvarin G (2002) Monoclinic structure of unpoled morphotropic high piezoelectric PMN-PT and PZN-PT compounds. Phys Rev B 65:064106–4 p
- 60. Singh AK, Pandey D (2002) Evidence for *M_B* and *M_C* phases in the morphotropic phase boundary region of (1 − *x*)[Pb(Mg_{1/3}Nb_{2/3})O₃] − *x*PbTiO₃: a rietveld study. Phys Rev B 67: 064102−12 p
- 61. Singh AK, Pandey D, Zakharko O (2003) Confirmation of M_B -type monoclinic phase in Pb [(Mg_{1/3}Nb_{2/3})_{0.71}Ti_{0.29}]O₃: a powder neutron diffraction study. Phys Rev B 68:172103–4 p

66 2 Two-Phase States

62. Li J-B, Rao GH, Liu GY, Chen R, Liang JK (2004) Effect of Ti on the stability of phases in the (1 - x)Pb(Mg_{1/3}Nb_{2/3})O₃-xPbTiO₃ solid solution. Ferroelectrics 313:71–80

- 63. Tu C-S, Hugo Schmidt V, Shih I-C, Chien R (2003) Phase transformation via a monoclinic phase in relaxor-based ferroelectric crystal (PbMg_{1/3}Nb_{2/3}O_{3)1-x}(PbTiO₃)_x. Phys Rev B 67: 020102–4 p
- 64. Abplanalp M, Barošová D, Bridenbaugh P, Erhart J, Fousek J, Günter P, Nosek J, Šulc M (2002) Scanning force microscopy of domain structures in Pb(Zn_{1/3}Nb_{2/3})O₃–8%PbTiO₃ and Pb(Mg_{1/3}Nb_{2/3})O₃–29% PbTiO₃. J Appl Phys 91:3797–3805
- 65. Guo Y, Luo H, He T, Xu H, Yin Z (2002) Domain configuration and ferroelectric related properties of the (110)_{cub} cuts of relaxor-based Pb(Mg_{1/3}Nb_{2/3})O₃–PbTiO₃ single crystals. Jpn J Appl Phys Pt 1(41):1451–1454
- Shvartsman VV, Kholkin AL (2004) Domain structure of 0.8Pb(Mg_{1/3}Nb_{2/3})O₃–0.2PbTiO₃ studied by piezoresponse force microscopy. Phys Rev B 69:014102–5 p
- 67. Bokov AA, Ye Z-G (2002) Ferroelectric properties of monoclinic Pb(Mg_{1/3}Nb_{2/3})O₃–PbTiO₃ crystals. Physical Review B 66, 094112–5 p
- 68. Bokov AA, Ye Z-G (2004) Domain structure in the monoclinic *Pm* phase of Pb(Mg_{1/3}Nb_{2/3}) O₃–PbTiO₃ single crystals. J Appl Phys 95:6347–6359
- 69. Bokov AA, Ye Z-G (2008) Field-induced shift of morphotropic phase boundary and effect of overpoling in (1 x)Pb(Mg_{1/3}Nb_{2/3})O₃ xPbTiO₃ piezocrystals. Appl Phys Lett 92:082901-3 p
- Tu C-S, Tsai C-L, Chen JS, Hugo Schmidt V (2002) Orientation dependence and electric-field effect in the relaxor-based ferroelectric crystal (PbMg_{1/3}Nb_{2/3}O₃)_{0.68}(PbTiO₃)_{0.32}. Phys Rev B 65:104113–11 p
- 71. Wang YuU (2006) Three intrinsic relationships of lattice parameters between intermediate monoclinic M_C and tetragonal phases in ferroelectric Pb[(Mg_{1/3}Nb_{2/3})_{1-x}Ti_x]O₃ and Pb[(Zn_{1/3}Nb_{2/3})_{1-x}Ti_x]O₃ near morphotropic phase boundaries. Phys Rev B 73:014113–13 p
- Viehland D (2000) Symmetry-adaptive ferroelectric mesostates in oriented Pb(BI_{1/3}BII_{2/3})O₃– PbTiO₃ crystals. J Appl Phys 88:4794–4806
- 73. Bhattacharyya S, Jinschek JR, Cao H, Wang YuU, Li J, Viehland D (2008) Direct high-resolution transmission electron microscopy observation of tetragonal nanotwins within the monoclinic M_C phase of Pb(Mg_{1/3}Nb_{2/3})O₃–0.35PbTiO₃ crystals. Appl Phys Lett 92:142904–3 p
- 74. Jin YM, Wang YU, Khachaturyan AG, Li JF, Viehland D (2003) Conformal miniaturization of domains with low domain-wall energy: monoclinic ferroelectric states near the morphotropic phase boundaries. Phys Rev Lett 91:197601–4 p
- Wang H, Zhu J, Lu N, Bokov AA, Ye Z-G, Zhang XW (2006) Hierarchical micro-/nanoscale domain structure in M_C phase of (1 - x)Pb(Mg_{1/3}Nb_{2/3})O₃-xPbTiO₃ single crystal. Appl Physics Lett 89:042908-3 p
- Fu H, Cohen RE (2000) Polarization rotation mechanism for ultrahigh electromechanical response in single-crystal piezoelectrics. Nature 403:281–283
- 77. Topolov VYu (2007) Peculiarities of coexistence of heavily twinned phases in the (1 x)Pb (Mg_{1/3}Nb_{2/3})TiO₃-xPbTiO₃ solid solutions at 0.23 $\leq x \leq 0.30$. Crystallogr Rep 52:297–301
- Topolov VYu (2008) Heterophase (1 x)Pb(Mg_{1/3}Nb_{2/3})TiO₃-xPbTiO₃ solid solutions near the morphotropic phase boundary: different scenarios of stress relief. Ferroelectrics 376:89–98
- Topolov VYu (2003) Heterophase states in 0.10PbTiO₃-0.90Pb(Zn_{1/3}Nb_{2/3})O₃ crystals. Phys Solid State 45:1295–1297
- 80. Topolov VYu, Ye Z-G (2004) Coexistence of morphotropic phases in (1 x)Pb(Mg_{1/3}Nb_{2/3}) O₃– xPbTiO₃ solid solutions. Phys Rev B 70:094113–8 p
- Wada S, Park S-E, Cross LE, Shrout TR (1999) Engineered domain configuration in rhombohedral PZN-PT single crystals and their ferroelectric related properties. Ferroelectrics 221:147–155
- Zhang R, Jiang B, Cao W, Amin A (2002) Complete set of material constants of 0.93Pb (Zn_{1/3}Nb_{2/3})O₃-0.07PbTiO₃ domain engineered single crystal. J Mater Sci Lett 21:1877–1879

References 67

83. Ogawa T, Yamauchi Y, Numamoto Y, Matsushita M, Tachi Y (2002) Giant electromechanical coupling factor of k₃₁ mode and piezoelectric d₃₁ constant in Pb[(Zn_{1/3}Nb_{2/3})_{0.91}Ti_{0.09}]O₃ piezoelectric single crystal. Jpn J Appl Phys Pt 2 41:L55–L57

- 84. Topolov VYu, Turik AV (2001) Interphase boundaries and high piezoelectric activity of xPbTiO₃-(1 x)Pb(Zn_{1/3}Nb_{2/3})O₃ crystals. Phys Solid State 43:1117–1123
- 85. Topolov VYu, Turik AV (2002) An intermediate monoclinic phase and electromechanical interactions in xPbTiO₃–(1 x)Pb(Zn_{1/3}Nb_{2/3})O₃ crystals. Phys Solid State 44:1355–1362
- Park S-E, Shrout TR (1997) Ultrahigh strain and piezoelectric behavior in relaxor based ferroelectric single crystals. J Appl Phys 82:1804–1811
- Park S-E, Shrout TR (1997) Characteristics of relaxor-based ferroelectric single crystals for ultrasonic transducers. IEEE Trans Ultrason Ferroelectr Freq Control 44:1140–1147
- 88. Fujishiro K, Vlokh R, Uesu Y, Yamada Y, Kiat J-M, Dkhil B, Yamashita Y (1998) Optical observation of heterophases and domain structure in relaxor ferroelectrics Pb(Zn_{1/3}Nb_{2/3})O₃/9% PbTiO₃. Jpn J Appl Phys Pt 1(37):5246–5248
- 89. Ye Z-G, Dong M, Zhang L (1999) Domain structure and phase transitions in relaxor-based piezo-/ferroelectric (1 x)Pb(Zn_{1/3}Nb_{2/3})O₃–xPbTiO₃ single crystals. Ferroelectrics 229: 223–232
- 90. Topolov VYu, Ye Z-G (2001) Elastic matching of morphotropic phases in polydomain (1 x) Pb(Zn_{1/3}Nb_{2/3})O₃–xPbTiO₃ single crystals. Ferroelectrics 253:71–78
- Uesu Y, Yamada Y, Fujishiro K, Tazawa H, Enokido S, Kiat J-M, Dkhil B (1998) Structural and optical studies of development of the long-range order in ferroelectric relaxor Pb(Zn_{1/3}Nb_{2/3})O₃/9%PbTiO₃. Ferroelectrics 217:319–325
- 92. Belegundu U, Du XH, Cross LE, Uchino K (1999) In situ observation of domains in 0.9Pb (Zn_{1/3}Nb_{2/3})O₃-0.1PbTiO₃ single crystals. Ferroelectrics 221:67-71
- 93. Durbin MK, Hicks JC, Park S-E, Shrout TR (2000) X-ray diffraction and phenomenological studies of the engineered monoclinic crystal domains in single crystal relaxor ferroelectrics. J Appl Phys 87:8159–8164
- 94. Devonshire AF (1954) Theory of ferroelectrics. Adv Phys 3:85-130
- Abe K, Furukawa O, Imagawa H (1988) Calculations concerning the phase diagram, dielectric constant and lattice parameters for the Pb(Zn_{1/3}Nb_{2/3})O₃-PbTiO₃ solid solution. Ferroelectrics 87:55-64
- Noheda B, Cox DE, Shirane G, Park S-E, Cross LE, Zhong Z (2001) Polarization rotation via a monoclinic phase in the piezoelectric 92%PbZn_{1/3}Nb_{2/3}O₃–8%PbTiO₃. Phys Rev Lett 86:3891–3894

Chapter 3 Phase Coexistence Under Electric Field



Abstract Features of the phase coexistence in relaxor-ferroelectric single crystals under the electric field are discussed by taking into account results of the crystal-lographic description. The electric field is applied along one of the perovskite-cell directions, [001], [011] or [111]. Different scenarios of stress relief in the presence of complex domain structures and morphotropic phases are proposed by taking into account peculiarities of the unit-cell behaviour. The role of the intermediate polydomain monoclinic phase in forming the various heterophase states is described in the context of effective stress relief in different variants of the phase coexistence.

Experimental studies of relaxor-FE PMN–*x*PT and PZN–*x*PT SCs in an external direct-current electric field open up possibilities for observation of various heterophase states and DSs. An appearance of new FE phases induced by the electric field in SC cuts with fixed orientations of the main crystallographic axes gives rise to questions on conditions for stress relief in the wide temperature range and in the presence of the FE phases from different symmetry classes, on the preferable domain and twin orientations, on ZNSPs in polydomain SCs, etc. In this chapter, we discuss features of the phase coexistence in PMN–*x*PT and PZN–*x*PT SCs under the electric field applied along one of the perovskite-cell directions, [001], [011] or [111].

3.1 Heterophase Pb(Mg_{1/3}Nb_{2/3})O₃ at the Induced Phase Transition

PMN demonstrates the typical relaxor behaviour with the broad maximum of dielectric permittivity $\varepsilon(T)$ [1, 2]. In the last decades, this material has been the prototype for perovskite-structure relaxors [2]. The disordered cubic $(Pm\bar{3}m)$ structure of PMN SC remains stable at temperatures 5 K $\leq T \leq$ 800 K without significant evidence for a structural phase transition in the region of max $\varepsilon(T)$. Temperature $T_{\rm m}$ that corresponds to max $\varepsilon(T)$, moves to higher temperature with increasing measuring frequency, and this behaviour is typical of a dielectric

relaxation [1, 2]. The dissipation factor $tg\delta$ is also characterized by a maximum that moves with changes in measuring frequency [1]. No macrodomains are observed in PMN SCs, however chemically inhomogeneous polar nanodomains were revealed by high-resolution electron microscopy [3] and diffuse scattering of the X-ray and neutron diffraction lines [4] in the wide temperature range. Evidence for the electric-field-induced transition from the disordered $Pm\bar{3}m$ phase to the polar rhombohedral (R3m) phase is obtained in experimental studies [4–6], and this phase transition belongs to the first-order type. In addition to the change in the unit-cell parameters and dielectric anomalies, current pulses and optical polar macrodomains and interphase boundaries were observed at this induced phase transition [5, 6]. In Sect. 3.1, we discuss crystallographic aspects of heterophase states in PMN SCs at the electric-field-induced phase transition.

According to experimental data [5, 6], the nucleation of the polar phase is observed inside the cubic phase and the propagation of the interphase boundaries is registered at the field-induced phase transition. The birefringent macrodomains of the rhombohedral phase appear in (100) and (110) SC platelets of PMN in the electric field $E \parallel [100]$ and $E \parallel [110]$, respectively (the Miller indices are given in the perovskite unit-cell axes). The formation of the single-domain rhombohedral phase is observed in (111) SC platelets. On the (111) plane, the induced phase transition is revealed by the onset of an interphase boundary between the cubic and rhombohedral phases. For example, if $E \parallel [111]$ and E = 0.3 MV/m, then the interphase boundary appears at T = 230 K [7]. During the establishment of the polar phase, the interphase boundary travelled through the SC sample while the polar phase gained the area of the disappearing disordered phase. As a result, the single-domain state was registered in (111) SC platelets at the end of the induced phase transition. The induced polar phase remains optically isotropic when observing on the poling [111] direction. Some features of the induced phase transition in PMN SCs are shown in Fig. 3.1. It should be noted that the poled state of PMN remains metastable and can be switched by an electric field with the

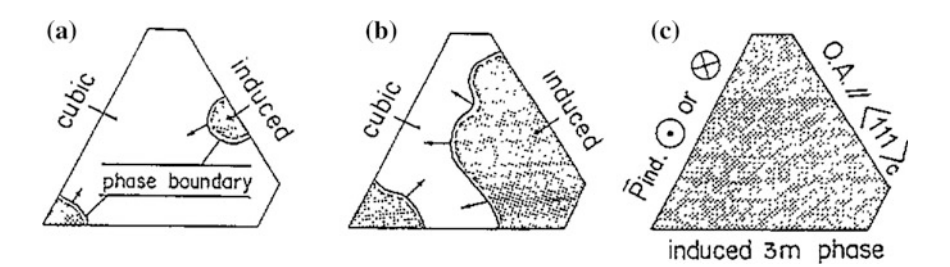


Fig. 3.1 Schematic representation of the main stages of the electric-field-induced phase transition in the (111) platelet of PMN SC: a the onset of the phase induction shown up by the appearance of the interphase boundary that separates the initial cubic and induced rhombohedral phases, b the propagation of the interphase boundary through the SC platelet with the growth of the induced rhombohedral phase, and c the single-domain of the induced rhombohedral phase behaving isotropically along the [111] perovskite-cell direction (reprinted from paper by Topolov et al. [7], with permission from IOP Publishing)

opposite E direction. At temperatures T = 175-200 K, the switching process proceeds at E = 0.3 MV/m. Optical domain observations show that the 180° switching of the induced polarization takes place via an intermediate ferroelastic orientation states of the rhombohedral phase, and these orientation states give rise to the birefringent lamellar non- 180° domains. These domains transform into an isotropic section, but with the induced polarization P_{ind} is reversed by 180° .

Our crystallographic analysis of elastic matching of the phases in an electric field shows that the interphase boundaries in PMN SCs can be conical (see the domain state-interface diagram in Fig. 2.7a), and no complete stress relief is attained. The conical configuration of the interphase boundaries is confirmed in experimental studies of PMN SCs [5–7] in the electric field. To consider the possible interphase boundaries in the (111) platelet, we carry out a transformation of the co-ordinate axes $(X_1X_2X_3) \rightarrow (X_1'X_2'X_3')$ so that the OX_1 and OX_3 axes are rotated by 45° and the OX_3' axis coincides with the normal vector $\mathbf{n_0} \parallel [111]$ (Fig. 2.7b). The conical surface in the co-ordinate system $(X_1'X_2'X_3')$ is described by the equation similar to (1.12):

$$\sum_{i,i=1}^{3} D'_{ij} x'_i x'_j = 0, (3.1)$$

where
$$D_{11}' = \frac{1}{4}(D_{11} + D_{33}) + \frac{1}{2}(D_{22} - D_{13}) + \frac{\sqrt{2}}{2}(D_{12} - D_{23}),$$

$$D_{22}' = \frac{1}{4}(D_{11} + D_{33}) + \frac{1}{2}(D_{22} - D_{13}) - \frac{\sqrt{2}}{2}(D_{12} - D_{23}), D_{33}' = \frac{1}{2}(D_{11} + D_{33}) + D_{13},$$

$$D_{12}' = -\frac{1}{4}(D_{11} + D_{33}) + \frac{1}{2}(D_{13} + D_{22}), D_{13}' = \frac{1}{3}(D_{12} + D_{23}) - \frac{\sqrt{2}}{4}(D_{33} - D_{11}), \text{ and}$$

 $D'_{23} = \frac{1}{2}(D_{12} + D_{23}) + \frac{\sqrt{2}}{4}(D_{33} - D_{11})$. The matrix elements D_{ij} are determined in the co-ordinate system $(X_1X_2X_3)$ in terms of the unit-cell distortions of the coexisting phases [see (1.7) and Sect. 2.2.1].

We evaluated D_{ij} and determinant $D = \det |D_{ij}||$ in wide ranges of the parameters x_r and y_r that characterize the relative thickness of mechanical twins (Fig. 2.7a) in the rhombohedral phase. The determinant D characterizes the level of strains at the phase coexistence [8], and in the case of the electric-field-induced transition in PMN SCs, we have $|D| \approx 10^{-10} - 10^{-8}$, however on average, $|D_{ij}| \approx 10^{-3}$ [7]. The considerable difference between |D| and $|D_{ij}|$ may be the reason [7] for a small mechanical stress at the interphase boundary and for a certain unsteadiness that leads to their ephemeral appearance at the induced phase transition, to the different fragments of several conical surfaces and to the visible changes in the DS [5, 6]. In general, one can emphasize that various heterophase states in PMN SCs are closely connected with the formation of the conical interphase boundaries under conditions for considerable stress relief.

Analysis of invariants of (3.1) in the wide x_r and y_r ranges shows that the possible interphase boundary sections on the (111) plane of the plate-like PMN sample are ellipses [7]. The ellipse axes are rotated in the $(X_1'OX_2')$ plane by an angle $\alpha_{\rm el} = \arctan \left[2D_{12}'/(D_{11}' - D_{22}') \right]/2$ that strongly depends on x_r and y_r . The diversity of orientations of the possible section on the (111) plane in connection with the $\alpha_{\rm el}(x_r, y_r)$ dependence [7] testifies to the plurality of the interphase boundaries and DSs at the electric-field-induced phase transition in PMN SCs.

As for the $P_{\text{ind},k}$ vectors in the macrodomains of the rhombohedral phase with respect to the normal-vector orientation $n_0 \parallel [111]$ (Fig. 2.7b), we note that the angle between $P_{\text{ind},1}$ and the (111) perovskite-cell plane approximately equals 35.26° [7]. This value is in good agreement with experimental data [7] on the induced phase and its rhombohedral distortion.

In general, results on the crystallographic analysis of the phase coexistence in PMN SCs [7] show that the elastic interaction between the macrodomains or phase regions and the internal mechanical stress play the important role in the kinetics of the electric-field-induced phase transition $Pm\overline{3}m - R3m$ that is accompanied by the formation of various conical interphase boundaries.

3.2 Domain State–Interface Relationships at Electric Field $E \parallel [001]$

3.2.1 Heterophase $(1 - x)Pb(Mg_{1/3}Nb_{2/3})O_3$ -xPbTiO₃

The intermediate M_A , M_B and M_C phases of the FE nature were revealed in PMN–xPT SCs in some ranges of temperature T and electric field E [9–12]. The monoclinic symmetry of these phases allows a rotation of the spontaneous polarization vector [13, 14] between the fixed orientations related to the higher symmetry phases, such as tetragonal and rhombohedral phases. The intermediate phases play the role of bridging phases near the MPB [15] and make a lower free-energy path [13] of the rotation of the spontaneous polarization vector in the perovskite unit cell between the [111] direction (rhombohedral phase) and [001] direction (tetragonal phase).

Experimental results [10, 11, 16] on phase transitions in electric-field-cooled PMN–xPT SCs near the MPB show that the electric field $E \sim 0.1$ MV/m induces the intermediate phases, and the E orientation influences the phase sequence with decreasing temperature. For example, in PMN–0.30PT SCs, the following phase sequences are observed [10, 11]: cubic \rightarrow tetragonal \rightarrow rhombohedral at E = 0, cubic \rightarrow tetragonal \rightarrow M_C \rightarrow M_A at $E \parallel$ [001] and cubic \rightarrow tetragonal \rightarrow orthorhombic \rightarrow M_B at $E \parallel$ [110], where the crystallographic directions are related to the perovskite unit-cell axes. Moreover, the following phase sequences are observed [16] in PMN–0.35PT SCs on cooling: cubic \rightarrow tetragonal \rightarrow M_C at $E \parallel$ [001] and cubic \rightarrow tetragonal \rightarrow orthorhombic at $E \parallel$ [110]. As a rule, the electric-field-cooled PMN–xPT SCs exhibit more simple DSs in comparison with those formed on zero-field-cooling [10, 11, 16].

Modified x–T diagrams were proposed by Cao et al. [12] for electric-field-cooled PMN–xPT SCs (0.15 $\leq x \leq$ 0.38) at E = 0.1 MV/m and two orientations of the electric-field vector, $E \parallel$ [001] and $E \parallel$ [110]. In these diagrams, the rhombohedral phase of the zero-field-cooled state is replaced by either the M_A (at $E \parallel$ [001]) or M_B phase (at $E \parallel$ [110]). The intermediate M_C phase observed on zero-field cooling at $E \parallel$ [001] is replaced by the orthorhombic phase as electric-field cooling is carried out at $E \parallel$ [110]. In the x–T diagram related to $E \parallel$ [001], the tetragonal– M_A phase boundary shifts towards the lower PT content, namely, to x = 0.25. At the same time, the extended region in the diagram related to $E \parallel$ [110] is entirely replaced by the orthorhombic phase. The experimental results [12] suggest that the phase stability of PMN–xPT SCs is fragile even at the visible distance from the MPB (over 0.1 on the x scale) and a strong dependence of the phase states on the direction of the external electric field E is observed. Thus, the picture of heterophase states in PMN–xPT SCs becomes complicated and depends on many physical and crystal-lographic factors to be studied.

In Sect. 3.2.1, we discuss features of the phase coexistence and stress relief in PMN-xPT SCs

- (i) at E = 0 and $E \parallel [001]$ and
- (ii) at $E \parallel [001]$ and various compositions around the MPB.

3.2.1.1 Phase Sequences and Diagrams at $x \ge 0.30$

The cubic–tetragonal phase transition in FE SCs can be accompanied by the formation of interphase boundaries that obey conditions (1.18) for ZNSPs (see, for instance, Table 1.1). In these SCs the tetragonal phase is separated into the 90° domains 1–2, 2–3 or 1–3 (Fig. 3.2) with the optimal volume fractions $n_T^{\rm opt}$ and $1-n_T^{\rm opt}$ (see Sect. 2.2.1). Cooling in the electric field $E \parallel [001]$ ($E=0.1~{\rm MV/m}$) leads, for example, to $n_T^{\rm opt}=0.547$ or 0.508 [17] for PMN–0.30PT or PMN–0.32PT SC, respectively. A tendency $n_T^{\rm opt}\to 0.5$ is accounted for by the unit-cell behaviour of electric-field-cooled PMN–xPT SCs: according to experimental data [10, 18], the unit-cell parameters a_T and c_T of the tetragonal phase and the unit-cell parameter a_C of the cubic phase are linked by a relation $c_T-a_C\approx a_C-a_T$. The ZNSPs are parallel to the {hk0} planes of the perovskite unit cell, where the Miller indices h and k depend on a_T , c_T and a_C .

Among domains 1, 2 and 3 in the tetragonal phase (Fig. 3.2), only domain 1 is characterized by the unit-cell vector c_T and the spontaneous polarization vector $P_{s,1}$ which are parallel to the electric field $E \parallel [001]$. We assume that the tetragonal phase is split into domains 1–2 and the volume fractions of domains 1 and 2 equal n_1 and $1-n_1$, respectively. The M_C phase is assumed to be split into domains 4–7 (Fig. 3.2), and their volume fractions are defined in terms of parameters f_M and v_M as follows:

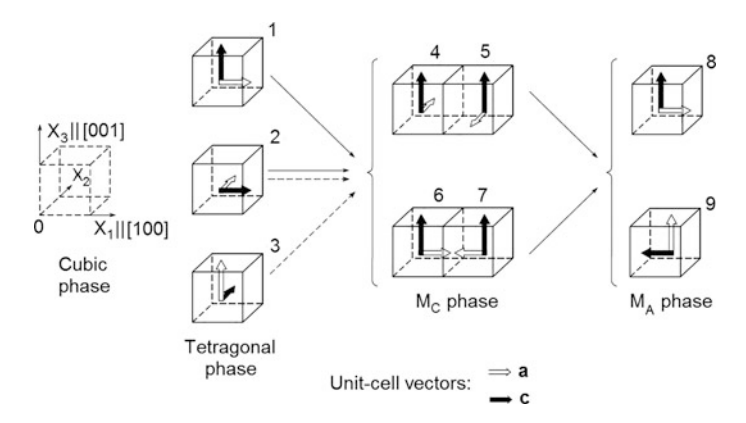


Fig. 3.2 Schematic arrangement of non-180° domains (twin components) in PMN–xPT SCs near the MPB. The perovskite unit cell of the paraelectric cubic phase is shown by dashed lines

$$n_{C4} = f_M(1 - v_M), n_{C5} = (1 - f_M)(1 - v_M), n_{C6} = f_M v_M, \text{ and } n_{C7} = (1 - f_M)v_M.$$
(3.2)

The parameter f_M characterizes the volume fraction of domain 4 in the twin 4–5 or the volume fraction of domain 6 in the twin 6–7 (Fig. 3.2). The parameter v_M characterizes the volume fraction of the twin 6–7 in the four-component twin 4–7. In general, the orientations of the crystallographic axes of the aforementioned domains (Fig. 3.2) are given taking into account that [001]-field cooling fixes the prototype c axis [16].

Distortion matrices of the polydomain tetragonal and M_C phases are written by analogy with $||N_{ij}^{(5-7)}||$ from (2.4) and with $||N_{ij}^{(MC)}||$ from (2.8), respectively. Examples of the domain state–interface diagrams calculated for the tetragonal– M_C phase coexistence at E || [001] are shown in Fig. 3.3. Calculations were performed using the experimental unit-cell parameters from work [19]. As follows from the analysis of the heterophase states in electric-field-cooled PMN–xPT SCs, the arrangement of the curves and their configurations in the diagrams (Fig. 3.3) highly depend on the molar concentration x and parameter f_M . The latter circumstance suggests that distortions of the polydomain M_C phase play a decisive role in the formation of ZNSPs at the interphase boundaries.

The presence of the line $v_M = 1$ in the range $0 \le n_1 \le 1$ (Fig. 3.3) is accounted for by the equality of the unit-cell parameters $a_T = b_M$ [19] at the tetragonal– M_C phase transition in the studied range of molar concentrations x. We see that conditions (1.18) for ZNSPs are satisfied in various ranges of v_M and n_1 , where the boundaries between regions I and III (Fig. 3.3) are located. Moreover, ZNSPs also correspond to segments of the line $v_M = 1$ over regions I and III because conditions (1.18) are valid in this volume-fraction range.

Differences in the diagrams at $x \ge 0.33$ (Fig. 3.3e–g) are mainly associated with monotonic changes in the jumps of the unit-cell parameters [19] at the phase

transition. An increase in the parameter f_M results in a 'straightening' of the boundaries between regions I and III (Fig. 3.3b–e). In the diagrams built for $f_M = 0.5$, there is a line $n_1 = \text{const}$, along which the parameter v_M can vary over a wide range (Fig. 3.3a, e–g). As the shear distortions in the polydomain M_C phase at $f_M = 0.5$ disappear, the area of region IV, where conditions (1.17) are valid, reaches a maximum (compare Fig. 3.3d, e to Fig. 3.3f, g). We mention that conditions (1.17) correspond to an imaginary cone apex, and no planar or conical interphase boundary would appear hereby.

The important feature of the diagrams shown in Fig. 3.3 is that the mutual arrangement of the line $n_1 = {\rm const}$ and the point $n_1 = n_T^{\rm opt}$ on the abscissa (the $n_T^{\rm opt}$ value is found from conditions (1.18) for ZNSPs at the cubic–tetragonal phase transition) changes with an increase in x. Assuming that the DS in the tetragonal phase formed under the conditions for ZNSPs remains unchanged up to the tetragonal– M_C phase transition (i.e. condition $n_1 = n_T^{\rm opt}$ or $n_1 = 1 - n_T^{\rm opt}$ holds), one can consider some variants of the formation of the interphase boundaries that also obey conditions (1.18). For example, ZNSPs at x = 0.31 and $f_M = 0.5$ (Fig. 3.3a) correspond to $n_1 = n_T^{\rm opt}$ and $v_M = v_M^{\rm opt}$, $n_1 = n_T^{\rm opt}$ and $v_M = 1$, or $n_1 = 1 - n_T^{\rm opt}$ and $v_M = 1$. We also see that the vertical line $n_1 = n_T^{\rm opt}$ would lie close to the boundary between regions I and III (Fig. 3.3a), i.e. almost complete stress relief would be achieved at various volume fractions of the twin 6–7 in the M_C phase (Fig. 3.2). At x = 0.33 and $0 < f_M < 0.2$, the boundary between regions I and III lies at $n_1 > n_T^{\rm opt}$ (cf. Fig. 3.3b, c) and covers a relatively wide range of v_M . Such a location means that in the immediate vicinity of the MPB, different DSs can be formed under the conditions for ZNSPs.

heterophase consider states in PMN-0.30PT electric-field-cooling at $E \parallel [001] \parallel OX_3$. Domain types 1–2 (tetragonal phase), 4–7 (M_C phase) and 8–9 (M_A phase) are shown in Fig. 3.2. Volume fractions of the domains in the M_A phase are n_8 (see domain 8 in Fig. 3.2) and $1 - n_8$ (see domain 9 in Fig. 3.2). Diagrams shown in Fig. 3.4 were calculated using the unit-cell parameters [10] measured at E = 0.1 MV/m. The diagram in Fig. 3.4a differs from the diagrams calculated for x = 0.30 (Fig. 3.3a) and x = 0.33 (Fig. 3.3e) at E = 0because of the change in the balance of the jumps of the unit-cell parameters during the tetragonal-M_C phase transition. If the DS of the tetragonal phase in the electric field E remains unchanged up to the tetragonal–M_C phase transition (i.e. $n_1 = n_T^{\text{opt}}$ or $n_1 = 1 - n_T^{\text{opt}}$), the interphase boundary between the polydomain tetragonal and M_C phases obeys conditions (1.18) for ZNSPs at $v_M = v_M^{\text{opt}}$ (see the horizontal boundary between regions I and III in Fig. 3.4a). A relatively small increase (about 10%) in the volume fraction n_1 , as compared to the n_T^{opt} value, leads to the formation of the interphase boundaries that obey conditions (1.18) at $0 \le v_M \le v_M^{\text{opt}}$ (see the vertical boundary in Fig. 3.4a). The single-domain tetragonal phase $(n_1 = 0 \text{ or } 1)$ can also coexist with the polydomain M_C phase at $v_M = v_M^{\text{opt}}$ or $v_M = 1 - v_M^{\text{opt}}$ (Fig. 3.4a), and conditions (1.18) for ZNSPs hold. It should be noted that similar tendencies in the elastic matching of the FE phases manifest themselves at the tetragonal-M_C phase transition [20] in electric-field-cooled PMN-0.32PT SCs at $E \parallel [001]$.

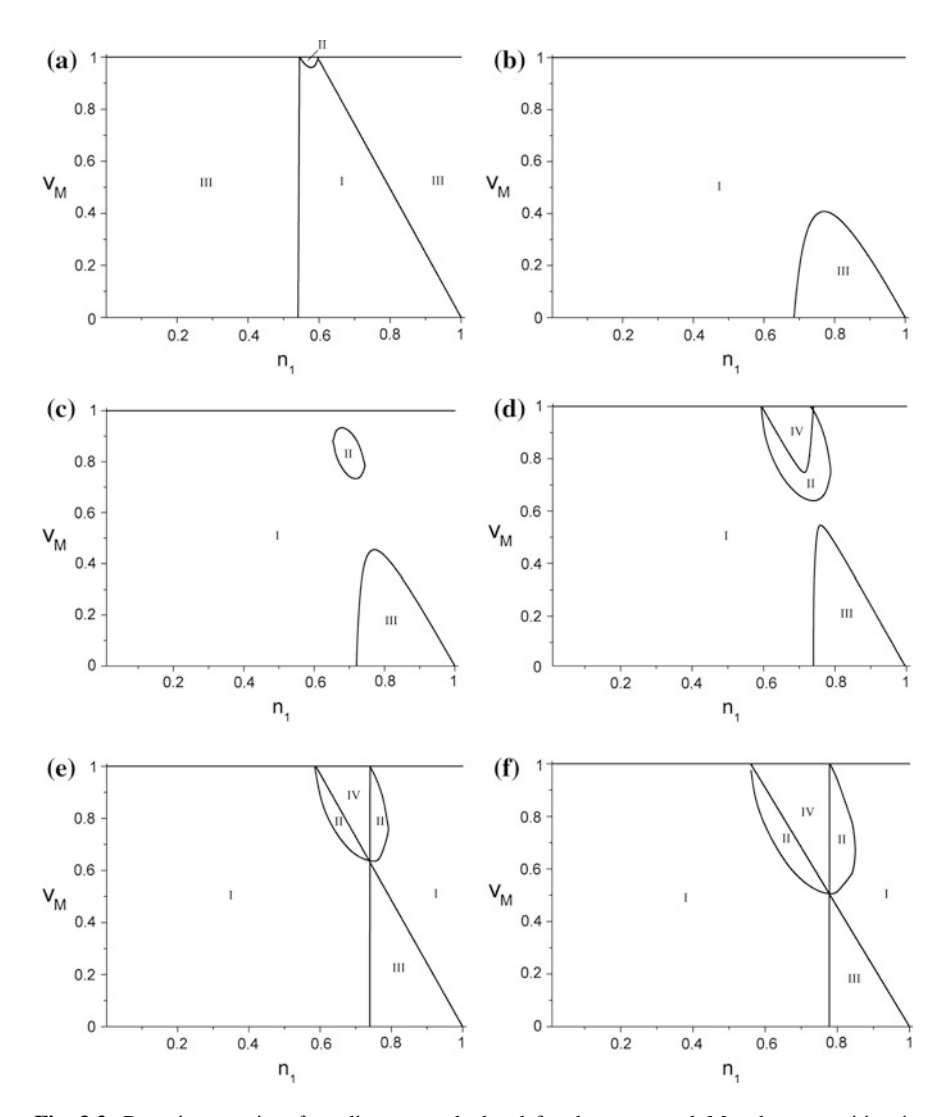


Fig. 3.3 Domain state–interface diagrams calculated for the tetragonal– M_C phase transition in zero-field-cooled PMN–xPT SCs with x=0.31 (a), 0.33 (b–e), 0.35 (f), and 0.37 (g). In the M_C phase $f_M=0.5$ (a, e–g), 0 (b), 0.2 (c), and 0.4 (d). Conditions (1.14), (1.15), (1.16) and (1.17) are valid in regions I, II, III and IV, respectively (reprinted from paper by Topolov [17], with permission from Pleiades Publishing)

The diagram that describes the M_C – M_A phase coexistence is shown in Fig. 3.4b. It resembles a fragment of the diagram from Fig. 3.4a near the intersection of the lines n_1 = const and v_M = const despite differences in symmetry and DSs of the coexisting phases. The mutual arrangement of the boundaries between regions I and III and the points $v_M = v_M^{\text{opt}}$ determined in accordance with the diagram from

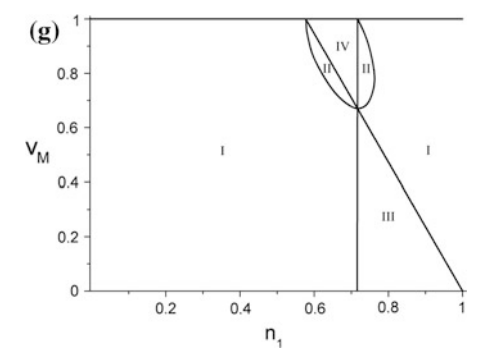


Fig. 3.3 (continued)

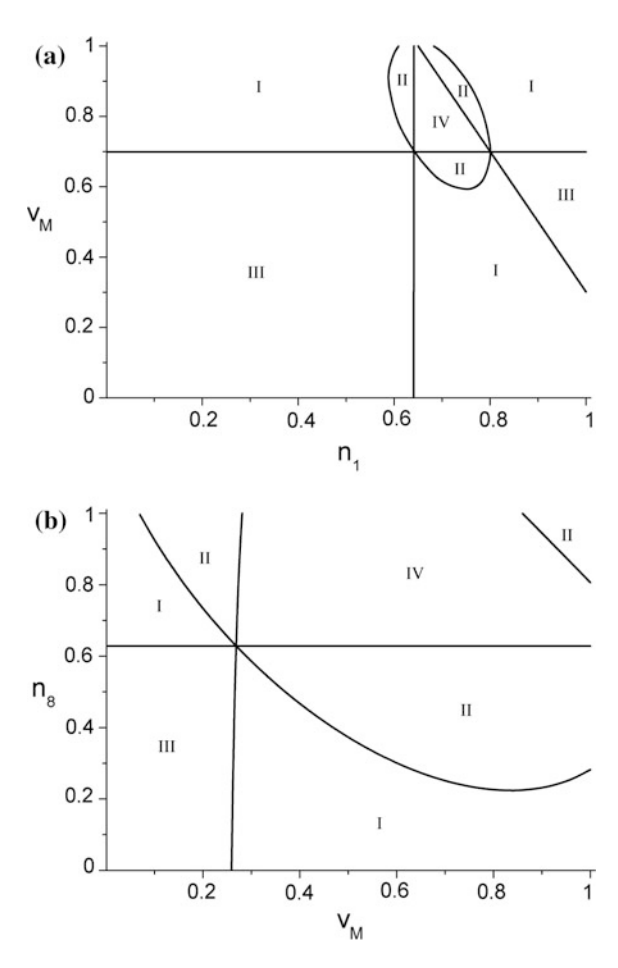


Fig. 3.4 Domain state–interface diagrams calculated for PMN–0.30PT SCs cooled in the electric field $E \parallel [001]$ (E = 0.1 MV/m): (a) the tetragonal– M_C phase transition, domain types 1–2 and 4–7 (see Fig. 3.2) and (b) the M_C – M_A phase transition, domain types 4–7 and 8–9 (see Fig. 3.2). In the M_C phase $f_M = 0.5$. Conditions (1.14), (1.15), (1.16) and (1.14) are valid in regions I, II, III and IV, respectively (reprinted from paper by Topolov [17], with permission from Pleiades Publishing)

Fig. 3.4a indicates that the formation of ZNSPs at the M_C – M_A phase transition is characterized by specific features. If $v_M = 0.700$ (see the line between regions I and III in Fig. 3.4a) and the DS of the M_C phase remains unchanged up to the M_C – M_A phase transition, the interphase boundaries separating these phases are conical in shape (see regions I and II in Fig. 3.4b). Only considerable changes in the v_M value would promote the formation of ZNSPs at the M_C – M_A phase transition: as seen from Fig. 3.4b, the boundary between regions I and III corresponds to the volume fractions $0.25 < v_M < 0.30$, and these v_M values strongly differ from $v_M = 0.700$ in the diagram shown in Fig. 3.4a.

One of the boundaries between regions I and III undergoes a specific rearrangement: instead of the boundary at $n_1 = 0.641$ in Fig. 3.4a, we obtain the boundary at $n_8 = 0.628$ in Fig. 3.4b. This means that the volume fractions of domain types 1 and 8 (Fig. 3.2) with similar orientations of the unit-cell vectors become almost equal after the tetragonal– M_C and M_C – M_A phase transitions in the electric field $E \parallel [001]$. In this context, we mention an analogy with the constancy of the volume fractions of the non-180° domains in the tetragonal and M_A phases of PZT (see Table 2.2) over the wide temperature range at E = 0.

3.2.1.2 Phase Sequences and Diagrams at $x \leq 0.28$

The further analysis of heterophase states in the electric field $E \parallel [001]$ is carried out taking into account results [21] on PMN–xPT SCs with $x=0.28,\,0.27$ and 0.24. It is assumed that the FE phases at $E \parallel [001] \parallel OX_3$ are split into the non-180° domains as shown in Fig. 3.5a, b. Jumps in the unit-cell parameters [22] at the cubic–tetragonal phase transition in PMN–0.28PT SC ($T_C \approx 382 \text{ K}, E \parallel [001]$ and E=50 kV/m) promote the formation of ZNSPs along the interphase boundaries. The corresponding optimal volume fractions of the 90° domains in the tetragonal phase are n_T^{opt} and $1-n_T^{\text{opt}}$, where $n_T^{\text{opt}}=0.545$ at x=0.28 [21].

On electric-field cooling (E = 50 kV/m), the tetragonal phase in the (001) cut of PMN-0.28PT transforms to the M_A phase [22] over a temperature transition window of about 10 K. As a consequence of electric-field cooling in a range from 362 to 358 K, the unit-cell parameter a_T of the tetragonal phase exhibits a jump in value of $|a_T(358 \text{ K}) - a_T(362 \text{ K})|/a_T(362 \text{ K}) \approx 0.06\%$ [22], whereas $c_T(T)$ exhibited only a slight continuous decrease. However, under a lower field E = 25 kV/m, the electric-field-cooled sample of PMN-0.28PT does not exhibit any anomaly in a_T over the same vicinity of the tetragonal- M_A phase transition [12]. Changes in the unit-cell parameter a_T can influence the coexistence of the tetragonal and M_A phases due to lowering the elastic energy by achieving elastic compatibility. Accordingly, the difference in the unit-cell parameters for PMN-0.28PT SC cooled under different electric fields can affect the metastable tetragonal- M_A phase equilibrium. In work [21], two different scenarios of the phase coexistence and stress relief were discussed.

In the first scenario, conditions for stress relief were considered using the experimental unit-cell parameters [22] of the tetragonal (at temperature $T_{\rm I} = 358$ K) and M_A (at temperature $T_{\rm II} = 356$ K) phases. An analysis of invariants [see (1.13)]

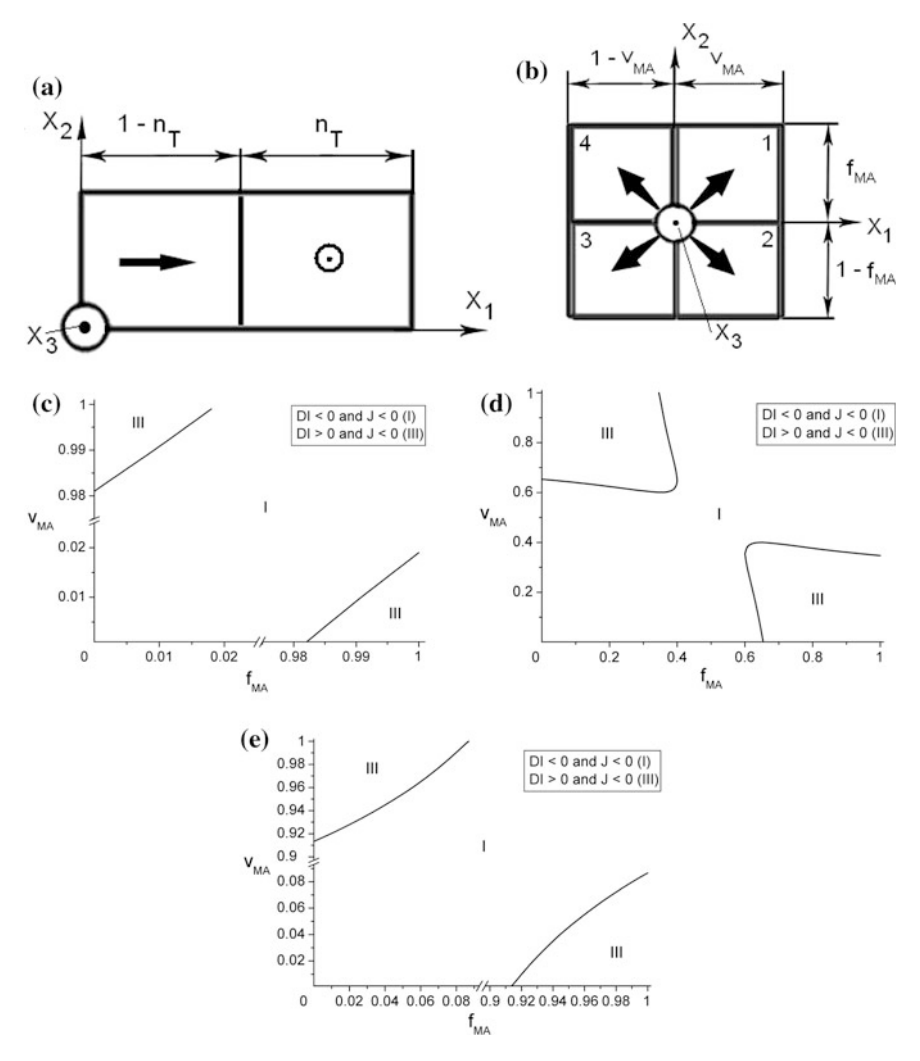


Fig. 3.5 Schematic arrangement of domains in the tetragonal (**a**) and M_A (**b**) phases and domain state—interface diagrams (**c**-**e**) calculated for the tetragonal— M_A phase transition in electric-field-cooled PMN–0.28PT SCs at $E \parallel [001]$ (E = 50 kV/m). The co-ordinate axes OX_j in schematics (**a**) and (**b**) are parallel to the perovskite unit-cell axes in the cubic phase. Graphs (**c**), (**d**) and (**e**) correspond to the volume fraction of the 90° domains $n_T = 0.65$, 0.80 and 0.95, respectively. Parameters v_{MA} and f_{MA} characterize the relative thickness of twins in the M_A phase (schematic b) on the OX_1 and OX_2 direction, respectively. Conditions (1.14) and (1.16) are satisfied in regions I and III, respectively (reprinted from paper by Topolov et al. [21], with permission from the American Institute of Physics)

for the interphase boundaries separating the phases split into the non-180° domains (see Fig. 3.5a, b) shows that conditions for complete stress relief in heterophase PMN–0.28PT SC are unfavourable. These interphase boundaries would be ZNSPs at fairly small n_T values ($0 \le n_T \le 0.260$), however, cooling under $E \parallel [001]$ promotes the volume fraction n_T to be larger than 1/2 (see Fig. 3.5a). For $n_T > 1/2$, there are no f_{MA} and v_{MA} values that obey conditions (1.18) for ZNSPs, and therefore, stress relief in such a heterophase state becomes problematic. Regions of the polydomain tetragonal phase in the temperature range of 362–358 K cannot be separated by ZNSPs, due to the aforementioned jump in the unit-cell parameter a_T that results in the inequality $|a_T(358 \text{ K}) - a_T(362 \text{ K})|/a_T(362 \text{ K})| > |c_T(358 \text{ K}) - c_T(362 \text{ K})|/c_T(362 \text{ K})|/21$].

In the second scenario of the phase coexistence in PMN-0.28PT SCs, we used the experimental unit-cell parameters at T = 362 and 356 K. These parameters are accurate to within 2% of measured ones [12] for PMN-0.28PT SCs at the tetragonal- M_A phase transition under E = 25 kV/m and promote favourable conditions for the formation of ZNSPs. According to results from work [21], the tetragonal- M_A interphase boundaries oriented along the ZNSPs would appear for $0.648 \le n_T$ ≤ 0.991 , with $0.103 \leq n_T - n_T^{\text{opt}} \leq 0.446$. This implies that slight changes in the DS (Fig. 3.5a) caused by 90° domain-wall displacements under $E \parallel [001]$ would promote effective stress relief that allows for stable heterophase states. The diagrams for heterophase states in PMN-0.28PT SCs (Fig. 3.5c-e) follow the second scenario of changes in the unit-cell parameters and suggest that conditions (1.18) for ZNSPs hold at the boundaries between regions I and III. The corresponding non-180° DSs of the tetragonal and M_A phases can coexist over wide ranges of n_T , f_{MA} , and v_{MA} . At $n_T \to 1$, a considerable shift of the boundaries between regions I and III (cf. Fig. 3.5d, e) favours the stability of an almost single-domain M_A state $(f_{MA} \rightarrow 1 \text{ or } v_{MA} \rightarrow 1).$

Certain tendencies towards stress relief are also revealed [21] for the (001) cut of PMN–0.27PT SC cooled in the electric field $E \parallel$ [001]. The optimal volume fractions of the 90° domains (Fig. 3.5a) at the cubic–tetragonal phase transition are $n_T^{\rm opt}$ and $1-n_T^{\rm opt}$ ($n_T^{\rm opt}=0.675$ according to data [21]). The domain state–interface diagrams for the tetragonal–M_A phase transition in PMN–0.27PT SCs and related heterophase domain states are similar to those shown in Fig. 3.5c–e. The interphase boundaries obey conditions (1.18) for ZNSPs in the wide volume-fraction range (0 $\leq n_T \leq$ 0.930) [21], therefore, no additional 90° domain-wall displacements are required. The similarity between the diagrams for PMN–0.28PT (Fig. 3.5c–e) and PMN–0.27PT is accounted for by analogous interrelations between the unit-cell parameters of the tetragonal and M_A phases as follows:

$$b_{MA} - a_T < c_T - c_{MA} < a_{MA} - a_T. (3.3)$$

However, for PMN-0.28PT, the unit-cell behaviour from the first scenario does not obey condition (3.3), owing to a decrease in the difference $a_{MA} - a_T$ after taking into account the jump in a_T .

Contrary to PMN–0.28PT, the unit-cell behaviour of PMN–0.24PT in the vicinity of the cubic– M_A phase transition [22] does not allow for the formation of ZNSPs. For each pair of parameters (f_{MA} , v_{MA}) from ranges of $0 \le f_{MA} \le 1$ and $0 \le v_{MA} \le 1$, calculations [21] reveal that the interphase boundaries between the cubic and polydomain M_A phases are conical: all pairs (f_{MA} , v_{MA}) in the diagram are related to region III only. These features associated with the unit-cell behaviour [22] in PMN–0.24PT are not required to follow conditions (1.18) for ZNSPs. It is possible that the distorted cubic phase that exists over a narrow temperature range between the cubic and M_A phases (as shown in the x–T diagram [22]) could promote stress relief: either by changes in the balance of diagonal distortions or by forming a metastable three-phase equilibrium that involves the unstrained cubic, distorted cubic and M_A phases.

In addition, the shear angle ω_{MA} of the perovskite unit cell in the M_A phase was varied [21] over the range of 0.04° – 0.10° . Such a variation results in small changes (less than 3%) in the (f_{MA} , v_{MA}) values related to the ZNSP curves in the diagrams shown in Fig. 3.5c–e. This means that the shear distortions of the polydomain M_A phase do not give rise to a considerable stress field in a heterophase SC sample.

Thus, changes in the unit-cell parameters of the electric-field-cooled PMN–xPT SCs at $E \parallel [001]$ open up various stress-relief possibilities in heterophase states and enable us to conclude that the correlation between the unit-cell parameters in the neighbouring phases remains on electric-field-cooling (at moderate E values) and promotes effective lowering the elastic energy of heterophase SC samples.

3.2.2 Heterophase $(1 - x)Pb(Zn_{1/3}Nb_{2/3})O_3 - xPbTiO_3$

PZN–xPT SCs are interesting objects for the study of the intermediate phases and phase coexistence in compositions near the MPB under the external electric field. Durbin et al. [23] studied behaviour of rhombohedral PZN–0.08PT SCs poled in the electric field $E \parallel [001]$. Experimental results [23] show that the electric field induces a new heterogeneous state. This state is interpreted as a metastable monoclinic phase induced by the coexistence of the tetragonal and rhombohedral phases. The presence of the metastable orthorhombic phase was discussed in work [24] that comprises the electric-field-dependent polarization data on plate-like PZN–0.08PT SCs oriented along the (001), (110) and (111) perovskite unit-cell plane. The orthorhombic phase was also observed [25] in PZN–xPT SCs (x = 0.08–0.10) poled in the electric field $E \parallel [001]$.

The field-induced phase states in rhombohedral PZN–xPT SCs at $E \parallel [001]$ were studied and interpreted [26] within the framework of the polarization–rotation concepts [13, 14]. Moreover, behaviour of the unit-cell parameters on dependence of E can account for the ultrahigh piezoelectric strains in PZN–xPT SCs. We mention that the problem of the ultrahigh piezoelectric strains (over 1%) in rhombohedral PZN–xPT SCs (x < 0.09) with engineered DSs was earlier discussed in paper [27] published before the discovery of the intermediate FE phases.

The longitudinal strain behaviour at $E \parallel [001]$ is associated [27] with the electric-field-induced rhombohedral-tetragonal phase transition that is accompanied by the polarization-vector inclination in the rhombohedral phase towards [001].

According to experimental data on PZN–0.045PT SCs [26], the polarization vector rotates from the [111] perovskite-cell direction (rhombohedral phase) to [001] (tetragonal phase) via the intermediate M_A phase, and this rotation is caused by the electric field $E \parallel$ [001]. Contrary to PZN–0.045PT, the polarization-vector rotation in PZN–0.08PT SC leads to the phase sequence [26] rhombohedral– M_A – M_C –tetragonal, and this distinction is concerned with a closeness of the composition with x=0.08 to the MPB. As seen from experimental results [26], the M_C and tetragonal phase coexist in PZN–0.08PT SCs under the electric field in the range 0.7 MV/m < E < 2 MV/m.

Model concepts [28] on the rhombohedral–tetragonal interphase boundary in domain-engineered PZN–xPT SCs near the MPB were developed to predict a contribution Δd_{33} from the interphase-boundary displacement into the longitudinal piezoelectric coefficient $d_{33}=d_{33}(E)$. Topolov and Turik [28] showed that the $\Delta d_{33}/d_{33}$ ratio depends on E and can vary in a range 0.5–0.9. The very large d_{33} values in domain-engineered PZN–0.08PT SC are explained by the considerable contribution $\Delta d_{33}/d_{33}\approx 0.8$ –0.9 [28] at the stage when the non-180° domains in the rhombohedral phase are intensively replaced by the single-domain tetragonal phase [27] induced in the field $E \parallel [001]$. It should be added that the model concepts [28] were applied [29] to describe the electric-field-induced rhombohedral– M_C phase transition in heavily twinned PZN–xPT SCs (x=0.08–0.09) and to predict the corresponding contribution Δd_{33} caused by the interphase-boundary displacement in the field $E \parallel [001]$. Evaluations [29] show that the $\Delta d_{33}/d_{33}$ ratio at the coexistence of the rhombohedral and M_C phases considerably depends on E and takes values from about 0.5 to 0.9.

Below, we consider examples of the phase coexistence and stress relief in PZN-xPT SCs under the electric field $E \parallel [001]$.

3.2.2.1 Elastic Matching of Phases at x = 0.08-0.09

To analyse the phase coexistence in PZN–xPT SCs near the MPB, we assume that a stress-free sample is split into the non-180° domains. Possible orientations of these domains are shown in Fig. 2.5 (rhombohedral phase, E = 0), Fig. 2.7 (rhombohedral phase, E > 0) and Fig. 3.2 (tetragonal phase, domains 1–2 and M_C phase, domains 4–7). Volume fractions of the domains in the rhombohedral phase are written in terms of the volume-fraction parameters x_R and y_R (see Sect. 2.2.1). Domains 1 and 2 of the tetragonal phase are characterized by the volume fractions n_T and 1 – n_T , respectively. Domains 4–7 of the M_C phase are characterized by the volume fractions defined in (3.2).

Interesting examples of elastic matching of the morphotropic phases along the ZNSPs are given in Table 3.1. Calculations of the optimal volume fractions of the domains were carried out [30] by using the room-temperature unit-cell parameters

Coexisting phases	x	E (MV/m)	Optimal volume fractions that correspond to elastic matching along ZNSPs
Rhombohedral and tetragonal	0.09	0	$n_{T,\text{opt}} = 0.620 \text{ or } n_{T,\text{opt}}' = 0.380^{\text{a}}$
Rhombohedral and $M_{\rm C}$	0.08	0	$v_{M,\text{opt}} = 0.775 \text{ or } v_{M,\text{opt}}' = 0.225^{\text{b}}$
		0.5	$v_{M,\text{opt}} = 0.801 \text{ or } v_{M,\text{opt}}' = 0.199$
		1.0	$v_{M,\text{opt}} = 0.873 \text{ or } v_{M,\text{opt}}' = 0.127$
		1.5	$v_{M,\text{opt}} = 0.980 \text{ or } v_{M,\text{opt}}' = 0.020$
		2.0	$ v_{M,\text{opt}} > 1$ or $v_{M,\text{opt}}' < 0$, i.e., no ZNSPs are possible
M _C and tetragonal	0.08-		$M_C \rightarrow tetragonal^c$
		0	$n_{T,\text{opt}} = 0.438 \text{ or } n_{T,\text{opt}}' = 0.562$
		0.5	$n_{T,\text{opt}} = 0.461 \text{ or } n_{T,\text{opt}}' = 0.539$
		1.0	$n_{T,\text{opt}} = 0.519 \text{ or } n_{T,\text{opt}}' = 0.481$
		1.5	$n_{T,\text{opt}} = 0.588 \text{ or } n_{T,\text{opt}}' = 0.412$
		2.0	$n_{T,\text{opt}} = 0.762 \text{ or } n_{T,\text{opt}}' = 0.238$
		3.0–3.5	$n_{T,\text{opt}} \approx 1 \text{ or } n_{T,\text{opt}}' \approx 0$
			$Tetragonal \rightarrow M_C^d$
		2.0	$v_{M,\text{opt}} = 0.429 \text{ or } v_{M,\text{opt}}' = 0.571$
		1.5	$v_{M,\text{opt}} = 0.274 \text{ or } v_{M,\text{opt}}' = 0.726$
		1.0	$v_{M,\text{opt}} = 0.245 \text{ or } v_{M,\text{opt}}' = 0.755$
		0.5	$v_{M,\text{opt}} = 0.224 \text{ or } v_{M,\text{opt}}' = 0.776$
		0	$v_{M,\text{opt}} = 0.217 \text{ or } v_{M,\text{opt}}' = 0.783$

Table 3.1 Elastic matching of FE phases in PZN–xPT SCs under the electric field $E \parallel [001]$ (reprinted from paper by Topolov [30], with permission from the American Physical Society)

of PZN–xPT from papers by Noheda et al. [14] (rhombohedral and monoclinic phases, x = 0.08) and by Kuwata et al. [31] (tetragonal phase, $x \approx 0.09$). Estimations of the unit-cell parameters in the tetragonal phase were made [30] by using the experimental electric-field dependences [14] of the unit-cell parameters $a_M(E)$, $b_M(E)$ and $c_M(E)$ in the M_C phase. An extrapolation of the $a_M(E)$, $b_M(E)$ and $c_M(E)$ curves to values obeying the condition $a_M(E') = b_M(E') \neq c_M(E')$ corresponds to the electric-field-induced phase transition to the tetragonal phase.

The calculated field dependences of the optimal domain volume fractions (Table 3.1) are characterized by slight sensitivity to changes in the parameters x_R and y_R (polydomain rhombohedral phase, see Fig. 2.5) and f_M [polydomain M_C phase, see Fig. 3.2 and (3.2)]. Any variations of these parameters over a range [0, 1] lead to negligible (less than 1%) changes in the optimal volume fractions listed in Table 3.1. This constancy is caused by a weak influence of the shear unit-cell

^aResults of calculations for $x_R = y_R = 0$ or $x_R = y_R = 1$ before the discovery of the electric-field-induced M_C phase, see also Table 2.3

^bResults of calculations for $x_R = y_R = 1/2$ and $f_M = 1/2$

^cResults of calculations for $v_M = 1$ and $f_M = 1/2$

^dResults of calculations for $n_T = 1$ and $f_M = 1/2$

distortions of several domain types on elastic matching of the polydomain phases in PZN–xPT SCs [30].

Table 3.1 contains two sets of values of the optimal volume fractions that range from 0 to 1. These values were found without taking into account the energy of the electrostatic interaction 'FE domain—field'. However, this interaction becomes very important in the tetragonal phase split into 90° domains with the spontaneous polarization vectors $P_{s1} \parallel OX_3$ (domain 1) and $P_{s2} \parallel OX_1$ (domain 2). This implies that increasing E at the electric-field-induced M_C -tetragonal phase transition gives rise to a wide propagation of the domains with $P_{s1} \parallel E \parallel OX_3$, and such behaviour corresponds to the calculated $n_{T,\text{opt}}(E)$ dependence (Table 3.1) only. Contrary to $n_{T,\text{opt}}(E)$, the $n_{T,\text{opt}}'(E)$ dependence in the section ' $M_C \rightarrow$ tetragonal' of Table 3.1 is omitted because of $n_{T,\text{opt}}' \rightarrow 0$ with increasing E. The orientations of the interphase boundaries, that separate the polydomain phases with the optimal volume fractions from Table 3.1 and obey conditions (1.18) for ZNSPs, are close to $\{0kl\}$ in the perovskite unit cell.

The results on the rhombohedral– M_C phase coexistence (Table 3.1) shed light on peculiarities of behaviour of PZN–xPT SCs in the vicinity of $E=E_0=1.5$ MV/m. As shown in Table 3.1, values $v_{M,\mathrm{opt}}\approx 1$ and $v_{M,\mathrm{opt}}'\approx 0$ correspond to a simplification of the DS in the M_C phase. Apparently, at $E\geq 1.5$ MV/m, SC samples contain only two domain types in the M_C phase, and no displacements of (010) domain walls are expected [30]. Due to this simplification of the DS in the M_C phase, the unit-cell vectors of domains b_{Mk} are arranged to be parallel to either the OX_1 or OX_2 axis all over the SC sample. The above-mentioned domain-wall displacements at $E < E_0$ are accompanied by strains ξ_{pq}^i induced because $a_M \neq b_M$. Estimations based on formulae from work [32] result in induced strains at absolute values $\left|\xi_{pq}^i\right| \leq (a_M - b_M)/b_M$. Taking into account the experimental electric-field dependences [14] $a_M(E)$ and $b_M(E)$, we obtain $\left|\xi_{pq}^i(E_0)\right| \leq 0.6\%$. This value is comparable with the longitudinal piezoelectric strain $\xi_{33}\approx 0.5\%$ measured [33] on PZN–0.08PT SC samples.

Specific jumps [34] in the piezoelectric coefficient $d_{31}(E)$ and elastic compliance $s_{11}^E(E)$ at $E \approx E_0$ are also caused [30] by the simplification of the DS in the M_C phase. At the same time, no jump in the dielectric permittivity $\varepsilon_{33}^\sigma(E)$ takes place at $E \approx E_0$, and this constancy may be explained in terms of the unit-cell vectors of the M_C phase. The simplification of the DS does not affect the arrangement of the unit-cell vectors c_{Mk} (see domains 4–7 in Fig. 3.2) because $c_{Mk} \parallel E \parallel$ [001] in all the domain types. The spontaneous polarization vector P_{sk} of the domain of the kth type rotates [13] from the [101] to [001] direction of the perovskite unit cell, and the angle $(P_{sk}, ^k E)$ remains constant for all the domain types at E = const. As a consequence, dielectric response of each domain is equal along the OX_3 axis at $E \approx E_0$. It should be added that appreciable changes in the strain-field loop $\xi_{33}(E)$ [33] and the unit-cell parameter $c_M(E)$ [14] are also registered in a vicinity of E_0 . On increasing the field strength $(E \geq E_0)$, the $\xi_{33}(E)$ dependence is characterized by a considerable decrease in the slope and gives rise to a non-monotonic dependence of the piezoelectric coefficient $d_{33}(E)$ [35].

Finally, the optimal volume fractions of domains (Table 3.1) at small E values obey conditions [29]

$$n_{T,\text{opt}}(Rh-Tg) \approx \nu_{M,\text{opt}}(Rh-Mc) \cdot \nu'_{M,\text{opt}}(Tg-Mc)$$
 (3.4)

and

$$n'_{T.\text{opt}}(Rh-Tg) \approx v_{M,\text{opt}}(Rh-Mc) n_{T,\text{opt}}(Mc-Tg),$$
 (3.5)

where abbreviations Rh, Tg and Mc denote the rhombohedral, tetragonal and M_C phases, respectively. So, according to data from Table 3.1, the left and right parts of (3.4) at E=0 equal 0.620 and 0.775×0.783 (i.e. about 0.607), respectively. On increasing E, the right part of (3.5) would equal 0.622 (at E=0.5 MV/m), 0.659 (at E=1.0 MV/m), etc. As follows from Table 3.1, the left and right parts of (3.5) at E=0 equal 0.380 and 0.339, respectively. At E=0.5 MV/m and 1.0 MV/m, the right part of (3.5) equals 0.369 and 0.459, respectively. An interpretation of (3.4) and (3.5) is given in Appendix B by taking into account the mutual arrangement of the spontaneous polarization vectors of individual domains of the phases coexisting in PZN–xPT SCs under the electric field $E \parallel [001]$.

3.2.2.2 Diagrams at x = 0.045

In the present subsection we consider the phase coexistence of the tetragonal and M_A phases at the electric-field-induced phase transition. It is assumed that these phases are split into the non-180° domains shown schematically in Fig. 3.5a, b and $E \parallel [001] \parallel OX_3$. According to experimental data [26], the tetragonal-M_A phase transition in PZN-0.045PT SC occurs with increasing field near $E \approx 1.1$ MV/m at room temperature. It is reasonable to assume that the tetragonal phase being stable at higher fields is either a single-domain state or splits into the 90° domains with a significant prevalence for the domain type with the spontaneous polarization vectors $P_{T,1} ||E||$ [001] (Fig. 3.5a), i.e. at the volume fraction $n_T \to 1$. The diagrams (Fig. 3.6) calculated for this phase coexistence show, that at $n_T \to 1$, the ZNSPs would appear only in narrow ranges of parameters (f_{MA}, v_{MA}) . We remind that conditions (1.18) for ZNSPs are valid at the boundaries between regions I and III in the diagrams shown in Fig. 3.6. In the case of volume fractions $n_T < 0.9$, the M_A phase is split into the domains shown in Fig. 3.5b, and with increasing n_T , the distinct prevalence of one domain type over others is expected (cf. Fig. 3.6b, c) so that conditions $f_{MA} \to 0$ and $v_{MA} \to 1$, or $f_{MA} \to 1$ and $v_{MA} \to 0$ are valid. The possibility of the coexistence of the two single-domain phases at the induced phase transition is energetically close to the required conditions (1.18) for ZNSPs. Taking into account the domain orientations shown in Fig. 3.5a, b, one can show that the formation of the interphase boundaries at significant stress relief is caused by the following relations between the unit-cell parameters at the tetragonal-M_A phase transition in PZN-0.045PT SC [21]:

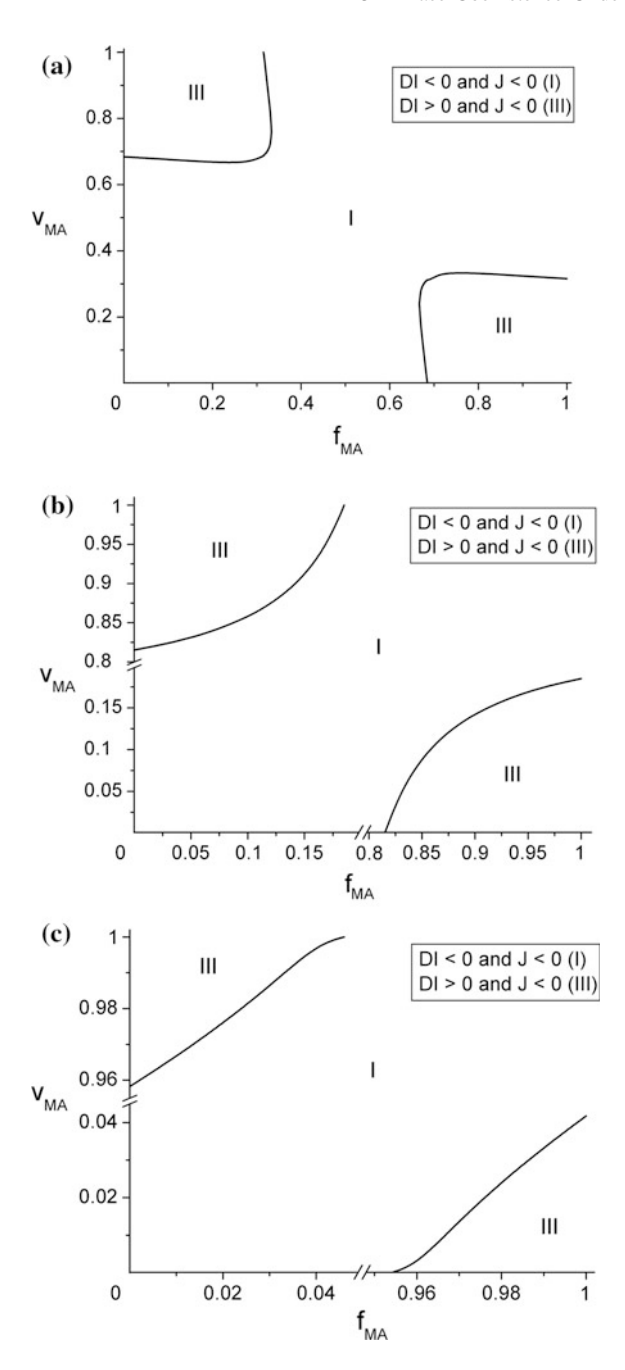


Fig. 3.6 Domain state–interface diagrams calculated for the electric-field-induced tetragonal– M_A phase transition in PZN–0.045PT SCs with $E \parallel [001]$. Graphs (a), (b) and (c) correspond to the volume fraction of the 90° domains $n_T = 0.90$, 0.95 and 0.99, respectively. Conditions (1.14) and (1.16) are valid in regions I and III, respectively (reprinted from paper by Topolov et al. [21], with permission from the American Institute of Physics)

$$a_T < a_{MA}, a_T = b_{MA} \text{ and } c_T > c_{MA}.$$
 (3.6)

Earlier we mentioned elastic matching of the untwined antiferroelectric $P222_1$ and Pba2 phases in PbHfO₃ SCs and elastic matching of the untwined FE P4mm and Cm phases in PZT (see Sect. 2.1.2)—in both materials conditions (1.18) for ZNSPs are valid at E=0. An examination of experimental data [36] shows that the unit-cell parameters of PZT with x=0.46 (i.e. a composition just at the MPB between the tetragonal and M_A phases) obey conditions (3.6). However, contrary to conditions (3.6), the perovskite unit-cell parameter b of PbHfO₃ undergoes a jump at the first-order phase transition $P222_1 \rightarrow Pba2$ [37].

3.3 Domain State–Interface Relationships at Electric Field $E \parallel [110]$

Experimental results on heterophase PMN–xPT and PZN–xPT SCs in the electric field $E \parallel [110]$ were published in a series of papers (see, e.g. [38–42]). Liu and Lynch studied [40] the polarization switching and phase transition in PZN–0.045PT SCs under the electric field $E \parallel [110]$. The electric-field-induced rhombohedral–orthorhombic phase transition is observed in PMN–0.30PT [38, 39] and PZN–0.045PT SCs at $E \parallel [110]$ [40]. The rotation of the spontaneous polarization vector at this phase transition is explained in terms of work [13].

Examples of DSs observed in the [110] poling direction of PZN-0.045PT SC are given in papers [41, 42]. It is shown that cracks and domain walls may introduce each other in an interactive way [41]. The phase sequences studied on cooling the SC samples under the electric field $E \parallel [110]$ are represented as follows: cubic \rightarrow tetragonal \rightarrow orthorhombic \rightarrow M_B (PMN-0.30PT [11] and PZN-0.045PT [43]) and cubic → tetragonal → orthorhombic (PMN-0.35PT SC) [16]. Yao et al. underline that experimental results [43] on the phase sequence in PZN-0.045PT SCs differ from the phase sequence observed by Renault et al. [44]. As noted by Yao et al., PZN-0.045PT SC has an intermediate state that is different from the ground state observed on cooling at E = 0. This intermediate state is concerned with the constraint imposed by the field $E \parallel [110] [43]$. Yao et al. revealed the M_B-orthorhombic phase coexistence so that a certain volume fraction of the orthorhombic phase transforms to the M_B phase immediately. After the field removal of E, some volume fraction persists as orthorhombic. Based on these and other experimental results, the authors of work [43] concluded that the M_B phase is the ground-state condition for the studied (110) SCs.

Below we consider examples of the domain state-interface diagrams related to the phase transitions at $E \parallel [110]$. Orientations of the non-180° domains are introduced with respect to the perovskite unit-cell axes. In the tetragonal phase, there are two domain types shown in Fig. 3.5a. The orthorhombic phase is split into the domains with the spontaneous polarization vectors $P_O^{(1)} \parallel [110]$ (volume fraction n_O)

and $P_O^{(2)} \parallel [0\overline{1}1]$ (volume fraction $1-n_O$). Domains in the M_B phase are characterized by the spontaneous polarization vectors $P_{MB}^{(1)} \parallel [11p]$ (volume fraction n_{MB}) and $P_{MB}^{(2)} \parallel [1\overline{1}\overline{p}]$ (volume fraction $1-n_{MB}$). Distortion matrices of the aforementioned polydomain phases can be written by analogy with (2.4) and (2.8). The experimental unit-cell parameters of PMN–0.30PT and PMN–0.35PT SCs [11, 16] are used to build the domain state–interface diagrams for the phase coexistence at $E \parallel [110]$.

The tetragonal—orthorhombic phase transition in PMN-0.30PT SC cooled at $E \parallel [110]$ can be accompanied by the formation of the interphase boundary that obeys conditions (1.18) for ZNSPs at the volume fraction $n_O = 0.587$, 0.709 or 1 (Fig. 3.7a). We note that the value $n_O = 1$ is related to the single-domain orthorhombic phase with the spontaneous polarization $P_O^{(1)} \parallel E \parallel$ [110]. At the tetragonal—orthorhombic phase transition in PMN-0.35PT SC, the formation of the

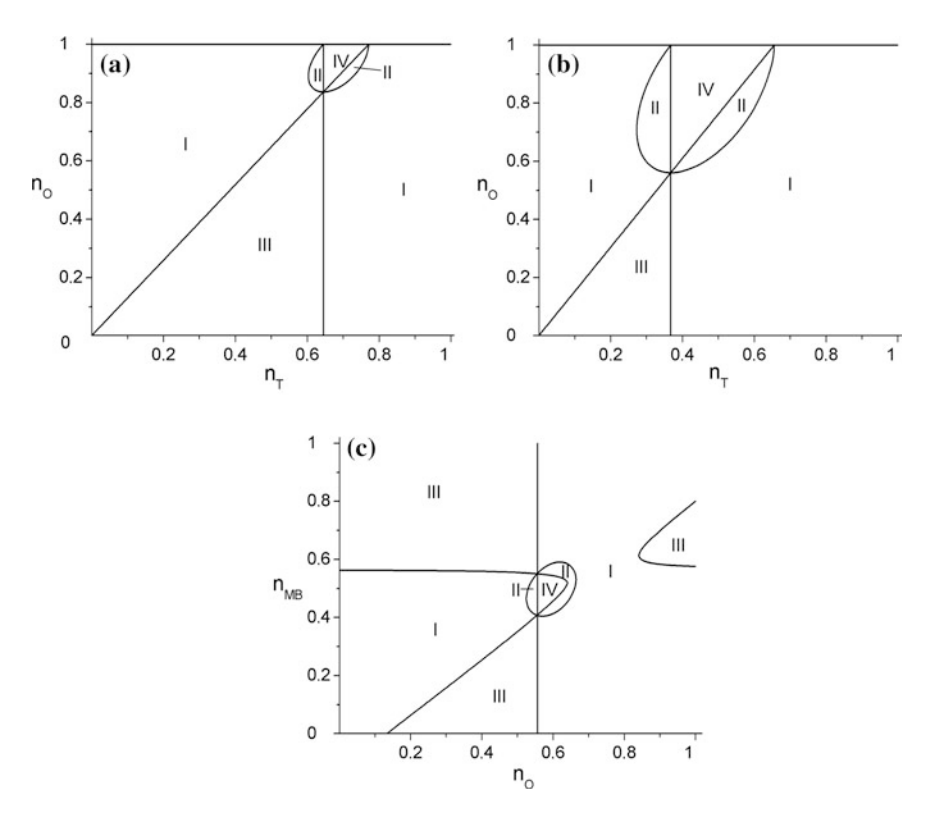


Fig. 3.7 Domain state–interface diagrams of interfaces calculated for the electric-field-induced phase transitions in PMN–xPT SCs with $E \parallel [110]$. Graphs (a) and (b) correspond to the tetragonal–orthorhombic phase transition at x = 0.30 and 0.35, respectively. Graph (c) corresponds to the orthorhombic–M_B phase transition at x = 0.30. Conditions (1.14), (1.15), (1.16) and (1.17) are satisfied in regions I, II, III and IV, respectively (reprinted from paper by Topolov [45], with permission from the American Institute of Physics)

ZNSPs is possible at small changes in the volume fraction n_T only. As seen from Fig. 3.7b, the values $n_T = n_T^{\text{opt}}$ almost correspond to joints of regions I, II and III, or I, II and IV. In the diagrams (Fig. 3.7a, b), there are the long lines that separate regions I and III and, therefore, obey conditions (1.18). It seems to be probable that a minor change in the DS in the tetragonal phase would promote the appearance of the single-domain orthorhombic phase with $P_O^{(1)} \parallel E$. Indeed, the single-domain orthorhombic phase is observed in PMN–xPT SCs (x = 0.30 [11], 0.33 [9] and 0.35 [16]) cooled in the field $E \parallel [110]$.

The diagram calculated for the orthorhombic– M_B phase transition (Fig. 3.7c) allows two variants of ZNSPs. If the volume fraction $n_O=1$ (as found for the tetragonal–orthorhombic phase transition, see Fig. 3.7a), then the interphase boundary between the orthorhombic and M_B phases becomes the ZNSP at the volume fraction $n_B=0.576$ or 0.801 (see Fig. 3.7c, right side). At $n_O=0.587$ or 0.709 (that is concerned with the ZNSP at the tetragonal–orthorhombic phase transition in PMN–0.30PT SC), the interphase boundary between the orthorhombic and M_B phases does not obey conditions (1.18) for ZNSPs, however, the ZNSPs take place at $n_O<0.55$ (see lines between regions I and III in Fig. 3.7c, middle part). This means that the coexistence of the orthorhombic and M_B phases at complete stress relief needs an additional minor DS rearrangement that may be stimulated by the electric field applied to the SC sample.

3.4 Domain State–Interface Relationships at Electric Field $E \parallel [111]$

There is a restricted group of papers that report results on behaviour of PMN–xPT, PZN-xPT and other FE solid solutions under the electric field $E \parallel [111]$. Among the publications on this subject we mention papers [46–49]. Phase transitions were experimentally studied [47] in electric-field-cooled PMN-0.30PT SCs at E | [111]. The corresponding phase sequence observed at E = 0.2 MV/m is represented as follows: cubic \rightarrow tetragonal \rightarrow orthorhombic \rightarrow M_B. The unit-cell parameters of electric-field-cooled PMN-0.30PT SCs were studied in the wide temperature range [47]. An experimental study of the DS and phase transitions in PZN-0.08PT SCs and strain-field loops measured on these SC samples at $E \parallel [111]$ was carried out in work [48]. The most probable version of the phase sequence in PZN-0.08PT SCs is orthorhombic \rightarrow M_B \rightarrow rhombohedral with the rotation of the polarization vector in the $(10\overline{1})$ plane of the perovskite unit cell [48], and this sequence is consistent with the well-known concepts [13]. The rhombohedral phase arising in PZN-0.08PT SCs under the electric field is characterized as quasi-monodomain [48]. The DS was also studied [49] in PZN-0.05PT SCs under the electric field $E \parallel$ [111]. According to Lee et al., the field applied along this perovskite unit-cell direction enhances the rhombohedral distortion of the crystal structure and stabilizes domain boundaries oriented normal to the [110] direction. Hereby the band-shaped domain pattern in the rhombohedral phase is present after the [111]-field removal [49].

In this section, we analyse heterophase states and DSs in PMN–0.30PT SCs cooled under $E \parallel [111]$. Domain orientations in the studied FE phases (Fig. 3.8a) suggest that the electric field $E \parallel [111]$ would promote the formation of three non-180° domain types having equivalent orientations relative to the E vector in the tetragonal, orthorhombic or M_B phase. Angles between the spontaneous polarization and electric-field vectors are determined [46] for the jth domain type in the tetragonal, orthorhombic and M_B phases as

$$\psi_T = (\mathbf{P_{Tj}}, ^{\wedge} \mathbf{E}) = \arccos(1/\sqrt{3}), \ \psi_O = (\mathbf{P_{Oj}}, ^{\wedge} \mathbf{E}) = \arccos(\sqrt{2/3}) \text{ and }$$

$$\psi_{MB} = (\mathbf{P_{MBj}}, ^{\wedge} \mathbf{E}) = \arccos\left[(p+2)/\sqrt{3(p^2+2)}\right], \tag{3.7}$$

respectively, where j=1, 2 and 3, and 0 . The angles from (3.7) do not depend on the orientation of domains in their respective phase, and such an independence violates at other orientations of the <math>E vector, e.g. at $E \parallel [001]$ or $E \parallel [110]$. It is assumed that the perovskite unit-cell vectors (a_j, b_j, c_j) of the individual domain types shown in Fig. 3.8, a are arranged approximately along the following directions: ([100], [010], [010]) for j=1, ([001], [100], [010]) for j=2, and ([010], [001], [100]) for j=3.

Distortion matrices of the tetragonal, orthorhombic and M_B phases are given by

$$\begin{aligned} \left| \left| N_{kl}^{(T)} \right| \right| &= m_T \begin{pmatrix} \varepsilon_a & 0 & 0 \\ 0 & \varepsilon_a & 0 \\ 0 & 0 & \varepsilon_c \end{pmatrix} + n_T \begin{pmatrix} 1 & 0 & 0 \\ 0 & \cos \varphi_T & \sin \varphi_T \\ 0 & -\sin \varphi_T & \cos \varphi_T \end{pmatrix} \begin{pmatrix} \varepsilon_a & 0 & 0 \\ 0 & \varepsilon_a & 0 \\ 0 & 0 & \varepsilon_c \end{pmatrix} \\ &+ (1 - m_T - n_T) \begin{pmatrix} \cos \varphi_T & 0 & -\sin \varphi_T \\ 0 & 1 & 0 \\ \sin \varphi_T & 0 & \cos \varphi_T \end{pmatrix} \begin{pmatrix} \varepsilon_c & 0 & 0 \\ 0 & \varepsilon_a & 0 \\ 0 & 0 & \varepsilon_a \end{pmatrix}, \end{aligned}$$
(3.8)

$$\begin{split} \left| \left| N_{kl}^{(O)} \right| \right| &= m_O \begin{pmatrix} \eta_a & 0 & 0 \\ 0 & \eta_a & 0 \\ 0 & 0 & \eta_c \end{pmatrix} + n_O \begin{pmatrix} 1 & 0 & 0 \\ 0 & \cos \varphi_O & \sin \varphi_O \\ 0 & -\sin \varphi_O & \cos \varphi_O \end{pmatrix} \begin{pmatrix} \eta_a & 0 & 0 \\ 0 & \eta_c & 0 \\ 0 & 0 & \eta_a \end{pmatrix} \\ &+ (1 - m_O - n_O) \begin{pmatrix} \cos \varphi_O & 0 & -\sin \varphi_O \\ 0 & 1 & 0 \\ \sin \varphi_O & 0 & \cos \varphi_O \end{pmatrix} \begin{pmatrix} \eta_c & 0 & 0 \\ 0 & \eta_a & 0 \\ 0 & 0 & \eta_a \end{pmatrix} \end{split}$$

$$(3.9)$$

and

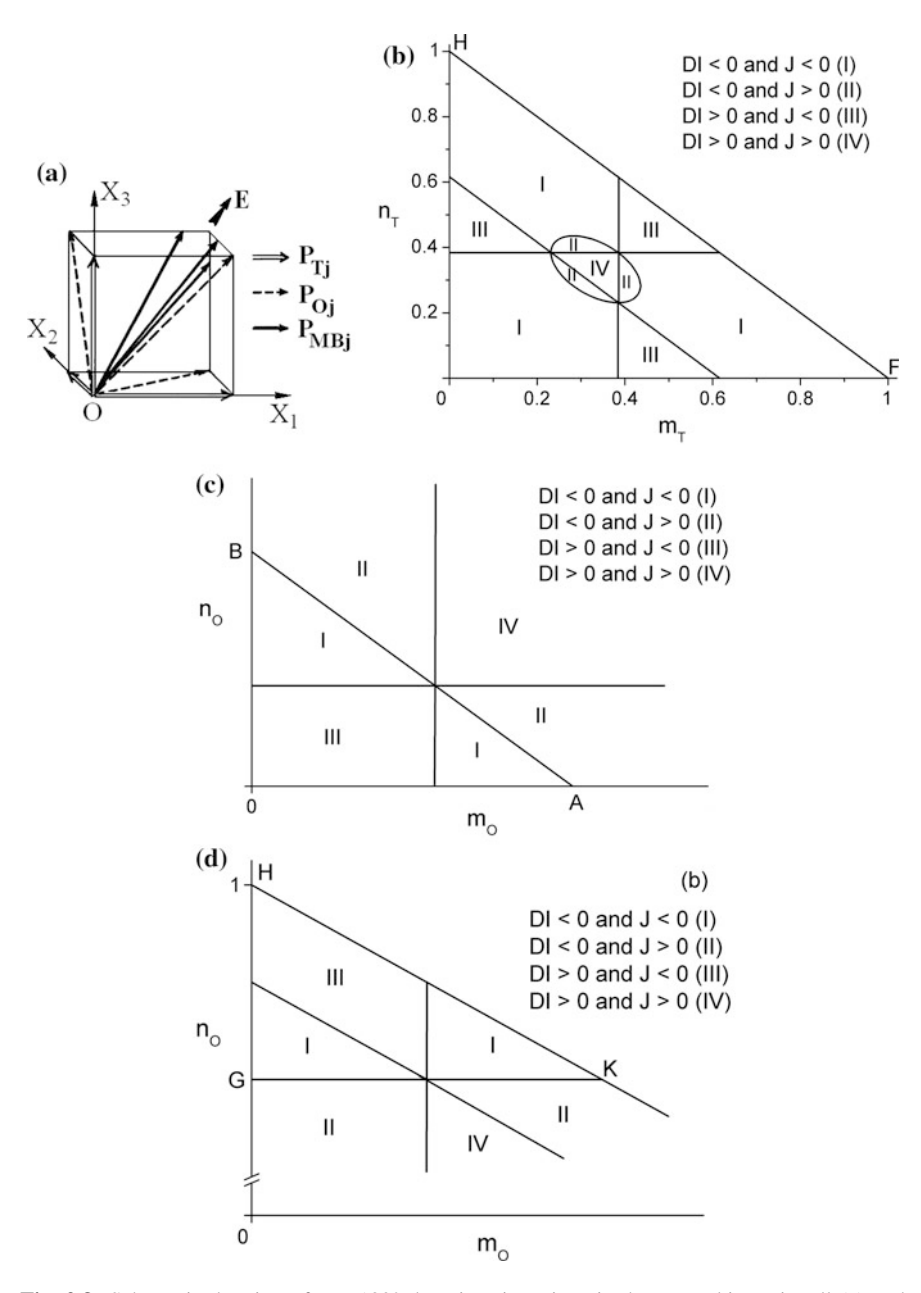


Fig. 3.8 Schematic drawing of non-180° domain orientations in the perovskite unit cell (a) and domain state—interface diagrams calculated for the cubic—tetragonal (b), tetragonal—orthorhombic (c-e) and orthorhombic— M_B (f-h) phase transitions in field-cooled PMN-0.30PT SCs with the electric field $E \parallel$ [111]. Spontaneous polarization vectors P_{Tj} , P_{Oj} , and P_{MBj} (j=1,2 and 3) are related to the domains in the tetragonal, orthorhombic and M_B phases, respectively. Co-ordinate axes OX_k are parallel to the perovskite unit-cell axes in the cubic phase as follows: $OX_1 \parallel$ [100], $OX_2 \parallel$ [010] and $OX_3 \parallel$ [001]. Conditions (1.14), (1.15), (1.16) and (1.17) are valid in regions I, II, III and IV, respectively (reprinted from paper by Topolov et al. [46], with permission from IOP Publishing)

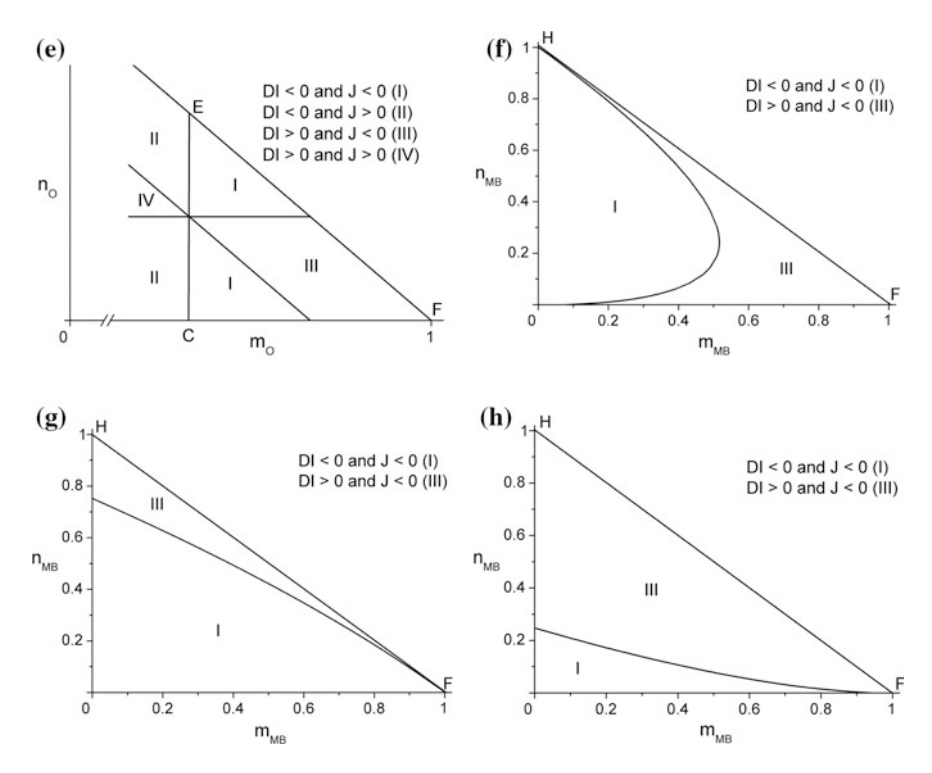


Fig. 3.8 (continued)

$$\begin{aligned} \left| \left| N_{kl}^{(MB)} \right| \right| &= m_{MB} \begin{pmatrix} \lambda_{a} & \lambda & 0 \\ \lambda & \lambda_{a} & 0 \\ 0 & 0 & \lambda_{a} \end{pmatrix} + n_{MB} \begin{pmatrix} 1 & 0 & 0 \\ 0 & \cos \varphi_{MB} & \sin \varphi_{MB} \\ 0 & -\sin \varphi_{MB} & \cos \varphi_{MB} \end{pmatrix} \begin{pmatrix} \lambda_{a} & 0 & \lambda \\ 0 & \lambda_{c} & 0 \\ \lambda & 0 & \eta_{\lambda_{a}} \end{pmatrix} \\ &+ (1 - m_{MB} - n_{MB}) \begin{pmatrix} \cos \varphi_{MB} & 0 & -\sin \varphi_{MB} \\ 0 & 1 & 0 \\ \sin \varphi_{MB} & 0 & \cos \varphi_{MB} \end{pmatrix} \begin{pmatrix} \lambda_{c} & 0 & 0 \\ 0 & \lambda_{a} & \lambda \\ 0 & \lambda & \lambda_{a} \end{pmatrix}, \end{aligned}$$
(3.10)

respectively. In (3.8) m_T and n_T are the volume fractions of the first and second domain types, and ε_a and ε_c are the unit-cell distortions expressed in terms of the unit-cell parameters of the tetragonal phase. The angle $\varphi_T = \arccos[2\varepsilon_a\varepsilon_c/(\varepsilon_a^2 + \varepsilon_c^2)]$ from (3.8) is introduced to account for rotations of the crystallographic axes of the adjacent domains (see Sect. 2.1). The volume fractions m_T and n_T from (3.8) obey the inequality

$$0 < m_T + n_T < 1. (3.11)$$

The similar inequalities,

$$0 \le m_O + n_O \le 1 \tag{3.12}$$

and

$$0 \le m_{MB} + n_{MB} \le 1, \tag{3.13}$$

are introduced for the volume fractions of the domains in the orthorhombic and M_B phases, respectively. The rotation angles $\varphi_O = \arccos \left[2\eta_a \eta_c / (\eta_a^2 + \eta_c^2) \right]$ and $\varphi_{MB} = \arccos \left[2\lambda_a \lambda_c / (\lambda_a^2 + \lambda_c^2) \right]$ from (3.9) and (3.10), respectively, are defined by analogy with φ_T .

The domain state-interface diagrams (Fig. 3.8b-h) were built using the unit-cell parameters [47] of PMN-0.30PT SC cooled under the electric field $E \parallel$ [111]. Due to a lack of experimental values of the monoclinic angle (β_{MB}) or the shear angle ($\omega_{MB} = 90^{\circ} - \beta_{MB}$) as a function of temperature in the M_B phase, the values of ω_{MB} were taken from a range of 0.04°-0.10°. These values are consistent with the experimental data known [16] for monoclinic PMN-xPT SCs near the MPB at E=0. The validity of conditions (3.11)-(3.13) means that all the regions and boundaries in the diagrams are to be considered in the triangle *OHF* shown, for example in Fig. 3.8b, f-h.

The cubic–tetragonal interphase boundaries can be determined from the diagram in Fig. 3.8b. This diagram was calculated using the distortion matrix $||N_{kl}^{(T)}||$ from (3.8). Conditions (1.18) for ZNSPs are valid at the boundaries separating regions I and III (see Fig. 3.8b), and the corresponding optimal volume fractions of the 90° domains in the tetragonal phase are $m_T^{\text{opt}} = 0.384$ or 0.616, and $n_T^{\text{opt}} = 0.384$ or 0.616. These values are in full compliance with the predictions based on formulae [50] for any two types of the 90° domains (see Fig. 3.8a) in the tetragonal phase. The lines defined by conditions $m_T = m_T^{\text{opt}}$ and $0 \le n_T \le n_T^{\text{opt}}$, or $n_T = n_T^{\text{opt}}$ and $0 \le m_T \le n_T^{\text{opt}}$ (see Fig. 3.8b) reflect the important role of the two 90° domain types in stress relief. The third 90° domain type would slightly affect the balance of distortions in the polydomain tetragonal phase because of the presence of two independent linear unit-cell distortions in each domain type [see elements ε_a and ε_c in matrices from (3.8)].

Before the consideration of the tetragonal–orthorhombic phase coexistence, we assume that the volume fractions $m_T = m_T^{\rm opt}$ and $n_T = n_T^{\rm opt}$ of the domains in the tetragonal phase occur at the boundaries between regions I and III in Fig. 3.8b, and that these volume fractions remain unchanged prior to the tetragonal–orthorhombic transition on cooling the SC sample. Distortion matrices of the coexisting phases are taken from (3.8) and (3.9). The diagrams represented in the (m_O, n_O) co-ordinate plane contains a few short lines that separate regions I and III (Fig. 3.8c–e) and obey conditions (1.18) for ZNSPs. Independent of the values for $(m_T^{\rm opt}, n_T^{\rm opt})$ pairs at the boundary between regions I and III in Fig. 3.8b, conditions

(1.18) are valid at the coexistence of the polydomain tetragonal and near single-domain orthorhombic phases. As follows from paper [46], inequalities |OA| < 0.01, |OB| < 0.01, |CE| < 0.01, |CF| < 0.01, |GH| < 0.10, and |GK| < 0.01 (see Fig. 3.8, c–e) hold for all $(m_T^{\rm opt}, n_T^{\rm opt})$ points lying on boundaries between regions I and III in Fig. 3.8b. This means that the formation of the single-domain orthorhombic phase would result only in a slightly stressed state. Such favourable conditions for stress relief in heterophase PMN–0.30PT SCs and the 'fine' structure of the diagrams in Fig. 3.8c–e for the near single-domain orthorhombic phase states stems from the equality of the perovskite unit-cell parameters $a_T = c_O$ [47] at the phase transition. We also note that the like phase coexistence under the electric field was not studied in SCs of related FE solid solutions.

Further cooling the PMN-0.30PT SC sample under the electric field $E \parallel$ [111] results in the orthorhombic-M_B phase transition. Taking into account data in Fig. 3.8c-e, we assume that the orthorhombic phase becomes single-domain and is characterized by one of the following distortion matrices:

$$\begin{vmatrix} \left| N_{kl}^{(O,I)} \right| \right| = \begin{pmatrix} \eta_a & 0 & 0 \\ 0 & \eta_a & 0 \\ 0 & 0 & \eta_c \end{pmatrix}, \left| \left| N_{kl}^{(O,II)} \right| \right| = \begin{pmatrix} \eta_a & 0 & 0 \\ 0 & \eta_c & 0 \\ 0 & 0 & \eta_c \end{pmatrix} \text{ or } \left| \left| N_{kl}^{(O,III)} \right| \right| \\
= \begin{pmatrix} \eta_c & 0 & 0 \\ 0 & \eta_a & 0 \\ 0 & 0 & \eta_a \end{pmatrix}.$$
(3.14)

While the orientations of the spontaneous polarization vectors P_{Oj} of domains provide ψ_Q = const for j = 1, 2 and 3 [see (3.7)], one can consider three possible variants of elastic matching of the single-domain orthorhombic and polydomain M_B phases. The corresponding diagrams are shown in Fig. 3.8f-h. The single-domain orthorhombic phase is described by one of the distortion matrices from (3.14): $||N_{kl}^{(O,I)}||$ (Fig. 3.8f), $||N_{kl}^{(O,II)}||$ (Fig. 3.8g) or $||N_{kl}^{(O,III)}||$ (Fig. 3.8f). The diagrams in Fig. 3.8f–h are simplified, relative to those shown in Fig. 3.8c-e, because of equalities $a_O = b_O = a_{MB} = b_{MB}$ [47]. Irrespective of the orientation of the P_{Oi} vectors [see Fig. 3.8a and (3.14)], the M_B phase promotes the formation of ZNSPs over the almost entire range of the volume fractions n_{MB} (Fig. 3.8f) or m_{MB} (Fig. 3.8g, h). Of particular interest are the points ($m_{MB} = 0$, $n_{MB} = 1$) in Fig. 3.8f and ($m_{MB} = 1$, $n_{MB} = 0$) in Fig. 3.8g. These points correspond to the single-domain M_B phase coexisting with the single-domain orthorhombic phase on [111] field cooling. Thus, the rotation of the spontaneous polarization vector towards $E \parallel [111]$ (Fig. 3.8a) leads to the distinct simplification of the DSs in the low-temperature phases of PMN-0.30PT SCs. In other words, despite the equal angles between the spontaneous polarization and electric-field vectors [see (3.7)] in each of the FE phases of PMN–0.30PT SC, changes in its unit-cell parameters promote the simplification of the DSs in the coexisting orthorhombic and M_B phases. This simplification takes place as long as the angles ψ_O and ψ_{MB} from (3.7) are considerably less than ψ_T . These and other results [46] undoubtedly suggest that there is an essential correlation between the domain states and unit-cell behaviour in heterophase PMN-0.30PT SCs under the electric field $E \parallel [111].$

3.5 Role of Intermediate Phases in Heterophase States

In Chap. 2 and this chapter we considered various two-phase states and stress-relief ways in FE solid solutions near the MPB. These states are observed at the first-order structural (polymorphic, morphotropic and electric-field-induced) phase transitions, including those on cooling in the electric field. In conclusion, we focus attention on the following items.

- (i) Possibilities of stress relief at elastic matching of phases in PZT solid solutions are concerned with the non-180° domains in the tetragonal or M_A phase. The intermediate M_A phase promotes the effective stress relief in heterophase states near the MPB in a wide temperature range. The line of ZNSPs determined for heterophase PZT compositions ($x \approx 0.46$ –0.48) is parallel to the tetragonal– M_A MPB at the x–T diagram.
- (ii) Behaviour of the unit-cell parameters in the phase-transition region predetermines the outcome of the formation of various DSs and heterophase structures. Information about these structures is important for the interpretation of experimental results in wide ranges of temperature *T*, molar concentration *x* and electric field *E*.
- (iii) Despite structural distinctions, the intermediate monoclinic phases appearing in PMN–xPT and PZN–xPT SCs close to the MPB favour elastic matching of FE phases from different symmetry classes either along ZNSPs or under conditions for significant stress relief.
- (iv) Different scenarios of stress relief in the heterophase PMN-xPT system with complex DSs are proposed by taking into account peculiarities of the unit-cell behaviour. The correlation between the non-180° DSs in different heterophase states of studied SCs stems from the co-ordinated unit-cell behaviour.
- (v) The model of interpenetrating phases in the MPB region is well suited to various two-phase states (rhombohedral + M_C, M_C + tetragonal and M_B + M_C) that take place in the PMN-xPT system. Hereby, the intermediate polydomain M_C phase plays the important role in forming the various heterophase states and provides a unique link favouring effective stress relief in different variants of the phase coexistence.
- (vi) Different phase sequences observed in PMN–xPT SCs under the electric field $E \parallel [001]$, $E \parallel [110]$ or $E \parallel [111]$ and the related domain state–interface diagrams enable us to conclude that the simplification of the DS and even the formation of the single-domain phase proceed under conditions for complete stress relief, and these conditions are valid in the wide temperature range covering a few phase transitions.

In general, the results on the phase coexistence and stress-relief conditions in FE solid solutions at E=0 (Chap. 2) and $E\neq 0$ (this chapter) supplement each other. We believe that the crystallographic method developed in our recent research and the domain state–interface diagrams put forward to describe various two-phase

systems will stimulate new experimental and theoretical studies of FE solid solutions, their crystal structure, DS, phase states and physical properties. This method enables us to understand how a metastable state in a phase-transition region can be stabilized by elastic interactions between phases and/or domains of several types, and how this metastability can be altered by changes in domain patterns, temperature T, molar concentration x and electric field E.

References

- Smolensky GA, Bokov VA, Isupov VA, Krainik NN, Pasynkov RE, Sokolov AI, Yushin NK (1985) Physics of ferroelectric phenomena. Nauka, Leningrad (in Russian)
- Cross LE (2008) Relaxor ferroelectrics. In: Heywang W, Wersing W, Lubitz K (eds) Piezoelectricity. Evolution and future of a technology. Springer, Berlin, pp 132–155
- Chen J, Chan HM, Harmer MP (1989) Ordering structure and dielectric properties of undoped and La/Na-doped Pb[Mg_{1/3}Nb_{2/3}]O₃. J Am Ceram Soc 72:593–598
- De Mathan N, Husson E, Calvarin G, Morell A (1991) Structural study of a poled PbMg_{1/3}Nb_{2/3}O₃ ceramic at low temperature. Mater Res Bull 26:1167–1172
- 5. Ye Z-G, Schmid H (1993) Optical, dielectric and polarization studies of the electric field-induced phase transition in Pb(Mg_{1/3}Nb_{2/3})O₃ [PMN]. Ferroelectrics 145:83–108
- Ye Z-G (1998) Relaxor ferroelectric complex perovskites: structure, properties and phase transitions. Key Eng Mater 155–156:81–122
- 7. Topolov VY, Ye Z-G, Schmid H (1995) A crystallographic analysis of macrodomain structure in Pb(Mg_{1/3}Nb_{2/3})O₃. J Phys: Condens Matter 7:3041–3049
- Topolov VY, Rabe H, Schmid H (1993) Mechanical stresses and transition regions in polydomain Pb₂CoWO₆ crystals. Ferroelectrics 146:113–121
- Lu Y, Jeong DY, Cheng Z-Y, Zhang QM, Luo H, Yin Z, Viehland D (2001) Phase transitional behavior and piezoelectric properties of the orthorhombic phase of Pb(Mg_{1/3}Nb_{2/3})O₃–PbTiO₃ single crystals. Appl Phys Lett 78:3109–3111
- Bai F, Wang N, Li J, Viehland D, Gehring PM, Xu G, Shirane G (2004) X-ray and neutron diffraction investigations of the structural phase transformation sequence under electric field in 0.7Pb(Mg_{1/3}Nb_{2/3})O₃–0.3PbTiO₃ crystal. J Appl Phys 96:1620–1627
- Cao H, Bai F, Wang N, Li J, Viehland D, Xu G, Shirane G (2005) Intermediate ferroelectric orthorhombic and monoclinic M_B phases in [110] electric-field-cooled Pb(Mg_{1/3}Nb_{2/3})O₃–30% PbTiO₃ crystals. Phys Rev B 72:064104–6 p
- 12. Cao H, Li J, Viehland D (2006) Fragile phase stability in (1 x)Pb(Mg_{1/3}Nb_{2/3}O₃) xPbTiO₃ crystals: a comparison of [001] and [110] field-cooled phase diagrams. Phys Rev 73:184110–9 p
- Fu H, Cohen RE (2000) Polarization rotation mechanism for ultrahigh electromechanical response in single-crystal piezoelectrics. Nature 403:281–283
- Noheda B, Cox DE, Shirane G, Park S-E, Cross LE, Zhong Z (2001) Polarization rotation via a monoclinic phase in the piezoelectric 92%PbZn_{1/3}Nb_{2/3}O₃-8%PbTiO₃. Phys Rev Lett 86:3891–3894
- Noheda B, Cox DE (2006) Bridging phases at the morphotropic boundaries of lead oxide solid solutions. Phase Transitions 79:5–20
- Cao H, Li J, Viehland D (2006) Monoclinic M_C vs orthorhombic in [001] and [110] electric-field-cooled Pb(Mg_{1/3}Nb_{2/3}O₃)–35%PbTiO₃ crystals. Appl Phys Lett 88:072915–3 p
- 17. Topolov VY (2006) Comparative analysis of the twin and heterophase structures in (1 x)Pb (Mg_{1/3}Nb_{2/3})O₃-xPbTiO₃ crystals. Phys Solid State 48:1334–1341

References 97

 Cao H, Bai F, Li J, Viehland D, Xu G, Hiraka H, Shirane G (2005) Structural phase transformation and phase boundary/stability studies of field-cooled Pb(Mg_{1/3}Nb_{2/3}O₃)-32% PbTiO₃ crystals. J Appl Phys 97:094101-4 p

- 19. Noheda B, Cox DE, Shirane G, Gao J, Ye Z-G (2002) Phase diagram of the ferroelectric relaxor (1-x)Pb $(Mg_{1/3}Nb_{2/3})O_3 x$ PbTi O_3 . Phys Rev B 66:054104–10 p
- Viehland D, Li JF, Amin A (2002) Electromechanical and elastic isotropy in the (011) plane of 0.7Pb(Mg_{1/3}Nb_{2/3})O₃–0.3PbTiO₃ crystals: inhomogeneous shearing of polarization. J Appl Phys 92:3985–3989
- 21. Topolov VYu, Cao H, Viehland D (2007) Correlation between non-180° domain structures in $(1 x)Pb(A_{1/3}Nb_{2/3})O_3$ –xPbTiO₃ single crystals (A = Mg or Zn) under an applied [001] electric field. J Appl Phys 102:024103–6 p
- 22. Cao H, Li J, Viehland D (2006) Structural origin of the relaxor-to-normal ferroelectric transition in Pb(Mg_{1/3}Nb_{2/3}O₃)-xPbTiO₃. J Appl Phys 100:034110–4 p
- Durbin MK, Hicks JC, Park S-E, Shrout TR (2000) X-ray diffraction and phenomenological studies of the engineered monoclinic crystal domains in single crystal relaxor ferroelectrics. J Appl Phys 87:8159–8164
- Viehland D (2000) Symmetry-adaptive ferroelectric mesostates in oriented Pb(BI_{1/3}BII_{2/3})O₃ PbTiO₃ crystals. J Appl Phys 88:4794–4806
- 25. La-Orauttapong D, Noheda B, Ye Z-G, Gehring PM, Toulouse J, Cox DE, Shirane G (2002) Phase diagram of the relaxor ferroelectric (1 *x*)Pb(Zn_{1/3}Nb_{2/3})O₃ *x*PbTiO₃. Phys Rev B 65: 144101–7 p
- 26. Noheda B, Zhong Z, Cox DE, Shirane G, Park S-E, Rehrig P (2002) Electric-field-induced phase transitions in rhombohedral Pb(Zn_{1/3}Nb_{2/3})_{1-x}Ti_xO₃. Phys Rev B 65:224101–7 p
- Park S-E, Shrout TR (1997) Ultrahigh strain and piezoelectric behavior in relaxor based ferroelectric single crystals. J Appl Phys 82:1804–1811
- 28. Topolov VYu, Turik AV (2001) Interphase boundaries and high piezoelectric activity of xPbTiO₃ (1 x)Pb(Zn_{1/3}Nb_{2/3})O₃ crystals. Phys Solid State 43:1117–1123
- 29. Topolov VYu, Turik AV (2002) An intermediate monoclinic phase and electromechanical interactions in xPbTiO₃ (1 x)Pb(Zn_{1/3}Nb_{2/3})O₃ crystals. Phys Solid State 44:1355–1362
- 30. Topolov VY (2002) Intermediate monoclinic phase and elastic matching in perovskite-type solid solutions. Phys Rev B 65:094207–6 p
- 31. Kuwata J, Uchino K, Nomura S (1981) Phase transitions in the $Pb(Zn_{1/3}Nb_{2/3})O_3 PbTiO_3$ system. Ferroelectrics 37:579–582
- Bondarenko EI, Topolov VYu, Turik AV (1990) The effect of 90° domain wall displacements on piezoelectric and dielectric constants of perovskite ferroelectric ceramics. Ferroelectrics 110:53–56
- Durbin MK, Jacobs EW, Hicks JC, Park S-E (1999) In situ x-ray diffraction study of an electric field induced phase transition in the single crystal relaxor ferroelectric 92%Pb(Zn_{1/3}Nb_{2/3})O₃– 8%PbTiO₃. Appl Phys Lett 74:2848–2850
- 34. Paik D-S, Park S-E, Wada S, Liu S-F, Shrout TR (1999) E-field induced phase transition in $\langle 001 \rangle$ -oriented rhombohedral 0.92Pb(Zn_{1/3}Nb_{2/3})O₃-0.08PbTiO₃ crystals. J Appl Phys 85:1080–1083
- 35. Bellaiche L, García A, Vanderbilt D (2001) Electric-field induced polarization paths in $Pb(Zr_{1-x}Ti_x)O_3$ alloys. Phys Rev B64:060103–4 p
- 36. Noheda B, Cox DE, Shirane G, Guo R, Jones B, Cross LE (2001) Stability of the monoclinic phase in the ferroelectric perovskite PbZr_{1-x}Ti_xO₃. Phys Rev B 63:014103–6 p
- Leontiev NG, Kolesova RV, Eremkin VV, Fesenko OE, Smotrakov VG (1984) Space group of high-temperature lead hafnate orthorhombic phase. Kristallografiya 29:395–397 (in Russian)
- 38. Viehland D, Li JF (2002) Anhysteretic field-induced rhombhohedral to orthorhombic transformation in ⟨110⟩-oriented 0.7Pb(Mg_{1/3}Nb_{2/3})O₃−0.3PbTiO₃ crystals. J Appl Phys 92:7690−7692

- 39. Feng Z, Luo H, Guo Y, He T, Xu H (2003) Dependence of high electric-field-induced strain on the composition and orientation of Pb(Mg_{1/3}Nb_{2/3})O₃–PbTiO₃ crystals. Solid State Commun 126:347–351
- Liu T, Lynch CS (2003) Ferroelectric properties of [110], [001] and [111] poled relaxor single crystals: measurements and modeling. Acta Mater 51:407

 –416
- Liu T, Lynch CS (2005) Characterization and modeling of relaxor single crystals. Integr Ferroelectr 71:173–179
- 42. Liu T, Lynch CS (2006) Domain engineered relaxor ferroelectric single crystals. Continuum Mech Thermodyn 18:119–135
- 43. Yao J, Cao H, Ge W, Li J, Viehland D (2009) Monoclinic M_B phase and phase instability in [110] field cooled Pb(Zn_{1/3}Nb_{2/3})O₃-4.5%PbTiO₃ single crystals. Appl Phys Lett 95:052905–3 p
- Renault A-E, Dammak H, Calvarin G, Gaucher P, Thi MP (2005) Electric-field-induced orthorhombic phase in Pb[(Zn_{1/3}Nb_{2/3})_{0.955}Ti_{0.045}]O₃ single crystals. J Appl Phys 97:044105–6 p
- 45. Topolov VY (2006) Links between polydomain phases in electric-field-cooled (1 x)Pb $(Mg_{1/3}Nb_{2/3})O_3 x$ PbTi O_3 single crystals. Appl Phys Lett 89:082904–3 p
- 46. Topolov VYu, Cao H, Viehland D (2007) Phase coexistence in [111] electric-field-cooled 0.7Pb(Mg_{1/3}Nb_{2/3})O₃–0.3PbTiO₃ crystals. J Phys: Condens Matter 19:246224–9 p
- 47. Cao H, Li J, Viehland D (2006) Electric-field-induced orthorhombic to monoclinic M_B phase transition in [111] electric field cooled $Pb(Mg_{1/3}Nb_{2/3})O_3 30\%PbTiO_3$ crystals. J Appl Phys 100:084102–5 p
- 48. Davis M, Damjanovic D, Setter N (2005) Electric-field-induced orthorhombic to rhombohedral in [111]_C-oriented 0.92Pb(Zn_{1/3}Nb_{2/3})O₃ 0.08PbTiO₃. J Appl Phys 97:064101–6 p
- 49. Lee J-K, Yi JY, Hong K-S, Park S-E, Millan J (2002) Domain configuration and crystal structure of Pb(Zn_{1/3}Nb_{2/3})O₃ 5%PbTiO₃ crystals as a function of the electric-field direction. J Appl Phys 91:4474–4478
- 50. Fesenko EG, Gavrilyachenko VG, Semenchev AF (1990) Domain structure of multiaxial ferroelectric crystals. Rostov University Press, Rostov-on-Don (in Russian)

Chapter 4 Three-Phase States



Abstract Examples of the three-phase states in ferroelectric solid solutions are described in terms of the crystallographic and thermodynamic methods. Model concepts concerned with a series of interphase boundaries that obey conditions for complete stress relief in heterophase and heavily twinned single crystals are developed to highlight the specifics of the three-phase state and the role of specific domain types in stress relief. Conditions for complete stress relief are discussed for sole solid-solution compositions near the morphotropic phase boundary. Diagrams that describe volume fractions of the phases coexisting in ferroelectric solid solutions at complete stress relief in three-phase samples are put forward.

Experimental studies on FEs and related materials show that they are characterized by various heterophase states. Among the heterophase states that have been studied in the last decades, the three-phase states are of particular interest for a number of reasons. First, the three-phase states appear at almost equal volume densities of the free energy of the coexisting phases. This phase coexistence is often affected by an internal stress field [1-4] caused by jumps in the unit-cell parameters at the first-order phase transition. Changes in temperature and molar concentration favour the appearance of the three-phase states in perovskite-type solid solutions [5–9] near the MPB. Second, the three-phase states in FEs and related materials are observed, as a rule, in fairly narrow temperature and molar-concentration ranges [1, 5-10], under electric or mechanical fields [1] on certain directions, etc. Third, effective stress relief in the three-phase region promotes a decrease in the energy of the heterophase system as a whole and, thereby, plays an important role in the kinetics of the structural phase transitions. Fourth, the presence of the neighbouring phases with different types of domains (including the intermediate FE phases in perovskite-type PZT, PMN-xPT, PZN-xPT, and (1 - x)BiFeO₃ - xPbTiO₃) [5, 7-11] makes the problem of the three-phase states more complicated. This circumstance stimulates the study of possible variants of domain orientations and elastic matching to describe the phase coexistence.

In this context, it becomes timely to study the three-phase states and conditions for the stress relief in the FE solid solutions near the MPB, where the coexistence of

phases from different symmetry classes is observed. In this chapter, we analyse some examples of the three-phase states and develop model concepts concerned with a presence of a series of interphase boundaries that obey conditions for ZNSPs in heterophase and heavily twinned SCs.

4.1 Model of Three-Phase Single Crystal

The crystallographic description of the three-phase states and conditions for ZNSPs in a SC sample was first proposed in paper [5] on the phase coexistence in PbZrO₃ and PZT SCs at $x \approx 0.22$. The study of the three-phase states in these SCs was carried out in the 1990s, i.e. before the discovery of the intermediate M_A phase in PZT (see Sect. 2.1.2). It is assumed that a phase I coexists with phases II and III (Fig. 4.1a). These phases appear and grow in adjacent regions of the SC sample. The distortion matrices of the phases I, II and III in the stress-free state are $\|M_{ij}\|$, $\|N_{ij}\|$ and $\|P_{ij}\|$, respectively. An influence of a mechanical stress field of the phase I (the initial stress-free phase) on the phases II and III is allowed for in the distortion matrices

$$||R_{ij}|| = ||N_{ig}|| \cdot ||M_{gj}||$$
 (4.1)

(phase II) and

$$||L_{ij}|| = ||P_{ig}|| \cdot ||M_{gj}||$$
 (4.2)

(phase III). The following two variables are introduced: m and 1-m are volume fractions of the phases I and II, respectively, on the left from the boundary CD (Fig. 4.1a) and n and 1-n are volume fractions of the phases I and III, respectively, on the right from the boundary CD. The distortion matrix of the region I–II on the left from the boundary CD is given by

$$\|K_{ij}^{(1)}\| = m\|M_{ij}\| + (1-m)\|R_{ij}\|,$$
 (4.3)

where $||R_{ij}||$ is taken from (4.1). The region I–III on the right from the boundary *CD* is characterized by the distortion matrix

$$\|K_{ij}^{(2)}\| = n\|M_{ij}\| + (1-n)\|L_{ij}\|,$$
 (4.4)

where $||L_{ij}||$ is defined in (4.2). Conditions for ZNSPs along the interphase boundaries AB, CD and EF (Fig. 4.1a) are represented in the form similar to that in conditions (1.5) and (1.6):

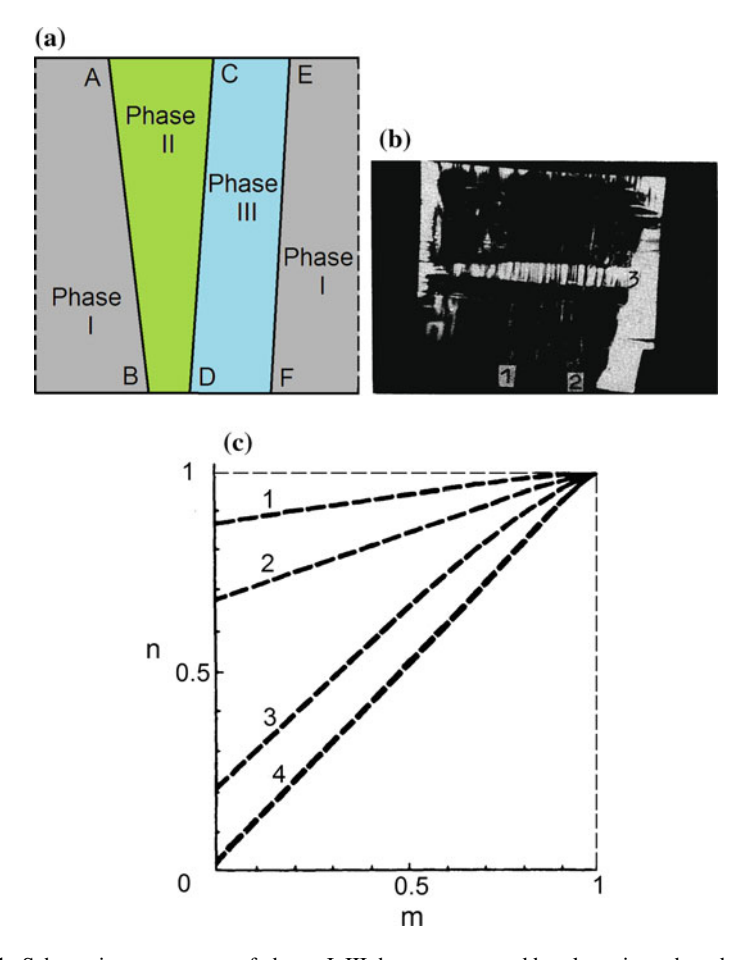


Fig. 4.1 Schematic arrangement of phases I–III that are separated by planar interphase boundaries (a), three-phase state in PbZrO₃ SC (b) and diagram that links the volume fractions m and n [see (4.3) and (4.4)] at the coexistence of the cubic (1), rhombohedral (2) and orthorhombic (3) phases in PbZrO₃ SC (c). Volume fractions t and u take the following values: t = 0.1 and u = 0.116 (curve 1), t = 0.3 and $u = 8.97 \cdot 10^{-2}$ (curve 2), t = 0.3 and u = 0.884 (curve 3), and t = 0.3 and t = 0.910 (curve 4) (b and c reprinted from paper by Topolov et al. [5], with permission from Taylor & Francis)

$$\det \left\| D_{ij}^{({\rm I-II})} \right\| = 0 \text{ and } \left[D_{ij}^{({\rm I-II})} \right]^2 - D_{ii}^{({\rm I-II})} D_{jj}^{({\rm I-II})} \ge 0, \tag{4.5}$$

$$\det \left\| D_{ij}^{({\rm I-III})} \right\| = 0 \ \ \text{and} \ \left[D_{ij}^{({\rm I-III})} \right]^2 - D_{ii}^{({\rm I-III})} D_{jj}^{({\rm I-III})} \ge 0, \tag{4.6}$$

$$\det ||D_{ij}|| = 0 \text{ and } (D_{ij})^2 - D_{ij}D_{jj} \ge 0, \tag{4.7}$$

where $D_{ij}^{(\mathrm{I-II})} = \sum_{k=1}^{3} \left(R_{ik} R_{jk} - M_{ik} M_{jk} \right)$ (phase coexistence I–II, interphase boundary AB in Fig. 4.1a), $D_{ij}^{(\mathrm{I-III})} = \sum_{k=1}^{3} \left(L_{ik} L_{jk} - M_{ik} M_{jk} \right)$ (phase coexistence III–I, interphase boundary EF in Fig. 4.1a) and $D_{ij} = \sum_{k=1}^{3} \left(K_{ik}^{(2)} K_{jk}^{(2)} - K_{ik}^{(1)} K_{jk}^{(1)} \right)$ (phase coexistence I–II and III–I, interphase boundary CD in Fig. 4.1a) are written in terms of the matrix elements from (4.1) to (4.4) by analogy with (1.7). The matrix elements from (4.7) are written in the general form [5] as $D_{ij} = a_{ij} + b_{ij}n + c_{ij}n^2 - d_{ij}m - e_{ij}m^2$, where a_{ij} , b_{ij} , c_{ij} , d_{ij} and e_{ij} are functions of the unit-cell parameters of the phases I–III and depend on DSs in these phases. Taking into account that determinant from (4.7) is a polynomial of degree 6 in terms m and n, we note that no algebraic formulae for roots of (4.7) are available. In this situation, one can vary the volume fractions m and n to obey conditions (4.5)–(4.7) for complete stress relief in the three-phase SC sample.

4.2 Application of Model Concepts to PbZrO₃ and Pb(Zr₁ $_{-x}$ Ti_x)O₃ ($x \approx 0.22$)

4.2.1 Phase Coexistence in PbZrO₃ Single Crystals

In PbZrO₃ SCs, two first-order phase transitions are observed in the relatively narrow temperature range (about 10 K [12]) below T = 500 K. On cooling the paraelectric cubic (Pm3m) phase transforms into the FE rhombohedral (R3m) phase at, and then the R3m phase transforms into the antiferroelectric orthorhombic (*Pbam*) phase [12]. The three-phase state (see, for instance, Fig. 4.1b) occurs due to some diffuseness and hysteresis of the phase transitions. As a rule, the three-phase states in PbZrO₃ SCs are characterized by instability as a result of its considerable sensitivity to external and internal stress fields in the SC sample. The internal stress field caused by jumps in the unit-cell parameters of the coexisting phases influences the domain and interphase boundaries, the distribution of domains over the sample and the temperature range of the phase coexistence. According to experimental data [12], this temperature range can be from 0 to 10 K. The internal stress field can also lead to the formation of metastable domain patterns without distinct and stable domain boundaries therein. Such behaviour of PbZrO₃ SCs is accounted for by two main reasons as follows. First, there is a small difference (about 6.3 J/mol [13]) between the free energies of the FE rhombohedral and antiferroelectric orthorhombic phases. Second, high sensitivity of the temperature range, where the FE phase is stable, to the mechanical load. For example, a hydrostatic pressure of 0.5 kbar leads to a contraction of the 5 K-range of the phase existence to 0 K [14].

As is known from the crystallographic study of the two-phase states in PbZrO₃ SCs, both the cubic-rhombohedral [15] and rhombohedral-orthorhombic interphase boundaries obey conditions (1.5) and (1.6) for ZNSPs at fixed volume fractions of the non-180° domains (twin components). The domains in the rhombohedral phase are characterized by the spontaneous polarization vectors $P_{R1}(P_r; -P_r; P_r)$ (volume fraction $x_R = 0.248$) and $P_{R2}(-P_r; P_r; P_r)$ (volume fraction $1 - x_R = 0.752$) in the rectangular coordinate system $(X_1X_2X_3)$ with the axes parallel to the perovskite unit-cell axes. The orthorhombic phase is split into the twins with the spontaneous antipolarization vectors $\pm P_{O1}(0; P; P)$ (volume fraction u = 0.868) and $\pm P_{O2}(P; 0; P)$ (volume fraction 1 - u = 0.868). The violation of conditions (4.7) at the aforementioned x_R and u values, 0 < m < 1 and 0 < n < 1 does not lead to the formation of ZNSPs at the interphase boundary CD shown in Fig. 4.1a. The presence of the excessive stress can be the essential reason for the unstable three-phase states observed in PbZrO₃ SCs [5].

One can assume that the relatively small stress is present in the SC sample at the initial stage of the phase transition. This stress may be concerned with inclusions of the metastable phase or with structural defects in the initial cubic phase. The metastable phase can influence the balance of distortions and validity of conditions (4.5)–(4.7) below the Curie temperature, and such a role is suitable for the orthorhombic phase with the anisotropic spontaneous strains. The diagram shown in Fig. 4.1c was calculated under conditions that the inclusion of the orthorhombic phase with $\pm P_{O1}(0; P; P)$ and the volume fraction t in the cubic-phase matrix favours the validity of conditions (4.5)–(4.7) at the interphase boundaries AB, CD and EF (Fig. 4.1a). It is seen that the twins with $\pm P_{01}$ and $\pm P_{02}$ in the orthorhombic phase (volume fractions u and 1 - u, region II in Fig. 4.1a) considerably influence the relationship between the volume fractions m and n (Fig. 4.1c). In our opinion, this influence is again concerned with the anisotropic spontaneous strains of the orthorhombic phase, including that split into the non-180° domains (twins). Contrary to the orthorhombic phase, changes in the volume fraction x_R of domains in the rhombohedral phase (region III in Fig. 4.1c) do not affect the n(m) dependence appreciably. It should be noted that the approximation of the inclusion with the small volume fraction u enables us to treat the n(m) dependence as a sufficiently correct one at $m \to 1$ and $n \to 1$. The dashed curves in Fig. 4.1c exhibit the general tendency of the three-phase coexistence and the possibility of the appearance of the metastable orthorhombic phase prior to the formation of the intermediate rhombohedral phase.

As follows from experimental data [5] on phase transitions in plate-like $PbZrO_3$ SCs, the planar interphase boundaries are not observed in the three-phase samples. The formation of the interphase boundaries of the complicated configuration (see, for instance, Fig. 4.1b) is concerned with the internal mechanical stress field, and stress-relief possibilities remain restricted at various domain (twin) patterns in the coexisting phases.

4.2.2 Phase Coexistence in $Pb(Zr_{I-x}Ti_x)O_3$ Single Crystals $(x \approx 0.22)$

Conditions (4.5)–(4.7) were also examined by using the experimental data [16] on the unit-cell parameters of PZT SCs with $x \approx 0.22$. This composition is located in the x–T diagram of PZT SCs [17] close to the triple point ($x = x_{tr}$ and $T = T_{tr}$) where the paraelectric cubic (Pm3m), FE rhombohedral (R3m) and FE tetragonal (P4mm) phases coexist (see also Fig. 2.1a). The polydomain rhombohedral phase cannot be elastically matched with the cubic phase along the ZNSP, while the cubic and polydomain tetragonal phase are matched along the ZNSP. The corresponding optimal volume fraction of the 90° domains in the tetragonal phase (see possible orientations of the domains in Fig. 2.2b, c) equals either 0.273 or 0.727 [5]. Interrelations between the unit-cell parameters suggest that single-domain regions of the tetragonal phase (region II in Fig. 4.1a) can be matched along the ZNSP with the single-domain rhombohedral phase (region III in Fig. 4.1a) in the presence of relatively small regions (about 7% in the volume) of the cubic phase (region I in Fig. 4.1a).

The phase sequence (cubic + tetragonal) \rightarrow rhombohedral is consistent with the presence of the beak-like bend of the rhombohedral-tetragonal (R3m - P4mm) phase boundary near the triple point towards the rhombohedral phase (see [17] and Fig. 2.1a). In PZT SC with $x \approx 0.22$, the tetragonal phase plays the role of the intermediate phase between the vast regions of thermodynamic stability of the cubic and rhombohedral phases and, therefore, promotes the effective stress relief in the heterophase system.

4.3 Application of Model Concepts to $(1-x)Pb(Mg_{1/3}Nb_{2/3})O_3-xPbTiO_3$

Three-phase states were studied in PMN–xPT solid solutions near the MPB (see, e.g. [7, 10, 18]). An analysis of elastic matching of the rhombohedral, M_C and tetragonal phases in PMN–xPT was carried out in terms of the model introduced in Sect. 4.1 and by using the room-temperature unit-cell parameters measured around the MPB [18]. Below, we consider some features of the three-phase coexistence and stress relief in the PMN–xPT system at room temperature.

It is assumed that the tetragonal phase is split into domains 1-2 (see domain orientations in Fig. 3.2) with the volume fractions n_T and $1 - n_T$, respectively. The M_C phase is split into domains 4–7 (see domain orientations in Fig. 3.2), and their volume fractions n_{Ci} are defined in terms of f_M and w_M as follows: $n_{C4} = f_M(1 - w_M)$, $n_{C5} = (1 - f_M)(1 - w_M)$, $n_{C6} = f_M w_M$, and $n_{C7} = (1 - f_M)w_M$. The rhombohedral phase is split into domains shown in Fig. 2.5, and the volume fractions o_j of these domains are written in terms of x_R and y_R by analogy with (3.2) (see also Sect. 2.2.1). If we take into account the unit-cell parameters for molar concentrations x = 0.30

(rhombohedral), 0.33 (M_C phase) and 0.39 (tetragonal phase), then one can find a great number of interphase boundaries that obey conditions (4.5)–(4.7) for ZNSPs. These ZNSPs are achieved at the variation of the volume fraction v_R of the rhombohedral phase in the wide range. The calculated optimal volume fractions $v_R = v_R(x)$, $v_M = v_M(x)$ (M_C phase) and $v_T = v_T(x)$ (tetragonal phase) at elastic matching under conditions (4.5)–(4.7) are shown in Fig. 4.2. The corresponding interphase boundaries are oriented along the ZNSPs that are approximated by the Miller indices {h0l} in the perovskite cubic unit cell.

The optimal volume fractions $v_i(x)$ of the morphotropic phases (Fig. 4.2) do not undergo considerable changes upon the variation of the unit-cell parameters of these phases at $0.30 \le x \le 0.39$. However, as the v_R value approaches zero at $0.33 \le x \le 0.39$, elastic matching of the M_C and tetragonal phases does not obey conditions for ZNSPs. Moreover, increasing the v_T value from $v_T = 0.16$ to $v_T = 0.99$ at x > 0.335 leads to violation of conditions (4.5)–(4.7) and to increasing the internal stress at the M_C -tetragonal interphase boundary.

Such unusual elastic matching, as three phases can be matched along ZNSPs at low molar concentrations x, but two phases near the same MPB cannot be matched along ZNSPs with increasing x, attests to the following points [10]. First, contrary to heterophase PZT solid solutions studied near the triple point (see Sect. 4.2.2), the phase coexistence in PMN–xPT is to be analysed at variable unit-cell parameters, especially in connection with the formation of a possible minor intermediate orthorhombic phase [18]. This means that it is necessary to increase the molar concentration x from 0.30 to

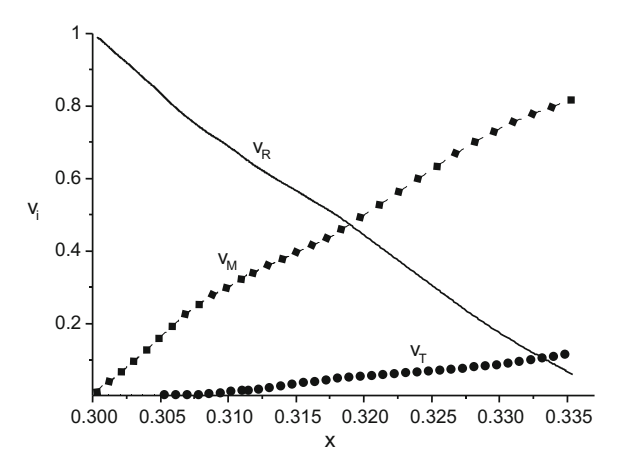


Fig. 4.2 Volume fractions $v_i(x)$ of the phases coexisting in PMN–xPT solid solutions within the framework of the model of three-phase SC. Subscripts R, M and T denote the rhombohedral, M_C and tetragonal phases, respectively. Calculations were made at $x_R = y_R = 1/2$, $f_M = 1/2$, $0 < w_M < 1$, and $0 < n_T < 1$, and the $v_i(x)$ dependences satisfy conditions for ZNSPs at the interphase boundaries AB, CD and EF in Fig. 4.1a (reprinted from paper by Topolov and Ye [10], with permission from the American Physical Society)

0.35 or higher (i.e. towards tetragonal PbTiO₃) in order to satisfy conditions for ZNSPs at the coexistence of the $M_{\rm C}$ (or orthorhombic) and tetragonal phases. Second, as far as dealing with the variable unit-cell parameters of the morphotropic phases, their elastic matching and molar-concentration behaviour in PMN–xPT can be described in terms of new models, in which the electromechanical interaction between the coexisting domain regions is taken into consideration. In this context, it should be noted that the study of the electromechanical interaction is to be based on the full sets of elastic, piezoelectric and dielectric constants measured on single-domain SCs in each separate phase. To the best of our knowledge, such the full sets measured at room temperature are available for a restricted number of the FE phases of PMN–xPT and PZN–xPT SCs (see, e.g. [19, 20]).

An example of the three-phase state studied within the framework of the modified model [11] is considered in Sect. 4.4.

4.4 Three-Phase Coexistence and Complete Stress Relief in $(1 - x)Pb(Zn_{1/3}Nb_{2/3})O_3$ -xPbTiO₃

In this section, we discuss results on heterophase structures in PZN–xPT SCs around the MPB (0.06 < x < 0.11). In the x–T diagram [21] of the PZN–xPT system, the tetragonal, orthorhombic and rhombohedral phases (all with FE properties) are present near the MPB. As noted by Noheda [22], in orthorhombic PZN–xPT SCs, the M_C phase is extremely close in energy, and a very small electric field $E \parallel [001]$ is enough to induce the M_C phase. As seen from the polarization path [111] \rightarrow [001] in the perovskite unit cell (Fig. 2.8), the spontaneous polarization vector of the M_C phase is parallel to the [h01] unit-cell direction (0 < h < 1) while the orthorhombic phase is characterized by the spontaneous polarization vector being parallel to the [101] unit-cell direction. Neutron diffraction measurements performed on PZN–0.09PT SC samples [23] testify to the presence of the intermediate phase that is either orthorhombic or M_C . Such a difference can be accounted for by the fact that the free energies of the orthorhombic and M_C are nearly degenerated in the MPB region.

Experimental studies of PZN–xPT SCs [24] show that the intermediate $M_{\rm C}$ phase coexists with both the rhombohedral and tetragonal phases in the fairly wide range of molar concentrations x (near the MPB) at room temperature. The dependence of the volume fraction of the $M_{\rm C}$ phase on x in the three-phase system is non-monotonic contrary to the dependences found [24] for the rhombohedral and tetragonal phases.

The study of the three-phase states in PZN-xPT SCs is carried out within the framework of the model [11] that develops the concepts of interpenetrating phases [25] and three-phase states [5, 10]. A stress-free SC sample is represented as a set of two types of two-phase regions, *ABCF* and *CDEF* (Fig. 4.3). Each region consists of a matrix (the intermediate M_C phase) and a plate-like inclusion (either rhombohedral or tetragonal phase as shown in Fig. 4.3). It is assumed that the regions

ABCF and CDEF are uniformly distributed in the SC sample. Volume fractions of the rhombohedral, M_C and tetragonal phases in this sample are

$$m_R = (1-m)v_R, m_M = (1-m)(1-v_R) + m(1-v_T) \text{ and } m_T = mv_T,$$
 (4.8)

respectively. The orientations and volume fractions of the non-180° domains in the coexisting FE phases coincide with those described in Sect. 4.3 (see Fig. 2.5 and domains 1, 2 and 4–7 in Fig. 3.2). These domains are assumed to be separated by planar unstrained domain walls (or domain boundaries) whose orientations are determined in terms of work by Fousek and Janovec [26].

The rhombohedral and M_C phases in the region ABCF as well as the tetragonal and M_C phases in the region CDEF region (Fig. 4.3) are separated by the interphase boundaries that obey conditions (4.5) and (4.6) for ZNSPs. The SC sample is regarded as a set of regions like the adjacent polydomain phases with permissible domain walls therein. The distortion matrices of the two-phase regions ABCF and CDEF are written as

$$\left\| K_{ij}^{(1)} \right\| = \nu_R \left\| K_{ig}^{(2)} \right\| \cdot \left\| N_{gj}^{(R)} \right\| + (1 - \nu_R) \left\| N_{ij}^{(M)} \right\| \tag{4.9}$$

and

$$\left\| K_{ij}^{(2)} \right\| = \nu_T \left\| K_{ig}^{(1)} \right\| \cdot \left\| N_{gj}^{(T)} \right\| + (1 - \nu_T) \left\| N_{ij}^{(M)} \right\|, \tag{4.10}$$

respectively, where $\left\|N_{gj}^{(R)}\right\|$, $\left\|N_{ij}^{(M)}\right\|$ and $\left\|N_{gj}^{(T)}\right\|$ are the distortion matrices of the rhombohedral, $\mathbf{M}_{\mathbf{C}}$ and tetragonal phases, respectively. We note that the distortion

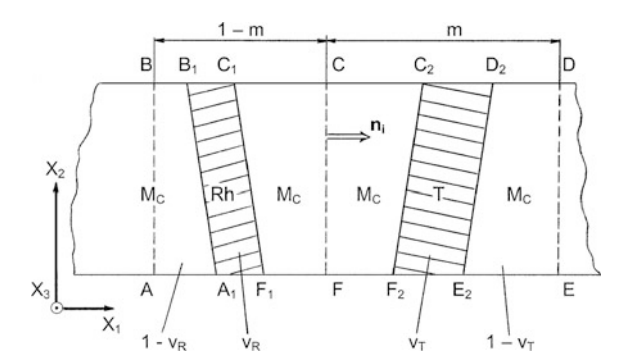


Fig. 4.3 Cross section of the three-phase SC sample by the (X_1OX_2) plane. Coordinate axes OX_j are parallel to the perovskite unit-cell axes in the cubic phase. n_i is the normal vector of the interphase boundary CF between the two-phase regions ABCF and CDEF. Coexisting phases are M_C , Rh (rhombohedral) and T (tetragonal). v_R is the volume fraction of the rhombohedral phase in the two-phase region ABCF, v_T is the volume fraction of the tetragonal phase in the two-phase region CDEF, and m is the volume fraction of the two-phase region CDEF in the fragment CDEF of the three-phase sample (reprinted from paper by Topolov [11], with permission from IOP Publishing)

matrices $\left\|K_{ij}^{(1)}\right\|$ and $\left\|K_{ij}^{(2)}\right\|$ from (4.9) and (4.10) differ from those in (4.3) and (4.4). Now the distortion matrices $\left\|K_{ij}^{(1)}\right\|$ and $\left\|K_{ij}^{(2)}\right\|$ are present in the right-hand side of (4.9) and (4.10) [cf. them and (2.12)] so that the mutual influence of the internal stress fields of the phases in the regions *ABCF* and *CDEF* is taken into account by analogy with the model of interpenetrating phases (Sect. 2.3). Elastic matching of the regions *ABCF* and *CDEF* leads to the formation of the ZNSP along the boundary *CF* (Fig. 4.3), while conditions (4.7) are valid for matrix elements $D_{ij} = \sum_{k=1}^{3} \left(K_{ik}^{(2)}K_{jk}^{(2)} - K_{ik}^{(1)}K_{jk}^{(1)}\right)$ expressed in terms of $\left\|K_{ij}^{(1)}\right\|$ and $\left\|K_{ij}^{(2)}\right\|$ from (4.9) and (4.10).

Elastic matching of the two-phase regions *ABCF* and *CDEF* is studied [11] using the unit-cell parameters measured [24] at room temperature. For this study, the unit-cell parameters of the morphotropic phases are taken at the following molar concentrations: $x_R = 0.06$ (the rhombohedral phase, the left side of the x range), $x_M = 0.08$ (the M_C phase, the middle part of the x range where no changes in the unit-cell parameters are observed) and $x_T = 0.11$ (the tetragonal phase, the right side of the x range). Experimental work on PZN–xPT and related solid solutions do not contain data on densities of the morphotropic phases as well as on interconnections between the molar concentration x of heterophase SC and the volume fraction x of the two-phase region shown in Fig. 4.3. In this context, it is assumed that the effective molar concentration of the three-phase SC sample is

$$x_{\text{eff}} = m_R x_R + m_M x_M + m_T x_T,$$
 (4.11)

where the volume fractions m_R , m_M and m_T have been introduced in (4.8). In addition, it is assumed [11] that a linear approximation for m = m(x) is possible in the range $[x_R, x_T]$ and that the following boundary conditions for the volume fraction m are valid at dm/dx = const > 0: m = 0 for $x_R = 0.06$ and m = 1 for $x_T = 0.11$.

As follows from the analysis of the three-phase states in PZN–xPT SCs, any variations in the x_R , y_R and f_M values cannot strongly change the conditions for ZNSPs. This peculiarity is accounted for by the negligible influence of the shear unit-cell distortions of the domains in the rhombohedral and M_C phases over the whole x range. Among various orientations $n_i(h_i \ k_i \ l_i)$ of the boundary CF [see Fig. 4.3 and (1.8)], that satisfies conditions (4.7) for ZNSPs in the three-phase SC sample, we regard $n_i \parallel (100)$ or $n_i \parallel (010)$ as most probable orientations. They are also parallel to the permissible domain (twin) walls [26] in the M_C phase, and this circumstance promotes complete stress relief.

Examples of the three-phase states in PZN-xPT SCs with a system of ZNSPs, including those along the boundary CF with the normal vector $\mathbf{n_i} \parallel (100)$ or $\mathbf{n_i} \parallel (010)$ are illustrated by means of the molar-concentration dependences in Fig. 4.4. A transition from the heavily twinned rhombohedral phase (case of $x_R = y_R = 1/2$, see Fig. 2.5) to the single-domain one (case of $x_R = y_R = 1$) results in increasing the

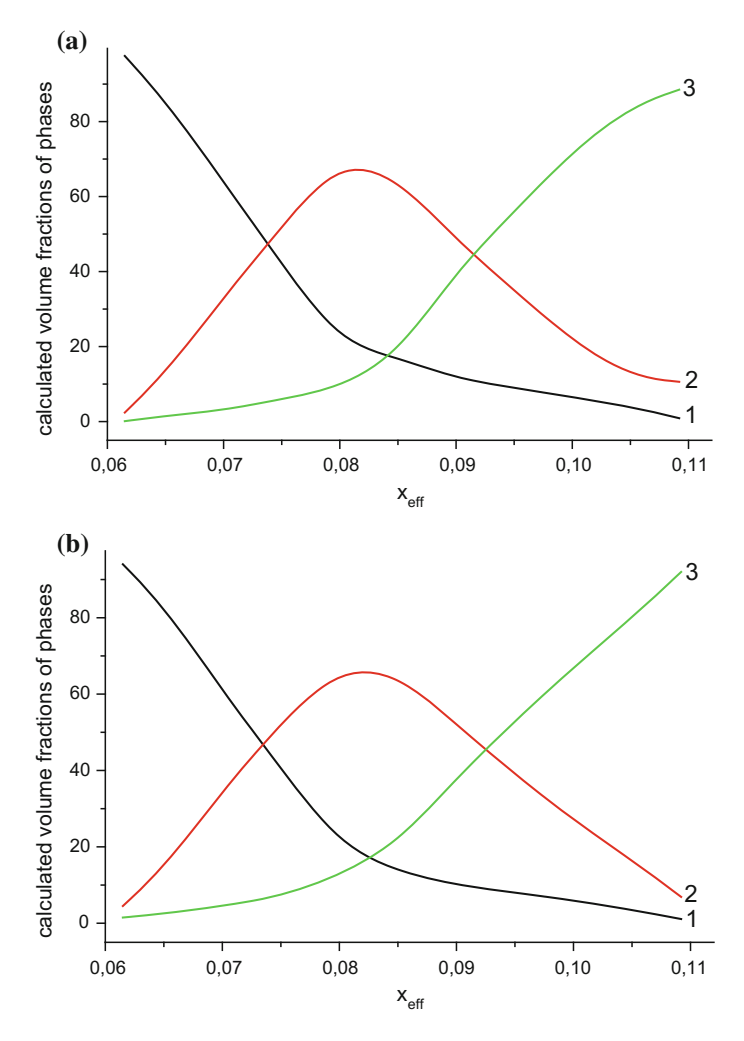


Fig. 4.4 Calculated molar-concentration dependences of the volume fractions $v_i(x_{\text{eff}})$ (in percent) of the morphotropic phases in PZN–xPT SCs. Calculations were made at $u_R = g_R = 1/2$ (a) and $u_R = g_R = 1$ (b). Curves 1, 2 and 3 in each graph are related to $v_R(x_{\text{eff}})$, $v_M(x_{\text{eff}})$ and $v_T(x_{\text{eff}})$, respectively (reprinted from paper by Topolov [11], with permission from IOP Publishing)

volume fractions m_M and m_T in some degree at $x_{\rm eff} < 0.07$, where $x_{\rm eff}$ is taken from (4.11). This effect is concerned with the active role of the non-180° domains in the M_C and tetragonal phases in stress relief over the heterophase sample. The aforementioned changes in the 71° (109°) DS of the rhombohedral phase (Fig. 2.5) slightly affect the location of max $v_M(x_{\rm eff})$ (cf. curves 2 in Fig. 4.4a, b), and this fact testifies to the passive role of the rhombohedral phase in the stress relief at the phase coexistence. Indeed, the distortion matrix of the rhombohedral phase [see (2.6)] comprises three equal diagonal elements that do not give rise to the anisotropy of

spontaneous strains ξ_{jj}^s (j=1,2 and 3) at various volume fractions of the domains shown in Fig. 2.5. As a consequence, the stress-relief possibilities caused by the rhombohedral phase in the three-phase PZN–xPT SC sample are restricted. The calculated $v_i(x_{\rm eff})$ curves shown in Fig. 4.4 are in good agreement with the experimental molar-concentration dependences of the volume fractions of the coexisting phases [24]. It is important to underline that both the unit-cell parameters of the coexisting phases and their volume fractions were determined on the same PZN–xPT SC samples in work [24], and therefore, one can directly compare the calculated and experimental results on the three-phase states. Such combinations of the FE phases around the MPB were not studied in other FE solid solutions and related materials. Thus, one can characterize PZN–xPT SCs as a unique system in which the three-phase states '... – (rhombohedral + M_C) – (M_C + tetragonal) – ...' (Fig. 4.3) provide complete stress relief and, therefore, promote a vanishing elastic energy in a wide x range.

4.5 Thermodynamic Description of Three-Phase States in Ferroelectric Solid Solutions

The nucleation of the new phase at the first-order phase transition in FE SCs was considered in the thermodynamic study [27–29] of the coexistence of phases from different symmetry classes. In this study the internal mechanical stress of the electrostrictive nature is taken into account. The thermodynamic description of the two-phase state was carried out for the paraelectric–FE [27, 28] and FE–FE [30] phase transitions in perovskite-type SCs, including the morphotropic phase transition [29]. Thermodynamic criteria of the new-phase nucleation in the presence of the internal stress field were put forward, and the validity of these criteria in FE SCs was examined in papers [27–30]. The three-phase states in the presence of the internal stress field were first described in terms of thermodynamics in work [6], where the phase coexistence in PZT SCs was studied. In this section, we extend thermodynamic formalism and introduce a system of thermodynamic and concentration criteria of the new-phase nucleation in FE solid solutions near the triple point.

It is assumed that the paraelectric cubic (I in Fig. 4.1a), FE tetragonal (II in Fig. 4.1a) and FE rhombohedral (III in Fig. 4.1a) phases coexist in PZT SC near the triple point shown in Fig. 2.1a. The tetragonal and rhombohedral phases are split into the non-180° domains (see Sect. 4.2.2). Moduli of the spontaneous polarization vector in the domains equal P_T (tetragonal phase) and P_R (rhombohedral phase). The depolarizing-field energy of the SC sample vanishes due to the formation of the 180° domains in the FE phases and due to the screening of electric fields of bound charges by free charge carriers.

An analysis of the elastic interaction between the phases [28, 29] shows that the induced strain of a nucleus of the rhombohedral phase is written in the form [6]

$$\xi_{jk}^{i,R} = A_{jk} P_R^2 - \left[B_{jk} P_T^2 y_T + M_{jk} P_0^2 (1 - y_T) \right], \tag{4.12}$$

where A_{jk} , B_{jk} and M_{jk} are the renormalized electrostrictive coefficients of the rhombohedral, tetragonal and cubic phases, respectively, P_0 is the spontaneous polarization of the matrix phase (in case of the cubic phase $P_0 = 0$), and $p_0 = 0$, are the spontaneous polarization of the spontaneous phase is $p_0 = 0$, and $p_0 = 0$

$$F = f_R^{(n)} v_R + f_T^{(n)} v_T + f_C^{(M)} (V - v_R - v_T), \tag{4.13}$$

where $f_R^{(n)}$, $f_T^{(n)}$ and $f_C^{(M)}$ are volume densities of the free energy of the rhombohedral, tetragonal and cubic phases, respectively, superscripts (n) and (M) are related to the nucleus and matrix, respectively. The volume densities of the free energy $f_R^{(n)}$, $f_T^{(n)}$ and $f_C^{(M)}$ from (4.13) are represented in the form of the Devonshire-type expansion [31–34] in terms of P_R , P_T and P_0 , respectively. For instance, the volume density of the free energy of single-domain BaTiO₃-type SC at the uniform distribution of the spontaneous polarization $P_s(P_1; P_2; P_3)$ is represented [34] as follows:

$$\begin{split} f = &\alpha \left(P_{1}^{2} + P_{2}^{2} + P_{3}^{2}\right) + \frac{1}{2}\beta_{1}'\left(P_{1}^{4} + P_{2}^{4} + P_{3}^{4}\right) + \frac{1}{3}\gamma_{1}\left(P_{1}^{6} + P_{2}^{6} + P_{3}^{6}\right) \\ &+ \beta_{2}'\left(P_{1}^{2}P_{2}^{2} + P_{2}^{2}P_{3}^{2} + P_{3}^{2}P_{2}^{2}\right) + \gamma_{2}\left[P_{1}^{4}\left(P_{2}^{2} + P_{3}^{2}\right) + P_{2}^{4}\left(P_{3}^{2} + P_{1}^{2}\right) + P_{3}^{4}\left(P_{1}^{2} + P_{2}^{2}\right)\right] \\ &+ \gamma_{3}P_{1}^{2}P_{2}^{2}P_{3}^{2} + \frac{1}{2}c_{11}\left(\xi_{11}^{2} + \xi_{22}^{2} + \xi_{33}^{2}\right) + c_{12}\left(\xi_{11}\xi_{22} + \xi_{22}\xi_{33} + \xi_{33}\xi_{11}\right) \\ &+ \frac{1}{2}c_{44}\left(\xi_{12}^{2} + \xi_{23}^{2} + \xi_{31}^{2}\right) + q_{11}\left(P_{1}^{2}\xi_{11} + P_{2}^{2}\xi_{22} + P_{3}^{2}\xi_{33}\right) + q_{12}\left[P_{1}^{2}\left(\xi_{22} + \xi_{33}\right) + P_{2}^{2}\left(\xi_{33} + \xi_{11}\right) \right. \\ &+ P_{3}^{2}\left(\xi_{11} + \xi_{22}\right)\right] + 2q_{44}\left(P_{1}P_{2}\xi_{12} + P_{2}P_{3}\xi_{23} + P_{3}P_{1}\xi_{31}\right). \end{split} \tag{4.14}$$

In (4.14), $\alpha = \alpha_0$ ($T - T_0$), β_1' , β_2' , γ_1 , γ_2 and γ_3 are thermodynamic coefficients of the expansion, c_{ab} are elastic moduli, ξ_{jk} are strains, $q_{11} = -(Q_{11}c_{11} + 2Q_{12}c_{12})$, $q_{12} = -[Q_{11}c_{12} + Q_{12}(c_{11} + c_{12})]$ and $q_{44} = -Q_{44}c_{44}/2$ are electrostriction constants of SC, α_0 = const, and T_0 is Curie–Weiss temperature of the first-order phase transition. The thermodynamic coefficients β_1' and β_2' are related to clamped SC, and for the stress-free state, the thermodynamic coefficients β_1 and β_2 are introduced as follows: $\beta_1 = \beta_1' + q_{11}Q_{11} + 2q_{12}Q_{12}$ and $\beta_2 = \beta_2' + q_{11}Q_{12} + q_{12}(Q_{11} + Q_{12}) + q_{44}Q_{44}$. Equation (4.14) is valid in the vicinity of the first-order phase transition, as a rule, in a temperature range from a few degrees to some tens degrees [34, 35]. Taking into account the induced strain [see (4.12)], caused by

jumps in the unit-cell parameters, and applying (4.14) to each phase in the heterophase sample, we represent (4.13) as

$$F = (\alpha P_R^2 + \frac{1}{2}\beta_R P_R^4 + \frac{1}{3}\gamma_R P_R^6 + f_R^*)\nu_R + \left(\alpha P_T^2 + \frac{1}{2}\beta_T P_T^4 + \frac{1}{3}\gamma_T P_T^6 + f_T^*\right)\nu_T + \left(\alpha P_0^2 + \frac{1}{2}\beta_1 P_0^4 + \frac{1}{3}\gamma_1 P_0^6\right)(V - \nu_R - \nu_T),$$

$$(4.15)$$

where α , β_R , γ_R , ..., γ_1 are thermodynamic coefficients in the stress-free single-domain phase, f_R^* and f_T^* are volume densities of the elastic and electrostriction energy of the nucleus of the rhombohedral phase and of the inclusions of the tetragonal phase, respectively. The thermodynamic coefficients β_R and β_T from (4.15) are linear combinations of β_j , and γ_R and γ_T from (4.15) are linear combinations of γ_j [see (4.14)].

In the case of small induced strains from (4.12), the volume density of the elastic and electrostriction energy of the nucleus of the rhombohedral phase $f_R^* = \sum_{\kappa,\lambda=1}^6 c_{\kappa\lambda} \xi_{\kappa}^{i,R}$ is written using the single-subscript notation [36] for the induced strain, and this expression is represented in terms of P_R , P_T and P_0 as follows:

$$f_R^* = \frac{1}{2} \left[\delta_R P_R^4 + \delta_T P_T^4 y_T^2 + \delta_0 P_0^4 (1 - y_T)^2 - 2\delta_{RT} P_R^2 P_T^2 y_T + 2\delta_{0T} P_0^2 P_T^2 (1 - y_T^2) - 2\delta_{0R} P_0^2 P_R^2 (1 - y_T) \right].$$

$$(4.16)$$

In (4.16), $\delta_R = \sum_{\kappa,\lambda=1}^6 c_{\kappa\lambda}A_{\kappa}A_{\lambda}$, $\delta_T = \sum_{\kappa,\lambda=1}^6 c_{\kappa\lambda}B_{\kappa}B_{\lambda}$ and $\delta_0 = \sum_{\kappa,\lambda=1}^6 c_{\kappa\lambda}M_{\kappa}M_{\lambda}$ are the electrostriction parameters that characterize elastic effects in the rhombohedral, tetragonal and cubic phases, respectively, A_{κ} , B_{κ} and M_{κ} are the renormalized electrostriction coefficients in the single-subscript notation, $\delta_{RT} = \frac{1}{2} \sum_{\kappa,\lambda=1}^6 c_{\kappa\lambda} (A_{\kappa}B_{\lambda} + B_{\kappa}A_{\lambda})$, $\delta_{0T} = \frac{1}{2} \sum_{\kappa,\lambda=1}^6 c_{\kappa\lambda} (M_{\kappa}B_{\lambda} + B_{\kappa}M_{\lambda})$ and $\delta_{0R} = \frac{1}{2} \sum_{\kappa,\lambda=1}^6 c_{\kappa\lambda} (M_{\kappa}A_{\lambda} + A_{\kappa}M_{\lambda})$ are the electrostriction parameters that describe elastic effects at the rhombohedral–tetragonal, cubic–tetragonal and cubic–rhombohedral phase transitions, respectively. The volume density of the elastic and electrostriction energy of the inclusion of the tetragonal phase $f_T^* = \sum_{\kappa,\lambda=1}^6 c_{\kappa\lambda} \xi_{\kappa}^{i,T} \xi_{\lambda}^{i,T}$ is written by taking into account (4.12) and (4.16) as follows:

$$f_T^* = \frac{1}{2} \left[\delta_T P_T^4 + \delta_R P_R^4 z_R^2 + \delta_0 P_0^4 (1 - z_R)^2 - 2\delta_{0T} P_0^2 P_T^2 (1 - z_R) - 2\delta_{RT} P_R^2 P_T^2 z_R + 2\delta_{0R} P_0^2 P_R^2 (1 - z_R^2) \right].$$

$$(4.17)$$

The thermodynamic equilibrium between the three phases coexisting in SC is expressed by equalities $f_R^{(n)} = f_C^{(M)}(1-y_T) + f_T^{(n)}y_T$ and $f_T^{(n)} = f_C^{(M)}(1-z_R) + f_R^{(n)}z_R$ which are represented, by taking into consideration (4.15), as

$$\alpha P_T^2 + \frac{1}{2}\beta_T P_T^4 + \frac{1}{3}\gamma_T P_T^6 + f_T^* = \alpha P_0^2 + \frac{1}{2}\beta_1 P_0^4 + \frac{1}{3}\gamma_1 P_0^6$$
 (4.18)

and

$$\alpha P_R^2 + \frac{1}{2}\beta_R P_R^4 + \frac{1}{3}\gamma_R P_R^6 + f_R^* = \alpha P_0^2 + \frac{1}{2}\beta_1 P_0^4 + \frac{1}{3}\gamma_1 P_0^6.$$
 (4.19)

If phase I is paraelectric (see Fig. 4.1a) and, therefore, $P_0 = 0$, then one can reduce (4.16) and (4.17) to the following form:

$$f_R^* = \frac{1}{2} (\delta_R P_R^4 + \delta_T P_T^4 y_T^2 - 2\delta_{RT} P_R^2 P_T^2 y_T) = \delta_R^* P_R^4 / 2$$
 (4.20)

and

$$f_T^* = \frac{1}{2} (\delta_T P_T^4 + \delta_R P_R^4 y_R^2 - 2\delta_{RT} P_R^2 P_T^2 z_R) = \delta_T^* P_T^4 / 2, \tag{4.21}$$

where δ_R^* and δ_T^* are generalized electrostriction parameters [6]. The analysis of (4.18) and (4.19) with due regard for (4.20) and (4.21) enables one to find temperatures of the nucleation of phases III and I (at the molar concentration $x \approx \text{const}$) or molar concentrations at which the nucleation of phases III and I starts (at $T \approx \text{const}$). Taking into account conditions for thermodynamic stability of the heterophase system, one can derive the following criteria of the nucleation and steady-state growth of the new phase [6]:

$$\beta_R + \delta_R^* < 0 \tag{4.22}$$

[nucleus (rhombohedral) – matrix (cubic + tetragonal)],

$$\beta_R + 3\delta_R^* < 0 \tag{4.23}$$

[nucleus (cubic) – matrix (rhombohedral + tetragonal)],

$$\beta_T + \delta_T^* < 0 \tag{4.24}$$

[nucleus (tetragonal) – matrix (cubic + rhombohedral)], and

$$\beta_T + 3\delta_T^* < 0 \tag{4.25}$$

[nucleus (cubic) – matrix (tetragonal + rhombohedral)]. It is assumed that the steady-state growth of the phase occurs under condition that the volume of the nucleus exceeds the critical volume and surface effects are to be neglected. In the case of violation of criteria (4.22)–(4.25), three-phase states would not occur, and as consequence, the phase transition would proceed on the stability-loss boundaries of the initial phase. These boundaries are determined from (4.18) and (4.19).

Additional thermodynamic limitations on the three-phase coexistence are imposed by values of the electrostriction parameters from (4.16) and (4.17). In the approximation of the weak dependence on T and x, for example, the parameter δ_R^* from (4.20) should obey conditions for min $\delta_R^*(y_T)$, where y_T characterizes the volume fraction of the tetragonal phase (i.e. II in Fig. 4.1a) in the two-phase (cubic-rhombohedral, I–III) medium. Relationships $y_{T,\text{opt}} = (\delta_{RT}/\delta_T)(P_R/P_T)^2$ and $\delta_T > 0$ correspond to min $\delta_R^*(y_T)$ and have the physical meaning at $0 < y_{T,\text{opt}} \ll 1$, i.e. as the inequality

$$0 < \delta_{RT} (P_R/P_T)^2 \ll \delta_T \tag{4.26}$$

holds. Condition (4.26) is reduced to the inequality

$$0 < \sum_{\kappa, \lambda = 1}^{6} c_{\kappa\lambda} (A_{\kappa} B_{\lambda} + B_{\kappa} A_{\lambda}) \ll 2 \sum_{\kappa, \lambda = 1}^{6} c_{\kappa\lambda} B_{\kappa} B_{\lambda} (P_{T}/P_{R})^{2}$$

$$(4.27)$$

written in terms of renormalized electrostrictive coefficients from (4.12). The limitations similar to those in (4.26) and (4.27) can be introduced [6] for various combinations of phases I–III in PZT SCs. By analogy with (4.26) and (4.27), the following inequalities are introduced for the three-phase states:

$$0 < \delta_{RT} (P_T / P_R)^2 \ll \delta_R \tag{4.28}$$

and

$$0 < \sum_{\kappa, \lambda = 1}^{6} c_{\kappa\lambda} (A_{\kappa} B_{\lambda} + B_{\kappa} A_{\lambda}) \ll 2 \sum_{\kappa, \lambda = 1}^{6} c_{\kappa\lambda} A_{\kappa} A_{\lambda} (P_{R}/P_{T})^{2}$$

$$(4.29)$$

[nucleus (tetragonal) – matrix (cubic + rhombohedral), phase II is rhombohedral],

$$0 < 2\delta_{RT} (P_T/P_R)^2 \ll \delta_R \tag{4.30}$$

and

$$0 < \sum_{\kappa,\lambda=1}^{6} c_{\kappa\lambda} (A_{\kappa} B_{\lambda} + B_{\kappa} A_{\lambda}) \ll \frac{1}{2} \sum_{\kappa,\lambda=1}^{6} c_{\kappa\lambda} A_{\kappa} A_{\lambda} (P_{R}/P_{T})^{2}$$
 (4.31)

[nucleus (cubic) - matrix (tetragonal + rhombohedral), phase II is rhombohedral],

$$0 < 2\delta_{RT} (P_R/P_T)^2 \ll \delta_T \tag{4.32}$$

and

$$0 < \sum_{\kappa, \lambda = 1}^{6} c_{\kappa\lambda} (A_{\kappa} B_{\lambda} + B_{\kappa} A_{\lambda}) \ll \frac{1}{2} \sum_{\kappa, \lambda = 1}^{6} c_{\kappa\lambda} B_{\kappa} B_{\lambda} (P_{T}/P_{R})^{2}$$

$$(4.33)$$

[nucleus (cubic) – matrix (rhombohedral + tetragonal), phase II is tetragonal]. Thus, the following criteria are introduced for the three-phase system: the thermodynamic criteria 4.22–4.25 (nucleation of phase III) and the concentration criteria 4.26, 4.28, 4.30 and 4.32 (existence of inclusions of phase II). The aforementioned concentration criteria are also represented in terms of renormalized electrostrictive coefficients [see (4.27), (4.29), (4.31), and (4.33)].

The validity of the criteria in the three-phase PZT system near the triple point was discussed in paper [6]. As noted in Sect. 4.2.2, the interphase boundary that obeys conditions for ZNSPs can appear at the cubic–tetragonal phase transition. The conditions for ZNSPs are violated at elastic matching of the cubic and rhombohedral phases at any volume fractions of the 71° (109°) domains. Due to the formation of the ZNSP, the coefficients B_{jk} from (4.12) approach zero. As a consequence, $\delta_T \to 0$, and expressions for δ_{RT} , δ_{0T} , δ_R^* , and δ_T^* [see (4.16), (4.17), (4.20) and (4.21)] are simplified.

Results on the thermodynamic study [6] show that the obvious difference between values of jumps in the spontaneous polarization in single-domain PZT SCs near the triple point ($x \approx 0.22$) influences the three-phase state to some extent. According to data [37], the jump $P_R(T_{C'}) = 0.05$ C/m² to the left of the triple point (i.e. in the rhombohedral phase) is considerably less than the jump $P_T(T_{C''}) = 0.25$ C/m² to the right of the triple point (i.e. in the tetragonal phase), where $T_{C'}$ and $T_{C''}$ are Curie temperatures at the cubic–rhombohedral and cubic–tetragonal phase transitions, respectively. These jumps influence the thermodynamic coefficients from (4.15) and, for example, give rise to the significant difference between β_R and β_T : according to data at $x \approx x_{tr}$ [6], $\beta_R = -8.2 \times 10^7$ J m⁵ C⁻⁴ in the vicinity of $T = T_{C'}$ and $\beta_T = -1.0 \times 10^9$ J m⁵ C⁻⁴ in the vicinity of $T = T_{C''}$. This difference provides more favourable conditions for the formation of the tetragonal phase in the two-phase (cubic–rhombohedral) SC sample and for the formation of the cubic phase in the two-phase (tetragonal–rhombohedral) SC sample than for other variants.

Considerable stress relief is required at the cubic-rhombohedral interphase boundaries in cases where the nucleus of the rhombohedral phase appears in two-phase (cubic-tetragonal) SC or the nucleus of the cubic phase appears in two-phase (rhombohedral-tetragonal) SC. This requirement stems from a restricted possibility to satisfy criteria (4.22) and (4.23) because of the relatively small $|\beta_R|$ value. The problem of the stress relief is also concerned with peculiarities of the spontaneous strain ξ_{ik}^s of the perovskite unit cell of PZT SC in the vicinity of $x = x_{tr}$ and $T = T_C$. These peculiarities are inseparably linked with the behaviour of the electrostrictive coefficients Q_{ij} due to the relation [38] between ξ_{ik}^s and the spontaneous polarization. As follows from data [37], Q_{11} , $|Q_{12}|$ and Q_{44} of PZT SC ($x \approx x_{tr}$), in comparison with the analogous properties of PbZrO₃ SC, increase approximately by factors of 1.6, 1.9 and 1.3, respectively. This behaviour leads to an increase in $|A_{ik}|$ from (4.12) and influences the validity range of the concentration criteria for phase II [see (4.27), (4.29), (4.31), and (4.33)]. The violation of the criteria makes the three-phase coexistence impossible and gives rise to the subsequent phase transitions, for example, phase I \rightarrow phase II and then phase II \rightarrow phase III. This change in the phase-transition kinetics is consistent with the possible occurrence of the second-order phase transitions in PZT SCs at $x > x_{tr}$, namely, close to the tricritical point found [39] at the cubic–tetragonal phase boundary of the x–T diagram.

In general, the validity of the concentration and thermodynamic criteria in PZT SCs is in agreement with experimental data [17, 39] on heterophase states observed in the vicinity of the triple point. Moreover, the phase-transition directions being parallel to the x and T axes of the diagram in Fig. 2.1a, are consistent with the region that is characterized by the noticeable beak-like bending of the phase boundaries in the x-T diagram of PZT SCs (see also [17, 39]). It should be added that a similar bending is present in the x-T diagrams of many FE perovskite-type solid solutions (see, for instance, the x-T diagrams of PMN-xPT [40], PZN-xPT [41], $Pb(Zr_{1-x}Sr_x)O_3$ [42], and $(Pb_{1-x}Sr_x)ZrO_3$ [43]). Moreover, the refinement of the x-T diagrams after the discovery of the intermediate FE phases in solid solutions of PZT, PMN-xPT and PZN-xPT (see Chap. 2) did not lead to appreciable changes in the bending of the phase boundaries [7, 18, 21, 44, 45] near the triple point where the cubic, rhombohedral and tetragonal phases coexist. As in the x-T diagram built for PZT SCs [17, 39], the beak in the x-T diagrams of the aforementioned solid solutions (SCs or ceramics) has the similar orientation so that the point of the beak is located at the cubic-rhombohedral phase boundary (see, for instance, the curve between the C and R regions in Fig. 2.1a). As is known from experimental data on the temperature dependence of the spontaneous polarization in PZT, PMN-xPT, PZN-xPT, Pb($Zr_{1-x}Sn_x$)O₃, (Pb_{1-x}Sr_x)ZrO₃, etc., the spontaneous polarization jump $P_R(T_C)$ at the cubic-rhombohedral phase boundary is less than the spontaneous polarization jump $P_T(T_C^{"})$ at the cubic-tetragonal phase boundary where the beak-like region in the x-T diagram (Fig. 2.1a) broadens to a considerable extent. The assumption that the bending in the x-T diagram of the FE solid-solution system depends on the ratio of the jumps $P_R(T_C')/P_T(T_C'')$ [6] finds indirect confirmations.

4.6 Crystallographic and Thermodynamic Studies of Three-Phase States

In this chapter, we have analysed three-phase states in PbZrO $_3$ SCs and PZT, PMN $_x$ PT and PZN $_x$ PT solid solutions. To study the three-phase states in these materials, we developed the crystallographic and thermodynamic methods. The models proposed at the crystallographic description of the three-phase states are applicable in restricted ranges of temperature T and molar concentration x where polydomain/heterophase states occur. The limits of application of these models are concerned with peculiarities of the phase-transition kinetics and DSs, with fluctuations of the new phase, etc. Very recently, a new example of the three-phase states was studied in lead-free (Ba $_{0.85}$ Ca $_{0.15}$)(Ti $_{0.90}$ Zr $_{0.10}$)O $_3$ ceramic samples, and stress-relief conditions were analysed for the non-poled and poled samples [46]. Some results on this three-phase coexistence are highlighted in Sect. 6.3.

Features of the three-phase states considered in this chapter are formulated as follows.

- (i) The diagram that links the volume fractions of the phases coexisting in PbZrO₃ SC (Fig. 4.1c) enables one to predict some features of the three-phase state affected by individual types of the non-180° domains (twin components) in the FE rhombohedral and antiferroelectric orthorhombic phases.
- (ii) Elastic matching of the polydomain morphotropic phases in the PMN–xPT system shows that only in a restricted composition range (in the vicinity of x = 0.30), complete stress relief is achieved in the three-phase state (rhombohedral + M_C + tetragonal). Such a restriction mainly stems from the molar-concentration behaviour of the unit-cell parameters of the aforementioned phases in the range $0.30 \le x \le 0.39$ at room temperature.
- (iii) Elastic matching of the polydomain morphotropic phases in the PZN–xPT system (0.06 < x < 0.11) is described in terms of the model wherein the mutual influence of the internal stress fields of the phases in the adjacent two-phase regions (Fig. 4.3) is taken into account. The comparison of the modelling and experimental results enables us to conclude that the three-phase states '... (rhombohedral + M_C) (M_C + tetragonal) ...' provide complete stress relief over a wide molar-concentration x range at room temperature and that the intermediate M_C phase plays the decisive role in the stress relief at elastic matching around the MPB.
- (iv) Thermodynamic formalism of the new-phase nucleation at the first-order phase transition was extended to describe the three-phase PZT system in the presence of the internal stress field. The thermodynamic description of the three-phase states is based on six electrostriction parameters [see (4.16)] that are concerned with the induced strain at the interphase boundaries. Hereby, the thermodynamic criteria [see (4.22)–(4.25)] and concentration criteria [see (4.26), (4.28), (4.30) and (4.32)] are introduced to take into account the internal stress field caused by the three-phase coexistence.

(v) Substantially different jumps in the spontaneous polarization of the rhombohedral $[P_R(T_{C'})]$ and tetragonal phases $[P_T(T_{C''})]$ of PZT SC in the vicinity of the triple point influence the ratio of the thermodynamic coefficients β_R/β_T and the phase coexistence for which the thermodynamic and concentration criteria are valid. The thermodynamic study of the three-phase PZT system suggests that there is a certain relation of the aforementioned jumps to the noticeable beak-like bending of the phase boundaries in the x-T diagram (Fig. 2.1a). The convexity of the rhombohedral-tetragonal boundary near the triple point in the x-T diagram of PZT and related solid solutions is concerned with the inequality $P_T(T_{C''}) > P_R(T_{C'})$.

References

- Ye Z-G, Rivera J-P, Schmid H (1991) Electric field and stress-induced phase transition in Cr-Cl boracites. Ferroelectrics 116:251–258
- Ye Z-G (1993) Examples of domain studies of electric field or stress-induced phase transitions in the ferroic crystals of Cr₃B₇O₁₃Cl, Cd₂Nb₂O₇ and Pb(Mg_{1/3}Nb_{2/3})O₃. Ferroelectrics 140:319–326
- Topolov VY, Ye Z-G (1996) Formation of the stress-induced mm2 phase at the ferroelastic antiferroelectric 43m—42m phase transition in Cr–Cl boracite. J Phys: Condens Matter 8:6087–6094
- Ortiz-Lopez J, Luty F (1988) Optical studies of thermal cycling and hysteresis effects in elastic order-disorder phase transformations. I. Pure alkali-metal cyanide crystals. Phys Rev B 37:5452–5460
- Topolov VYu, Turik AV, Fesenko OE, Eremkin VV (1995) Mechanical stresses and three-phase states in perovskite-type ferroelectrics. Ferroelectr Lett Sect 20:19–26
- Topolov VYu (1998) Some features of three-phase states in PbZr_{1-x}Ti_xO₃ crystals. Crystallogr Rep 43:68–73
- Zekria D, Glazer AM (2004) Automatic determination of the morphotropic phase boundary in lead magnesium niobate titanate Pb(Mg_{1/3}Nb_{2/3})_(1-x)Ti_xO₃ within a single crystal using birefringence imaging. J Appl Crystallogr 37:143–149
- 8. Shuvaeva VA, Glazer AM, Zekria D (2005) The macroscopic symmetry of Pb($Mg_{1/3}Nb_{2/3}$)₁ $_{-x}Ti_xO_3$ in the morphotropic phase boundary region (x = 0.25-0.5). J Phys: Condens Matter 17:5709–5723
- Zhu W-M, Guo H-Y, Ye Z-G (2009) Domain structure and phase symmetry of multiferroic BiFeO₃-PbTiO₃ single crystals studied by piezoresponse force microscopy. IEEE Trans Ultrason Ferroelectr Freq Control 56:1569–1573
- Topolov VY, Ye Z-G (2004) Coexistence of morphotropic phases in (1 x)Pb(Mg_{1/3}Nb_{2/3})O₃ xPbTiO₃ solid solutions. Phys Rev B 70:094113–8 p
- Topolov VY (2004) Unique three-phase states in (1 x)Pb(Zn_{1/3}Nb_{2/3})O₃ xPbTiO₃ single crystals. J Phys: Condens Matter 16:2455–2461
- 12. Topolov VY, Balyunis LE, Turik AV, Eremkin VV, Sori BI (1992) S-type twinning (domain) boundaries in PbZrO₃ crystals. Sov Phys—Crystallogr 37:223–226
- Sawaguchi E (1953) Ferroelectricity versus antiferroelectricity in solid solutions of PbZrO₃ and PbTiO₃. J Phys Soc Jpn 8:615–629
- Samara GA (1970) Pressure and temperature dependence of the dielectric properties and phase transitions of the antiferroelectric perovskites: PbZrO₃ and PbHfO₃. Phys Rev B 1:3777–3786

References 119

 Topolov VYu, Balyunis LE, Turik AV, Bah IS, Fesenko OE (1992) Interphase boundaries at cubic-rhombohedral phase transition in PbZrO₃ crystals. Bull Russ Acad Sci Phys 56:1588–1593

- Eremkin VV (1987) Structural phase transitions in single crystals of solid solutions of lead zirconate-titanate. Thesis, Cand. Sci. (Phys. & Math.). Rostov State University, Rostov-on-Don (in Russian)
- Eremkin VV, Smotrakov VG, Fesenko EG (1990) Structural phase transitions in PbZr_{1-x}Ti_xO₃ crystals. Ferroelectrics 110:137–144
- 18. Noheda B, Cox DE, Shirane G, Gao J, Ye Z-G (2002) Phase diagram of the ferroelectric relaxor (1 x)Pb $(Mg_{1/3}Nb_{2/3})O_3 x$ PbTiO₃. Phys Rev B 66:054104–10 p
- Zhang R, Jiang B, Cao W (2003) Single-domain properties of 0.67Pb(Mg1/3Nb2/3)O3– 0.33PbTiO3 single crystals under electric field bias. Appl Phys Lett 82:787–789
- Cao H, Hugo Schmidt V, Zhang R, Cao W, Luo H (2004) Elastic, piezoelectric, and dielectric properties of 0.58Pb(Mg_{1/3}Nb_{2/3})O₃–0.42PbTiO₃ single crystal. J Appl Phys 96:549–554
- 21. La-Orauttapong D, Noheda B, Ye Z-G, Gehring PM, Toulouse J, Cox DE, Shirane G (2002) Phase diagram of the relaxor ferroelectric (1 *x*)Pb(Zn_{1/3}Nb_{2/3})O₃ *x*PbTiO₃. Phys Rev B 65:144101–7 p
- Noheda B (2002) Structure and high-piezoelectricity in lead oxide solid solutions. Curr Opin Solid State Mater Sci 6:27–34
- Yamada Y, Uesu Y, Matsuda M, Fujishiro K, Cox DE, Noheda B, Shirane G (2002) Symmetry of high-piezoelectric Pb based complex perovskites at the morphotropic phase boundary: II. Theoretical treatment. J Phys Soc Jpn 71:966–970
- 24. Bertram R, Reck G, Uecker R (2003) Growth and correlation between composition and structure of $(1 x)Pb(Zn_{1/3}Nb_{2/3})O_3 xPbTiO_3$ crystals near the morphotropic phase boundary. J Cryst Growth 253:212–220
- 25. Topolov VY (2003) Heterophase states in $0.10PbTiO_3-0.90Pb(Zn_{1/3}Nb_{2/3})O_3$ crystals. Phys Solid State 45:1295-1297
- Fousek J, Janovec V (1969) The orientation of domain walls in twinned ferroelectric crystals.
 J Appl Phys 40:135–142
- Turik AV, Chernobabov AI, Topolov VYu (1983) Role of mechanical stresses in ferroelectric phase transitions. Sov Phys—Solid State 25:1640–1641
- Turik AV, Chernobabov AI, Topolov VY (1984) Relaxation of internal mechanical stresses and phase transition thermodynamics in ferroelectrics. Sov Phys—Solid State 26:2176–2177
- Topolov VYu, Turik AV (1990) Elastic effects at the morphotropic phase transition in solid solutions of the PbZr_{1-x}Ti_xO₃ system. Izvestiya SKNTs VSh. Yestestvennye Nauki N 1 (69):72–77 (in Russian)
- Topolov VY, Turik AV (1987) On an elastic interaction between polar phases at phase transitions in ferroelectrics. Deposed at VINITI. Reg. No. 1546-B87 (in Russian)
- 31. Devonshire AF (1949) Theory of barium titanate. Part I. Philos Mag 40:1040-1063
- 32. Devonshire AF (1951) Theory of barium titanate. Part II. Philos Mag 42:1065-1079
- 33. Devonshire AF (1954) Theory of ferroelectrics. Adv Phys 3:85–130
- 34. Kholodenko LP (1971) Thermodynamic theory of barium-titanate-type ferroelectrics. Zinatne, Riga (in Russian)
- 35. Smolensky GA, Bokov VA, Isupov VA, Krainik NN, Pasynkov RE, Sokolov AI, Yushin NK (1985) Physics of ferroelectric phenomena. Nauka, Leningrad (in Russian)
- 36. Nye J (1964) Physical properties of crystals. Clarendon Press, Oxford
- Haun MJ, Zhuang ZQ, Furman E, Jang SJ, Cross LE (1989) Thermodynamic theory of the lead zirconate-titanate solid solution system, part III: Curie constant and sixth-order polarization interaction dielectric stiffness coefficients. Ferroelectrics 99:45–54
- 38. Zheludev IS (1971) Electrical properties. In: Physics of crystalline dielectrics, vol 2. Plenum, New York
- 39. Eremkin VV, Smotrakov VG, Fesenko EG (1989) Phase transitions in the system of solid solutions of lead zirconate-titanate. Fizika Tverdogo Tela 31(6):156–162 (in Russian)
- 40. Choi SW, Shrout TR, Jang DJ, Bhalla AS (1989) Dielectric and pyroelectric properties in the $Pb(Mg_{1/3}Nb_{2/3})O_3 PbTiO_3$ system. Ferroelectrics 100:29–38

 Kuwata J, Uchino K, Nomura S (1981) Phase transitions in the Pb(Zn_{1/3}Nb_{2/3})O₃–PbTiO₃ system. Ferroelectrics 37:579–582

- Bah ST, Smotrakov VG, Fesenko OE (1991) Growth of PbZr_{1-x}Sn_xO₃ single crystals and their phase T, x diagram. Ferroelectrics 124:79–83
- Tarek AS, Smotrakov VG, Kozakov AT, Dem'yanchenko VA, Fesenko OE, Leont'ev NG (1993) Manufacturing and investigation of PbZrO₃ SrZrO₃ crystals solid solutions.
 Izvestiya RAN. Seriya Fizicheskaya 57(3):135–137 (in Russian)
- 44. Noheda B, Cox DE, Shirane G, Guo R, Jones B, Cross LE (2001) Stability of the monoclinic phase in the ferroelectric perovskite PbZr_{1-x}Ti_xO₃. Phys Rev B 63:014103–6 p
- 45. Eitel R, Randall CA (2007) Octahedral tilt-suppression of ferroelectric domain wall dynamics and the associated piezoelectric activity in Pb(Zr, Ti)O3. Phys Rev B 75:094106–8 p
- 46. Topolov VY, Brajesh K, Ranjan R, Panich AE (2017) Plausible domain configurations and phase contents in two- and three-phase BaTiO₃-based lead-free ferroelectrics. J Phys D Appl Phys 50:065307–11 p

Chapter 5 Overlapping Structures and Transition Regions



Abstract Examples of heterogeneous single crystals and conditions for stress relief in them are discussed in terms of the crystallographic method. Heterogeneity is associated with overlapping structures (i.e. the presence of two different crystal structures) and transition regions, for instance narrow bands near domain or interphase boundaries where unit-cell parameters undergo changes. These heterogeneous states differ from those observed in macroscopically large samples at the phase coexistence or at the interaction between ferroelectric polydomain (twinned) regions. Interpretation of experimental results is carried out by taking into account possible versions of changes in the unit-cell parameters.

In this chapter, we consider examples of heterogeneous SCs of relaxor-FE SCs and discuss conditions for stress relief in them. Heterogeneity is associated with overlapping structures (i.e. the presence of two different crystal structures) and transition regions, for instance narrow bands near domain or interphase boundaries where changes in unit-cell parameters take place. These heterogeneous states differ from those observed in macroscopically large samples at the phase coexistence or at the interaction between polydomain (twinned) regions. In this context, the study of possible versions of the unit-cell variations becomes important for an interpretation of experimental results and broadens knowledge in the field of heterogeneous FE materials.

5.1 Overlapping Structures in Pb(Zn_{1/3}Nb_{2/3})O₃

Overlapping (dual) structures were revealed in PZN–xPT SCs [1, 2] with molar concentrations $0 \le x \le 0.08$ and rhombohedral symmetry (R3m) of bulk samples at room temperature. Xu et al. [2] discovered a new phase in bulk PZN SCs by means of high-energy X-ray diffraction. The X-ray beams from electrons accelerated by a voltage of 67 keV [2] were used for a penetration into the inside phase of the SC sample. This inside phase of PZN SC ($phase\ X$ in terms of [2]) clearly differs from the ground phase with the rhombohedral distortion. The phase X is

characterized by a slight tetragonal distortion [1] (unit-cell parameters obey conditions $a_{\rm in}=b_{\rm in}\neq c_{\rm in}$ and $\alpha_{\rm in}=\beta_{\rm in}=\gamma_{\rm in}=90^\circ$, where $c_{\rm in}/a_{\rm in}\approx 1.001$) or by an average cubic lattice [2] with $a_{\rm in}=b_{\rm in}=c_{\rm in}$ and $\alpha_{\rm in}=\beta_{\rm in}=\gamma_{\rm in}=90^\circ$. Hereafter, we use subscript to denote the inside phase, for instance the phase X in the overlapping structure. X-ray diffraction studies [3] show that the difference between the linear unit-cell parameters $a_{\rm in}$, $b_{\rm in}$ and $c_{\rm in}$ in the phase X is less than 0.02%, and the unit-cell parameters of the phase X remain almost constant in a temperature range from 10 to 700 K.

The room-temperature unit-cell parameters measured on PZN SCs at different X-ray penetration depths (i.e. in experiments at different accelerating voltages) are ascribed to different phases (*phase X*, *phase Y* and *phase Z*) [1]. The unit-cell parameters are related to the bulk (phase X) and surface (phases Y and Z) structures of the heterogeneous SC samples in which internal mechanical stress fields can play an important role. X-ray diffraction measurements [1] performed on poled PZN SC samples highlight the distinctions between the unit-cell parameters of the inside and the outer layer, but both the bulk and surface structures at room temperature have rhombohedral distortions. In other words, the unit-cell parameters of the inside and outer (with subscript *out*) phases obey conditions $a_{\rm in} = b_{\rm in} = c_{\rm in}$, $\alpha_{\rm in} = \beta_{\rm in} = \gamma_{\rm in} < 90^{\circ}$, $a_{\rm out} = b_{\rm out} = c_{\rm out} < a_{\rm in}$ and $\alpha_{\rm out} = \beta_{\rm out} = \gamma_{\rm out} < \alpha_{\rm in}$. These conditions also hold for the unit-cell parameters measured recently [2] on PZN-0.045PT and PZN-0.08PT SCs.

As follows from high-energy X-ray diffraction studies [1, 2], the thickness of the outer layer is about (1–5) \times 10⁻⁵ m. The outer layer and the inside phase in PZN–0.045PT and PZN–0.08PT SCs are rhombohedrally distorted so that the unit-cell parameters [2] $a_{\rm in}$ and $\alpha_{\rm in}$ of the inside phase and $a_{\rm out}$ and $\alpha_{\rm out}$ of the outer layer are interrelated by inequalities $a_{\rm in} > a_{\rm out}$ and $\alpha_{\rm in} > \alpha_{\rm out}$.

The existence of two different unit-cell shapes and the average cubic lattice of the phase X were also studied [4, 5] in PMN–xPT SCs with molar concentration x = 0, 0.20 and 0.27. In the range $0 \le x \le 0.27$ the ground state is rhombohedral [6–8] at room temperature. The considerable dependence of the strain on the penetration depth was studied [5] on PMN SCs over a distance of about 3×10^{-4} m. Such a distance undoubtedly exceeds the thickness of the outer layer where the phase X is observed. At small molar concentrations x, the phase X in both PZN–xPT and PMN–xPT SCs is characterized by a ferroelectric polar order without the lattice distortion [2, 4]. This unusual decoupled state is regarded [4] as a special confined form of the above-mentioned rhombohedral (R3m) phase.

X-ray diffuse scattering measurements [9] on PZN–xPT SCs with $x=0,\,0.045$ and 0.08 enabled one to conclude that the main contribution to the intensities comes from static lattice distortions. These distortions stem from local polarized nanosized regions that would appear in SC samples at Burns temperature $T_{\rm d}$, where $T_{\rm d}-T_{\rm C}\sim10^2$ K and $T_{\rm C}$ is Curie temperature of the FE phase transition. It is shown within the framework of the model of planar correlations [9] that the [111]-type polarization is typical of the studied PZN–xPT SCs with $x=0,\,0.045$ and 0.08 at $T<T_{\rm C}$. This polarization is also typical of the polarized nanosized regions in a wide temperature range. However, it remains unclear how the lattice distortions and

polarization characteristics influence the outer and inside phases, their physical properties, evolution, elastic-matching conditions, etc.

Despite the studied structural features of the inside and outer phases, distinctions between the physical properties of these phases as well as links between the crystallographic characteristics and physical properties were not considered in detail in experimental studies. It seems probable that these distinctions influence the physical properties and phase coexistence in SCs near the MPB. In Sect. 5.2, we analyse examples of elastic matching in the overlapped structures in PZN SCs.

5.2 S_j —Interface Relationships in Pb($Zn_{1/3}Nb_{2/3}$)O₃

It is assumed that, in the rhombohedral phases of PZN–xPT SCs, there are different orientation states S_j in which the unit-cell vectors (a, b, c) are arranged approximately along the following directions: ([100], [010], [001]) (j = 1), ([100], [010], [001]) (j = 2), ([100], [010], [001]) (j = 3), ([100], [010], [001]) (j = 4), ([100], [010], [001]) (j = 5), ([100], [010], [001]) (j = 6), ([100], [010], [010]) (j = 7), and ([100], [010], [001]) (j = 8). These directions are represented in the perovskite axes. We note the term 'approximately' because of slight deviations from the aforementioned directions that are caused by shear distortion of the rhombohedral phase. The orientation states S_j can correspond to microdomains [10]. Such microdomains with a size under 10^{-7} m and with the [111]-type polarization are likely to exist in the outer layer [3] where the considerable rhombohedral unit-cell distortion develops. The orientation states S_j are characterized by the distortion matrices $||R_j||$ as follows:

$$||R_{1}|| = ||R_{5}|| = \begin{pmatrix} \mu_{a} & \mu & \mu \\ \mu & \mu_{a} & \mu \\ \mu & \mu & \mu_{a} \end{pmatrix},$$

$$||R_{2}|| = ||R_{6}|| = \begin{pmatrix} \mu_{a} & -\mu & -\mu \\ -\mu & \mu_{a} & \mu \\ -\mu & \mu & \mu_{a} \end{pmatrix},$$

$$||R_{3}|| = ||R_{7}|| = \begin{pmatrix} \mu_{a} & -\mu & \mu \\ -\mu & \mu_{a} & -\mu \\ \mu & -\mu & \mu_{a} \end{pmatrix}, \text{ and }$$

$$||R_{4}|| = ||R_{8}|| = \begin{pmatrix} \mu_{a} & \mu & -\mu \\ \mu & \mu_{a} & -\mu \\ -\mu & -\mu & \mu_{a} \end{pmatrix},$$

$$||R_{4}|| = ||R_{8}|| = \begin{pmatrix} \mu_{a} & \mu & -\mu \\ \mu & \mu_{a} & -\mu \\ -\mu & -\mu & \mu_{a} \end{pmatrix},$$

where the unit-cell distortions $\mu_a = a_R \cos \omega_R / a_C$ and $\mu = a_R \sin \omega_R / a_C$ are expressed in terms of the unit-cell parameters a_R and ω_R of the rhombohedral phase

and a_C of the cubic phase. The unit-cell parameter a_C is assumed to be extrapolated to a temperature at which the overlapped structure is studied.

The inside and outer phases are described by the distortion matrices written in terms of the matrices from (5.1). For instance, the distortion matrix $||N_{ij}||$ of the outer phase in PZN SC is written as

$$||N_{ij}|| = \sum_{j} v_{j} ||R_{j}||,$$
 (5.2)

where v_j is the volume fraction of the S_j region (Table 5.1). The volume fraction v_j can be expressed in terms of the parameters u_R and g_R by analogy with x_R and y_R in Fig. 2.5. The distortion matrix of the inside phase (phase X) in PZN SC is

$$||M_{ij}|| = \begin{pmatrix} v_a & 0 & 0 \\ 0 & v_a & 0 \\ 0 & 0 & v_a \end{pmatrix}, \tag{5.3}$$

where $v_a = a_X/a_C$, and a_X is the unit-cell parameter of the inside phase. The distortion matrices from (5.2) to (5.3) are used for the classification of the interphase boundaries in the overlapping structures. This classification carried out by using the unit-cell parameters of PZN SC [1–3] is illustrated by a series of S_j —interface diagrams (Fig. 5.1). These diagrams are built by analogy with the domain state—interface diagrams considered in Chaps. 2 and 3.

Table 5.1 Characteristics of orientation states S_j in phases that can form overlapping structures in PZN SCs

Inside phase	S_j	v_j	Outer phase	S_j	$ v_j $	Diagrams
Rhombohedral poled	S ₁ or S ₅ S ₂ or S ₆ S ₁ or S ₅ S ₂ or S ₆	$ \begin{vmatrix} m \\ 1 - m \\ m \\ 1 - m \end{vmatrix} $	Rhombohedral poled	S ₃ or S ₇ S ₄ or S ₈ S ₁ or S ₅ S ₂ or S ₆	$ \begin{vmatrix} n \\ 1 - n \\ n \\ 1 - n \end{vmatrix} $	Figure 5.1a Figure 5.1b
X, cubic lattice	_	-	Rhombohedral unpoled	S_1 or S_5 S_2 or S_6	$(1 - u_R)(1 - g_R)$ $(1 - u_R)g_R$ $u_R(1 - g_R)$ u_Rg_R	Figure 5.1c
X, tetragonal lattice	-	-	Rhombohedral unpoled	S_2 or S_6	$(1 - u_R)(1 - g_R)$ $(1 - u_R)g_R$ $u_R(1 - g_R)$ u_Rg_R	Region of the imaginary cone apex [conditions (1.17) are valid] at $0 \le u_R \le 1$ and $0 \le g_R \le 1$

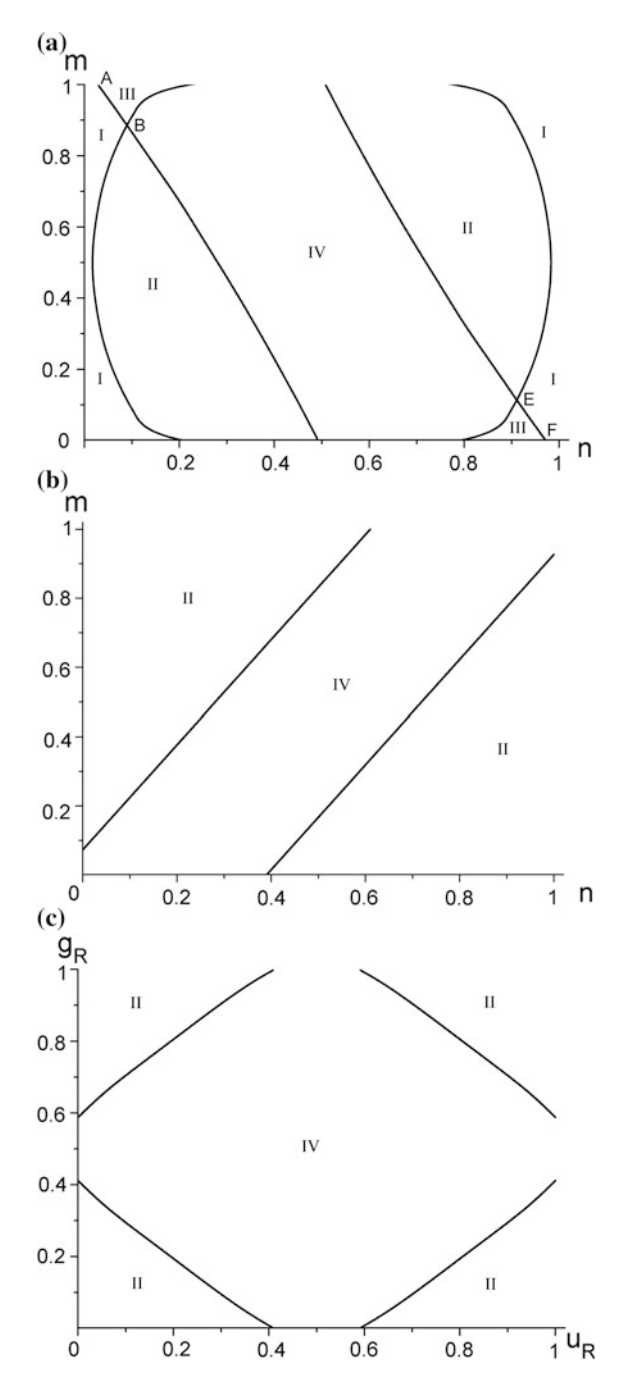


Fig. 5.1 S_J —interface diagrams calculated for poled (**a**, **b**) and unpoled (**c**) PZN SCs at room temperature. Variants of the phase coexistence and orientation states are listed in Table 5.1. Conditions (1.14), (1.15), (1.16) and (1.17) are valid in regions I, II, III and IV, respectively (reprinted from paper by Topolov [12], with permission from the American Physical Society)

The important example of elastic matching of the phases is shown in Fig. 5.1a, where short curves AB and EF represent the volume fractions that obey conditions (1.18) for ZNSPs. The volume fractions n and m of the S_i regions (Table 5.1), that promote complete stress relief, obey the condition $n \approx 1 - m$ in narrow ranges 0.03 < n < 0.09 and 0.91 < n < 0.97. At these volume fractions, the elastic interaction between the orientation states in the adjacent phases becomes like that between non-180° domains in PbZrO₃ SC with the S-type domain boundary [11] in the FE R3m phase. The corresponding orientations of the ZNSPs in the poled PZN SC sample are characterized by normal vectors $n_1(h_1, k_1, l_1) \perp n_2(1/\sqrt{2}, -1/\sqrt{2}, 0)$ with respect to the perovskite unit cell, where $h_1 = k_1$ and $|l_1| \gg h_1$. It should be noted that no other possibility for the formation of the ZNSP is found in the diagrams from Fig. 5.1. In this context, it is assumed that the overlapped structures in PZN SCs undergo some change or reconstruction for a further stress relief. This stress-relief way may differ, for example in variants of elastic matching shown in Fig. 5.1b, c. This assumption also concerns elastic matching of the untwinned tetragonally distorted phase X and the outer rhombohedral phase with various S_i regions in the unpoled PZN SC sample, because the related unit-cell parameters from papers [1, 2] obey conditions (1.17) and no effective stress relief is achieved.

As follows from simple comparison of the diagrams shown in Fig. 5.1a, b the orientation states of the inside phase of PZN SC play the key role in the stress relief in the overlapping structure. Elastic matching of the analogous orientation states in the rhombohedral phases (e.g. S_1 and S_2), as well as the presence of the untwinned phase X result in restricted possibilities of stress relief. As a consequence, the diagrams shown in Fig. 5.1b, c comprise the only real cone region II and the large region IV of the imaginary cone apex. The aforementioned distinctions between the diagrams in Fig. 5.1 take place at almost equal ratios $r_a = a_{\text{out}} \cos \omega_{\text{out}}/(a_{\text{in}} \cos \omega_{\text{in}})$ of the longitudinal distortions and at small differences $\Delta \omega = \omega_{\text{out}} - \omega_{\text{in}} = \alpha_{\text{in}} - \alpha_{\text{out}}$ between the unit-cell shear angles ω_{out} and ω_{in} in the coexisting phases [12].

The diagram that comprises regions II and IV, as shown in Fig. 5.1c is typical of elastic matching in unpoled PZN SC at temperatures 250 K $\leq T \leq$ 350 K and in unpoled PZN-0.045PT and PZN-0.08PT SCs at room temperature. The corresponding diagrams are calculated using the unit-cell parameters measured in work [1, 2, 13]. As follows from the calculated data, the considerable internal stress in PZN-xPT SCs are present at the coexistence of the inside and outer phases even if various orientation states appear in these phases. The presence of the considerable stress is in agreement with experimental results of work [3] where the elastic interaction between the inside and outer layers is compared with the substrate clamping effect on ferroelectric thin films. Xu et al. [3] emphasized the important role of the clamping effect in the decoupling between the lattice distortion and the ferroelectric polarization in PZN SC and noted possible inducing the additional stress in PZN SCs at the phase transition. The stressed state and the strong distortion of the outer layer were noted [5] in the experimental study of the spatially resolved neutron diffraction on unpoled PMN SC.

It should be added that one of the stress-relief mechanisms is associated [14, 15] with misfit dislocations or misfit strains. Misfit dislocations caused by structural phase transitions in solids can be arranged in configurations which lower the elastic energy. As a rule, such dislocations are of the edge character with the Burgers vector lying along the interface and an extra half-plane is related to the crystal part with the smaller spacing. However, a dependence of the misfit energy [15, 16] related to these configurations on a series of factors (e.g. orientation of the interface) remains unknown for SCs of PZN–xPT, PMN–xPT and other FE solid solutions. The possible stress-relief way may be concerned with the misfit strain, i.e. a homogeneous strain of a certain part of the SC sample can lead to the complete elimination of the misfit. This effect takes place in the presence of transition regions [17–21] observed in polydomain and/or heterophase SCs. In Sect. 5.3, we consider examples of the transition regions and conditions for the stress relief in PZN–xPT SCs.

5.3 Transition Regions in $(1 - x)Pb(Zn_{1/3}Nb_{2/3})O_3 - xPbTiO_3$

The transition regions were studied in a series of FE and ferroelastic SCs, for instance, polydomain (twinned) BaTiO₃ [17], KH₂PO₄ [18] and RBa₂Cu₃O_{7-δ} (R = Y, Ho, etc.) [11, 22–25], and heterophase BaTiO₃ [19, 20], Pb₂CoWO₆ [26] and CH₃NH₃Al(SO₄)₂·12 H₂O [21]. As is known from the X-ray and TEM studies [17–21], the transition regions are characterized by continuous changes in the unit-cell parameters. The changes in the unit-cell parameters are accompanied by changes in the physical characteristics of SC parts arranged in different directions from the transition regions. It concerns, for example the transition from one domain type to another, from one twin component to another in polydomain (twinned) SCs, or from phase 1 to 2 in heterophase SCs. Results of work [19, 20] show that the interaction between the regions with the 90° domains at the FE phase transition in BaTiO₃ SC is associated with the transition regions and the mechanical stress field caused by the phase coexistence. Diffused interfaces, caused by the presence of the transition regions in SC samples, are an alternative to fringes between the coexisting phases. The diffused interfaces are energetically more favourable than semicoherent interfaces [14] that can appear in connection with interfacial misfit dislocations.

The crystallographic description of some transition regions in FE and ferroelastic SCs was proposed in a series of papers [12, 25–28]. In this section, we apply the ZNSP concepts to study possibilities of elastic matching of the inside and outer phases of PZN–xPT SCs at the formation of the transition regions.

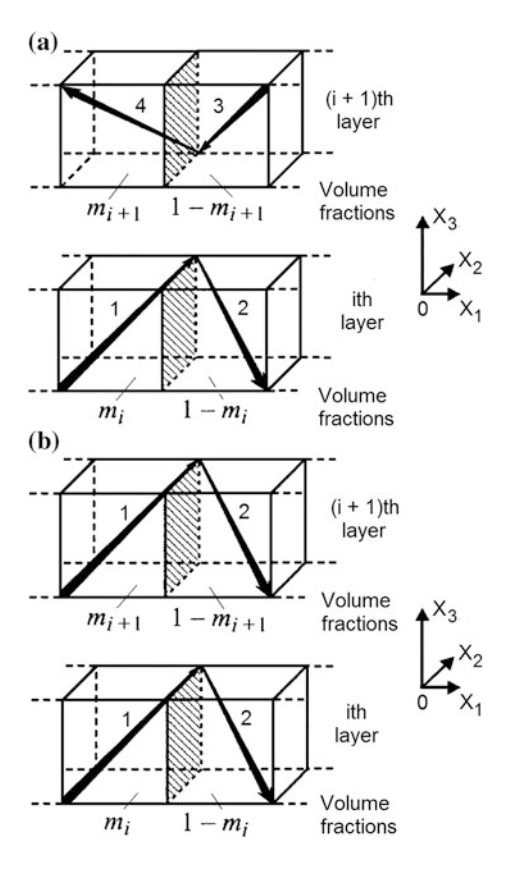
Experimental results [2] on the development of the rhombohedral distortion in the inside and outer phases of PZN–xPT SCs with 0 < x < 0.1 testify to the analogous shape of the curves $\omega = \omega(x)$ for the shear angle in the perovskite unit cell of these phases. The analogy suggests that the shear distortions of the PZN–xPT unit cell change monotonously from the inside to the outer layer at x = const.

The modelling of the transition region is carried out in terms of the unit-cell distortions that change to satisfy conditions for ZNSPs. It is supposed that the transition region in unpoled PZN–xPT SCs represents as a set of layers (i = 1, 2, 3, etc.) separated by the {100}-type planes of the perovskite unit cell (Fig. 5.2). Both the linear unit-cell parameter $a_i = |a_i| = |b_i| = |c_i|$ and the shear angle $\omega_i = 90^\circ - \alpha_i$ change from one layer to other. Each layer is divided into regions that are regarded as orientation states with defined orientations of the unit-cell vectors or the spontaneous polarization vectors.

The distortion matrices of the *i*th and (i + 1)th layers shown in Fig. 5.2a are given by

$$\left\| M_{ab}^{(i)} \right\| = (1/a_C) \begin{pmatrix} a_i \cos \omega_i & a_i \sin \omega_i (2m_i - 1) & a_i \sin \omega_i (2m_i - 1) \\ a_i \sin \omega_i (2m_i - 1) & a_i \cos \omega_i & a_i \sin \omega_i \\ a_i \sin \omega_i (2m_i - 1) & a_i \sin \omega_i & a_i \cos \omega_i \end{pmatrix}$$

Fig. 5.2 Two versions of the arrangement of adjacent layers in transition regions of PZN–xPT SCs. Co-ordinate axes OX_j are parallel to the perovskite unit-cell axes in the cubic phase, and directions of the spontaneous polarization in the orientation states S_j (j = 1, 2, 3, and 4) are shown by arrows



and

$$\begin{split} \left\| \mathcal{M}_{ab}^{(i+1)} \right\| &= (1/a_C) \\ &\times \begin{pmatrix} a_{i+1} \cos \omega_{i+1} & a_{i+1} \sin \omega_{i+1} (2m_{i+1}-1) & -a_{i+1} \sin \omega_{i+1} (2m_{i+1}-1) \\ a_{i+1} \sin \omega_{i+1} (2m_{i+1}-1) & a_{i+1} \cos \omega_{i+1} & a_{i+1} \sin \omega_{i+1} \\ -a_{i+1} \sin \omega_{i+1} (2m_{i+1}-1) & -a_{i+1} \sin \omega_{i+1} & a_{i+1} \cos \omega_{i+1} \end{pmatrix}, \end{split}$$

respectively. In accordance with the alternation of the layers (Fig. 5.2), the distortion matrices of the (i+2)th, (i+4)th, ..., (i+2p)th layers are written like $\|M_{ab}^{(i)}\|$ in terms of the unit-cell parameters with subscripts i+2, i+4, ..., i+2p, respectively. The distortion matrices of the (i+3)th, ..., (i+2p+1)th layers are written by analogy with $\|M_{ab}^{(i+1)}\|$ in terms of the unit-cell parameters with subscripts i+3, ..., i+2p+1, respectively. The distortion matrix $\|M_{X,ab}\|$ of the phase X with the cubic lattice is written in (5.3). The distortion matrices of the ith and (i+p)th layers of the transition region shown in Fig. 5.2b are $\|M_{ab}^{(i)}\|$ and

$$\begin{split} \left\| M_{ab}^{*(i+p)} \right\| &= & (1/a_C) \\ &\times \begin{pmatrix} a_{i+p} \cos \omega_{i+p} & a_{i+p} \sin \omega_{i+p} \left(2m_{i+p} - 1 \right) & a_{i+p} \sin \omega_{i+p} \left(2m_{i+p} - 1 \right) \\ a_{i+p} \sin \omega_{i+p} \left(2m_{i+p} - 1 \right) & a_{i+p} \cos \omega_{i+p} & a_{i+p} \sin \omega_{i+p} \\ a_{i+p} \sin \omega_{i+p} \left(2m_{i+p} - 1 \right) & a_{i+p} \sin \omega_{i+p} & a_{i+p} \cos \omega_{i+p} \end{pmatrix}, \end{split}$$

respectively, where p = 1, 2, ...

Elements of the $||D_{ab}^{(i, i+1)}||$ matrix are written in the form similar to that shown in (1.7):

$$D_{ab}^{(i,i+1)} = \sum_{f=1}^{3} \left(M_{af}^{(i+1)} M_{bf}^{(i+1)} - M_{af}^{(i)} M_{bf}^{(i)} \right)$$
 (5.4)

for the layers shown in Fig. 5.2a or

$$D_{ab}^{(i,i+1)} = \sum_{f=1}^{3} \left(M_{af}^{*(i+1)} M_{bf}^{*(i+1)} - M_{af}^{(i)} M_{bf}^{(i)} \right)$$
 (5.5)

for the layers in Fig. 5.2b. These layers are matched along the ZNSPs as conditions [12, 28]

$$\det \left\| D_{ab}^{(i,i+1)} \right\| = 0 \quad \text{and} \quad J^{(i,i+1)} < 0 \tag{5.6}$$

hold. We mention that conditions (5.6) are similar to conditions (1.18) formulated for planar interphase boundaries, but now the matrix elements $D_{ab}^{(i,i+1)}$ are taken from (5.4) [or from (5.5)], and $J^{(i,i+1)}$ is expressed in terms of $D_{ab}^{(i,i+1)}$ is as follows:

$$J^{(i,i+1)} = \begin{vmatrix} D_{11}^{(i,i+1)} & D_{12}^{(i,i+1)} \\ D_{21}^{(i,i+1)} & D_{22}^{(i,i+1)} \end{vmatrix} + \begin{vmatrix} D_{22}^{(i,i+1)} & D_{23}^{(i,i+1)} \\ D_{32}^{(i,i+1)} & D_{33}^{(i,i+1)} \end{vmatrix} + \begin{vmatrix} D_{33}^{(i,i+1)} & D_{33}^{(i,i+1)} \\ D_{13}^{(i,i+1)} & D_{11}^{(i,i+1)} \end{vmatrix}$$

$$(5.7)$$

The further simplification of conditions (5.4)–(5.7) is possible on assumption that the volume fractions related to the orientation states in all the layers are equal, i.e. $m_i = 1/2$, where i = 1, 2, ..., and N at the coexistence of the rhombohedral (inside and outer) phases, i = 2, 3, ..., and N or i = 1, 2, ..., and N - 1 at the coexistence of the rhombohedral (outer) and X phases, and N is the total number of the layers in the transition region. Due to this simplification, the location of the interfaces $x_1 = \text{const}$ in each layer (Fig. 5.2) remains almost unchanged over the whole transition region. The structures '... $-S_4 - S_1 - S_4 - S_1 - ...$ ' or '... $-S_3 - S_2 - S_3 - S_2 - ...$ ' (Fig. 5.2a) and '... $-S_1 - S_1 - ...$ ' or '... $-S_2 - S_2 - ...$ ' (Fig. 5.2b) can be regarded as structures with the variable unit-cell parameters over the transition region. As a consequence, for both the systems of the layers shown in Fig. 5.2, determinant from conditions (5.6) is given by

$$\det \left\| D_{ab}^{(i,i+1)} \right\| = \left| \begin{array}{ccc} D_{11}^{(i,i+1)} & 0 & 0 \\ 0 & D_{22}^{(i,i+1)} & D_{23}^{(i,i+1)} \\ 0 & D_{23}^{(i,i+1)} & D_{22}^{(i,i+1)} \end{array} \right|.$$

The adjacent *i*th and (i + 1)th layers in the transition region are separated by the ZNSP so that the unit-cell parameters of these layers obey conditions (5.6). Relationships between the unit-cell parameters of the *i*th and (i + 1)th layers in this case are written as follows:

$$a_{i+1}\cos\omega_{i+1} = a_i\cos\omega_i \tag{5.8}$$

or

$$a_{i+1}(\cos\omega_{i+1} + \sin\omega_{i+1}) = a_i(\cos\omega_i - \sin\omega_i)$$
 (5.9)

or

$$a_{i+1}(\cos\omega_{i+1} - \sin\omega_{i+1}) = a_i(\cos\omega_i + \sin\omega_i)$$
 (5.10)

for the orientation states shown in Fig. 5.2a, and (5.8) and

$$a_{i+1}(\cos\omega_{i+1} + \sin\omega_{i+1}) = a_i(\cos\omega_i + \sin\omega_i)$$
 (5.11)

or

$$a_{i+1}^{2}\cos\omega_{i+1}(\cos\omega_{i+1} + 2\sin\omega_{i+1}) = a_{i}^{2}\cos\omega_{i}(\cos\omega_{i} + 2\sin\omega_{i})$$
 (5.12)

for the orientation states shown in Fig. 5.2b. In the presence of the phase X, it is additionally assumed that equalities $a_i = a_X$ and $\omega_i = 0$ hold for the layers with i = 1 or i = N.

Examples of variations of the unit-cell parameters, for which one of (5.8)–(5.12) holds, are considered in papers [12, 28]. These variations suggest that there are different stress-relief ways in unpoled PZN–xPT SCs. The interfaces separating the adjacent layers (Fig. 5.2) at these variations obey conditions (5.6) for ZNSPs and are parallel to the perovskite-cell {100} planes with accuracy to 3%. This orientation almost coincides with the orientation determined [29, 30] for the 71° (109°) domain walls in rhombohedral phases of perovskite-type FEs.

The arrangement of the polydomain layers shown in Fig. 5.2b is of an independent interest due to the simultaneous fulfilment of (5.11) and (5.12) over the whole transition region in PZN SC, while in PZN-xPT SCs with x = 0.045 and 0.08, the number of the similar conditions is three and two, respectively. This circumstance and the possibility of the formation of ZNSPs in the presence of four orientation states (see Fig. 5.2a) suggest that the overlapped structure with two rhombohedral phases and the related transition regions in PZN-xPT SCs with $x \geq 0.045$ arise from a stress field affected by the neighbouring FE tetragonal (P4mm) phase [2, 31].

5.4 Stress Relief at Variable Unit-Cell Parameters

In this chapter, we have analysed examples of elastic matching of the related phases in the overlapping structure and proposed the crystallographic description of the transition region that can also be concerned with the overlapped structure. A system of the S_j —interface diagrams is put forward to describe the role of the orientation states in the formation of the overlapping structure in PZN SCs. Conditions for complete stress relief in PZN–xPT SCs are examined at the formation of the overlapped structure and in the transition region, and some versions of the unit-cell behaviour are taken into consideration to describe specifics of elastic matching. It is shown that the stress-relief mechanisms depend on the orientation states in the FE rhombohedral phases (Table 5.1) or on variants of the unit-cell behaviour [see (5.8)–(5.12)] over the transition region. The results discussed in this chapter develop the elastic-matching concept (Sect. 1.1) and show potential applications of the crystallographic method described in Chap. 1.

References

- Xu G, Zhong Z, Bing Y, Ye Z-G, Stock C, Shirane G (2003) Ground state of the relaxor ferroelectric Pb(Zn_{1/3}Nb_{2/3})O₃. Phys Rev B 67:104102–104105
- 2. Xu G, Hiraka H, Shirane G, Ohwada K (2004) Dual structures in (1-x)Pb $(Zn_{1/3}Nb_{2/3})O_3-x$ PbTi O_3 ferroelectric relaxors. Appl Phys Lett 84:3975–3977
- Xu G, Zhong Z, Bing Y, Ye Z-G, Stock C, Shirane G (2004) Anomalous phase in the relaxor ferroelectric Pb(Zn_{1/3}Nb_{2/3})O₃. Phys Rev B 70:064107–6
- Xu G, Viehland D, Li JF, Gehring PM, Shirane G (2003) Evidence of decoupled lattice distortion and ferroelectric polarization in the relaxor system PMN–xPT. Phys Rev B 68:212410–212414
- Conlon KH, Luo H, Viehland D, Li JF, Whan T, Fox JH, Stock C, Shirane G (2004) Direct observation of the near-surface layer in Pb(Mg_{1/3}Nb_{2/3})O₃ using neutron diffraction. Phys Rev B 70:172204–4
- 6. Noheda B, Cox DE, Shirane G, Gao J, Ye Z-G (2002) Phase diagram of the ferroelectric relaxor (1 x)Pb(Mg_{1/3}Nb_{2/3})O₃–xPbTiO₃. Phys Rev B 66:054104–054110
- 7. Shuvaeva VA, Glazer AM, Zekria D (2005) The macroscopic symmetry of $Pb(Mg_{1/3}Nb_{2/3})_1 _xTi_xO_3$ in the morphotropic phase boundary region (x = 0.25-0.5). J Phys Condens Matter 17:5709–5723
- 8. Singh AK, Pandey D, Zakharko O (2006) Powder neutron diffraction study of phase transitions in and a phase diagram of $(1-x)[Pb(Mg_{1/3}Nb_{2/3})O_3] xPbTiO_3$. Phys Rev B 74:024101–024118
- 9. Xu G, Zhong Z, Hiraka H, Shirane G (2004) Three-dimensional mapping of diffuse scattering in Pb(Zn_{1/3}Nb_{2/3})O₃–xPbTiO₃. Phys Rev B 70:174109–174110
- Mulvihill ML, Cross LE, Cao W, Uchino K (1997) Domain-related phase transition like behavior in lead zinc niobate relax or ferroelectric single crystals. J Am Ceram Soc 80:1462–1468
- Ossipyan YUA, Afonikova NS, Parsamyan TK, Shekhtman VSH, Shmyt'ko IM (1988) Structure of boundaries between twins and twin complexes in YBa₂Cu₃O_{7-x} single crystals. Piss'ma v ZhETF 47:501–504 (in Russian)
- 12. Topolov VYu (2005) Heterophase states and dual structures in (1 x)Pb $(Zn_{1/3}$ Nb_{2/3})O₃-xPbTiO₃ single crystals. Phys Rev B 71:134103–134110
- Lebon A, Dammak H, Calvarin G, Ould Ahmedou I (2002) The cubic-to-rhombohedral phase transition of Pb(Zn_{1/3}Nb_{2/3})O₃: a high-resolution X-ray diffraction study on single crystals. J Phys Condens Matter 14:7035–7044
- Shiflet GJ (1986) Low energy dislocation structures caused by phase transformation. Mater Sci Eng 81:61–100
- Van der Merwe JH (1991) Misfit dislocation generation in epitaxial layers. Crit Rev Solid State Mater Sci 17:187–209
- Jesser WA, Kuhlmann-Wilsdorf D (1967) On the theory of interfacial energy and elastic strain of epitaxial overgrowths in parallel alignment on single crystal substrates. Physica Status Solidi 19:95–105
- Afonikova NS, Shekhtman VSH, Shmyt'ko IM (1985) Crystal-geometrical aspects of domain and domain complex conjugates and structure memory in BaTiO₃. Fizika Tverdogo Tela 27:3201–3207 (In Russian)
- 18. Afonikova NS, Borovikov VV, Shmyt'ko IM (1987) Structure of interphase and interdomain boundaries in KDP. Fizika Tverdogo Tela 29:813–817 (in Russian)
- Malis T, Gleither H (1979) On the structure of the ferroelectric-paraelectric transformation interface in barium titanate. I. Basic structure and characteristics. J Appl Phys 50:4920–4923
- Malis T, Gleither H (1979) On the structure of the ferroelectric-paraelectric transformation interface in barium titanate. II. Influence of domain boundaries. Ibid. 4924–4927
- Bagautdinov BSH, Glushkov VF, Magataev VK, Shmyt'ko IM (1991) Structural aspects of the phase transition in MASD crystals. Fizika Tverdogo Tela 33:3128–3136 (in Russian)

References 133

22. Shmyt'ko I, Shekhtman V, Ossipyan YU, Afonikova N (1989) Twin structure and structure of twin boundaries in 1–2–3–O_{7–x} crystals. Ferroelectrics 97:151–170

- Hiroi Z, Takano M, Ikeda Y, Takeda Y, Bando Y (1988) Coherent intergrowth structure of tetragonal and orthorhombic Ba₂YCu₃O_{7-x} observed by transmission electron microscopy. Jpn J Appl Phys Pt 2(27):L141–L144
- Ossipyan YuA, Afonikova NS, Borodin VA, Chernyshova LI, Shekhtman VSH, Shmyt'ko IM
 Quasitwins in HoBa₂Cu₃O_{7-x} single crystals. Fizika Tverdogo Tela 31(1):200–204
- 25. Topolov VYu, Fesenko EG (1990) Transition regions in $RBa_2Cu_3O_{7-\delta}$ crystals. Supercond Phys Chem Technol 3:927–932
- Topolov VYu, Rabe H, Schmid H (1993) Mechanical stresses and transition regions in polydomain Pb₂CoWO₆ crystals. Ferroelectrics 146:113–121
- Topolov VYu (1993) Crystallographic interpretation of transitional regions in twinned crystals. Ferroelectrics 140:313–318
- 28. Topolov VYu (2005) Dual structures and transition regions in $xPbTiO_3 (1 x)$ $Pb(Zn_{1/3}Nb_{2/3})O_3$ crystals. Phys Solid State 47:1346–1352
- Fousek J, Janovec V (1969) The orientation of domain walls in twinned ferroelectric crystals.
 J Appl Phys 40:135–142
- Balyunis LE, Topolov VYu, Bah IS, Turik AV (1993) The S-type domain and twin boundaries in plate-like PbZrO₃ crystals having complicated twinned structures. J Phys Condens Matter 5:1419–1426
- 31. La-Orauttapong D, Noheda B, Ye Z-G, Gehring PM, Toulouse J, Cox DE, Shirane G (2002) Phase diagram of the relaxor ferroelectric (1 *x*)Pb(Zn_{1/3}Nb_{2/3})O₃–*x*PbTiO₃. Phys Rev B 65:144101–7 p

Chapter 6 Relations Between Domain States and Heterophase Structures in Lead-Free Ferroelectric Solid Solutions



Abstract Examples of domain structures and elastic matching of phases in a few systems of lead-free perovskite-type ferroelectric solid solutions are described by taking into account the crystallographic method and model concepts on heterophase samples. Features of heterophase (two- or three-phase) states and phase contents in the lead-free systems near the morphotropic phase boundary are discussed, and some variants of elastic matching of polydomain phases and heterophase regions are considered. Diagrams that link volume fractions of specific domain types and phase contents at complete stress relief in heterophase samples near the morphotropic phase boundary are analysed, and calculated results on the phase contents are in agreement with experimental data.

Numerous examples of heterophase states analysed in Chaps. 2–5 are related to lead-containing FE solid solutions, for instance, PZT, PMN–xPT and PZN–xPT. These solid solutions with compositions near the MPB exhibit high piezoelectric performance, considerable electromechanical coupling [1–3], various DSs and heterophase structures [4–6]. However, the lead-containing FE materials are toxic and volatile during processing and, therefore, can have a negative influence on the environment and further applications. In the last decades, there is an increasing need to use novel lead-free FE materials [7–10] instead of conventional lead-containing FE ceramics and SCs from the viewpoint of the environmental impact, technological problems, and predictable physical properties and related parameters.

An important problem in modern materials science and physics of active dielectrics is to develop new eco-friendly FE and piezoelectric materials whose physical properties [10–12] can be comparable to the properties of conventional lead-based FE materials [13–16]. The most widely studied lead-free FE solid solutions are based on one of the following compounds with the perovskite-type structure: $(K_xNa_{1-x})NbO_3$, $(Na_{1/2}Bi_{1/2})TiO_3$ (NBT) or $BaTiO_3$ [7–12]. In the literature, there are full sets of room-temperature electromechanical constants measured on domain-engineered lead-free FE SCs, see, for instance [11, 12]. These SCs poled along [001] of the perovskite unit cell are of significant interest due to large values

of the piezoelectric coefficients d_{3j} , h_{3j} and g_{3j} , electromechanical coupling factors k_{33} , k_t , and other parameters which exceed the similar parameters of many poled FE ceramics of the PZT and PbTiO₃ types [15, 16].

In this chapter, we discuss examples of the DSs and elastic matching of phases in a few systems of lead-free perovskite-type FE solid solutions. We apply the crystallographic method developed in Chaps. 2 and 4 to interpret features of heterophase states and phase contents in the lead-free systems near the MPB.

6.1 Phase Coexistence in $(1 - x)(Na_{1/2}Bi_{1/2})TiO_3 - xBaTiO_3$

The $(1-x)(\mathrm{Na_{1/2}Bi_{1/2}})\mathrm{TiO_3}$ – $x\mathrm{BaTiO_3}$ (NBT– $x\mathrm{BT}$) system [17] is of interest due to the FE and piezoelectric properties that depend on the composition, temperature, poling conditions and other factors. The NBT crystal structure has been under discussion after high-resolution diffraction experiments. These experiments suggested a monoclinic structure (Cc symmetry) of NBT instead of the conventional rhombohedral structure (R3c symmetry) at room temperature [18]. However, as follows from work [19], the monoclinic phase with the Cc symmetry does not correspond to the ground state, but this phase is a manifestation of a local in-phase tilt disorder. The important piezoelectric properties of NBT–xBT near the MPB were reported by Takenaka et al. [20], and the composition at x = 0.06 is of specific interest for piezotechnical applications. By analogy with PZT [13–16], Takenaka et al. considered a coexistence of the FE rhombohedral and FE tetragonal phases in NBT–xBT at the critical composition [20].

According to results [17], the following variants of the phase coexistence are observed in NBT–*x*BT near the MPB at room temperature:

- (i) FE monoclinic + FE rhombohedral phases in annealed samples at x = 0.05,
- (ii) FE tetragonal + FE rhombohedral phases in poled samples at x = 0.06-0.065, and
- (iii) FE tetragonal and paraelectric cubic phases in annealed samples at x = 0.07.

6.1.1 Domain States and Elastic Matching of Phases

To interpret features of the phase coexistence in NBT–xBT [21], we consider an SC sample (or a ceramic grain) that contains the aforementioned phases separated by planar interphase boundaries, see the schematics in Fig. 6.1. The FE phases are split into domains with unit-cell orientations shown in Fig. 6.1. The monoclinic phase (Fig. 6.1a) and tetragonal phase (Fig. 6.1b, c) are represented by the following regions: the main region (polydomain) and the interlayer (single domain). It is assumed that the volume fraction of the interlayer is small in comparison to the volume fraction of the adjacent region [21], i.e. conditions $v_m^* \rightarrow 0$ (Fig. 6.1a) and $v_t^* \rightarrow 0$ (Fig. 6.1b, c) hold.

Validity of conditions (1.18) for the ZNSPs and complete stress relief in the heterophase structure shown in Fig. 6.1, a is examined using the distortion matrices of the rhombohedral and monoclinic phases. We remind the reader that some examples of the distortion matrices of the polydomain FE phase are given in Sects. 2.1 and 2.2. After the examination of conditions (1.18), we find optimal volume fractions of specific domain types (for instance, $(x_r; y_r)$ pairs for the rhombohedral phase, see Fig. 6.1a). Conditions (1.18) are then examined at the boundary that separates the rhombohedral + monoclinic region at the optimal volume fractions of the domains therein, and the interlayer monoclinic phase (see the middle part of Fig. 6.1a). Based on these results, we study links between the volume fraction of several domain types in the rhombohedral phase and the volume fraction of the coexisting monoclinic phase. The similar two-stage examination is also applied to the heterophase structures shown in Fig. 6.1b and c.

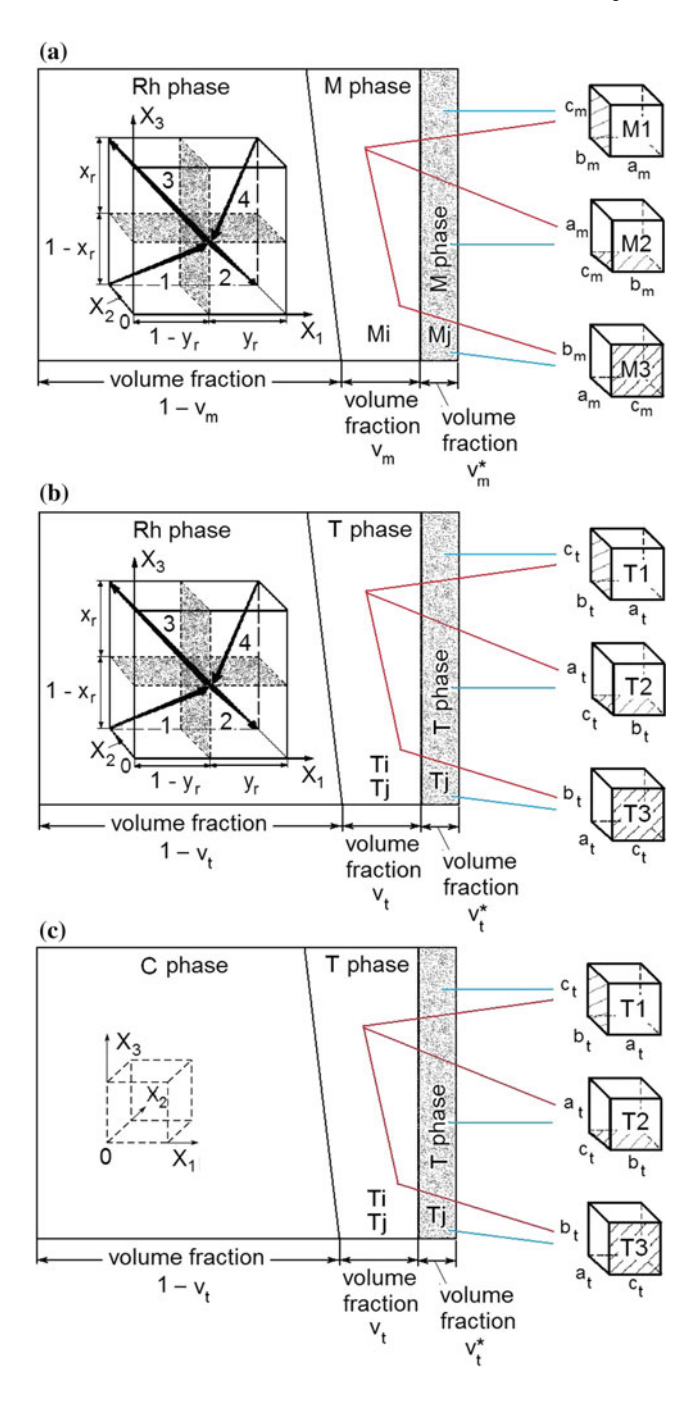
In our analysis, we use experimental values of the room-temperature unit-cell parameters of NBT-xBT [6, 21].

6.1.2 Phase Contents Near the Morphotropic Phase Boundary

Our results on the heterophase structure shown in Fig. 6.1a are given in Table 6.1. As follows from Table 6.1, the single-domain monoclinic phase (Mi region in Fig. 6.1a) can coexist with the rhombohedral phase (Rh region in Fig. 6.1a) that is split into domains of two types. The tendency '1 + 2 domain types' is observed at six various combinations of the domain types Mi–Mj of the monoclinic phase including its interlayer. A boundary separating the Mi and Mj regions in Fig. 6.1, a plays the role of the interphase boundary and domain wall simultaneously. As follows from our analysis of elastic matching of the adjacent regions in NBT–0.05BT, complete stress relief is achieved in the presence of the single-domain monoclinic phase in the main two-phase region (see Fig. 6.1a, middle part).

An important feature of the phase coexistence in NBT-0.05BT consists in a wide range of permissible volume fractions of the monoclinic phase v_m (see the fifth column in Table 6.1), and this coexistence leads to average $\langle v_m \rangle$ values that are also found in the wide range, see the sixth column in Table 6.1. In our opinion, distortions of the single-domain monoclinic phase lead to the considerable variations of $\langle v_m \rangle$ in heterophase samples. For NBT-0.05BT at room temperature, the 'overall' average volume fraction of the monoclinic phase is $\langle v_m \rangle = 0.558$ (see footnote b in Table 6.1), and the $\langle v_m \rangle$ value is in agreement with the experimental value $v_m = 0.60$ [17].

In the case of the tetragonal–rhombohedral phase coexistence, we assume that the tetragonal phase is split into the T2 domain (volume fraction n_t) and T3 domain (volume fraction $1 - n_t$), and the interlayer domain is oriented as T2 (see Fig. 6.1b). Elastic matching of the phases enables us to achieve complete stress



∢Fig. 6.1 Schematic arrangement of the rhombohedral (Rh) + monoclinic (M) **a** rhombohedral (Rh) + tetragonal (T) **b** and cubic (C) + tetragonal (T) phases **c** Orientations of domains (mechanical twins) in the FE monoclinic and tetragonal phases are shown on right sides of schematics. Orientations of domains (mechanical twins) in the FE rhombohedral phase are shown by means of spontaneous polarization vectors in left parts of **a** and **b**. a_m , b_m and c_m are linear unit-cell parameters of the monoclinic phase, a_t , $b_t = a_t$ and c_t are linear unit-cell parameters of the tetragonal phase. v_m is the volume fraction of the monoclinic phase in the two-phase state (**a**), and v_t is the volume fraction of the tetragonal phase in the two-phase states (**b** and **c**). Interlayer phases with volume fractions v_m * and v_t * are shown as shaded areas. Co-ordinate axes OX_j are parallel to the unit-cell vectors in the paraelectric cubic phase (reprinted from paper by Topolov et al. [21], with permission from Taylor & Francis)

Table 6.1 Calculated volume fractions of the M phase at the Rh–M phase coexistence in annealed NBT–0.05BT samples. Notations of domain types are shown in Fig. 6.1 (reprinted from paper by Topolov et al. [21], with permission from Taylor & Francis)

Domain type in the monoclinic phase (Mi	Domain type in the interlayer monoclinic phase	Volume-fraction parameters in the rhombohedral phase		Calculated volume fraction of the monoclinic	Average volume fraction of the monoclinic
region)		χ_r	y_r	phase v_m	phase < <i>v</i> _m >
M1	M2	0	0.781	_a	
		0	0.141	_a	
		1	0.219	0.0807	
		1	0.859	0.907	0.517
		0.152	0	0.562	
		0.765	0	_a	
		0.236	1	_a	
		0.848	1	_a	
M1	M3	0	0.781	0.937	
		0	0.141	0.569 or 0.952	
		1	0.219	0.0197 or 0.995	
		1	0.859	0.106 or 0.959	0.736
		0.152	0	0.983	
		0.765	0	0.995	
		0.236	1	0.8423	
		0.848	1	_a	
M2	M1	0	0.0776	0.382 or 0.967	
		0	0.922	0.169 or 0.996	
		1	0.229	0.935	
		1	0.771	0.706	0.669
		0.219	0	0.937	
		0.859	0	0.569 or 0.952	
		0.294	1	0.0197 or 0.995	
		0.859	1	0.106 or 0.959	

(continued)

Table 6.1 (continued)

Domain type in the monoclinic phase (Mi	Domain type in the interlayer monoclinic	Volume-fraction parameters in the rhombohedral phase		Calculated volume fraction of the monoclinic	Average volume fraction of the monoclinic
region) ph	phase	χ_r	y_r	phase v_m	phase < <i>v</i> _m >
M2	M3	0	0.0776	0.166	
		0	0.922	0.321	
		1	0.229	0.190	
		1	0.771	_a	0.333
		0.219	0	_a	
		0.859	0	_a	
		0.294	1	0.0807	
		0.859	1	0.907	
M3	M1	0	0.0776	0.236	
		0	0.922	0.678	
		1	0.229	_a	
		1	0.779	_a	0.318
		0.0776	0	0.321	
		0.922	0	0.165	
		0.229	1	0.190	
		0.771	1	_a	
M3	M2	0	0.0776	0.996	
		0	0.922	0.976	
		1	0.229	0.848	
		1	0.779	_a	0.774 ^b
		0.0776	0	0.162 or 0.996	
		0.922	0	0.382 or 0.967	
		0.229	1	0.935	
		0.771	1	0.706	

^aConditions (1.18) are violated in the presence of the polydomain rhombohedral phase with the volume-fraction parameters (x_r, y_r) given in the same line

relief in the presence of the single-domain rhombohedral phase [21]. As follows from work [21], the average volume fraction of the tetragonal phase is $\langle v_t \rangle = 0.771$ (at x = 0.060) or $\langle v_t \rangle = 0.812$ (at x = 0.065), i.e. minor changes are observed near the MPB. It should be noted that the aforementioned $\langle v_t \rangle$ values are consistent with the experimental volume fraction of the tetragonal phase $v_t = 0.73$ [17] in poled NBT-0.065BT samples.

^bBased on values of $\langle v_m \rangle$ related to combinations of domain types M1–M2, M1–M3, ..., M3–M2, we obtain the 'overall' average volume fraction of the monoclinic phase $\langle v_m \rangle = 0.558$

6.1.3 Anisotropy of Unit-Cell Distortions and Heterophase Structures

The cubic–tetragonal phase coexistence in annealed NBT–0.070BT samples is analysed using the schematic from Fig. 6.1c. It is assumed that the tetragonal phase is split into the T2 (volume fraction n_t) and T3 domains (volume fraction $1 - n_t$), and the interlayer domain is oriented as T2. In the main heterophase region, the optimal volume fraction n_t , which obeys conditions (1.18) for ZNSPs, can be either 0.722 or 0.276. Then, the corresponding volume fractions of the tetragonal phase are $v_t = 0.829$ or 0.651, and the average value is $\langle v_t \rangle = 0.740$. It is seen that the volume fractions v_t are located in a narrower range in comparison to the volume fractions of the monoclinic phase v_m shown in Table 6.1. This can be concerned with specifics of the spontaneous strains of the perovskite unit cells in the FE phases of NBT–xBT near the MPB.

Our comparison of the volume fractions of the phases shown in Fig. 6.1 suggests that replacing the FE rhombohedral phase with the paraelectric cubic phase and poling the sample cannot give rise to considerable changes in the volume fraction of the adjacent tetragonal phase v_t . It looks probable that an appreciable anisotropy of the unit-cell distortions in the tetragonal phase (i.e. $\varepsilon_c I \varepsilon_a \approx 1.002$ at x = 0.065 and $\varepsilon_{cc} \varepsilon_a \approx 1.001$ at x = 0.070) [21] strongly influences relations between volume fractions of specific domain types and coexisting phases in NBT–xBT irrespective of the prehistory of the samples.

As follows from work [21], various possibilities of complete stress relief are observed in different two-phase states (i.e. rhombohedral-monoclinic and tetragonal-rhombohedral), and this feature is accounted for by the anisotropic unit-cell distortions of the major phase, either monoclinic or tetragonal. It should be added that the interlayer single-domain phase plays the passive role, and the volume fraction of this phase can be neglected [21].

6.2 Phase Coexistence in $Ba(Ti_{1-x}Ce_x)TiO_3$

Poled lead-free FE BaTiO₃-based ceramic samples are of interest due to their important piezoelectric properties [7–12]. A good example of the active influence of the modifying ion on the piezoelectric response is concerned with FE solid solutions of the Ba($Ti_{1-x}Ce_x$) TiO_3 system. Poled ceramics of this system with compositions near the MPB are of interest because the piezoelectric properties [12] are comparable to the properties of the conventional lead-containing FE ceramics such as PZT [13–16], ZTS and PCR [16]. A detailed structural characterization of the Ba ($Ti_{1-x}Ce_x$) TiO_3 system at various molar concentrations x and an analysis of heterophase states near the MPB are carried out in work [22]. In Sect. 6.2, we discuss an influence of some non-180° domain types on heterophase structures and phase contents in Ba($Ti_{1-x}Ce_x$) TiO_3 .

6.2.1 Relations Between Domain and Heterophase States Near the Morphotropic Phase Boundary

An interesting example of the heterophase state in $Ba(Ti_{1-x}Ce_x)TiO_3$ is related to x = 0.02. As follows from experimental results [22] for = 0.02, the FE tetragonal (*P4mm* symmetry) and FE orthorhombic (*Amm*2 symmetry) phases coexist at room temperature. The schematic of a possible heterophase structure is shown in Fig. 6.2, a. Hereafter, 'I' in Fig. 6.2a is the orthorhombic phase, 'II' is the tetragonal phase and 'I*' is the single-domain interlayer (orthorhombic phase). It is assumed that the coexisting phases I + II are split into non-180° domains whose orientations are shown in Fig. 6.2b, c.

In a case of similar orientations of the crystallographic axes of domains in the adjacent phases (as shown in Figs. 6.2b, c), conditions (1.18) for ZNSPs at the coexistence of the tetragonal and orthorhombic phases are valid at volume fractions

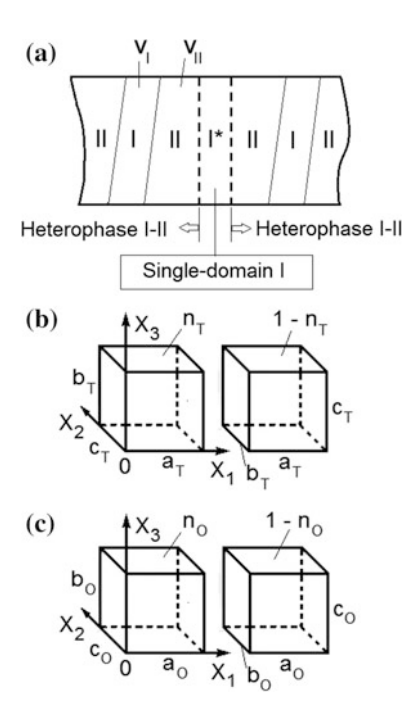


Fig. 6.2 Schematic of heterophase regions **a** and orientations of domain (twins) in the tetragonal **b** and orthorhombic **c** phases. v_I and v_{II} are volume fractions of phases I and II, respectively, in the heterophase region I–II **a**. a_T , b_T and c_T are perovskite unit-cell parameters in the tetragonal phase, n_T and $1 - n_T$ are volume fractions of domains in the tetragonal phase **b**. a_O , b_O and c_O are perovskite unit-cell parameters in the orthorhombic phase, n_O and $1 - n_O$ are volume fractions of domains in the orthorhombic phase. Axes of the rectangular co-ordinate system $(X_1X_2X_3)$ are parallel to the perovskite unit-cell axes in the cubic paraelectric phase (reprinted from paper by Topolov et al. [22], with permission from Elsevier)

 $0.568 \le n_T \le 0.871$. These volume fractions are related to the first domain type in the tetragonal phase. The corresponding optimal volume fractions of the first domain type in the orthorhombic phase n_O are given by curve 1 in Fig. 6.3a. The heterophase region, which contains phases that are split into the non-180° domains with optimal volume fractions $(n_T; n_O)$, can be elastically matched with the

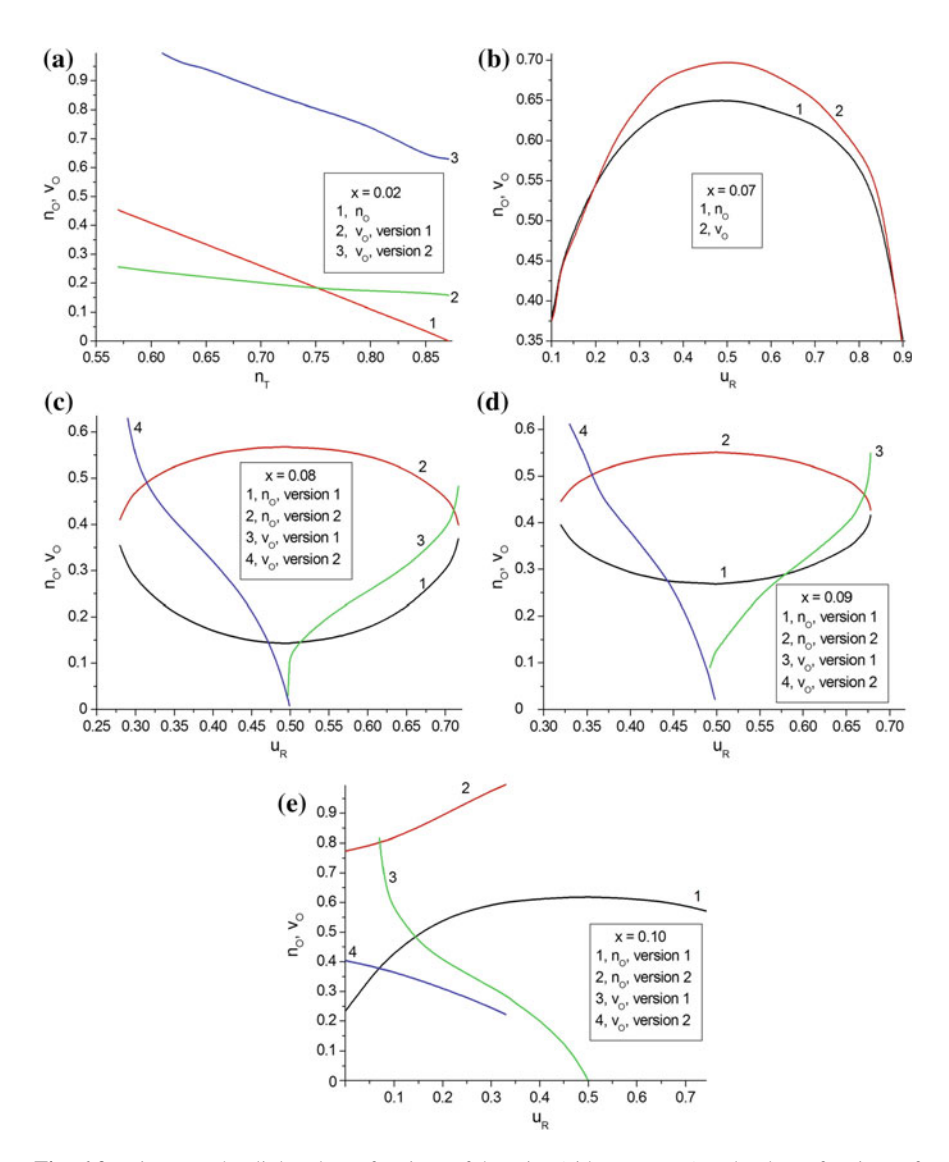


Fig. 6.3 Diagrams that link volume fractions of domains (either n_T or u_R) and volume fractions of the orthorhombic phase v_O in Ba(Ti_{1-x}Ce_x)TiO₃ at x = 0.02 **a**, x = 0.07 **b**, x = 0.08 **c**, x = 0.09 **d**, and x = 0.10 **e** (reprinted from paper by Topolov et al. [22], with permission from Elsevier)

single-domain interlayer of the orthorhombic phase. An important feature of the studied phase coexistence consists in two possible orientations of the crystallographic axes of domains in the orthorhombic phase. At these orientations, conditions (1.18) are valid for the boundaries that separate the heterophase region and interlayer, see Fig. 6.2a. The first version of the orientation is as in the second domain type with the volume fraction $1 - n_O$ (see Fig. 6.2c). The second version means that perovskite unit-cell vectors a_0 , b_0 and c_0 in the interlayer are almost parallel to the co-ordinate axes OX_3 , OX_2 and OX_1 , respectively. The volume fraction v_0 of the orthorhombic phase in the heterophase region is represented by either curve 2 (at the first version of the interlayer) or curve 3 (at the second version of the interlayer) in Fig. 6.3a. Based on these results, one can evaluate the volume fraction of the orthorhombic phase v_O . According to work [22], $v_O = 0.216$ (first version) or $v_Q = 0.851$ (second version). If these versions are characterized by equal probabilities in a large heterophase sample, then we obtain the average volume fraction of the orthorhombic phase $\langle v_0 \rangle = 0.534$. This is in agreement with the experimental value of the volume fraction $v_{O,exp} = 49.14\%$ at x = 0.02 and room temperature [22]. The difference between $\langle v_O \rangle$ and $v_{O,exp}$ can be accounted for by defects and internal mechanical stress fields in ceramic samples, by specifics of DSs in several grains, etc.

The next example of the heterophase structure is concerned with the coexistence of the FE rhombohedral and orthorhombic phases. Such a phase coexistence was studied in work [22] for x = 0.07-0.10. The orthorhombic phase is split into the non-180° domains as shown in Fig. 6.2c. As follows from the analysis of elastic matching of the orthorhombic and rhombohedral phases of Ba(Ti_{1-x}Ce_x)TiO₃ [22], complete stress relief at the planar interphase boundary can be achieved by splitting the rhombohedral phase into two domain types. It is assumed that their spontaneous polarization vectors are oriented almost along the following perovskite unit-cell directions: $[\overline{1}11]$ (at the volume fraction u_R) and $[1\overline{1}1]$ (at the volume fraction $1-u_R$). Some deviations of the orientations from the standard unit-cell directions are concerned with the shear unit-cell distortion in the rhombohedral phase (see Sect. 2.2).

Links between the volume fractions of the domains n_O and u_R in the coexisting phases are shown in Fig. 6.3b-d. At x = 0.07, we find the very variant of the link, and at x = 0.08–0.10 we find two variants of the link for each molar concentration x. All of these variants obey conditions (1.18) for ZNSPs. Taking into account these links, we obtain the volume fraction of the orthorhombic phase (see v_O curves in Fig. 6.3b-d). Conditions (1.18) are valid in the wide u_R ranges just near the MPB (see examples in Fig. 6.3b-d) and in the narrower u_R ranges (see, for instance, Fig. 6.3e) when we go away from the MPB. The following average volume fractions of the orthorhombic phase are evaluated by taking into account graphs in Fig. 6.3:

- (i) $\langle v_0 \rangle = 0.630$ (at x = 0.07),
- (ii) $\langle v_O \rangle = 0.333$ for the version 1 or 0.356 for the version 2 (at x = 0.08),

- (iii) $\langle v_o \rangle = 0.302$ for the version 1 or 0.318 for the version 2 (at x = 0.09), and
- (iv) $\langle v_0 \rangle = 0.297$ for the version 1 or 0.311 for the version 2 (at x = 0.10).

The experimental value of the volume fraction of the orthorhombic phase is $v_{O,exp} = 66.22\%$ at x = 0.07 [23]. One can confirm agreement between the predicted and experimental [22] volume fractions of the orthorhombic phase at x = 0.02-0.10, i.e. almost in the whole MPB region of Ba(Ti_{1-x}Ce_x)TiO₃.

6.2.2 Anisotropic Spontaneous Strains and Stress-Relief Conditions

In Sect. 6.2.1, we considered the interlayer I* (Fig. 6.2a) as a single-domain orthorhombic phase with a fixed orientation of the crystallographic axes. In a case of the interlayer I* represented by the single-domain tetragonal phase instead of the single-domain orthorhombic phase, conditions (1.18) for ZNSPs are violated. This means that the heterophase sample would contain excessive elastic energy because of incomplete stress relief. It should be added that conditions (1.18) are violated irrespective of the orientation of the crystallographic axes of the domains in the single-domain tetragonal phase. It seems to be probable that three different spontaneous strains along the unit-cell perovskite axes in the single-domain orthorhombic phase can promote stress relief in a heterophase region better than in the presence of the single-domain tetragonal phase. As is known, the unit cell in the tetragonal phase is characterized by the unit-cell parameters a_T , $b_T = a_T$ and $c_T \neq a_T$, and therefore, two equal spontaneous strains concerned with a_T and b_T are to be taken into account.

After replacing the single-domain orthorhombic interlayer I^* with a single-domain rhombohedral interlayer for molar concentrations $x \geq 0.07$, we also state violation of conditions (1.18) and emphasize the important role of the anisotropic spontaneous strains of the perovskite unit cell in the orthorhombic phase at stress relief in heterophase samples. It is obvious that the spontaneous strains of the perovskite unit cell of the adjacent rhombohedral phase do not exhibit the anisotropy along the co-ordinate axes and, therefore, the rhombohedral phase would play a passive role at stress relief in $Ba(Ti_{1-x}Ce_x)TiO_3$ near the MPB.

6.3 Features of Heterophase States in $Ba(Ti_{1-x}Zr_x)O_3$ and Related Solid Solutions

It is known from experimental data on the $Ba(Ti_{1-x}Zr_x)O_3$ system of FE solid solutions [24, 25] that an enhanced piezoelectric activity is observed in two-phase samples with compositions close to the MPB. Of specific interest is the $(Ba_{-y}Ca_y)(Ti_{1-x}Zr_x)O_3$ system: in its ceramic samples, unusual heterophase states concerned with the coexistence of three FE phases are observed, and considerable

piezoelectric activity is achieved [23, 26]. Despite the similarity of the phase diagrams of $(Ba_{1-y}Ca_y)(Ti_{1-x}Zr_x)O_3$, $Ba(Ti_{1-x}Zr_x)O_3$, $Ba(Ti_{1-x}Sn_x)O_3$ and $Ba(Ti_{1-x}Hf_x)O_3$ [27], the larger longitudinal piezoelectric coefficient $d_{33} \approx 600$ pC/N [23, 28] is achieved in poled $(Ba_{1-y}Ca_y)(Ti_{1-x}Zr_x)O_3$ ceramics. According to work [28], typical values of the piezoelectric coefficient d_{33} of poled Zr, Sn and Hf-modified BaTiO₃ ceramics are approximately 300–400 pC/N at room temperature. We remind the reader that the piezoelectric coefficient $d_{33} = 191$ pC/N is achieved in poled BaTiO₃ ceramic samples at room temperature [13, 15]. According to experimental data [24], Ba(Ti_{1-x}Zr_x)O₃ at room temperature is characterized by a coexistence of FE phases in a narrow molar-concentration range. In $(Ba_{0.85}Ca_{0.15})(Ti_{0.90}Zr_{0.10})O_3$ ceramic samples with the largest piezoelectric coefficient d_{33} (that is larger than d_{33} of the poled BaTiO₃ ceramic [13, 15] by approximately 3.1 times), a three-phase state is observed [26].

In Sect. 6.3, we discuss features of the phase coexistence in $Ba(Ti_{1-x}Zr_x)O_3$ and related lead-free FE solid solutions [29]. Hereby, we apply a model of the SC sample that contains the polydomain phases I and II, and a thin interlayer I* (see Fig. 6.2a). It is assumed that the coexisting phases are separated by the planar interfaces, and conditions for elastic matching of the phases hold.

At room temperature, Ba(Ti_{0.98}Zr_{0.02})O₃ is characterized by the coexistence of two FE phases, namely, tetragonal (P4mm symmetry) and orthorhombic (Amm2 symmetry). Elastic matching of these phases can lead to complete stress relief in different ways, in the presence of several domain types [29]. It is assumed that in the heterophase sample shown in Fig. 6.2a, I is the orthorhombic phase, II is the tetragonal phase, and I* is the interlayer of the orthorhombic phase. Our analysis of conditions for ZNSPs at the interfaces enables us to conclude [29] that the single-domain tetragonal phase can coexist with the polydomain orthorhombic phase and the interlayer of the single-domain orthorhombic phase. Complete stress relief is achieved in six cases listed in Table 6.2. Moreover, the optimal volume fraction of the orthorhombic phase $n_O \to 1$ or $n_O' \to 0$ (see Table 6.2) suggests that this phase is almost single domain irrespective of the variants of the domain arrangement. This is due to a minor change in the unit-cell parameter a at the morphotropic phase transition, and this facilitates achieving complete stress relief by elastic matching of the tetragonal and orthorhombic phases in Ba(Ti_{0.98}Zr_{0.02})O₃. As follows from experimental data on the perovskite unit-cell parameters of Ba(Ti_{0.98}Zr_{0.02})O₃, the condition $a_T = a_O$ holds [29] with accuracy to 0.05%. The average volume fraction of the orthorhombic phase $\langle v_O \rangle$ is in agreement with the experimental value, see Table 6.2. The $\langle v_Q \rangle$ value is calculated using the v_Q values from the fourth column of Table 6.2 on assumption that a uniform distribution of the heterophase regions with the aforementioned domain types is observed.

In Ba(Ti_{0.93}Zr_{0.07})O₃ at room temperature, the coexistence of the FE orthorhombic (*Anun*2 symmetry) and rhombohedral (*R*3*m* symmetry) phases is observed. At elastic matching of these phases, conditions for complete stress relief hold [29]. Now, we assume that in the heterophase sample shown in Fig. 6.2a, I is the orthorhombic phase, II is the rhombohedral phase, and I* is the single-domain

Domains in the orthorhombic ph	nase	Unit-cell vectors of the	Volume fraction ^b v _O
Unit-cell vectors of the domain types	Optimal volume	single-domain interlayer	
domain types	fraction [29]		
$\boldsymbol{a_o} \ OX_1, \boldsymbol{b_o} \ OX_2 \text{ and }$	$n_O = 0.898$	$ a_O OX_2, b_O OX_3$ and	0.917
$c_o OX_3$ (volume fraction n_O),		$ c_O OX_1$	
$a_o OX_3, b_o OX_2 \text{ and } c_o OX_1$		$\boldsymbol{a_0} \ OX_1, \boldsymbol{b_0} \ OX_3$ and	0.628
(volume fraction $1 - n_O$)		$ c_{O} OX_{2}$	
		$a_O OX_3, b_O OX_1$ and	0.487
		$ c_{O} OX_{2}$	
		$a_O OX_2, b_O OX_1$ and	0.487
		$ c_{O} OX_{3}$	
$\boldsymbol{a_O} \parallel OX_1, \boldsymbol{b_O} \parallel OX_2$ and	$n_{O}' = 0.066$	$ a_O OX_2, b_O OX_3$ and	0.855
$c_O OX_3 $ (volume fraction n_O'),		$ c_{O} OX_{1}$	
$\boldsymbol{a_O} \ OX_2, \boldsymbol{b_O} \ OX_1 \text{ and } \boldsymbol{c_O} \ OX_3$		$ a_O OX_2, b_O OX_1$ and	0.855
(volume fraction $1 - n_O'$)		$ c_O OX_3$	

Table 6.2 Volume fraction v_O of the orthorhombic phase that coexists with the single-domain tetragonal phase at complete stress relief in Ba(Ti_{0.98}Zr_{0.02})O₃

interlayer of the orthorhombic phase. The orthorhombic phase in each region I shown in Fig. 6.2a is split into two domain types, and orientations of the unit-cell vectors of these domains are listed in the first column of Table 6.2. The rhombohedral phase is represented by the domain types shown in Fig. 2.5. It should be noted that complete stress relief at the interfaces in the heterophase sample (Fig. 6.2a) is achieved in relatively wide ranges of volume fractions of the domains in the orthorhombic and rhombohedral phases [29]. As follows from results [29] on four versions of the elastic matching of these phases in Ba(Ti_{0.93}Zr_{0.07})O₃, the average volume fraction of the orthorhombic phase $\langle v_Q \rangle$ is approximately equal to the experimental value 58(5)% found in work [24]. Moreover, in the case of $y_R = 0$ and $x_R = 0.5$ (i.e. at equal volume fractions of two domain types in the rhombohedral phase, see Fig. 2.5), the optimal volume fraction of the domains in the orthorhombic phase would be $n_0' = 0.583$ [29], and this value is also close to the calculated $\langle v_O \rangle$ and experimental v_O values. We remind the reader that the domain arrangement and volume fraction n_{O} in the polydomain orthorhombic phase are shown in the first column of Table 6.2.

It is obvious that the difference between the volume fractions x_R and n_O' is relatively small. In other words, the coexisting phases are characterized by a similarity of their DSs that promote complete stress relief. The role of the rhombohedral phase in the heterophase Ba($\text{Ti}_{0.93}\text{Zr}_{0.07}$)O₃ sample has no analogs in related FE solid solutions. Complete stress relief and similar systems of domains and domain walls in the coexisting phases of Ba($\text{Ti}_{0.93}\text{Zr}_{0.07}$)O₃ would promote a relatively high

^aUnit-cell vectors in the domain of the tetragonal phase are oriented as follows: $a_T || OX_3, b_T || OX_2$ and $c_T || OX_1$. The co-ordinate axes OX_j are parallel to the unit-cell vectors in the cubic paraelectric phase

^bAverage value $\langle v_Q \rangle = 0.705$, experimental value $v_Q = 67(1)\%$ [24]

piezoelectric activity. The rhombohedral phase, that is split into domains of two types, influences the heterophase structure with the ratio of the volume fractions of the orthorhombic and rhombohedral phases is $k_{O-R} = v_O/v_R \approx 1$. This unique case of the elastic matching is accounted for by specifics of the perovskite unit-cell distortion in the rhombohedral phase ($\mu_{11} = \mu_{22} = \mu_{33}$ along the perovskite axes) at the relatively small shear angle $\omega_R < 0.1$. The perovskite unit-cell parameter a_R of the rhombohedral phase obeys the equality $a_R = c_O$ with accuracy to 0.06% and the equality $a_R = b_O$ with accuracy to 0.15% [29]. In general, the distortion of the polydomain rhombohedral phase becomes similar to the distortion of the cubic unit cell, and this facilitates complete stress relief in the heterophase structure.

Now we consider examples of three-phase states observed in FE solid solutions of the $(Ba_{1-y}Ca_y)(Ti_{1-x}Zr_x)O_3$ system. This system is of interest due to heterophase states and piezoelectric activity [14] in compositions near the MPB. For instance, experimental results [29] show that in $(Ba_{0.85}Ca_{0.15})(Ti_{0.90}Zr_{0.10})O_3$ at room temperature, the following FE phases coexist: tetragonal (P4mm symmetry), rhombohedral (R3m symmetry) and orthorhombic (Amm2 symmetry). Poling of $(Ba_{0.85}Ca_{0.15})(Ti_{0.90}Zr_{0.10})O_3$ leads to an increase in the fraction of the rhombohedral and orthorhombic phases in the ceramic sample [29].

To analyse examples of the three-phase coexistence in the BaTiO₃-based FE solid solutions, we put forward the model (Fig. 6.3) where a heterophase sample is regarded as a set of two types of two-phase regions, and each two-phase region is separated by planar interfaces. Here, we do not consider the interlayer such as I* in Fig. 6.2a. The volume fractions of coexisting phases v_T (T, tetragonal phase), v_O (O, orthorhombic phase) and v_R (Rh, rhombohedral phase) in the sample as a whole (Fig. 6.3) obey the condition

$$v_T + v_O + v_R = 1.$$
 (6.1)

The coexisting phases are split into non-180° domains that are components of mechanical twins.

Conditions (1.18) for complete stress relief in the two-phase sample are now applied to the interfaces in each two-phase region and between the two-phase regions (see Fig. 6.3). Elements of distortion matrices related to the two-phase regions are given by

 $D_{ab} = \sum_{f=1}^{3} \left(N_{af}^{(O)} N_{bf}^{(O)} - N_{af}^{(T)} N_{bf}^{(T)} \right) \quad \text{(orthorhombic + tetragonal } \quad \text{phases in}$ Fig. 6.3a or tetragonal + orthorhombic phases in Fig. 6.3b),

 $D_{ab} = \sum_{f=1}^{3} \left(N_{af}^{(O)} N_{bf}^{(O)} - N_{af}^{(R)} N_{bf}^{(R)} \right)$ (orthorhombic + rhombohedral phases in Fig. 6.3a or rhombohedral + orthorhombic phases in Fig. 6.3c), and

 $D_{ab} = \sum_{f=1}^{3} \left(N_{af}^{(T)} N_{bf}^{(T)} - N_{af}^{(R)} N_{bf}^{(R)} \right)$ (tetragonal + rhombohedral phases in Fig. 6.3b or rhombohedral + tetragonal phases in Fig. 6.3c). The two-phase regions

with the ZNSPs at the interfaces are described by distortion matrices that are represented in the general form as follows:

$$\begin{aligned} \left| \left| N_{ij}^{(O+T)} \right| \right| &= \nu_T \left| \left| N_{ij}^{(T)} \right| \right| + (1 - \nu_T) \left| \left| N_{ij}^{(O)} \right| \right| \text{and} \left| \left| N_{ij}^{(O+R)} \right| \right| \\ &= \nu_R \left| \left| N_{ij}^{(R)} \right| \right| + (1 - \nu_R) \left| \left| N_{ij}^{(O)} \right| \right|, \end{aligned}$$
(6.2)

$$\begin{aligned} \left| \left| N_{ij}^{(T+O)} \right| \right| &= v_O \left| \left| N_{ij}^{(O)} \right| \right| + (1 - v_O) \left| \left| N_{ij}^{(T)} \right| \right| \text{and} \left| \left| N_{ij}^{(T+R)} \right| \right| \\ &= v_R \left| \left| N_{ij}^{(R)} \right| \right| + (1 - v_R) \left| \left| N_{ij}^{(T)} \right| \right| \end{aligned}$$
(6.3)

and

$$\begin{aligned} \left| \left| N_{ij}^{(R+T)} \right| \right| &= v_T \left| \left| N_{ij}^{(T)} \right| \right| + (1 - v_T) \left| \left| N_{ij}^{(R)} \right| \right| \text{and} \left| \left| N_{ij}^{(R+O)} \right| \right| \\ &= v_O \left| \left| N_{ij}^{(O)} \right| \right| + (1 - v_O) \left| \left| N_{ij}^{(R)} \right| \right|. \end{aligned}$$
(6.4)

Distortion matrices from (6.2), (6.3) and (6.4) are related to the two-phase regions shown in Fig. 6.3a, b, c, respectively. These matrices also depend on volume fraction of the non-180° domain types. The volume fractions v_T , v_O and v_R from (6.2)–(6.4) obey (6.1). Based on the matrix elements from (6.2)–(6.4), we write D_{ab} by analogy with (1.7) and then examine conditions (1.18) for stress-free interfaces between different two-phase regions shown in Fig. 6.3.

A simple example of complete stress relief [29] is concerned with the presence of the rhombohedral phase split into four domain types at equal volume fractions, i.e. at $x_R = y_R = 0.5$ in Fig. 2.5. Such a polydomain region is characterized by linear distortions $\mu_{11} = \mu_{22} = \mu_{33}$ only, like a unit cell in the cubic phase. Unit-cell vectors in the domains of the tetragonal phase are oriented as follows: $a_T ||OX_3, b_T||$ OX_2 and $c_T ||OX_1$ (volume fraction n_T), and $a_T ||OX_1, b_T ||OX_3$ and $c_T ||OX_2$ (volume fraction $1 - n_T$). Two versions of the unit-cell orientation in the domains of the orthorhombic phase are shown in the first column of Table 6.2.

As follows from the analysis of the three-phase state in $(Ba_{0.85}Ca_{0.15})$ $(Ti_{0.90}Zr_{0.10})O_3$, conditions (1.18) for complete stress relief are violated at elastic matching of the two-phase regions shown in Fig. 6.3. However, the polydomain rhombohedral phase at $x_R = y_R = 0.5$ can be separated from the polydomain tetragonal phase with the interface that also obeys (1.18). The similar rhombohedral–orthorhombic interface obeys (1.18) at splitting the orthorhombic phase into the domains on both the versions (see the unit-cell orientations in the first column of Table 6.2). Hereby, the optimal volume fractions of the domain types in the tetragonal phase in the tetragonal–rhombohedral region are $n_T = 0.523$ and 0.472. Optimal volume fractions of the domain types in the orthorhombic phase in the rhombohedral–orthorhombic region are $n_O = 0.218$ and 0.782, or $n_O' = 0.362$ and 0.638 [29].

Changes in the unit-cell parameters at poling the $(Ba_{0.85}Ca_{0.15})(Ti_{0.90}Zr_{0.10})O_3$ sample lead to changes in conditions for elastic matching of the coexisting phases and promote stress-relief opportunities. It should be noted that the unit-cell parameters c_T and c_O undergo more appreciable changes at poling in comparison to the remaining parameters of $(Ba_{0.85}Ca_{0.15})(Ti_{0.90}Zr_{0.10})O_3$ [26]. Hereafter, our consideration of the three-phase states is carried out in two stages.

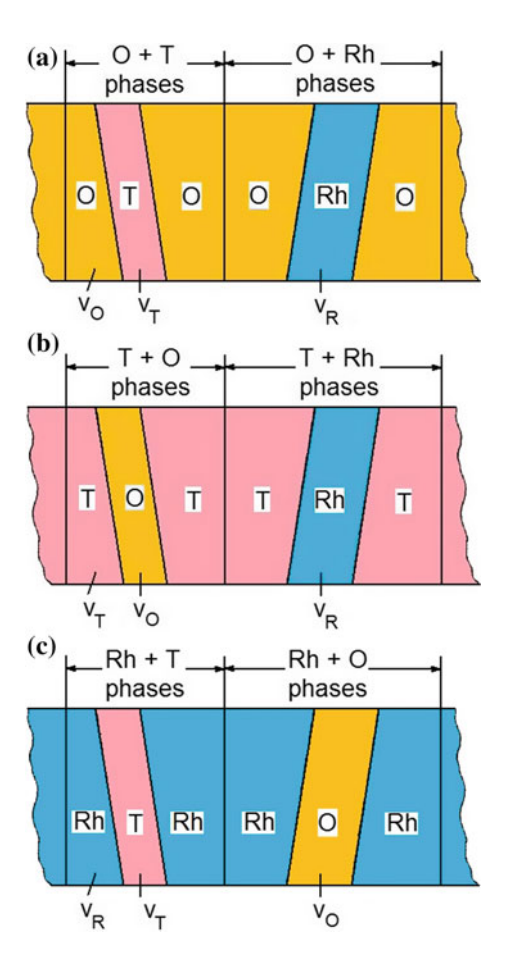
In the first stage, we assume that the rhombohedral phase becomes single domain at poling. As is known for PZT and related FE ceramics [15] with compositions near the MPB, the non-180° domain structure in the rhombohedral phase may undergo changes even in moderate electric fields. In the two-phase regions shown in Fig. 6.3, the rhombohedral phase can be elastically matched with the polydomain tetragonal or orthorhombic phase along the ZNSPs. The domain orientation related to the volume fractions n_{O}' and $1 - n_{O}'$ in the orthorhombic phase (see the first column in Fig. 6.2) does not lead to the ZNSP at the interface between the rhombohedral and orthorhombic phases.

Figure 6.5, a suggests that stress relief in the presence of the single-domain rhombohedral phase is restricted because of $D \neq 0$. We remind the reader that D is one of the invariants (1.13) that are used to characterize the interfaces and stress relief at the phase coexistence. Inequality $D \neq 0$ (see Fig. 6.5a) and violation of conditions (1.18) are observed at various ratios of the volume fractions of the coexisting phases k_{O-R} (orthorhombic and tetragonal phases) and k_{T-R} (tetragonal and rhombohedral phases). As is known from experimental data on $(Ba_{0.85}Ca_{0.15})(Ti_{0.90}Zr_{0.10})O_3$ [26], ratios of the volume fractions of the coexisting phases are $k_{O-R} = 1.18$ and $k_{T-R} = 1.29$. An influence of the polydomain tetragonal phase on the D value and stress-relief conditions is minor because the optimal volume fractions of the domains in the tetragonal phase are $n_T = 0.523$ and 0.472, i.e. approximately 1/2.

In the second stage, we assume that the rhombohedral phase remains polydomain on poling, and the non-180° domain types are shown in Fig. 2.5. Taking into account the DSs in the adjacent phases, we find the ZNSPs at the interfaces between the adjacent phases and two-phase regions (see the schematics in Fig. 6.4). Figure 6.5b, c suggests that complete stress relief (D=0 or more exactly DI=0) is achieved at the equal volume fractions of the four domain types in the rhombohedral phase (see Fig. 2.5) and at almost equal volume fractions of the domains in the tetragonal phase (i.e. $n_T \approx 0.5$). In contrast to the aforementioned phases, the orthorhombic phase is characterized by a considerable difference in the volume fractions of the domains. The similarity of the DSs in the rhombohedral and tetragonal phases and the 'incomplete' monodomenisation of the orthorhombic phase promote ZNSPs at the interfaces in the poled three-phase (Ba_{0.85}Ca_{0.15})(Ti_{0.90}Zr_{0.10})O₃ sample. The condition D=0 holds close to the aforementioned k_{O-R} and k_{T-R} ratios (see Fig. 6.5b, c).

The non-180° DSs in the rhombohedral and tetragonal phases with equal or almost equal volume fractions of the domain types at the three-phase coexistence can promote a large contribution from the domain-wall displacements into the

Fig. 6.4 Schematics of three-phase regions wherein the connecting phase is orthorhombic (O, schematic a), tetragonal (T, schematic b) or rhombohedral (Rh, schematic c). Volume fractions of the coexisting phases are v_O , v_T and v_R (reprinted from paper by Topolov et al. [29], with permission from IOP Publishing)



piezoelectric properties of the poled ceramic sample. It should be added that just in the poled (Ba_{0.85}Ca_{0.15})(Ti_{0.90}Zr_{0.10})O₃ ceramic samples, the largest piezoelectric coefficient d_{33} is achieved [26] in the (Ba_{1-y}Ca_y)(Ti_{1-x}Zr_x)O₃ system. The large d_{33} value can be associated, for instance, with a significant fraction of the tetragonal phase that undergoes a transformation into the rhombohedral phase at poling. The volume fractions of domains at the condition $x_R = y_R \approx n_T$ (see Fig. 6.4b, c) favour such a transformation without considerable stress fields. Hereby, we mention work [30, 31] where a contribution from the 90° domain-wall displacements in electromechanical constants of poled ceramic BaTiO₃ was evaluated under condition of the equidistant arrangement of the domain walls in an equilibrium state. In work [30, 31], the ceramic was considered as single phase, and two 90° domain types in the tetragonal phase were taken into account. The 90° DS in every grain is laminar and regular. Under weak electric or elastic fields, the contribution from the 90° domain-wall displacements in the piezoelectric coefficients d_{3j} of the poled ceramic

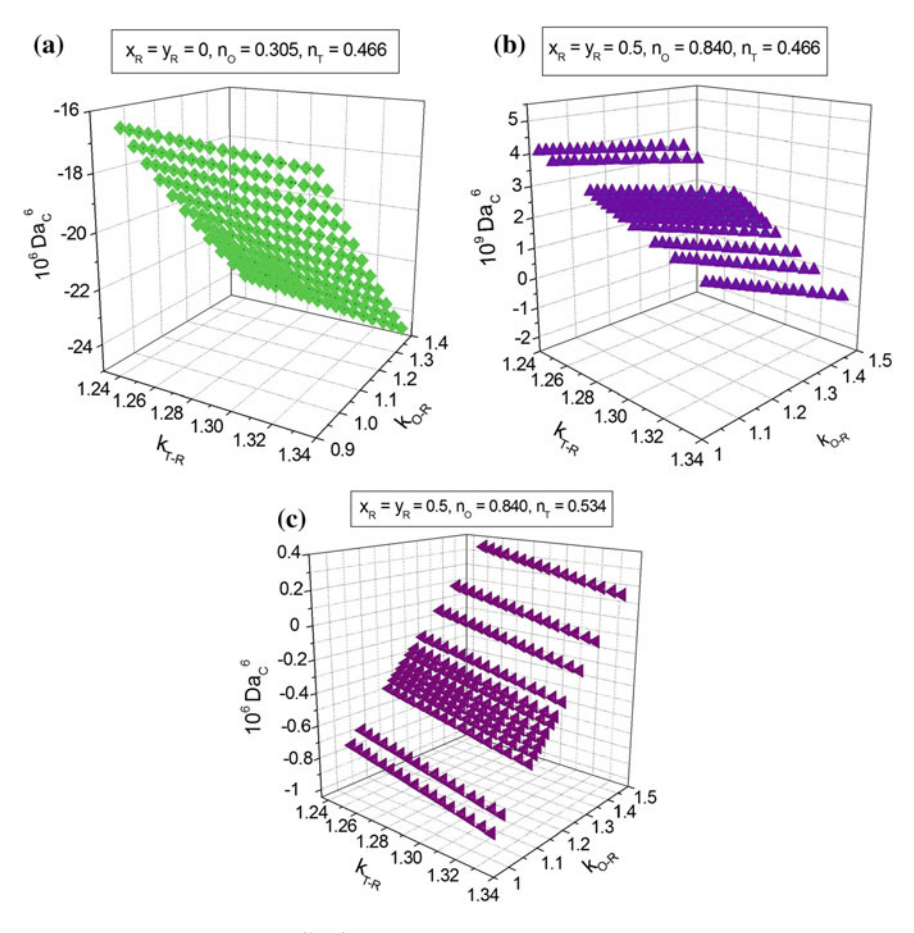


Fig. 6.5 Invariant D a_C^6 (in 10^{-60} m⁶) at the three-phase state in poled (Ba_{0.85}Ca_{0.15})(Ti_{0.90}Zr_{0.10})O₃ where a_C is the cubic unit-cell parameter. For any k_{T-R} and k_{O-R} values shown in the graphs, conditions J < 0 and $I \neq 0$ hold (reprinted from paper by Topolov et al. [29], with permission from IOP Publishing)

BaTiO₃ can reach about 60% [30, 31] at a high mobility of the domain walls in ceramic grains. In the three-phase $(Ba_{0.85}Ca_{0.15})(Ti_{0.90}Zr_{0.10})O_3$ sample, the mobility of the domain walls is high due to the MPB region, as is known, for instance, from the study of numerous poled PZT ceramics [13–16]. It seems to be very probable that the contribution from the non-180° domain-wall displacements related to the rhombohedral and tetragonal phases can influence the piezoelectric properties of poled $(Ba_{0.85}Ca_{0.15})(Ti_{0.90}Zr_{0.10})O_3$ ceramics in different ways. However, to date, a detailed study on the domain-wall contributions from two coexisting FE phases is not yet carried out.

6.4 Domain States and Phase Contents in $Ba(Ti_{1-x}Sn_x)O_3$ and $Ba(Ti_{1-x}Hf_x)O_3$ Near the Morphotropic Phase Boundary

Heterophase structures in Ba($\text{Ti}_{1-x}\text{Sn}_x$)O₃ and Ba($\text{Ti}_{1-x}\text{Hf}_x$)O₃ near the MPB were studied recently [32]. These lead-free FE materials in the poled state are of interest due to the piezoelectric properties. Values of the longitudinal piezoelectric coefficient d_{33} of poled Ba($\text{Ti}_{1-x}\text{Sn}_x$)O₃ and Ba($\text{Ti}_{1-x}\text{Hf}_x$)O₃ ceramics with compositions close to the MPB are approximately 300–400 pC /N [24], i.e. comparable to d_{33} of some PZT, ZTS and PCR ceramics based on Pb(Zr, Ti)O₃ [13, 15, 16].

Important common features of the $Ba(Ti_{1-x}Sn_x)O_3$ and $Ba(Ti_{1-x}Hf_x)O_3$ systems consist in the following. First, a small difference between the Sn and Hf ionic radii [33] may lead to similar heterophase states near the MPB. The $Ba(Ti_{1-x}Sn_x)O_3$ and $Ba(Ti_{1-x}Hf_x)O_3$ systems are characterized by similar phase diagrams [27]. Second, heterophase states are observed at the molar concentration $x \ge 0.02$ irrespective of the modifying ion. We add for comparison that the related $Ba(Ti_{1-x}Ce_x)O_3$ system is also characterized by heterophase states at $x \ge 0.02$, see Sect. 6.2. In Sect. 6.4, we discuss links between the DSs and phase contents in $Ba(Ti_{1-x}Sn_x)O_3$ and $Ba(Ti_{1-x}Hf_x)O_3$ near the MPB at room temperature.

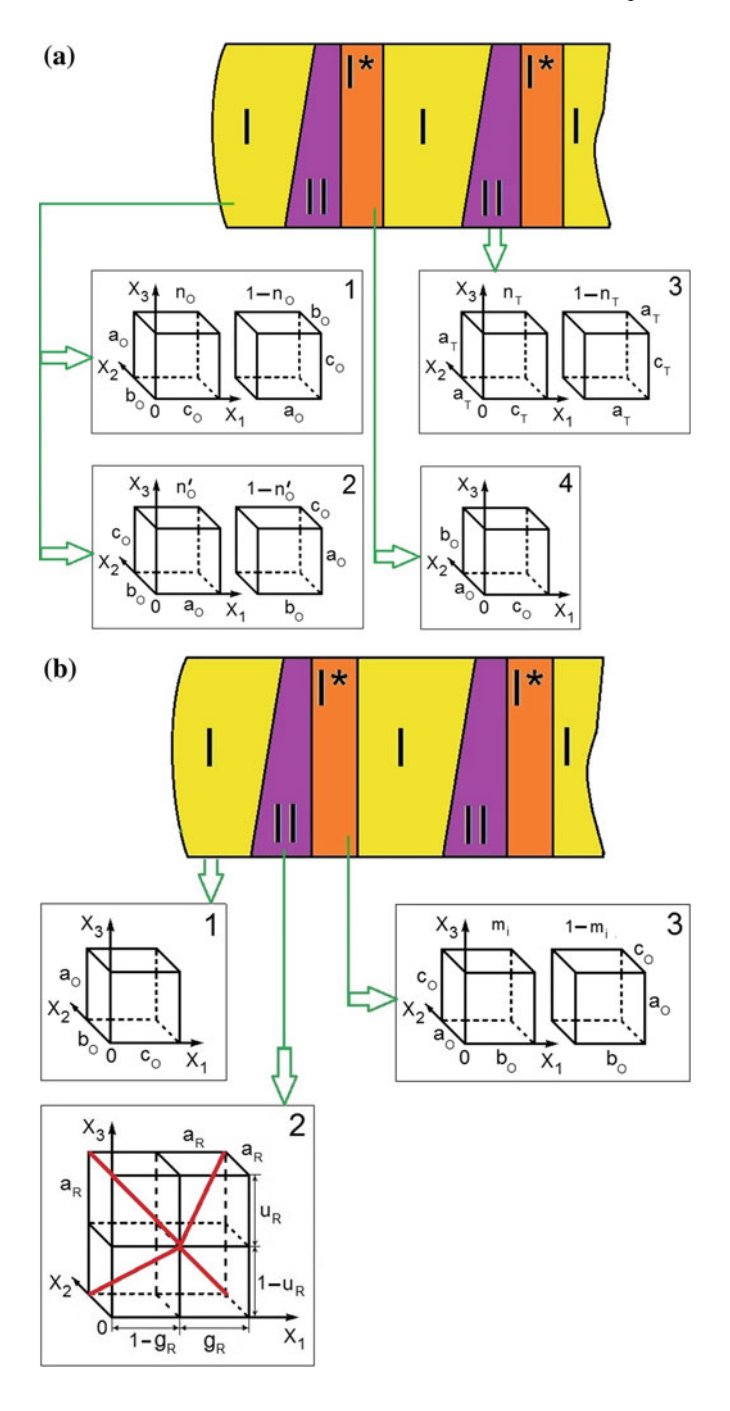
We consider an SC sample (ceramic grain) that contains the polydomain phases I and II, and these phases are separated by the planar interfaces (Fig. 6.6). The heterophase regions I–II are separated by thin interlayers I* of the phase I. Volume fractions of the phases I and II in the sample are v_I and v_{II} , respectively, and conditions for the volume fraction of the interlayers I* $v^* \ll v_I$ and $v^* \ll v_{II}$ are valid. In a case of elastic matching of the phases I, II and interlayers I* (Fig. 6.6), we examine conditions (1.18) for the I–II interface and then conditions (1.18) for the interface that separates the heterophase region (I + II) and the interlayer I* (see also Sect. 6.3).

Our analysis of elastic matching of the FE tetragonal and orthorhombic phases in $Ba(Ti_{1-x}Sn_x)O_3$ and $Ba(Ti_{1-x}Hf_x)O_3$ shows that complete stress relief can be achieved in different ways. One can consider two versions of heterophase structures [32] as follows.

In *version 1*, the orientations of domains in the orthorhombic phase are shown in inset 1 of Fig. 6.6a, and domains of the tetragonal phase are oriented as shown in inset 3 of Fig. 6.6a. The crystallographic axes in the interlayer of the single-domain orthorhombic phase are oriented as shown in inset 4 of Fig. 6.6a.

In *version* 2, the orthorhombic phase is split into domains whose orientations are shown in inset 2 of Fig. 6.6a, and orientations of domains in the tetragonal phase are shown in inset 3 of Fig. 6.6a. The interlayer of the orthorhombic phase is single domain, and its perovskite unit-cell vectors a_O , b_O and c_O are characterized by one of the following orientations in the heterophase sample:

(i) $a_0 ||OX_1, b_0||OX_3$ and $c_0 ||OX_2|$ (interlayer A),



∢Fig. 6.6 Schematics of heterophase structures in morphotropic regions. Orientations of the crystallographic axes in adjacent domains of the coexisting phases are shown in insets 1–4 $\bf a$ and 1–3 $\bf b$. Insets 1, 2 and 4 of $\bf a$ are related to the orthorhombic phase, and inset 2 of Fig. 6.5 $\bf a$ is related to the tetragonal phase. Insets 1 and 3 of $\bf b$ are related to the orthorhombic phase, and inset 2 of $\bf b$ is related to the rhombohedral phase. In inset 2 of $\bf b$, the largest space diagonals of the perovskite unit cells in the adjacent domains are shown. n_O , 1 − n_O , n_T , 1 − n_T , n_O ′ and 1 − n_O ′ are volume fractions of domain types shown in inset 1–3 of $\bf a$. u_R and u_R are parameters that characterize volume fractions of domain types shown in inset 2 of $\bf b$. m_i and 1 − m_i are volume factions of domain types in the interlayer at the rhombohedral–orthorhombic phase coexistence, see inset 3 in $\bf b$ (reprinted from paper by Topolov et al. [32], with permission from Wiley-VCH)

- (ii) $a_O \| OX_3, b_O \| OX_1 \text{ and } c_O \| OX_2 \text{ (interlayer B)},$
- (iii) $a_{o}||OX_{2}, b_{o}||OX_{3} \text{ and } c_{o}||OX_{1} \text{ (interlayer C) and}$
- (iv) or $\boldsymbol{a_0} \| OX_3$, $\boldsymbol{b_0} \| OX_2$ and $\boldsymbol{c_0} \| OX_1$ (interlayer D).

Figures 6.7 and 6.8 suggest that the volume fraction v_O of the orthorhombic phase strongly depends on the volume fraction n_T of the 90° domains in the tetragonal phase, and complete stress relief is achieved in heterophase samples described in terms of version 1. The strong $v_O(n_T)$ dependence is concerned with the inequality $c_T/a_T > c_O/a_O$ that holds for the unit-cell parameters of $Ba(Ti_{1-x}Sn_x)O_3$ and $Ba(Ti_{1-x}Hf_x)O_3$ in the morphotropic regions [32]. In our opinion, the considerable unit-cell distortion in the tetragonal phases of both the solid-solution systems plays the dominant role at elastic matching and phase contents of the phases. Moreover, the c_T/a_T ratio passes the minimum point near x = 0.06 in $Ba(Ti_{1-x}Sn_x)O_3$ or near x = 0.04 in $Ba(Ti_{1-x}Hf_x)O_3$, and the difference between c_T/a_T and c_O/a_O becomes minimal.

The diagrams built for Ba(Ti_{0.94}Sn_{0.06})O₃ (Fig. 6.7d) and Ba(Ti_{0.96}Sn_{0.04})O₃ (Fig. 6.8c) are similar and suggest that the near single-domain state of the tetragonal phase (at either $n_T \to 0$ or $n_T \to 1$) can lead to complete stress relief in heterophase samples. For diagrams shown in Figs. 6.7c, d and 6.8c, d, we see two solutions (i.e. two n_O values at a fixed n_T value) that correspond to complete stress relief in heterophase samples. The corresponding changes in the volume fraction v_O can be described by taking into account the two solutions. As a rule, the first solution is suitable to find v_O at the volume fraction $n_T < 0.2$, and the second solution plays the key role at $n_T > 0.5$. The diagrams shown in Figs. 6.7 and 6.8 enable us to state the important role of the 90° domains of the tetragonal phase in achieving complete stress relief. Due to these domains and related volume fractions n_T , we find different variants of the polydomain regions in the adjacent orthorhombic phase to satisfy conditions (1.18) for complete stress relief in Ba(Ti_{1-x}Sn_x)O₃ and Ba(Ti_{1-x}Hf_x)O₃.

Diagrams in Figs. 6.7 and 6.8 suggest that the single-domain and polydomain phases can be also elastically matched at complete stress relief, and in this case the number of domain types in the heterophase structure shown in Fig. 6.6, a would decrease. The single-domain tetragonal phase means that one of the equalities $n_T = 0$ or $n_T = 1$ holds. For the single-domain orthorhombic phase, one of the equalities $n_O = 0$ or $n_O = 1$ holds. Of specific interest is the diagram built for Ba

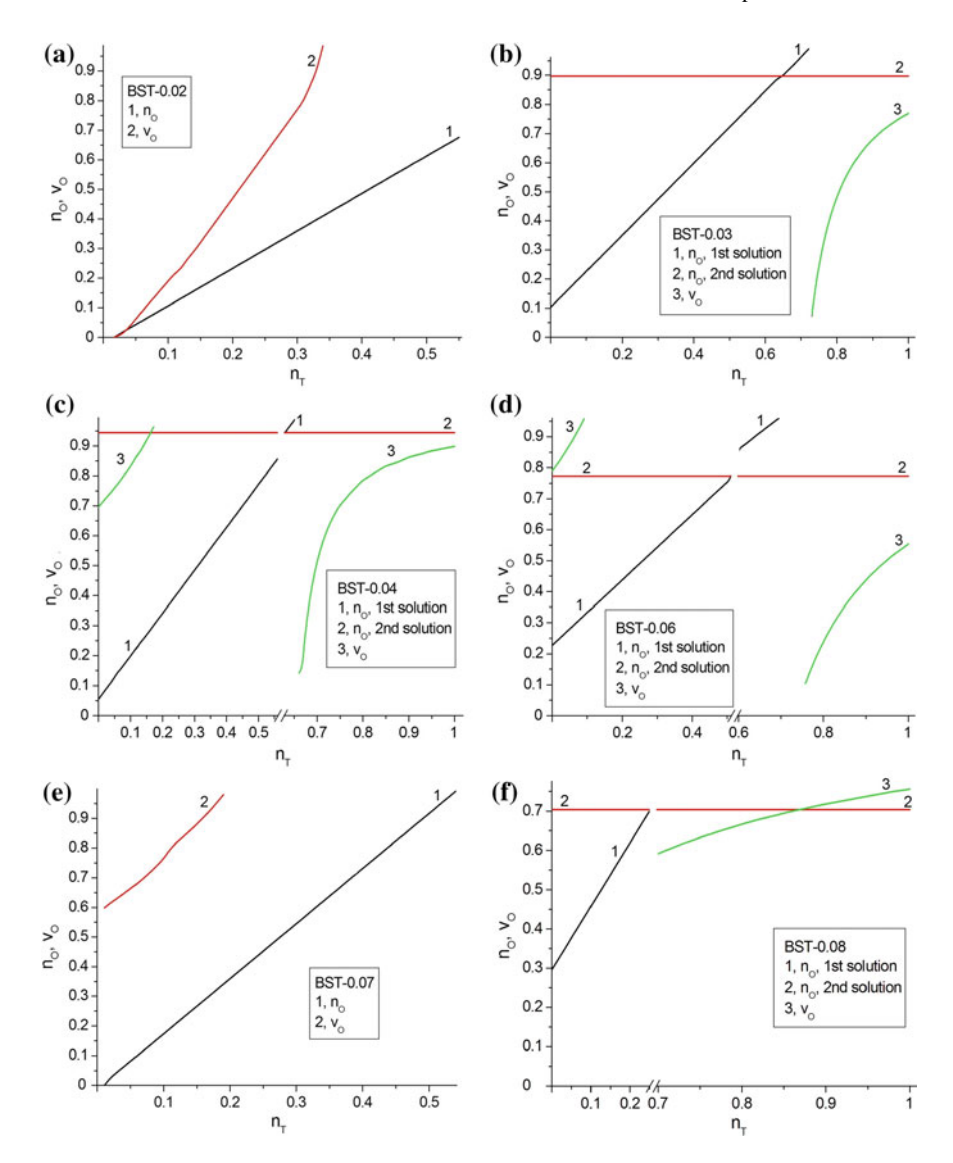


Fig. 6.7 Domain volume fractions–phase contents diagrams related to the tetragonal–orthorhombic phase coexistence in Ba($\text{Ti}_{1-x}\text{Sn}_x$)O₃, version 1, at complete stress relief: **a** x = 0.02, **b** x = 0.03, **c** x = 0.04, **d** x = 0.06, **e** x = 0.07, and **f** x = 0.08 (reprinted from paper by Topolov et al. [32], with permission from Wiley-VCH)

 $(Ti_{0.93}Hf_{0.07})O_3$, see Fig. 6.8e. As follows from experimental data on the unit-cell parameters [32], the difference between the c_T/a_T and c_O/a_O ratios in Ba $(Ti_{0.93}Hf_{0.07})O_3$ is approximately 1.9×10^{-3} and almost equals the difference between c_T/a_T and c_O/a_O related to Ba $(Ti_{0.92}Sn_{0.08})O_3$. However, the mutual arrangement of curves in Fig. 6.7, f differs from that in Fig. 6.8e. At the phase

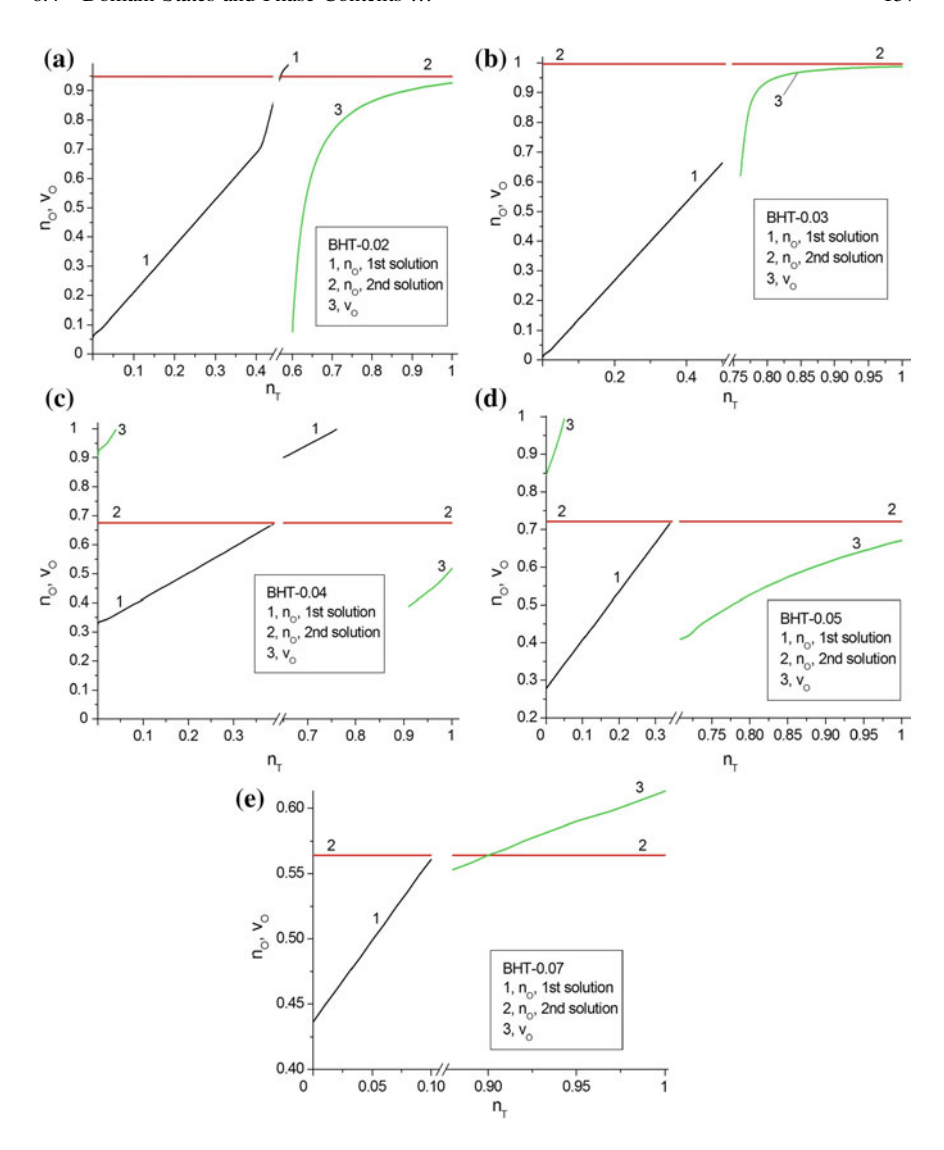


Fig. 6.8 Domain volume fractions—phase contents diagrams related to the tetragonal—orthorhombic phase coexistence in Ba($\text{Ti}_{1-x}\text{Hf}_x$)O₃, version 1, at complete stress relief: **a** x = 0.02, **b** x = 0.03, **c** x = 0.04, **d** x = 0.05, and **e** x = 0.07 (reprinted from paper by Topolov et al. [32], with permission from Wiley-VCH)

coexistence in Ba($Ti_{0.93}Hf_{0.07}$)O₃, we see the very restricted range of the volume fractions n_T (approximately 0.1) which corresponds to v_O at complete stress relief (see curve 3 in Fig. 6.8e). At the same phase coexistence in Ba($Ti_{0.92}Sn_{0.08}$)O₃, despite the periphery of the morphotropic region, the range of the volume fractions n_T corresponding to v_O is wider by approximately three times (see curve 3 in Fig. 6.7f) than in Ba($Ti_{0.93}Hf_{0.07}$)O₃. The reason consists in specifics of the unit-cell

behaviour in the tetragonal phase of Ba(Ti_{1-x}Hf_x)O₃ [32] near the MPB. At x > 0.05 and on increasing x, changes in the unit-cell parameters a_T and c_T of Ba(Ti_{1-x}Hf_x)O₃ do not promote stress relief at the tetragonal-orthorhombic phase coexistence.

Taking into account results on the volume fraction v_O in Ba(Ti_{1-x}Sn_x)O₃ and Ba(Ti_{1-x}Hf_x)O₃ (see Figs. 6.7 and 6.8) at complete stress relief, one can find the average volume fraction $\langle v_O \rangle$ of the orthorhombic phase. For Ba(Ti_{1-x}Sn_x)O₃, we have $\langle v_O \rangle = 0.422$ at x = 0.02, $\langle v_O \rangle = 0.623$ at x = 0.03, $\langle v_O \rangle = 0.743$ at x = 0.04, $\langle v_O \rangle = 0.780$ at x = 0.06, $\langle v_O \rangle = 0.736$ at x = 0.07 and $\langle v_O \rangle = 0.678$ at x = 0.08. For Ba(Ti_{1-x}Hf_x)O₃, the average volume fractions are $\langle v_O \rangle = 0.789$ at v = 0.02, $v_O \rangle = 0.871$ at v = 0.03, $v_O \rangle = 0.614$ at v = 0.04, $v_O \rangle = 0.639$ at v = 0.05 and $v_O \rangle = 0.584$ at v = 0.07 [32]. The aforementioned $v_O \rangle$ values are in agreement with experimental values of the volume fraction of the orthorhombic phase in both Ba(Ti_{1-x}Sn_x)O₃ and Ba(Ti_{1-x}Hf_x)O₃ near the MPB.

Version 2 of the tetragonal-orthorhombic phase coexistence is concerned with one of the single-domain interlayers (A, B, C or D). Our analysis of stress relief suggests that one the coexisting phases (see I or II in Fig. 6.6) can be single domain, and this leads to the minimal number of domain types in the coexisting phases. Based on the optimal volume fractions of domain types and taking into account the orientation of the crystallographic axes in the interlayer of the orthorhombic phase, one can find the volume fraction v_O in the heterophase structure and then average value of $\langle v_O \rangle$. For $Ba(Ti_{1-r}Sn_r)O_3, \langle v_O \rangle = 0.505$ x = 0.03, $\langle v_O \rangle = 0.610$ at x = 0.04, $\langle v_O \rangle = 0.694$ at x = 0.06, and $\langle v_O \rangle = 0.579$ at x = 0.08. For Ba(Ti_{1-x}Hf_x)O₃, $\langle v_O \rangle = 0.914$ at x = 0.02, $\langle v_O \rangle = 0.577$ at x = 0.05 and $\langle v_O \rangle = 0.616$ at x = 0.07 [32]. The aforementioned $\langle v_O \rangle$ values are consistent with experimental data on the volume fraction of the orthorhombic phase in Ba($Ti_{1-x}Sn_x$)O₃ and Ba($Ti_{1-x}Hf_x$)O₃ near the MPB.

The model of the heterophase structure shown in Fig. 6.6b was applied to the analysis of the rhombohedral–orthorhombic phase coexistence in Ba(Ti_{0.92}Hf_{0.08})O₃ [32]. Conditions (1.18) for complete stress relief in heterophase Ba(Ti_{0.92}Hf_{0.08})O₃ samples hold at the restricted number of domain types in the FE phases.

The non-180° DSs in the coexisting FE phases with equal or almost equal volume fractions of the domain types (i.e. $n_O \approx 0.5$, $n_{O'} \approx 0.5$ or $n_T \approx 0.5$, see Figs. 6.7 and 6.8) can lead to a considerable contribution from the domain-wall displacements [30, 31] in the piezoelectric properties of the poled FE ceramic sample. This important factor is to be taken into account when selecting lead-free FE ceramics for piezotechnical applications.

6.5 Behaviour of Unit-Cell Parameters and Heterophase Structures

In this chapter, we have analysed examples of DSs and heterophase structures in lead-free FE solid solutions, such as NBT–xBT, Ba(Ti_{1-x}Me_x)O₃ and (Ba_{1-y}Ca_y)(Ti_{1-x}Zr_x)O₃ with compositions near the MPB at room temperature,

where Me = Ce, Zr, Sn and Hf. The important feature of the studied systems consists in the presence of BaTiO₃ as one of the regular FEs [13-16] with the well-studied crystal structure and physical properties. In many cases, the phase coexistence is observed at small molar concentrations (< 5%) of one of the FE components. We state the validity of conditions (1.18) for complete stress relief in two- and three-phase samples with various compositions. Heterophase structures in these samples are considered in terms of models, see Figs. 6.1, 6.2a, 6.4 and 6.6. Interfaces that separate the coexisting phases and/or phases and interlayers are planar. Taking into account the unit-cell behaviour and domain orientations in the morphotropic phases, we find different versions of heterophase structures at complete stress relief, and this complicates the problem of the phase contents. We also take into consideration the anisotropy of the unit-cell distortions (or spontaneous strains), and this anisotropy influences stress relief to a certain degree. The average volume fraction of the phase was often found at taking into account different versions of heterophase structures and non-180° DSs therein. This points to the complete character of the polydomain/morphotropic structures in the studied solid-solution systems.

The diagrams in Figs. 6.3, 6.7 and 6.8 show links between volume fractions of specific domain types and phase contents near the MPB, and changing the molar concentration x in the related solid-solution systems $[Ba(Ti_{1-x}M_x)O_3]$ enables us to consider common features of the phase coexistence and the role of specific domain types. Hereby, we emphasize the decrease of the domain types at the phase coexistence: this is often concerned with the formation of a single-domain or near single-domain phase in a heterophase sample. The predicted data on the phase contents in the studied solid-solution systems near the MPB (Sects. 6.1–6.4) are in agreement with experimental results.

In conclusion, we state the effective application of the crystallographic method to analyse heterophase structures, domain states and stress relief, and to describe phase contents in lead-free FE solid solutions when changing their compositions and unit-cell parameters. Data on the studied heterophase structures can be taken into account to find contributions from the non-180° domain-wall displacements and coexisting phases in the piezoelectric properties of lead-free FE materials.

References

- Zhang R, Jiang B, Cao W (2001) Elastic, piezoelectric, and dielectric properties of multidomain 0.67Pb(Mg_{1/3}Nb_{2/3})O₃-0.33PbTiO₃ single crystals. J Appl Phys 90:3471-3475
- Zhang R, Jiang B, Cao W, Amin A (2002) Complete set of material constants of 0.93Pb(Zn_{1/3}Nb_{2/3})O₃-0.07PbTiO₃ domain engineered single crystal. J Mater Sci Lett 21: 1877-1879
- Davis M (2007) Picturing the elephant: giant piezoelectric activity and the monoclinic phases of relaxor-ferroelectric single crystals. J Electroceram 19:23–45
- Bokov AA, Ye Z-G (2006) Recent progress in relaxor ferroelectrics with perovskite structure.
 J Mater Sci 41:31–52

- 5. Shuvaeva VA, Glazer AM, Zekria D (2005) The macroscopic symmetry of $Pb(Mg_{1/3}Nb_{2/3})_{1-x}Ti_xO_3$ in the morphotropic phase boundary region (x=0.25-0.5). J Phys: Condens Matter 17:5709–5723
- Ye Z-G, Topolov VYu (2001) Complex domain and heterophase structures in Pb(Mg_{1/3}Nb_{2/3}) O₃–PbTiO₃ single crystals. Ferroelectrics 253:79–86
- Gupta S, Maurya D, Yan Y, Priya S (2012) Development of KNN-based piezoelectric materials. In: Priya S, Nahm S (eds) Lead-Free Piezoelectrics. Springer, New York, Dordrecht, Heidelberg, London, pp 89–119
- 8. Lee HJ, Zhang S (2012) Perovskite lead-free piezoelectric ceramics. Ibid. pp 291–309
- Zhang Q, Zhao X, Luo H (2012) Crystal growth and electric properties of Na_{0.5}Bi_{0.5}TiO₃– BaTiO₃ single crystals. Ibid. pp 337–352
- 10. Uchino K (2012) Applications of lead-free piezoelectrics. Ibid. pp 511-528
- Huo X, Zheng L, Zhang R, Wang R, Wang J, Sang S, Wang Y, Yang B, Cao W (2014) High
 quality lead-free (Li, Ta) modified (K, Na)NbO₃ single crystal and its complete set of elastic,
 dielectric and piezoelectric coefficients with macroscopic 4mm symmetry. CrystEngComm
 16:9828–9833
- 12. Huo X, Zhang R, Zheng L, Zhang S, Wang R, Wang J, Sang S, Yang B, Cao W (2015) (K, Na, Li)(Nb, Ta)O₃: Mn lead-free single crystal with high piezoelectric properties. J Am Ceramic Soc 98:1829–1835
- 13. Jaffe B, Cook WR, Jaffe H (1971) Piezoelectric Ceramics. Academic Press, London, New York
- 14. Smolensky GA, Bokov VA, Isupov VA, Krainik NN, Pasynkov RE, Sokolov AI, Yushin NK (1985) Physics of Ferroelectric Phenomena. Nauka, Leningrad (in Russian)
- 15. Xu Y (1991) Ferroelectric materials and their applications. North-Holland, Amsterdam, London, New York, Toronto
- Gorish AV, Dudkevich VP, Kupriyanov MF, Panich AE, Turik AV (1999) Piezoelectric Device-making. In: Physics of Ferroelectric Ceramics, vol 1. Radiotekhnika, Moscow (in Russian)
- 17. Garg R, Rao BN, Senyshyn A, Krishna PSR, Ranjan R (2013) Lead-free piezoelectric system (Na_{0.5}Bi_{0.5})TiO₃-BaTiO₃: Equilibrium structures and irreversible structural transformations driven by electric field and mechanical impact. Phys Rev B 88:014103–15
- Aksel E, Forrester JS, Jones JL, Thomas PA, Page K, Suchomel MR (2011) Monoclinic crystal structure of polycrystalline Na_{0.5}Bi_{0.5}TiO₃. Appl Phys Lett 98:152901–3p
- Rao BN, Ranjan R (2012) Electric-field-driven monoclinic-to-rhombohedral transformation in Na_{1/2}Bi_{1/2}TiO₃. Phys Rev B 86:134103–4p
- Takenaka T, Maruyama K, Sakata K (1991) (Bi_{1/2}Na_{1/2})TiO₃–BaTiO₃ system for lead-free piezoelectric ceramics. Jpn J Appl Phys Part 1 30:2236–2239
- Topolov VYu, Rao BN, Garg R, Ranjan R (2015) Interrelationship between interphase boundaries and phase contents near the critical compositions of lead-free ferroelectric (Na_{0.5}Bi_{0.5})TiO₃-BaTiO₃. Ferroelectrics 482:22–33
- 22. Topolov VYu, Brajesh K, Ranjan R (2016) Composition driven ferroelectric transformations in lead-free Ba(Ti₁ − xCex)O₃ (0.02 ≤ x ≤ 0.10). Mater Chem Phys 179:152–159
- 23. Liu W, Ren X (2009) Large piezoelectric effect in Pb-free ceramics. Phys Rev Lett 103:257602–4 p
- 24. Kalyani AK, Senyshyn A, Ranjan R (2013) Polymorphic phase boundaries and enhanced piezoelectric response in extended composition range in the lead free ferroelectric BaTi_{1-x}Zr_xO₃. J Appl Phys 114:014102–6 p
- Kalyani AK, Brajesh K, Senyshyn A, Ranjan R (2014) Orthorhombic-tetragonal phase coexistence and enhanced piezo-response at room temperature in Zr, Sn, and Hf modified BaTiO₃. Appl Phys Lett 104:252906–5 p
- Brajesh K, Tanwar K, Abebe M, Ranjan R (2015) Relaxor ferroelectricity and electric-field-driven structural transformation in the giant lead-free piezoelectric (Ba, Ca)(Ti, Zr)O₃. Phys Rev B 92: 224112–8 p

References 161

 Tian Y, Wei L, Chao X, Liu Z, Yang Z (2013) Phase transition behavior and large piezoelectricity near the morphotropic phase boundary of lead-free (Ba_{0.85}Ca_{0.15})(Zr_{0.1}Ti_{0.9})O₃ ceramics. J Am Ceram Soc 96:496–502

- Kalyani AK, Krishnan H, Sen A, Senyshyn A, Ranjan R (2015) Polarization switching and high piezoelectric response in Sn-modified BaTiO₃. Phys Rev B91:024101–13 p
- Topolov VYu, Brajesh K, Ranjan R, Panich AE (2017) Plausible domain configurations and phase contents in two- and three-phase BaTiO₃-based lead-free ferroelectrics. J Phys D Appl Phys 50:065307–065311
- Bondarenko EI, Topolov VYu, Turik AV (1990) The effect of 90° domain wall displacements on piezoelectric and dielectric constants of perovskite ceramics. Ferroelectrics 110:53–56
- 31. Bondarenko EI, Topolov VYu, Turik AV (1991) The role of 90° domain wall displacements in forming physical properties of perovskite ferroelectric ceramics. Ferroelectr Lett Sect 13:13–19
- 32. Topolov VYu, Kalyani AK, Brajesh K, Ranjan R, Panich AE (2017) Comparative study on heterophase structures in ferroelectric solid solutions based on barium titanate. Cryst Res Technol 52:1600299–11 p
- 33. Shannon RD (1976) Revised effective ionic radii and systematic studies of interatomic distances in halides and chalcogenides. Acta Crystallographica Sect A 32:751–767

Chapter 7 From a Unit Cell to Morphotropic Polydomain/Heterophase Structures



Different as are the kinds of properties investigated in the old and the new sciences, the methods followed differ in a still greater degree... The whole tendency is towards generalization.

A. Cayley, Geometry Physics is a form of insight and as such it's a form of art.

D. Bohm

7.1 Study on Domain and Heterophase Structures

The present monograph is devoted to the problem of heterogeneous states in FE solid solutions of the perovskite type. These materials undergo the first-order phase transitions in some ranges of temperature T (polymorphic phase transitions), molar concentration x (morphotropic phase transitions), electric field strength E (electric-field-induced phase transitions) and mechanical stress σ_{ij} (stress-induced phase transitions). At the first-order phase transitions, jumps in the unit-cell parameters give rise to the internal stress field and heterophase states. In these states two or three phases (FE, antiferroelectric, paraelectric, etc.) coexist, and then these states are replaced by the new stable phase. The new phase is often split into domains (mechanical twins) to promote a decrease of the excessive elastic energy of the heterophase system as a whole. The complexity of DS and conditions for complete stress relief at the phase coexistence is concerned with the unit-cell behaviour, changes in symmetry at the phase transition, fluctuations of the molar concentration near the MPB, and so on.

Progress has been achieved at the crystallographic description of the heterophase systems wherein the domain and interphase boundaries obey conditions (1.18) for complete stress relief (i.e. planar boundaries being parallel to ZNSPs) [1, 2] on different levels [3–5], for instance between the adjacent domains, in domain or twinned regions and between the neighbouring polydomain phases. The validity of conditions (1.18) and different variants of the formation of the interphase

boundaries along ZNSPs have been discussed for the systems wherein two or three phases coexist near the MPB. Recent studies of the representative perovskite-type FE solid solutions (PZT, PMN–xPT and PZN–xPT) show that transformations of the crystal structure therein are concerned with the formation of the intermediate (bridging) FE phase [6, 7] near the MPB, and this intermediate phase promotes complete stress relief in the system where complicated polydomain/heterophase structures are observed and/or undergo changes in external fields.

The crystallographic method put forward to analyse the heterophase states (see the schematic in Fig. 7.1) is applicable to various heterophase FE solid solutions and heterophase FE SCs, and agreement between the predicted and experimental data can be regarded as an indicator of the effectiveness of this method. Following the schematic shown in Fig. 7.1, we analysed the two- and three-phase states, the role of the internal stress field and the examples of the DS rearrangement in the FE solid solutions undergoing the first-order phase transitions caused by changes in T, x or E. The complete analysis of interconnections 'DSs—unit-cell parameters changes—heterophase structures—stress relief' is of value to predict an evolution of the heterogeneous states and characteristics of interphase boundaries in polydomain (often heavily twinned) SCs.

Numerous domain state-interface diagrams (Chaps. 2, 3 and 4), built for the interpretation of the heterophase states at changing T, x or E, enable us to generalize the stress-relief conditions in the presence of the polydomain phases from different symmetry classes and at different directions of the electric field vector E. The crystallographic description of elastic matching of the related phases (transition regions) in overlapping structures and the system of the S_{r} -interface diagrams enable us to characterize the role of the orientation states in the formation of the overlapping structure (Chap. 5). The elastic-matching concept is also useful to analyse features of the heterophase structures and phase contents in lead-free FE solid solutions (Chap. 6). Hereby the influence of specific domain types on the phase contents near the MPB is studied by taking into account stress relief, changes in the unit-cell parameters, etc. It should be added that for lead-free FE solid solutions based on BaTiO₃, the comparative study on two-phase and three-phase states, their DSs and heterophase structures has been carried out very recently [8]. Examples of heterophase structures in related FE solid solutions based on BaTiO₃ have been compared for a few compositions near the MPB [9].

It is believed that the methods for the description of various heterophase states and complicated DSs in FE and related materials will be of importance in further studies on multicomponent solid solutions, their domain states and phase contents. Such studies can shed light on relations between DSs and physical properties in heterophase structures observed near the MPB, on dependences of the properties on specific domain types and phase contents.

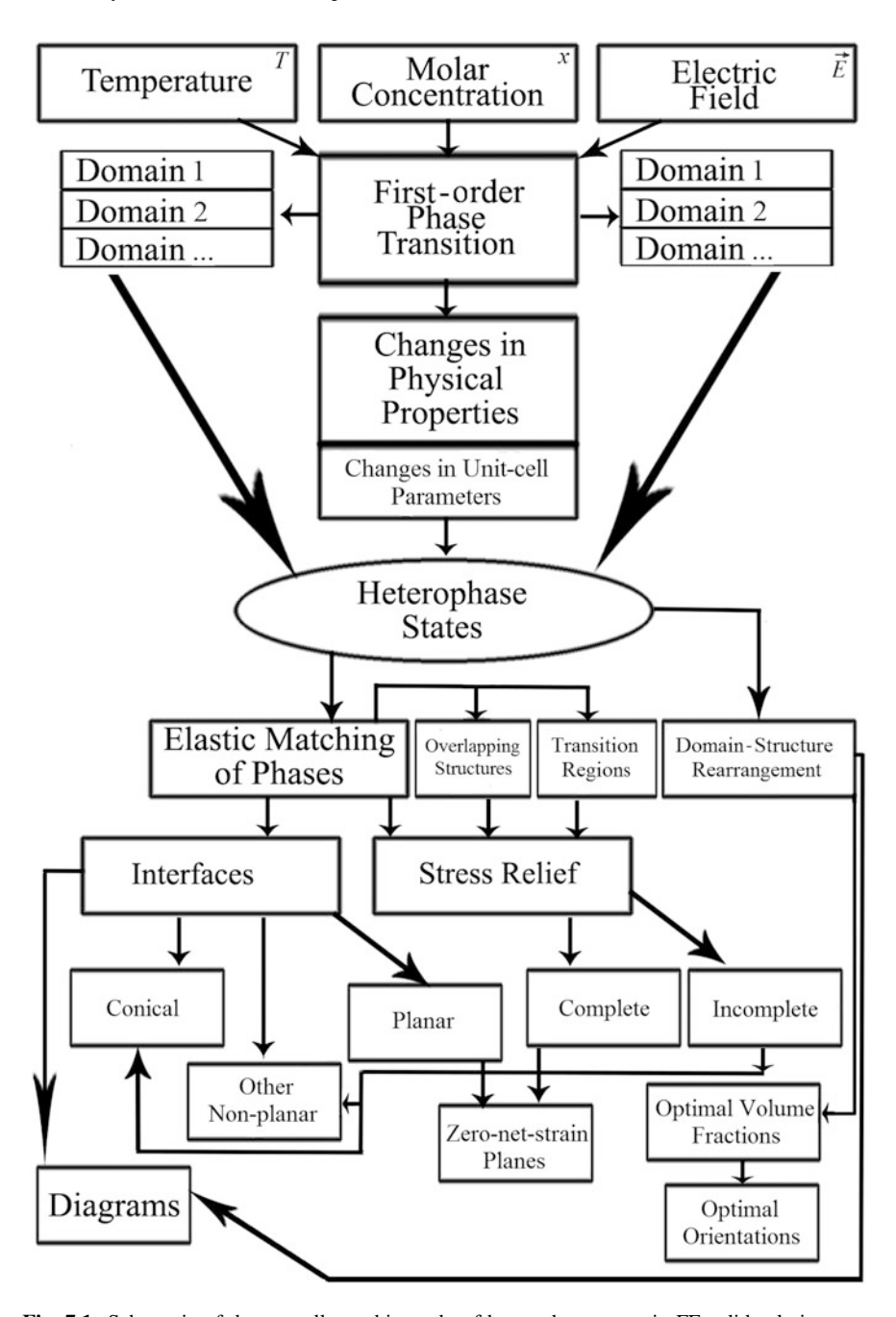


Fig. 7.1 Schematic of the crystallographic study of heterophase states in FE solid solutions

References

- Topolov VYu, Turik AV (1995) Crystallographic aspects of interfaces in ferroelectrics. Defect Diffus Forum Pt A 123–124:31–50
- Topolov VYu (1999) Interfaces in ferroelectrics and related materials with complex domain structures. Ferroelectrics 222:41–52
- 3. Jin YM, Wang YU, Khachaturyan AG, Li JF, Viehland D (2003) Adaptive ferroelectric states in systems with low domain wall energy: tetragonal microdomains. J Appl Phys 94:3629–3640
- Wang H, Zhu J, Lu N, Bokov AA, Ye Z-G, Zhang XW (2006) Hierarchical micro-/nanoscale domain structure in M_C phase of (1 − x)Pb(Mg_{1/3}Nb_{2/3})O₃−xPbTiO₃ single crystal. Appl Phys Lett 89:042908–3 p
- Zhao KY, Zeng HR, Song HZ, Hui SX, Li GR, Luo HS, Yin QR (2009) Intrinsic stress-induced adaptive ferroelectric domain rearrangement in the monoclinic Pb(Mg_{1/3}Nb_{2/3}) O₃-PbTiO₃ single crystal. Mater Lett 63:1715–1718
- Noheda B (2002) Structure and high-piezoelectricity in lead oxide solid solutions. Curr Opin Solid State Mater Sci 6:27–34
- Singh AK, Pandey D (2005) On the discovery of two new monoclinic phases in the morphotropic phase boundary region of Pb[(Mg_{1/3}Nb_{2/3})O₃]-xPbTiO₃ ceramics. Ferroelectrics 326:91–99
- Topolov VYu, Brajesh K, Ranjan R, Panich AE (2017) Plausible domain configurations and phase contents in two- and three-phase BaTiO₃-based lead-free ferroelectrics. J Phys D Appl Phys 50:065307–11 p
- 9. Topolov VYu, Kalyani AK, Brajesh K, Ranjan R, Panich AE (2017) Comparative study on heterophase structures in ferroelectric solid solutions based on barium titanate. Crystal Res Technol 52:1600299–11 p

Appendix A Methods for Description of Heterophase and Polydomain Single Crystals

A.1 Concepts on the Zero-Net-Strain Plane

In this section, we consider some trends in the development of the crystallographic methods that are applied to describe heterophase structures and non-180° DSs in FEs and related materials. In the last decades, this subject has been of interest because of experimental studies of heterogeneous FE and antiferroelectric SCs [1, 2]. These SCs undergo the first-order structural phase transitions and are split into domains (twins) below the Curie temperature T_C [1–3], and various examples of the DS formation and rearrangement are known [3–5]. Along with the symmetry and thermodynamic [1, 2, 6] aspects of the structural phase transitions in FEs and related materials, the crystallographic aspect of the heterophase structures and complex DSs [3] is also important, especially in the presence of multicomponent mechanical twins and at a sequence of the phase transitions in polydomain (twinned) SCs.

A way to the crystallographic description of the FE SCs at the first-order phase transition originates from the phenomenological theory of martensitic transformations. This theory put forward by Wechsler et al. [7] was first applied to the phase transition between the austenite (cubic symmetry) and martensite (tetragonal symmetry) phases in alloys. The modified theory was applied by Lieberman et al. [8] to the martensitic phase transition between the cubic and orthorhombic phases of the alloy. Wechsler et al. [7] also described the mechanism of the formation of the martensite phase. The plane separating the parent (high-temperature) and martensite phases in alloys is often termed 'the habit plane'. The habit plane is regarded [7] as a plane of zero mean distortion. At the crystallographic description of such a plane, the term 'ZNSP' is often used [2, 3]. There are a few crystallographically equivalent lattice correspondences at the formation of the ZNSP at the martensitic phase transition. In work [7, 8], the method was developed to calculate the orientation of the interphase boundary (or habit-plane indices) and optimal volume fractions of domain types (twin components) in the coexisting phase with lower symmetry. To calculate these characteristics, knowledge of crystal structures of the coexisting phases (unit-cell parameters and orientations of the unit-cell

vectors) is required. The important advantage of the theory [7, 8] is that no adjustable parameters are taken into consideration.

The main element in the theoretical treatment [7] is the distortion. It is shown that the pure distortion (or Bain distortion) is related to a small region that transforms homogeneously from the austenite phase to the martensite phase. Such a region represents the separate elastic domain or the twin component with the fixed orientation of the crystallographic axes. A matrix ||T|| is introduced to describe changes in a vector \mathbf{r}_i built in the single-domain region at the structural phase transition: $\mathbf{r}_i' = ||T||\mathbf{r}_i$. Taking into account that the martensite phase is split into the elastic domains with the known distortion matrices $||M_1||$ (first domain type) and $||M_2||$ (second domain type), one can represent the total (average) distortion matrix in the martensite phase as follows:

$$||E|| = (1-x)||M_1|| + x||M_2||, \tag{A.1}$$

where x is the volume fraction of the second domain type. The matrices $||M_i||$ from (A.1) are represented in the general form as

$$||M_i|| = ||\Phi_i||.||T_i||, \tag{A.2}$$

where $\|\Phi_i\|$ is the relative rotation matrix and $\|T_i\|$ is the matrix of the pure distortion of the *i*th domain type. It should be noted that

$$\det||M_i|| = \det||T_i|| = V_i/V_o \tag{A.3}$$

because of $\det \|\Phi_i\| = 1$ at any rotation of the crystallographic axes of the domain. In (A.3), V_i is the transformed volume of the domain and V_o is the original volume of the same domain in the austenite phase. From (A.1)–(A.3), one can derive that $\det \|E\| = (1-x)(V_1/V_o) + x(V_2/V_o)$. If the domains are from the same martensite phase, then

$$\det||E|| = \det||T_i|| = V_i/V_o \tag{A.4}$$

independently of the volume fraction x. A planar interphase boundary becomes the zero distortion plane (ZNSP) as the length of the vector \mathbf{r} built in the austenite phase suffers no change at the phase transition:

$$|r| = ||E||r|, \tag{A.5}$$

where ||E|| is taken from (A.1), and the vector ||E|| crosses a series of adjacent domains in the martensite phase and, therefore, suffers a rotation with respect to the austenite unit-cell basis. Equation (A.5) is used to find the possible orientations of the planar interphase boundary and optimal volume fractions of the domain types in the martensite phase. Equation (A.5) is also represented as follows:

$$|\mathbf{r}|^2 = \mathbf{r}||E||^T||E||\mathbf{r},\tag{A.6}$$

where superscript T is related to the transposed matrix. Equation (A.6) can be written in terms of eigenvalues λ_i of $||E||^T ||E||$ and components of the vector $\mathbf{r}(r_1, r_2, r_3)$ in the austenite unit-cell basis as follows:

$$(1-\lambda_1^2)r_1^2 + (1-\lambda_2^2)r_2^2 + (1-\lambda_3^2)r_3^2 = 0.$$
(A.7)

In (A.7), λ_i is the stretch along the *i*th crystallographic axis of the austenite unit cell, and this axis is parallel to the co-ordinate axis OX_i .

relationship between the phenomenological theory [7, invariant-plane-strain theory put forward by Bowles and Mackenzie [9] and the Eshelby's inclusion theory [10] extended to martensite was discussed in the literature. Mura et al. [11] showed that the three aforementioned theories become identical in case of the infinitesimal principal strains (or spontaneous strains of the unit cell) at the structural phase transition. Kato et al. [12] showed that the theories developed by Wechsler et al. [7] and Bowles and Mackenzie [9] are essentially identical to the approach based on the minimization of the elastic energy of the heterophase SC. Horikawa et al. [13] studied the stress-induced martensitic phase transition in alloys at quasi-static tensile loading. Results calculated on the basis of the phenomenological theory [7] agree to four digits with the values obtained by Horikawa et al. [13]. Agreement between the calculated and experimental results on the planar interphase boundaries at complete stress relief (ZNSPs) and the polydomain martensite phase suggests that the phenomenological theory [7, 8] can be applied to systems undergoing the diffusionless phase transitions with martensitic kinetics [2]. Among these systems, of particular interest are FE and related materials.

The crystallographic description of the non-180° domain (twin) walls in FEs and related materials is often carried out, following results from work [14-16]. The approach is based on the condition for the elastic compatibility of the adjacent domains or components of the mechanical twin [see (1.4)]. An examination of this condition is carried out in terms of spontaneous strains of the adjacent domains. It is obvious that in the presence of the planar wall separating two domains with different matrices of the spontaneous strains S'_{kl} and S''_{kl} , the condition for the constant length of the elementary vector ds can be valid on crossing the domain wall. In this case, the excessive elastic and electrostriction energy vanishes. However, it is unclear, whether the method developed in [14–16] is correct to consider the elastic interaction between two polydomain regions or phases. Following the theoretical concept [7, 8], the corresponding vector ds introduced in papers [14, 15] would be built in a medium split into the domains, and the length of such a vector could not be as small as possible because of crossing at least a few domains. The further approximation made by studying the cubic-tetragonal phase transition [2, 16, 17] of the martensitic type is concerned with neglecting the rotation of the crystallographic axes of the adjacent domains [7, 8] to obey the conditions for their elastic

compatibility. The relative rotation matrix is shown, for instance, in (2.1), and elements of this matrix are expressed [3, 4, 7, 8] in terms of either the unit-cell distortions or the unit-cell parameters of the polydomain phase. Following expression (5.3.3) from monograph [16], the matrix of the spontaneous strains of the polydomain tetragonal phase is written as

$$S'_{kl} = (1 - \alpha) \|\xi^{s1}\| + \alpha \|\xi^{s2}\|, \tag{A.8}$$

where $\|\xi^{s1}\|$ and $\|\xi^{s2}\|$ are matrices of spontaneous strains of the first and second domain types, respectively, and α is the volume fraction of the second domain type. The domain orientations [16] are those shown for domains 7 (volume fraction $1-\alpha$) and 6 (volume fraction α) in Fig. 2.2. The matrices $\|\xi^{s1}\|$ and $\|\xi^{s2}\|$ are written in the crystallographic axes of the paraelectric cubic phase. It is assumed that the matrix of spontaneous strains of the cubic phase is unity.

Taking experimental values of the jumps in the unit-cell spontaneous strains of PbTiO₃ SC at the cubic–tetragonal phase transition [2], we calculate the Miller indices (hkl) of the interphase boundary and the optimal volume fraction $\alpha_{\rm opt}$ of the second domain type. Based on the phenomenological theory [7], we obtain h=0.5552, k=0.8317, l=0.0045 and $\alpha_{\rm opt}=0.7629$. Based on (1.4) and (A.8), we calculate h=0.5552, k=0.8317, l=0 and $\alpha_{\rm opt}=0.7643$. In both cases, we have $k/h\approx 1.5$, and the interphase boundary is oriented close to the (230) perovskite unit cell. This orientation is confirmed in experimental studies [2] of the planar interphase boundary in PbTiO₃ SCs.

The generalization of the phenomenological theory from papers [7, 8] is carried out in work [18, 19] where the elastic matching of two polydomain FE phases is studied. This study is carried out in terms of distortion matrices ||M|| and ||N|| or the coexisting phases that may be separated by a planar stress-free boundary (ZNSP). The distortion matrices ||M|| and ||N|| are expressed in terms of the unit-cell distortions of the domain types (or twin components), their volume fractions and angles of mutual rotation of the crystallographic axes of the adjacent domains (see Sect. 1.1.4). The unit-cell distortions are given with respect to the crystallographic axes of the cubic (paraelectric, prototype) phase. As shown by Kuhn [19], the vector \mathbf{x} in the cubic phase is transformed into the vectors $||M||\mathbf{x}$ (low-temperature phase) and $||N||\mathbf{x}$ (high-temperature phase). The stress-free interphase boundary (i.e. ZNSP), which separates the phases with the distortion matrices ||M|| and ||N|| at the first-order phase transition, obeys the following condition for the constant length of the transformed vector:

$$|||M||x| = |||N||x| \tag{A.9}$$

Equation (A.9) represents the generalized expression in comparison to (A.5) that is applicable to the paraelectric–FE phase transition. The determination of the orientation of the interphase boundary and the optimal volume fractions of the domain types in the coexisting FE (antiferroelectric or ferroelastic) phases is carried out on the basis of the Metrat's algorithm, see (1.5)–(1.8). It is also shown [17] that

each combination of the volume fractions of the domains in the coexisting phases corresponds to at least one interphase boundary that obeys conditions (1.5) and (1.6) for ZNSPs. Numerous examples of the determination of the stress-free phase-boundary (ZNSP) orientations at various volume fractions in FE phases are shown for polydomain/heterophase KNbO₃ [16] and BaTiO₃ [17] SCs. It should be added that (A.9) represents the condition from (A.5) generalized for the elastic matching of the two polydomain phases. Like the vector \mathbf{r} from (A.5), the vector \mathbf{x} in (A.9) is built to cross a sequence of domains of different types. In this case, the phase is characterized as a region with distortions averaged over a macroscopic volume that contains all of the domain types, into which the phase has been split.

The Metrat's algorithm was modified in papers [3, 5] where the classification of the phase boundaries in PbZrO₃ SCs was put forward (see Sect. 1.2.2). This algorithm was applied to describe domain boundaries in heavily twinned SCs, the S-type boundaries in FE and antiferroelectric SCs (see Sect. 1.1.4), to refine the temperature dependence of the shear angle of the unit cell of PbZrO₃ SC in the orthorhombic phase [20] and to predict a behaviour of the interphase boundary in ferroelastic–FE Gd₂(MoO₄)₃ SC [21].

Changes in the unit-cell parameters of Gd₂(MoO₄)₃ SC do not obey conditions (1.5) and (1.6) for ZNSPs at the tetragonal—orthorhombic phase transition [21]. We note that the volume-fraction dependence of the volume density of elastic energy $f_{\rm elas}$ concerned with the phase coexistence in ${\rm Gd_2(MoO_4)_3}$ SC is consistent with the volume-fraction dependence of $|\det||D_{ij}||$ that characterizes the elastic compatibility of the coexisting tetragonal and orthorhombic phases. The volume density of elastic energy f_{elas} and $\det ||D_{ii}||$ written in terms of matrix elements from (1.7) depend on the volume fraction t of one of two domain types in the ferroelastic-FE orthorhombic phase of Gd₂(MoO₄)₃ SC. As shown in work [21], conditions $f_{\text{elas}}(t_{\text{opt}}) = 0$ and $\left| \det \left\| D_{ij}(t_{\text{opt}}) \right\| \right| = 0$ are achieved at equal values of the optimal volume fraction t_{opt} that is out of the range [0, 1]. Moreover, the preferable orientation of the crystallographic axes in the single-domain orthorhombic phase was predicted in work [21] and confirmed in experimental studies [22] of the interphase boundary in Gd₂(MoO₄)₃ SCs. The correlation between the volume-fraction dependences of f_{elas} and $|\det||D_{ij}|||$ was also shown for the tetragonalorthorhombic phase transition in BaTiO₃ SC [23] wherein two domain types of the tetragonal phase and four domain types of the orthorhombic phase are present. The further modification of the Metrat's algorithm was described in Chaps. 2, 4 and 5 of the present book, and agreement between the calculated and experimental data was shown for different solid solutions and in the presence of phases from different symmetry classes.

Authors of the recent monograph [16] noted that the approach applied to the tetragonal-orthorhombic phase transition in KNbO₃ (Metrat 1980) is conceptually close to that presented above (i.e. the approach developed in work [14, 15]). And then they write: 'However, the validity of the results obtained is questionable since a nonjustified criterion of the mechanical compatibility (see the first footnote in Sect. 2.2.4) was used in the calculations' ([16], p. 224). In the mentioned footnote

([16], footnote 14 in p. 62) we read: 'One comes across in the literature the use of the condition (2.2.10) with matrix D_{ij} defined as the difference between the squares of the spontaneous strain tensors in the domains. This condition is not justified unless it leads to results identical to those derived with the use of D_{ij} defined by (2.2.11)'. The paper denoted as Metrat, 1980 is [18] in the current list of references. We add that the condition (2.2.10) and (2.2.11) from [16] are represented [16] as Δ_{ij} . $ds_i ds_j = 0$ (the analogue of (1.2) in Chap. 1) and

$$\Delta_{ii} = \varepsilon_{Sii}(A) - \varepsilon_{Sii}(B) \tag{A.10}$$

(the analogue of Δ'_{kl} from (1.4) in Chap. 1 of the present monograph), respectively. The difference Δ_{ij} from (A.10) is 'a symmetric tensor with up to six independent components, and $\varepsilon_{Sij}(A)$ and $\varepsilon_{Sij}(B)$ are spontaneous strains in the domains' ([16], p. 62).

Below, we express an opinion on the aforementioned sentences from work [16]. First, paper [19], where the Metrat's algorithm has been analysed and justified, was not mentioned in work [16]. Second, our paper [21], where the volume density of elastic energy and the condition $f_{\text{elas}}(t_{\text{opt}}) = 0$ have been considered in the context of the interphase boundary studied on the basis of the Metrat's algorithm [18], was not mentioned in work [16]. Third, words 'across in the literature' ([16], p. 62) without due references become senseless to compare results from different algorithms, papers, calculations, etc. Many results in research are recognized and improved in the process of comparison with some results from earlier studies. Fourth, in our papers (see, e.g. [3–5, 20, 21] and Sect. 1.1.4 of the present monograph), Δ_{ij} from (A.10) was not defined 'as the difference between the squares of the spontaneous strain tensors in the domains' ([16], p. 62). The spontaneous strain tensor of an individual domain differs from the distortion matrix that is usually used in our crystallographic description [3-5]. Instead of the aforementioned difference between the squares of the spontaneous strain tensors, we operate with elements of $||D_{ij}||$ from (1.7) that is written in terms of unit-cell distortions of domains. Fourth, the condition that is not justified stems from the incorrect definition of Δ_{ii} in the footnote (see [16], p. 62). Fifth, authors of work [16] did not mentioned a difference between the results on the orientation of the simple S wall separating two domains in the orthorhombic phase of FE and antiferroelectric SCs (Sect. 1.1.4). This difference discussed in our papers [3, 24] stems from different approaches to describe the elastic matching between the adjacent domains (or domain regions). It is obvious that different criteria concerned with the aforementioned vectors ds and x near the interface would lead to different orientation relationships for the S wall, see, for instance, (1.10) and (1.11). Sixth, the fact that elements Δ_{ii} from (A.10) form the symmetric tensor points out the area of applications of the approach developed in work [14-16]. Any matrices of spontaneous strains or distortions of phases, wherein the mutual rotation of the crystallographic axes [7, 8] of the adjacent domains is taken into account, may be studied using other algorithms and approaches than those developed in work [14–16]. As is known from work [7, 8],

no requirement concerning symmetry of the distortion matrix of the polydomain (twinned) phase is introduced at the crystallographic description of elastic matching in terms of unit-cell distortions. Even in the simple case of two domain types at the martensitic phase transition [7], the distortion matrix from (A.1) is asymmetric because of the mutual rotation of the crystallographic axes of the adjacent domains.

An interesting example of the crystallographic description of the interphase boundary is considered in work [25]. Dudnik and Nepochatenko have put forward a method to determine possible orientations of the interphase boundaries in ferroelastic SCs. Among these SCs of particular interest is $Pb_3(PO_4)_2$ wherein six types of the interphase boundaries are observed at the first-order phase transition $R\overline{3}m-C2/c$. Elements of the coherent interphase boundary are regarded as common elements belonging to the coexisting phases. The interphase boundary that separates the paraelastic and single-domain ferroelastic phases in $Pb_3(PO_4)_2$ SC is approximated by a second-degree surface [see (1.12)] with coefficients D_{ij} expressed in terms of the unit-cell parameters a, b, c and β ($R\overline{3}m$ phase) and a', b', c' and $\beta' = \beta$ (C2/c phase) as follows [25]:

$$D_{11} = (c'/c)^{2} - 1, D_{22} = (b'/b)^{2} - 1,$$

$$D_{33} = (a'/a)^{2} + \operatorname{tg}^{2} \varphi[c'a'/(ca) - 1]^{2} - 1,$$

$$D_{13} = (c'a'/(ca))\operatorname{tg} \varphi[c'a'/(ca) - 1], \text{ and } D_{12} = D_{23} = 0.$$
(A.11)

In (A.11), φ is the angle between the crystallographic axis a and the co-ordinate axis OX_3 . The coefficients D_{ij} from (A.11) are consistent with those determined in terms of the Metrat's algorithm [18] [see also (1.7)] and cannot be represented as the difference between the squares of the spontaneous strain tensors of the coexisting phases. It is important to note that work [25] has been published at a similar time to Metrat's paper [18].

A.2 Comparison of Data

In this section, we consider examples of characteristics of interfaces and polydomain (twinned) phases in FE and antiferroelectric SCs. For comparison, these characteristics are calculated using different formulae, for instance, from papers [7, 14, 15, 18].

Experimental values of the jumps in spontaneous strains in BaTiO₃ SC [2] at the cubic–tetragonal phase transition are $\xi_a^s = -3.7 \times 10^{-3}$ (measured perpendicular to the spontaneous polarization vector in the *P4mm* phase) and $\xi_c^s = 1.2 \times 10^{-2}$ (measured parallel to the spontaneous polarization vector). Using these values, we find the following optimal volume fractions of the domain types 6 and 7 (Fig. 2.2) in the tetragonal phase: $m_{\rm opt} = 0.2941$ or 0.7059 (from the phenomenological theory [7]), $m_{\rm opt} = 0.2941$ or 0.7059 (from the Metrat's algorithm, [18]), and $m_{\rm opt} = 0.2936$ or 0.7064 [from the Sapriel's theory [15] and by taking into account the spontaneous strains S_{kl}' from (A.8)].

In the twinned antiferroelectric *Pbam* phase of PbZrO₃ SC, the thermal stability of the planar S walls [20, 26] is of particular interest. Now we consider the orientations of the twin components similar to those shown in Fig. 1.2. The distortion matrices of the twin components are given in (1.9). The orientation of the normal vector $n_2(hhl)$ to the S wall [20] is characterized by the l/h ratio that can be calculated in terms of either work [14] or work [18] [see (1.10) and (1.11)]. Table A.1 contains the l/h values calculated in different ways. The calculations were performed using the unit-cell parameters of PbZrO₃ from work [20]. It is seen that the $(l/h)_{\rm M}$ and $(l/h)_{\rm FJ}$ ratios from Table A.1 are almost constant in the wide temperature range, and the difference between these ratios does not exceed 1%. Thus, the data obtained using concepts [18] are in good agreement with the data calculated on the basis of formulae [14].

Various interphase boundaries observed at the cubic–rhombohedral (Pm3m-R3m) phase transition in PbZrO₃ SCs can be described in terms of work [5]. Crystallographic characteristics of these boundaries strongly depend on the volume fractions of the 71° (109°) domains in the rhombohedral phase. The distortion matrix $||N_{ij}||$ of the rhombohedral phase split into the 71° (109°) domains (Fig. 2.5) is given by (2.6). The matrix of average spontaneous strains in the same polydomain phase is represented as

$$||S'_{kl}|| = \begin{pmatrix} \xi^{s,R} & \xi^{s,R}(2y_R - 1) & \xi^{s,R}(2x_R - 1)(2y_R - 1) \\ \xi^{s,R}(2y_R - 1) & \xi^{s,R} & \xi^{s,R}(2x_R - 1) \\ \xi^{s,R}(2x_R - 1)(2y_R - 1) & \xi^{s,R}(2x_R - 1) & \xi^{s,R}(2x_R - 1) \end{pmatrix},$$
(A.12)

Table A.1 Temperature dependence of perovskite unit-cell parameters b_0 and ω_0 of PbZrO₃ SC^a and the ratio l/h that characterizes the orientation of the S wall in the twinned antiferroelectric *Pbam* phase

T(K)	$b_{\rm O},~10^{-10}~{\rm m}$	$\omega_{\rm O}$ (min)	(<i>l/h</i>) _M from (1.10)	(<i>l/h</i>) _{FJ} from (1.11)
295	4.1104	5.50	0.2652	0.2668
300	4.1110	5.45	0.2660	0.2676
340	4.1138	5.10	0.2638	0.2653
365	4.1169	4.95	0.2742	0.2756
390	4.1184	4.70	0.2696	0.2710
410	4.1214	4.35	0.2686	0.2699
430	4.1235	4.10	0.2675	0.2687
450	4.1264	3.85	0.2725	0.2736
470	4.1293	3.60	0.2784	0.2795
480	4.1310	3.35	0.2740	0.2749
490	4.1329	3.05	0.2665	0.2674
493	4.1334	3.00	0.2670	0.2678

^aAccording to experimental data [20], the unit-cell parameter $a=4.1606\times 10^{-10}\,\mathrm{m}$ at 295 K $\leq T \leq$ 493 K

where $\xi_a^{s,R}$ is the longitudinal unit-cell spontaneous strain, and $\xi^{s,R}$ is the shear unit-cell spontaneous strain. While no spontaneous strain would appear in the cubic phase, its matrix of spontaneous strains $||S_{ij}''||$ contains zero elements only. Taking experimental values of the unit-cell parameters of PbZrO₃ $a_{\rm R} = 4.1596 \times 10^{-10}$ m, $\omega_{\rm R} = 6'$ in the rhombohedral phase and $a_{\rm C} = 4.1570 \times 10^{-10}$ m in the cubic phase, we calculate $||D_{ij}(x_{\rm R}, y_{\rm R})||$ and $\|\Delta'_{kl}(x_R, y_R)\|$ in accordance with (1.7) and (1.4). The values of x_R and y_R , which obey conditions (1.18), are, for instance, $x_R = 0$ and $y_R = 0.2538$ or $x_R = 0$ and $y_{\rm R} = 0.7462$ (two domain types), $x_{\rm R} = 0.10$ and $y_{\rm R} = 0.2432$ or $x_{\rm R} = 0.10$ and $y_R = 0.7568$ (four domain types), and so on. In general, the values of x_R and y_R , which obey conditions (1.18), equal to the values obtained by using (1.4) and (A.12) with accuracy to 0.5%. Such a consistency is accounted for by the structural analogy between $||D_{ij}(x_R, y_R)||$ and $||\Delta'_{kl}(x_R, y_R)||$ at elastic matching of the cubic and rhombohedral phases. It is seen that $||N_{ij}||$ and $||S'_{kl}||$ from (2.6) and (A.12), respectively, are symmetric at $0 \le x_R \le 1$ and $0 \le y_R \le 1$, and, as a consequence, $||D_{ii}(x_R, y_R)||$ and $||\Delta'_{ij}(x_R, y_R)||$ are also symmetric.

An example of elastic matching of the single-domain tetragonal (*P4mm*) and single-domain orthorhombic (*C2mm*) phases in BaTiO₃ suggests that even in a case of two symmetric matrices, there is a difference between results obtained in terms of papers by Sapriel [15] and Metrat [18]. Spontaneous strains of the coexisting phases are given by matrices

$$||S'_{kl}|| = \begin{pmatrix} \xi_a^{s,T} & 0 & 0\\ 0 & \xi_a^{s,T} & 0\\ 0 & 0 & \xi_c^{s,T} \end{pmatrix} \text{ and } ||S''_{kl}|| = \begin{pmatrix} \xi_a^{s,O} & 0 & \xi^{s,O}\\ 0 & \xi_b^{s,O} & 0\\ \xi^{s,O} & 0 & \xi_c^{s,O} \end{pmatrix},$$
(A.13)

where $\xi_a^{s,T}$ and $\xi_c^{s,T}$ are spontaneous strains of the perovskite unit cell in the tetragonal phase, $\xi_a^{s,O}$, $\xi_b^{s,O}$, $\xi_c^{s,O}$ and $\xi^{s,O}$ are spontaneous strains of the perovskite unit cell in the orthorhombic phase. Distortion matrices of the tetragonal and orthorhombic phases are written in terms of the spontaneous strains as

$$||M_{kl}|| = \begin{pmatrix} 1 + \xi_a^{s,T} & 0 & 0\\ 0 & 1 + \xi_a^{s,T} & 0\\ 0 & 0 & 1 + \xi_c^{s,T} \end{pmatrix} \text{ and }$$

$$||N_{kl}|| = \begin{pmatrix} 1 + \xi_a^{s,O} & 0 & \xi^{s,O}\\ 0 & 1 + \xi_b^{s,O} & 0\\ \xi^{s,O} & 0 & 1 + \xi_c^{s,O} \end{pmatrix},$$

$$(A.14)$$

respectively. Equations (A.13) and (A.14) describe the single-domain states with similar orientations of the perovskite unit-cell vectors: in the tetragonal phase there are $a_T || [100]$, $b_T || [010]$ and $c_T || [001]$, and in the orthorhombic phase there are $b_O || [010]$ and a_O and a_O and a_O that are close to [100] and [001], respectively. Taking

experimental values of the perovskite unit-cell parameters of BaTiO₃ SC [28] $a_{\rm T}=3.992\times 10^{-10}$ m and $c_{\rm T}=4.035\times 10^{-10}$ m (tetragonal phase), $a_{\rm O}=4.013\times 10^{-10}$ m, $b_{\rm O}=3.989\times 10^{-10}$ m and $\omega_{\rm O}=0.13^{\circ}$ (orthorhombic phase), and $a_{\rm C}=4.002\times 10^{-10}$ m (extrapolated value of the unit-cell parameter of the cubic phase), we calculate matrices from (A.13) and (A.14) and then $\|\Delta'_{kl}\|$ and $\|D_{ij}\|$ from (1.4) and (1.7). The interphase boundary obeys conditions (1.14) and is characterized as a fragment of a conical surface. A transition from $\|D_{ij}\|$ calculated using matrices from (A.14) to $\|\Delta'_{kl}\|$ calculated using matrices from (A.13) is possible in a limiting case, when the condition

$$2(\xi_a^{s,O} - \xi_a^{s,T}) \gg (\xi^{s,O})^2 \tag{A.15}$$

is valid. Hereby, we omit conditions like $\xi_a^{s,O} + \xi_a^{s,T} \ll 2$ and $\xi_a^{s,O} \ll 1$ while these conditions are valid [1, 2, 6] at various structural phase transitions in FEs and related materials. We mention that the similar limiting case was considered at the determination of the orientation of the S wall in terms of the Metrat's algorithm [18] and the approach developed by Fousek and Janovec [14] [see (1.10) and (1.11) and the transition from $(l/h)_M$ to $(l/h)_{FI}$ in Sect. 1.1].

Taking into account (A.15), we represent the matrix elements of $||D_{ij}||$ as $D_{ij} \approx 2\Delta'_{ij}$, and therefore,

$$\det ||D_{ij}|| \approx 8 \det ||\Delta'_{ij}||. \tag{A.16}$$

For the tetragonal–orthorhombic interphase boundary in BaTiO₃ SC, we obtain $\det \|D_{ij}'\| = 2.550 \times 10^{-8}$ and $\det \|D_{ij}\|/8 = 2.557 \times 10^{-8}$, i.e. condition (A.16) is valid. The relatively small value of $\det \|D_{ij}\|$ is caused by a small difference $a_T - b_O$. As a consequence, considerable stress relief would be achieved at elastic matching of the single-domain phases.

For comparison, we analyse elastic matching at the orthorhombic–rhombohedral phase transition in BaTiO₃ SC. Matrices of spontaneous strains of the single-domain phases are written as

$$||S'_{kl}|| = \begin{pmatrix} \xi_a^{s,O} & 0 & \xi^{s,O} \\ 0 & \xi_b^{s,O} & 0 \\ \xi^{s,O} & 0 & \xi_c^{s,O} \end{pmatrix} \text{ and } ||S''_{kl}|| = \begin{pmatrix} \xi_a^{s,R} & \xi^{s,R} & \xi^{s,R} \\ \xi^{s,R} & \xi^{s,R} & \xi^{s,R} \\ \xi^{s,R} & \xi^{s,R} & \xi^{s,R} \\ \xi^{s,R} & \xi^{s,R} & \xi^{s,R} \end{pmatrix},$$
(A.17)

where $\xi_a^{s,O}$, $\xi_b^{s,O}$, $\xi_c^{s,O}$ and $\xi_c^{s,O}$ are spontaneous strains of the perovskite unit cell in the orthorhombic phase, $\xi_a^{s,R}$ and $\xi_c^{s,R}$ are spontaneous strains of the perovskite unit cell in the rhombohedral phase. Distortion matrices of the coexisting single-domain phases are represented as

$$||M_{kl}|| = \begin{pmatrix} 1 + \xi_a^{s,O} & 0 & \xi^{s,O} \\ 0 & 1 + \xi_b^{s,O} & 0 \\ \xi^{s,O} & 0 & 1 + \xi_c^{s,O} \end{pmatrix} \text{ and }$$

$$||N_{kl}|| = \begin{pmatrix} 1 + \xi_a^{s,R} & \xi^{s,R} & \xi^{s,R} \\ \xi^{s,R} & 1 + \xi_a^{s,R} & \xi^{s,R} \\ \xi^{s,R} & \xi^{s,R} & 1 + \xi_a^{s,R} \end{pmatrix}.$$

$$(A.18)$$

We use the following experimental values of the perovskite unit-cell parameters of BaTiO₃ SC [19, 28]: $a_{\rm O}=4.013\times 10^{-10}$ m, $b_{\rm O}=3.976\times 10^{-10}$ m and $\omega_{\rm O}=0.13^{\circ}$ (orthorhombic phase), $a_{\rm R}=3.998\times 10^{-10}$ m and $\omega_{\rm R}=0.15^{\circ}$ (rhombohedral phase), and $a_{\rm C}=3.998\times 10^{-10}$ m (cubic phase, extrapolated value). Like the boundary between the single-domain tetragonal and orthorhombic phases, the orthorhombic–rhombohedral interphase boundary obeys conditions (1.14). A link between $\det \|D_{ij}\|$, calculated using matrices from (A.18), and $\det \|\Delta'_{ij}\|$, calculated using matrices from (A.16): we obtain $\det \|\Delta'_{ij}\|=1.329\times 10^{-7}$ and $\det \|D_{ij}\|/8=1.331\times 10^{-7}$. In this case, $\det \|D_{ij}\|$ is about 5.2 times more than $\det \|D_{ij}\|$ at elastic matching of the single-domain tetragonal and orthorhombic phases in BaTiO₃ SC. Such an increase in $\det \|D_{ij}\|$ is concerned with the more appreciable changes in the unit-cell parameters of BaTiO₃ SC [19, 28] at the orthorhombic–rhombohedral phase transition in comparison to the changes at the tetragonal—orthorhombic phase transition.

To consider elastic matching of the single-domain FE rhombohedral (R3m) and untwined antiferroelectric orthorhombic (Pbam) phases in PbZrO₃ SC, we use unit-cell parameters [20] as follows: $a_{\rm O}=4.1606\times10^{-10}\,{\rm m}$, $b_{\rm O}=4.1334\times10^{-10}\,{\rm m}$ and $\omega_{\rm O}=2.5'$ (orthorhombic phase), $a_{\rm R}=4.1606\times10^{-10}\,{\rm m}$ and $\omega_{\rm R}=6.0'$ (rhombohedral phase), and $a_{\rm C}=4.1565\times10^{-10}\,{\rm m}$ (cubic phase, extrapolated value). Orientations of the crystallographic axes of the perovskite unit cell in the coexisting phases are described taking into account (A.17) and (A.18). Our evaluations show that $\det\left\|\Delta_{ij}'\right\|=-5.620\times10^{-10}\,{\rm and}\,{\rm det}\left\|D_{ij}\right\|/8=-5.617\times10^{-10},{\rm i.e.}$ (A.16) holds, and almost complete stress relief is achieved. This is accounted for by the equality $a_{\rm R}=a_{\rm O}$ at the rhombohedral—orthorhombic phase transition in PbZrO₃ SC [20]; however, the shear distortion of the unit cell influences elastic matching and leads to $\det\left\|\Delta_{ij}'\right\|\neq0$ and $\det\left\|D_{ij}\right\|\neq0$.

Now, we assume that the rhombohedral and orthorhombic phases in PbZrO₃ SC are split into the non-180° domains (twins). Small values of $\left|\det \left\|D_{ij}\right\|\right| \sim 10^{-10}$ at the coexistence of the same single-domain phases suggest that complete stress relief can be achieved at least in the presence of 90° twin components in the antiferroelectric orthorhombic phase. The FE rhombohedral phase is split into the 71° (109°) domains with the orientations shown in Fig. 2.5. The spontaneous antipolarization

vectors $\pm P_{ai}$ in the twin components of the orthorhombic phase are parallel to [101] (volume fraction t) and [10 $\bar{1}$] (volume fraction 1-t) of the perovskite unit cell, and the twin components are separated by the planar stress-free walls in accordance with concepts [14, 15]. Average spontaneous strains are represented by $\|S'_{kl}\|$ from (A.12) (rhombohedral phase) and by

$$||S_{kl}''|| = \begin{pmatrix} \xi_a^{s,O} & 0 & \xi^{s,O}(2t-1) \\ 0 & \xi_b^{s,O} & 0 \\ \xi^{s,O}(2t-1) & 0 & \xi_c^{s,O} \end{pmatrix},$$
(A.19)

(orthorhombic phase). Distortion matrices of the rhombohedral and orthorhombic phases are given by (2.6) and

$$||N_{kl}|| = \begin{pmatrix} 1 + \xi_a^{s,O} & 0 & \xi^{s,O}(2t-1) \\ 0 & 1 + \xi_b^{s,O} & 0 \\ \xi^{s,O}(2t-1) & 0 & 1 + \xi_c^{s,O} \end{pmatrix},$$
(A.20)

respectively. It is seen that, as in previous cases of the coexistence of the single-domain phases, the distortion matrices from (2.6) and (A.20) are symmetric. Hereafter, it is assumed that parameters $x_{\rm R}$ and $y_{\rm R}$ (Fig. 2.5) obey conditions (1.18) for ZNSPs at the cubic—rhombohedral phase transition. This means that no changes in the volume fractions of the 71° (109°) domains are expected in the relatively narrow (about 10 K [20]) range of the thermodynamic stability of the rhombohedral phase on cooling the SC sample.

Taking into account (A.12), (A.19) and (A.20) and values of the aforementioned unit-cell parameters $a_{\rm O}$, $b_{\rm O}$, $\omega_{\rm O}$, $a_{\rm R}$, $\omega_{\rm R}$ and $a_{\rm C}$ of PbZrO₃ SC, we find the optimal volume fractions ($t_{\rm opt}$)_M and ($t_{\rm opt}$)_S. These volume fractions are related to the 90° twin components with $\pm P_{a1}$ ||[101] and obey conditions (1.18) or those for ZNSPs in terms of spontaneous strains [15, 16]. We added subscript M (Metrat's approach) or S (Sapriel's approach) to distinguish the calculated values. Table A.2 contains ($x_{\rm R}$, $y_{\rm R}$) calculated for the cubic–rhombohedral phase transition [5] on the basis of the Metrat's algorithm. It should be mentioned that the difference between ($x_{\rm R}$, $y_{\rm R}$) calculated using the Metrat's approach and ($x_{\rm R}$, $y_{\rm R}$) obtained using the Sapriel's approach is less than 0.5%. Data from Table A.2 show that small differences ($t_{\rm opt}$)_M – ($t_{\rm opt}$)_S are observed at variations of $x_{\rm R}$ and $y_{\rm R}$ in wide ranges. In general, changes in the unit-cell parameters promote complete stress relief in PbZrO₃ SC at a restricted number domain types (twin components) of the coexisting phases. In our opinion, such elastic matching may be an indirect reason for the three-phase states observed in PbZrO₃ SCs (Sect. 4.2.1).

The above-given examples of elastic matching of phases in PbZrO₃ and BaTiO₃ SCs show that the correlation between $\left\|\Delta'_{ij}\right\|$ and $\left|\left|D_{ij}\right|\right|$ is observed in systems that are characterized by complete or considerable stress relief at the first-order phase transition.

x_{R}	УR	$(t_{ m opt})_{ m M}$	$(t_{\rm opt})_{\rm S}$
0	0.2538	0.4552	0.4542
0	0.7462	_a	_a
0.05	0.2498	0.4638	0.4627
0.05	0.7502	_a	_a
0.10	0.2432	0.4735 or 0.9934	0.4726 or 0.9934
0.10	0.7568	0.0230	0.0218
0.15	0.2311	0.4861 or 0.9522	0.4854 or 0.9522
0.15	0.7689	0.0443 or 0.0706	0.0453 or 0.0689
0.20	0.2023	0.5072 or 0.9293	0.5066 or 0.9292
0.20	0.7977	0.0698 or 0.1108	0.0708 or 0.1092
0.2538	0	0.6166	0.6161
0.2538	1	0,0685	0,0677
0.7462	0	0.3834	0.3839
0.7462	1	0.9315	0.9323
0.80	0.2023	0.0707 or 0.4928	0.0708 or 0.4934
0.80	0.7977	0.8892 or 0.9302	0.8908 or 0.9292
0.85	0.2311	0.0478 or 0.5139	0.0478 or 0.5146
0.85	0.7689	0.9294 or 0.9557	0.9311 or 0.9547
0.90	0.2432	0.0066 or 0.5265	0.0066 or 0.5274
0.90	0.7568	0.9770	0.9782
0.95	0.2498	0.5364	0.5373
0.95	0.7502	_a	_a
1	0.2538	0.5448	0.5458

Table A.2 Optimal volume fractions $(t_{\text{opt}})_{\text{M}}$ and $(t_{\text{opt}})_{\text{S}}$ of 90° twin components with the spontaneous antipolarization vector $\pm P_{a1} \| [101]$ at the phase transition R3m - Pbam in PbZrO₃ SC

0.7462

The application of the approach developed in work [14–16] to heterophase structures in solid solutions near the MPB may be problematic, as the unit-cell parameters of the two morphotropic FE (or antiferroelectric) phases are known; however, an extrapolated unit-cell parameter of the high-temperature paraelectric phase was not measured [6, 29–31]. In this case, a direct comparison of the unit-cell parameters of the morphotropic phases is needed, as shown for solid solutions of PZT (Sect. 2.1), PMN–xPT (Sect. 2.2), etc. It should be added that the Metrat's algorithm [18] was successfully applied to describe elastic matching of phases in antiferroelectric PbHfO₃ SC at the first-order phase transitions $Pm3m - P222_1 - Pba2$ [4]. The planar interphase boundaries and their orientations observed in PbHfO₃ SCs were described on the basis of the Metrat's algorithm. An 'exotic' effect of the 60° triple twin component on the interphase boundary between the antiferroelectric $P222_1$ and Pba2 phases was first predicted on the basis of the Metrat's algorithm and then confirmed in the experimental study [4].

^aNo value of $(t_{opt})_{M}$ or $(t_{opt})_{S}$ is found in the volume fraction range [0, 1], and the boundary separating the R3m and Pbam phases does not obey conditions (1.18) for ZNSPs

In conclusion, we underline that the Metrat's algorithm [18] and its further modifications (see, for instance, [3, 5, 20, 24, 32, 33]) are suitable to calculate the crystallographic characteristics of the polydomain (twinned) phases and interfaces separating the domain regions in heavily twinned SCs or polydomain phases in heterophase SCs. According to Scopus database (www.scopus.com, November 2017), Metrat's work [18] has been cited 37 times, and no comments on this paper have been published in *Ferroelectrics* and/or related periodicals since 1980.

References

- 1. Smolensky GA, Bokov VA, Isupov VA, Krainik NN, Pasynkov RE, Sokolov AI, Yushin NK (1985) Physics of ferroelectric phenomena. Nauka, Leningrad (in Russian)
- 2. Fesenko EG, Gavrilyachenko VG, Semenchev AF (1990) Domain structure of multiaxial ferroelectric crystals. Rostov University Press, Rostov-on-Don (in Russian)
- Topolov VYu, Turik AV (1995) Crystallographic aspects of interfaces in ferroelectrics. Defect Diff Forum Pt A 123–124:31–50
- Balyunis LE, Topolov VYu, Turik AV, Fesenko OE (1990) Optical and crystallographic studies of twin and phase boundaries in antiferroelectric PbHfO₃. Ferroelectrics 111:291–298
- Topolov VYu, Balyunis LE, Turik AV, Bah IS, Fesenko OE (1992) Interphase boundaries at cubic-rhombohedral phase transition in PbZrO₃ crystals. Bull Russian Acad Sci Phys 56:1588–1593
- Xu Y (1991) Ferroelectric materials and their applications. North-Holland, Amsterdam, London, New York, Toronto
- Wechsler MS, Lieberman DS, Read TA (1953) On the theory of the formation of martensite.
 Trans AIME, J Metals 197:1503–1515
- 8. Lieberman DS, Wechsler MS, Read TA (1955) Cubic to orthorhombic diffusionless phase change—experimental and theoretical studies of AuCd. J Appl Phys 26:473–484
- Bowles JS, Mackenzie JK (1954) The crystallography of martensite transformations. Acta Metall 2:129–138
- Eshelby J (1957) The determination of the elastic field of an ellipsoidal inclusion, and related problems. Proc Royal Soc (London) Pt A 241:376–396
- 11. Mura T, Mori T, Kato M (1976) The elastic field caused by a general ellipsoidal inclusion and the application to martensite formation. J Mech Phys Solids 24:305–318
- 12. Kato M, Miyazaki T, Sunaga Y (1977) Re-examination of the minimization of elastic energy and the phenomenological crystallographic theory in a martensitic transformation. Scr Metall 11:915–919
- 13. Horikawa H, Ichinose S, Morii K, Miyazaki S, Otsuka K (1988) Orientation dependence of $\beta_1 \to \beta_1'$ stress-induced martensitic transformation in a Cu–Al–Ni alloy. Metall Trans A 19:915–923
- Fousek J, Janovec V (1969) The orientation of domain walls in twinned ferroelectric crystals.
 J Appl Phys 40:135–142
- 15. Sapriel J (1975) Domain-wall orientations in ferroelastics. Phys Rev B 12:5128-5140
- Tagantsev AK, Cross LE, Fousek J (2010) Domains in ferroic crystals and thin films. Springer, New York, Dordrecht, Heidelberg, London
- Roytburd AL (1993) Elastic domains and polydomain phases in solids. Phase Transitions 45:1–33
- Metrat G (1980) Theoretical determination of domain structure at transition from twinned phase: application to the tetragonal-orthorhombic transition of KNbO₃. Ferroelectrics 26:801–804

- Kuhn W (1991) Domain structures induced by phase transitions in BaTiO₃ single crystals. Ferroelectr Lett Sect 13:101–108
- 20. Topolov VYu, Balyunis LE, Turik AV, Eremkin VV, Sori BI (1992) S-type twinning (domain) boundaries in PbZrO₃ crystals. Soviet Phys Crystallogr 37:223–226
- Topolov VYu, Turik AV (1990) Elastic interaction of phases of Gd₂(MoO₄)₃ crystals.
 Izvestiya Vysshikh Uchebnykh Zavedeniy, Fizika 33(3):68–72 (in Russian)
- 22. Nakamura T, Kondo T, Kumada A (1971) Observation of phase boundaries between ferroand paraelectric phases in Gd₂(MoO₄)₃ crystals. Solid State Commun 9:2265–2268
- Topolov VYu, Turik AV (1987) On the elastic interaction between polar phases at phase transitions in ferroelectrics. Deposed at VINITI. Reg. No 1546-B87, 3 March 1987, 47 p (in Russian)
- Topolov VYu (1999) Interfaces in ferroelectrics and related materials with complex domain structures. Ferroelectrics 222:41–52
- Dudnik EF, Nepochatenko VA (1980) Phase boundaries in a lead orthophosphate ferroelectric. Kristallografiya 25:981–988
- Balyunis LE, Topolov VYu, Bah IS, Turik AV (1993) The S-type domain and twin boundaries in plate-like PbZrO₃ crystals having complicated twinned structures. J Phys Condens Matter 5:1419–1426
- Tennery VJ (1966) High temperature phase transitions in PbZrO₃. J Am Ceram Soc 49:483–486
- 28. Kay HF, Vousden P (1949) Symmetry changes in barium titanate at low temperatures and their relation to its ferroelectric properties. Philos Mag 40:1019–1040
- Vasiliu F, Lucuţa PG, Constantinescu F (1983) Structure-sintering temperature relationship in PZT solid solutions at the morphotropic phase boundary. Physica Status Solidi (a) 80:637– 642
- Wersing W, Rossner W, Eckstein G, Tomandl G (1985) The morphotropic phase boundary in PZT ceramics prepared by spray drying of salt solutions and by the mixed oxide methods. Silicates Industriels 50:41–46
- 31. Helke G and Lubitz K (2008) Piezoelectric PZT ceramics. In: Heywang W, Wersing W, Lubitz K (eds) Piezoelectricity. Evolution and future of a technology. Springer, Berlin, pp 89–130
- 32. Topolov VYu (2009) Monoclinic phases and stress-relief conditions in (1-x)Pb $(Mg_{1/3}Nb_{2/3})O_3$ –xPbTiO $_3$ solid solutions. J Alloys Compd 480:568–574
- 33. Topolov VYu (2016) Domain and heterophase states in lead-free Ba(Ce_xTi_{1-x})O₃ solid solutions. Bull Russian Acad Sci Phys 80:1055–1058

Appendix B Optimal Volume Fractions in Terms of Angles Between Spontaneous Polarization Vectors Near the Morphotropic Phase Boundary

B.1 Optimal Volume Fractions and Polarization Rotations

In this section, we propose a crystallographic interpretation for relationships between the optimal volume fractions of the non-180° domains in the morphotropic phases. These relations were put forward for PZN-xPT SCs under $E \parallel [001]$ [see (3.4) and (3.5)] and for PZT at E = 0 [1]. Before the crystallographic description, we draw attention to Table 3.1 where dependences of the optimal volume fractions $n_{\text{T,opt}}(E), n'_{\text{T,opt}}(E), \nu_{\text{M,opt}}(E), \text{ and } \nu'_{\text{M,opt}}(E) \text{ are given. We note, for example, that at}$ the electric-field-induced phase transition, $n_T(E)$, characterizes the volume fraction of the 90° domains with the spontaneous polarization $P_{s1} \parallel E \parallel [001]$ in the tetragonal phase, and the spontaneous polarization vector $P_T = n_T P_{s1} + (1 - n_T) P_{s2}$ of a polydomain region would rotate towards the E vector with increasing E. Taking into account the orientations of P_{sk} (see domains 1–2 in Fig. 3.2), one can show that $P_{\rm T}E = n_{\rm T}P_{\rm s1}E$; therefore, $P_{\rm T}E\cos(P_{\rm T}, {}^{\wedge}E) = n_{\rm T}P_{\rm s1}E$ and $n_{\rm T} \sim \cos(P_{\rm T}, {}^{\wedge}E)$. The optimal volume fraction $n_{T, opt}$ is achieved at elastic matching of the coexisting phases along ZNSPs (see Sect. 3.2.2), and in this case one can expect a correlation between $n_{\rm T, opt}$ and cosine of an angle between the spontaneous polarization vectors of individual domains in the coexisting phases. Based on this assumption and results of work [1], we represent interrelations between the optimal volume fractions of the non-180 $^{\circ}$ domains [see (3.4) and (3.5)] as follows:

$$\cos \alpha_{Rh-Tg} \approx \cos \alpha_{Rh-Mc} \cos \alpha_{Tg-Mc},$$
 (B.1)

where α_{Rh-Tg} , α_{Rh-Mc} and α_{Tg-Mc} are the angles between the spontaneous polarizations of the non-180° domains (one type in each phase, see Fig.B.1a) in the neighbouring phases. Below, we examine the validity of (B.1) at possible domain orientations of the domains in the coexisting phases (Table B.1).

The orientation of the P_{Mc} vector (Table B.1) strongly depends on the mutual arrangement of the P_{Rh} and P_{T} vectors in the adjacent phases. It can be accounted for by the relation between the orientations of these vectors, as is known from the polarization rotation concepts [2, 3], see also the domain orientation and the

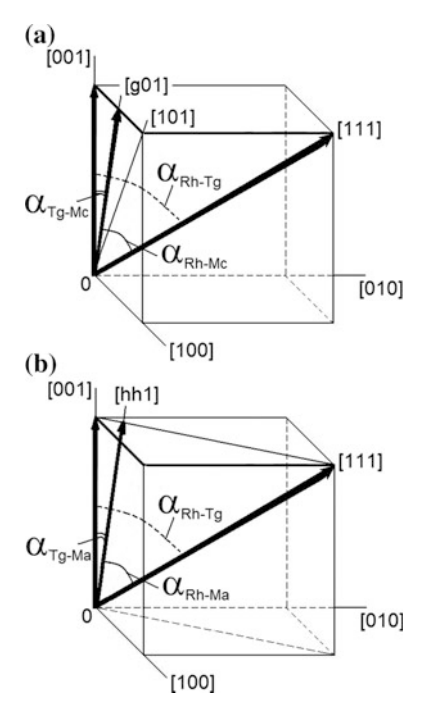


Fig. B.1 Angles between the spontaneous polarization vectors in the perovskite unit cell at phase transitions in PZN–xPT (a) and PZT (b). The spontaneous polarization vectors are oriented as follows: $P_{\mathbf{Rh}} \parallel [111]$ (rhombohedral phase), $P_{\mathbf{Tg}} \parallel [001]$ (tetragonal phase), $P_{\mathbf{Mc}} \parallel [g01]$ (M_C phase) and $P_{\mathbf{Ma}} \parallel [hh1]$ (M_C phase), where 0 < g < 1 and 0 < h < 1

polarization path [111] \rightarrow [001] in Fig. 2.8). Any intermediate orientations of the P_{Mc} vector (0 < g < 1) can be predicted if we take into account a field dependence of the angle $\alpha_{\text{Rh}-\text{Tg}}$ between the domains in the rhombohedral and tetragonal phase. The coexistence of the rhombohedral and tetragonal phases in PZN-0.08PT SCs was observed in a certain range of E [4]; however, reliable experimental values of the unit-cell parameters measured under the electric field E || [001] are unavailable for this and other compositions near the MPB. As a consequence, Table 3.1 does not contain the field dependence of the optimal volume fractions $n_{\text{T,opt}}$ and $n'_{\text{T,opt}}$ at the rhombohedral-tetragonal phase transition.

It should be added that conditions for the optimal volume fractions of the non-180° domains were also found [1] for PZT at E=0. In Sect. 2.1.2, we highlighted the virtual constancy of the optimal volume fractions of the non-180° domains (Table 2.2) at elastic matching of the morphotropic phases along ZNSPs. A comparison with (3.4)–(3.5) shows that the optimal volume fractions of the domains in the coexisting phases of the PZT system near the MPB are interrelated as follows:

Orientation of the spontaneous polarization vector $P_{\rm Rh}$ in the rhombohedral phase	Orientation of the spontaneous polarization vector P_{Tg} in the tetragonal phase	Miller index g and orientation of the spontaneous polarization vector P_{Mc} in the M_C phase ^a
[111]	Ⅱ [001]	$0 < g \ll 1$, P_{Mc} close to [001]
	II [100]	$g \approx 1$, P_{Mc} close to [101]
	[010]	b
[111]	Ⅱ [001]	b
	II [100]	$g \approx -1$, P_{Mc} close to $[\bar{1}01]$
	[010]	b
[11]	[001]	b
	II [100]	$g \approx -1$, P_{Mc} close to $[\bar{1}01]$
	[010]	b
[111]	[001]	$0 < g \ll 1$, P_{Mc} close to [001]
	II [100]	$g \approx 1$, P_{Mc} close to [101]
	II [010]	b

Table B.1 Validity of (B.1) at various orientations of spontaneous polarization vectors in the coexisting phases

$$n_{\text{T,opt}}(\text{Rh-Tg}) \approx n_{\text{M,opt}}(\text{Rh-Ma}) \cdot n_{\text{M,opt}}(\text{Tg-Ma})$$
 (B.2)

and

$$n'_{\text{T,opt}}(\text{Rh-Tg}) \approx n'_{\text{M,opt}}(\text{Rh-Ma}) \cdot n_{\text{T,opt}}(\text{Ma-Tg}). \tag{B.3}$$

In (B.2) and (B.3), $n_{T,opt}$, $n_{M,opt}$, $n'_{T,opt}$ and $n'_{M,opt}$ are the optimal volume fractions defined in Sect. 2.1.2, and abbreviations Rh, Tg and Ma denote the rhombohedral, tetragonal and M_A phases, respectively. Equations (B.2)–(B.3) differ from (3.4)–(3.5) that were formulated for PZN–xPT SCs with the intermediate M_C phase arising under the electric field $E \parallel [001]$. In our opinion, the main reason for such a difference is a result of the different polarization rotation paths in PZT and PZN–xPT [2, 3]. However, despite this difference, interrelations between the angles in the polarization rotation path (Fig. B.1b) can be represented by analogy with (B.1):

$$\cos \alpha_{Rh-Tg} \approx \cos \alpha_{Rh-Ma} \cos \alpha_{Tg-Ma}.$$
 (B.4)

In (B.4), α_{Rh-Tg} , α_{Rh-Ma} and α_{Tg-Ma} are the angles between the spontaneous polarization vectors of the non-180° domains (see Fig. B.1b), and subscripts denote the phase coexistence for which the angle is introduced: rhombohedral-tetragonal (Rh-Tg), rhombohedral-M_A (Rh-Ma) or tetragonal-M_A (Tg-Ma).

Table B.2 contains data on mutual orientations of the P_{Rh} , P_{Tg} and P_{Ma} vectors in the morphotropic phases of the PZT system. The possible orientations of the

 $^{{}^{}a}P_{\mathbf{Mc}} \parallel [g01]$ with respect to the perovskite unit cell

^bCondition (B.1) does not hold at the chosen domain orientations in the rhombohedral and tetragonal phases

Orientation of the spontaneous polarization vector P_{Rh} in the rhombohedral phase	Orientation of the spontaneous polarization vector P_{Tg} in the tetragonal phase	Miller index h and orientation of the spontaneous polarization vector P_{Ma} in the M_A phase ^a
[111]	[001]	$0 < h \ll 1$, P_{Ma} close to [001]
	[100]	$h \approx 1$, P_{Ma} close to [111]
	[010]	$h \approx 1$, P_{Ma} close to [111]
$ [1\bar{1}1] $	[001]	$ h \ll 1$, P_{Ma} close to [001]
	[100]	b
	[010]	b
[11]	[001]	$0 < h \ll 1$, P_{Ma} close to [001], or $h \approx -1$, P_{Ma} close to $[\bar{1}\bar{1}1]$
	[100]	$h \approx -1$, $P_{\mathbf{Mc}}$ close to $[\bar{1}\bar{1}1]$
	[010]	$h \approx -1$, P_{Mc} close to $[\bar{1}\bar{1}1]$
[111]	[001]	$ h \ll 1$, P_{Ma} close to [001]
	[100]	b
	[010]	b

Table B.2 Validity of condition (B.4) at various orientations of spontaneous polarization vectors in the coexisting phases of PZT

spontaneous polarization vector P_{Ma} in domains of the intermediate M_A phase are inseparably linked with the chosen orientations of P_{Rh} and P_{Tg} in the neighbouring phases (see Fig. B.1b), and this important link again points to the M_A phase as a bridging phase [5] in the MPB region of PZT. A more detailed analysis of (B.4) and the determination of limits of its validity (at possible changes in the DS, molar concentration x, temperature T, etc.) needs additional reliable experimental data on the unit-cell behaviour of PZT both just at the MPB and small deviations away from it.

We hope that the conditions similar to those represented in (B.1) and (B.4) may be formulated for various systems of FE solid solutions wherein the intermediate phases are detected close to the MPB.

References

- Topolov VYu, Turik AV (2002) An intermediate monoclinic phase and electromechanical interactions in xPbTiO₃ – (1 – x)Pb(Zn_{1/3}Nb_{2/3})O₃ crystals. Phys Solid State 44:1355–1362
- Fu H, Cohen RE (2000) Polarization rotation mechanism for ultrahigh electromechanical response in single-crystal piezoelectrics. Nature 403:281–283
- Noheda B, Cox DE, Shirane G, Park S-E, Cross LE, Zhong Z (2001) Polarization rotation via a monoclinic phase in the piezoelectric 92%PbZn_{1/3}Nb_{2/3}O₃–8%PbTiO₃. Phys Rev Lett 86:3891–3894

 $^{{}^{\}mathrm{a}}P_{\mathrm{Ma}} \parallel [hh1]$ with respect to the perovskite unit cell

^bCondition (B.4) does not hold at the chosen domain orientations in the rhombohedral and tetragonal phases

- 4. Kim S, Yang S-I, Lee J-K, Sun K (2001) Raman study of an electric-field-induced phase transition in $Pb(Zn_{1/3}Nb_{2/3})O_3-8\%PbTiO_3$. Phys Rev B 64:094105–5 p
- Noheda B, Cox DE (2006) Bridging phases at the morphotropic boundaries of lead oxide solid solutions. Phase Transitions 79:5–20

About the Author

Vitaly Yuryevich Topolov was born in Rostov-on-Don, Russia (former USSR) on 8 November 1961. He earned the qualification 'Physicist. Educator' (honours degree) in 1984 along with the degrees 'Candidate of Sciences (Physics and Mathematics)' and 'Doctor of Sciences (Physics and Mathematics)' in 1987 and 2000, respectively, all from the Rostov State University, Russia. From 1987 to 1991, he worked as a Research Scientist at the Institute of Physics at the Rostov State University. From 1991 to 2000, he worked as a Senior Lecturer (1991–1992) and an Associate Professor (1992–2000) of the Department of Physics at the Rostov State University. Since 2000, he has been a Professor of the same Department. Since December 2006, after reforming the Rostov State University, he is a Professor of the Department of Physics at the Southern Federal University (Rostov-on-Don, Russia).

Dr. V. Yu. Topolov was also a Visiting Scientist at the Moscow State University, Russia (former USSR, 1989), University of Saarland, Germany (1994–1995), Aachen University of Technology—RWTH Aachen, Germany (1998), Karlsruhe Research Center, Germany (2002 and 2003–2004), University of Bath, UK (2006, 2007, 2012, 2013, 2014, 2015, 2016 and 2017) and University of Rome Tor Vergata, Italy (2008). His research interests include heterogeneous ferroelectrics, smart materials, domain and heterophase structures, as well as electromechanical effects in ferroelectrics and related materials. He earned the special award from the International Science Foundation (1993) and the Soros Associate Professor title and awards from the International Soros Science-Educational Program and the Open Society Institute (1997, 1998, 2000 and 2001). He presented the best poster at the International Symposium on Ferroelectric Domains (China, 2000), the best oral report at the International Conference on Relaxation Phenomena in Solids (Russia, 2010), the best training aids in the Department of Physics, Southern Federal University (Russia, 2006 and 2011) and the best research works in the Department of High Technologies, Southern Federal University (Russia, 2008 and 2011). He is an author of four monographs published at Springer (London, UK, 2009; Berlin, Heidelberg, Germany, 2012; Berlin, Heidelberg, Germany, 2014; Cham, Switzerland, 2016), two edited monographs published at Springer (Cham, Heidelberg, New York, Switzerland, Germany, USA, 2014 and 2016), one edited

190 About the Author

monograph published at *Nova Science Publishers* (New York, USA, 2016), five chapters in monographs published at *Nova Science Publishers* (New York, USA, 2010–2013), and over 430 scientific papers, reviews, conference proceedings and abstracts. He has been included in the list of Active Russian Scientists.

He is Honorary co-worker of Higher Professional Education of the Russian Federation (Ministry of Education and Science of the Russian Federation, Moscow, Russia, 2009) and member of the International Biographical Centre Top 100 Educators (Cambridge, UK, 2010) and Top 100 Scientists (Cambridge, UK, 2012). Biographical data by him have been published in 'Dictionary of International Biography' (*IBC*, Cambridge, UK), '2000 Outstanding Intellectuals of the 21st Century' (*IBC*, Cambridge, UK) and 'Who's Who in the World' (*Marquis*, New Providence, USA).

Index

```
Domain boundary. See boundary
Boundary
                                                   Domain structure, 1, 20, 40, 56, 57, 59, 61, 84,
   domain, 10 See also domain wall, 131
                                                          151, 164
                                                      formation, 3, 5
       classification, 9
       S-type, 12
                                                      hierarchical, 41
   interphase, 6, 10, 13, 17, 19, 20, 45, 48, 57,
                                                      morphotropic, 35
       58, 70, 72, 75, 82, 93, 101, 102, 105,
                                                      rearrangement, 16
       107, 136, 137, 167–169, 171–174, 176,
                                                      similarity, 44
                                                   Domain wall, 3, 131, 137, 152
       177
   interphase
                                                      allowable, 6
       conical surface, 18
                                                      permissible planar, 7
       planar. See zero-net-strain plane
                                                      S, 11, 174
                                                       W_{\infty}-type, 7
C
                                                       W_{\rm f}-type, 7
Coefficient
                                                   \mathbf{E}
   thermodynamic, 111
Criterium of nucleation and growth, 113, 115,
                                                   Elastic and electrostriction energy, 112
                                                   Elastic matching, 6, 34, 53, 71, 83, 108, 117,
   concentration, 115, 116
                                                          126, 153, 175, 177, 184
   thermodynamic, 115, 116, 118
                                                   Electric field, 70, 81
                                                   Electrostriction parameter, 112
                                                      generalized, 113
Diagram, 18, 44, 45, 54, 63, 74, 85, 93, 94,
       101, 143, 156, 157, 159
   domain state-interface, 36-38, 48, 49, 51,
                                                   Ferroelastic, 7
       76, 77, 79, 80, 86–88, 90, 91, 93
                                                   Ferroelectric, 1
   phase, 25
                                                      lead-free, 135, 141, 153, 158, 159
   S<sub>i</sub>-interface, 125
   x–T, 25, 26, 32, 73, 106, 116, 118
Distortion, 10, 11, 121, 168
                                                   Heterophase state, 20, 44, 56, 75, 142, 145,
   matrix, 28, 36, 90, 100, 107, 123, 128, 149,
                                                          148, 153, 165
                                                      three-phase, 19, 20, 99, 101, 106-108, 110,
       170
   unit-cell, 29, 37, 43, 141, 144
                                                          117, 146, 150-152
Domain, 2, 28, 31, 34, 36, 38, 43, 47, 50, 53,
                                                      two-phase, 31, 47, 62, 95, 107
      56, 60, 73, 74, 79, 82, 87, 90, 103, 104,
       109, 139, 142, 147, 153, 155, 183, 184,
       186
                                                   Induced strain, 84, 112
                                                   Interface, 2, 153
   elastic, 4, 168 See also twin and twin
       component, 4
                                                   Interphase boundary. See boundary
```

© Springer International Publishing AG, part of Springer Nature 2018 V. Yu. Topolov, *Heterogeneous Ferroelectric Solid Solutions*, Springer Series in Materials Science 151, https://doi.org/10.1007/978-3-319-75520-5

192 Index

M	Piezoelectric properties, 136, 151, 158
Metrat's algorithm, 11, 13, 18, 171–173, 176, 178	Polarization path, 42
Miller indices, 10	R
Misfit dislocations, 127	Relaxor, 69
Model	
interpenetrating phases, 51, 52, 54, 60, 95	S
three-phase single crystal, 105	Sapriel's approach, 178
transition region, 128	Single crystal
Morphotropic phase boundary, 26, 33, 37, 39,	domain-engineered, 26, 55
56	relaxor-ferroelectric, 34, 41
N	Solid solution, 25, 163, 165
N	Spontaneous polarization vector, 72, 91, 94,
Nanodomain, 41, 70	110, 115, 118, 128, 183–185
	Spontaneous strain, 7, 11, 59, 169, 170, 172,
Ontimal adaptation 12	173, 175, 176, 178
Optimal orientation, 13	Stress relief, 5, 19, 20, 31, 34, 94, 95, 99, 109,
Optimal volume fraction, 13, 29, 33, 49, 51,	116, 126, 145, 150, 158, 164, 176
58, 60, 61, 83, 85, 93, 105, 147, 149,	complete, 29, 30, 39, 80, 140, 144, 147–149, 155 <i>See also</i> zero-net-strain
170, 179, 183, 184 Orientation state, 123, 124, 130	plane, 147
Outer layer, 122	plane, 147
Overlapping structure, 121, 126	T
overlapping suractione, 121, 120	Thermodynamic equilibrium, 113
P	Thermodynamic formalism, 110, 117
Phase	Transition region, 127, 128
coexistence, 27, 30, 35, 40, 41, 54, 55, 71,	Twin, 47
72, 74, 76, 80, 82, 136, 137, 139, 141,	Twin component, 3
144, 148, 158	
dominant, 40	U
ferroelectric, 42	Unit-cell parameter, 27, 39, 55, 62, 73, 80, 81,
inside, 121, 122, 124	85, 122, 123, 127, 129, 130, 146, 158,
intermediate, 54, 56, 72, 95, 99, 186	164, 174, 179, 184
interpenetrating. See model	
monoclinic, 25, 31, 39, 95	V
morphotropic, 109, 159, 185	Volume fraction, 109, 111, 144, 147, 148, 158
outer, 124	domain, 38, 74, 75, 78, 86, 92, 103
sequence, 87, 89, 95, 104	heterophase region, 52
single-domain, 8, 16 Phase transition, 3, 35, 43, 57, 114, 170	optimal. See optimal volume fraction
Phase transition, 3, 35, 43, 57, 114, 179 electric-field-induced, 70, 83, 85, 88	Z
first-order, 3, 14, 16, 17, 51, 102, 163,	Zero-net-strain plane, 5, 18, 31, 33, 35, 37, 44,
164, 167	45, 48, 50, 53, 55, 58, 61, 75, 78, 80, 84,
martensitic, 5, 167, 169	89, 94, 100, 103, 105, 115, 129, 131,
sequence, 16	150
Physical properties, 1	necessary conditions, 16, 30
Piezoelectric coefficient. See piezoelectric	
properties	